Gravitoturbulence, and its Interactions with the Magneto-Rotational Instability, in Accretion Disks

Von der Universität Bayreuth
zur Erlangung des Grades eines
Doktors der Naturwissenschaften (Dr. rer. nat.)
genehmigte Abhandlung

von

Lucas Löhnert

aus Münchberg

1.Gutachter Prof. Dr. Arthur Godfried Peeters
2.Gutachter Prof. Dr. Wolf-Christian Müller

Tag der Einreichung: 12.06.2023
Tag des Kolloquiums: 13.10.2023

Contents

Chapter 1

Zusammenfassung

Die hier gezeigten Arbeiten haben das Ziel die nichtlineare Entwicklung der Gravitationsinstabilität (GI, siehe z.B. Kratter & Lodato 2016) und von GI in Kombination mit der Magnetorotationsinstabilität, im Kontext von Akkretionsscheiben, zu untersuchen. Zu diesem Zweck werden numerische Simulationen von Akkretionsscheiben, in der lokalen Shearing-Box Approximation (siehe z.B. Balbus & Hawley 1998) durchgeführt und ausgewertet. Dabei wird nur ein kleiner Teil der Scheibe betrachtet, der, bei einem bestimmten Radius, mit dem Material der Scheibe mitrotiert. Im mitrotierenden Bezugssystem erscheint die differentielle Rotation der Akkretionsscheibe als lokale Scherströmung. Lokale Modelle sind dahingehend vorteilhaft, dass sie eine genauere Analyse der Turbulenz-Dynamik erlauben. Im Kontext der Magnetohydrodynamik beinhaltet das auch mögliche Dynamo-Prozesse. Zusammengefasst werden hier die drei Arbeiten Löhnert, Krätschmer, & Peeters (2020), Löhnert & Peeters (2022) und Löhnert & Peeters (2023). Aus Übersichtlichkeitsgründen werden die letztgenannten Arbeiten im Folgenden als LPK20, LP22 und LP23 abgekürzt.

Ziel der ersten Arbeit, LPK20, ist es eine bessere Einsicht in die Turbulenz-Struktur von GI zu gewinnen. Dabei wird ein effektiv zweidimensionales (razor-thin) Modell verwendet (siehe z.B. auch Gammie 2001), wobei angenommen wird, dass die vertikale Ausdehnung der Schreibe hinreichend klein ist, im Vergleich zu allen dynamisch relevanten, horizontalen Längenskalen. Für die Simulationen wird der Hydrodynamik-Code *DiskFlow* verwendet. Häufig wird Turbulenz mit einer Energiekaskade, hin zu immer kleineren Längenskalen, assoziiert oder auch einer inversen Kaskade, im Falle von zweidimensionaler Turbulenz (siehe z.B. Frisch 1995; Boffetta & Ecke 2012). Im Inertialbereich des kinetischen Leistungsspektrums führt die Kaskade zu einem spezifischen Potenzgesetz. Inwiefern das bei GI-Turbulenz auftritt ist nicht hinreichend klar (Kratter & Lodato 2016). Daher ist ein Ziel, in LPK20, die Turbulenz-Geometrie von GI genauer zu untersuchen. Dabei ist ein Resultat, dass die radialen Geschwindigkeitsfluktuationen, v_x, zu einem Potenzgesetz der Form k_x^{-2}, in der zugehörigen spektralen Leistungsdichte, führen, wobei k_x hier den radialen Wellenvektor darstellt. Das Skalengesetz ist konsistent mit dem Auftreten von hydrodynamischen Shocks (Diskontinuitäten), in der radialen Geschwindigkeitskomponente v_x. Dabei wird für eine generische Shock-Geometrie, $v_x(x)$, gezeigt, dass die zugehörige Fouriertransformation ein k_x^{-2}-Potenzgesetz im Energiespektrum reproduzieren kann. Es wird zudem demonstriert, dass die turbulenten Spannungen (Reynolds und gravitativ) durch ein einfaches Mischungsweg-Modell abgeleitet werden können. In diesem Zusammenhang wird die typische Längenskala durch die Shockgröße bestimmt und die typische Zeitskala durch die inverse Wachstumsrate der meist-instabilen Mode.

In vielen Fällen ist das Scheibenmaterial (Plasma) hinreichend ionisiert, sodass Magnetfelder im Fluid eingefroren sind. Eine Möglichkeit das Modell dahingehend zu erweitern ist eine magnetohydrodynamische Beschreibung. Kleine Magnetfeldstärken reichen aus um die Magnetorotationsinstabilität (MRI) auszulösen. In manchen Akkretionsscheiben könnten daher sowohl GI als auch MRI gle-

ichzeitig aktiv sein. Das kann, zum Beispiel, auf bestimmte Regionen in Protoplanetaren Scheiben (PPDs) zutreffen, die eine hinreichende Oberflächenmassendichte aufweisen und ausreichend ionisiert sind. Und eine Kobination von GI und MRI könnte insbesondere für aktive galaktische Kerne (AGNs) relevant sein (siehe z.B. Menou & Quataert 2001; Goodman 2003). Daher stellt sich die Frage ob und wie GI und MRI wechselwirken. In PPDs könnte die Wechselwirkung indirekt erfolgen, wobei GI und MRI in verschiedenen, räumlich getrennten Teilen der Scheibe aktiv sind. Verschiedene Akkretionsraten, von GI und MRI, könnten dann zu nicht-stetiger Akkretion führen (siehe z.B. Armitage, Livio, & Pringle 2001; Zhu, Hartmann, & Gammie 2009; Zhu, Hartmann, & Gammie 2010; Martin & Lubow 2011; Martin et al. 2012). Weniger klar ist das Resultat einer direkten Wechselwirkung der beiden Turbulenzmechanismen. Erste, globale Simulationen (Fromang et al. 2004; Fromang 2005) deuteten darauf hin, dass beide Instabilitäten gleichzeitig auftreten können, wobei MRI das Erscheinungsbild der GI beeinflussen kann. Neuere, lokale Simulationen (Riols & Latter 2018a; Riols & Latter 2019) deuten darauf hin, dass MRI von der GI unterdrückt werden könnte, wobei GI selbst zu einem Dynamoprozess führt. Dynamoaktivität in GI-Turbulenz wurde in vielen aktuellen Simulationen beobachtet (Riols & Latter 2018a; Riols & Latter 2019; Deng, Mayer, & Latter 2020; Riols et al. 2021; Béthune & Latter 2022), einschließlich der hier dargestellten Arbeiten, LP22 und LP23. Dabei geht die Arbeit LP22 detaillierter auf die Möglichkeit einer direkten Koexistenz zwischen GI und MRI ein, wobei ein wesentliches Resultat darin besteht, dass eine Koexistenz möglich ist. LP22 wird im folgenden Absatz kurz vorgestellt.

Die Simulationen in der ersten Arbeit, LPK20, sind rein hydrodynamisch und zudem zweidimensional. Für reine GI-Rechnungen kann das von Vorteil sein und erhebliche Ressourcen-Einsparungen bei den Simulationen bewirken. Allerdings sind die typischen MRI-Längenskalen kleiner als die typischen GI-Skalen und relevante Dynamik kann auch auf der mittleren Diskhöhe erfolgen. Daher wird das Modell in LP22 auf eine dreidimensionale Shearing-Box Anordnung erweitert, wobei für die Simulationen dann der MHD-Code Athena verwendet wird. Ausgangspunkt sind MHD-Simulationen reiner GI, mit verschwindendem Magnetfeld. Anschließend wird ein schwaches Magnetfeld, mit verschwindendem Netto-Fluss (zero-net-flux oder ZNF), in den reinen GI-Zustand eingebettet. Eine wesentliche Schlussfolgerung ist, dass die daraus resultierenden, saturierten Zustsände konsistent sind, mit einer Koexistenz von GI und MRI. Die beobachteten, turbulenten Spannungen können konsistent in Beiträge von GI und MRI zerlegt werden. In allen Fällen liegt das Verhältnis aus der Maxwell-Spannung und dem magnetischen Druck, $\langle -2B_x B_y \rangle / \langle |\mathbf{B}|^2 \rangle$, im $(0.3 - 0.4)$-Intervall, was genau dem MRI-typischen Wertebereich entspricht (siehe z.B. Hawley, Gammie, & Balbus 1995; Blackman, Penna, & Varnière 2008; Simon, Hawley, & Beckwith 2011; Hawley, Guan, & Krolik 2011; Salvesen et al. 2016). Zudem wird beobachtet, dass die horizontal gemittelte, magnetische Feldkomponente, B_y, als Funktion von der Höhe über der Disk-Mittelebene, zeitliche Oszillationen entwickelt. Letztere ähneln den Butterfly-Diagrammen, die häufig in MRI-Simulationen beobachtet werden (siehe z.B. Miller & Stone 2000; Turner 2004; Hirose, Krolik, & Stone 2006; Shi, Krolik, & Hirose 2010; Simon, Beckwith, & Armitage 2012; Salvesen et al. 2016). Die letztgenannten Resultate beziehen sich zumeist auf die saturierte Phase der Simulationen. Durch die niedrige, initiale Feldstärke ist MRI, direkt nach Einführung des Feldes, nicht aufgelöst, was sich durch einen niedrigen Quality-Faktor Q_{mri} (siehe z.B. Noble, Krolik, & Hawley 2010), ausdrückt. Dennoch wird eine anfängliche Feldverstärkung beobachtet, was darauf hindeutet, dass GI als Dynamo wirken kann. Für den saturierten Zustand wird gezeigt, dass die beobachteten Feldoszillationen konsistent sind, mit einem $\alpha - \Omega$ Dynamo-Mechanismus. Die exakten Dynamoparameter können dabei vom Abstand zur Disk-Mittelebene abhängen.

Die dritte Arbeit, LP23, ist ein Folgeartikel zu LP22. Ein wesentlicher Teil der Arbeit besteht darin, den Einfluss der GI-Stärke auf den Zustand von GI-MRI-Koexistenz zu testen. Die GI-Stärke wird dabei kontrolliert durch Variieren des Modells für Strahlungs-Kühlung (Heizung). Dabei ist zu beachten, dass GI durch thermische Selbstregulierung saturiert (Gammie 2001), wobei die turbulente Aufheizung ausgeglichen wird durch die Kühlung. Daher kann, je nach

Effizienz der Kühlung, die stärke von GI variieren. Alle getesteten Fälle, außer dem Fall mit der stärksten GI-Aktivität, sind konsistent mit GI-MRI-Koexistenz. Obwohl die GI-Aktvität signifikant variieren kann, führen alle Simulationen zu relativ ähnlichen Maxwellspannungen. Insbesondere das Verhältnis aus Maxwellspannung und magnetischem Druck ist konstant im MRI-typischen Intervall, wogegen die GI-Aktivität um den Faktor Zwei variiert. Alle Simulationen, ausgenommen der Fall mit der stärksten GI-Aktivität, entwickeln ein Butterfly-Diagramm im saturierten Zustand. In dem Fall mit der stärksten GI-Aktivität entsteht ein weniger ausgeprägtes, weniger reguläres Butterfly-Diagramm. Die horizontal gemittelten electro-motive-forces (EMFs) und magnetischen Feldkomponenten, als Funktion der Höhe über der Mittelebene, sind weitestgehend konsistent mit einer Superposition aus GI und MRI, wobei auch hier die Übereinstimmung für den Fall mit der stärksten GI am geringsten ist. Die letztgenannten Simulationen beziehen sich auf den Grenzfall idealer MHD. In realistischen Akkretionsscheiben, insbesondere in PPDs, können, als Folge geringer Ionisation, nicht-ideale Effekte relevant sein (siehe z.B. Armitage 2011). Die Entwicklung von MRI, in nicht-idealen Regimen, wurde in einer vielzahl von Simulationen untersucht, wobei ein wesentliches Resultat darin besteht, dass MRI nicht in allen Fällen auftreten kann. Der einfachste nicht-ideale Effekt is Ohm'sche Dissipation. Ähnlich der hydrodynamischen Reynolds-Zahl, Re, kann eine magnetohydrodynamische Reynolds-Zahl, Rm, definiert werden, indem die Viskosität durch den spezifischen Ohm'schen Widerstand ersetzt wird. Wenn Rm zu klein gewählt wird, kann MRI stark geschwächt oder ganz unterdrückt werden (siehe z.B. Sano & Stone 2002; Ziegler & Rüdiger 2001; Simon & Hawley 2009; Simon, Hawley, & Beckwith 2011). Daher wird in LP23 die Möglichkeit von GI-MRI-Koexistenz, mit zusätzlicher Ohm'scher Dissipation, untersucht. Wird Rm klein genug gewählt, entwickelt sich ein neuer, nichtlinearer Zustand, der qualitativ von GI-MRI-Koexistenz abweicht. In dem neuen Zustand werden höhere magnetische Feldstärken erreicht, was ebenfalls darauf hinweist, dass GI als Dynamo wirken kann. Zeitliche Oszillationen treten hier ebenfalls auf, allerdings bleiben Polaritätswechsel des Magnetfeldes aus. Im Gegensatz zu den Butterfly-Diagrammen entstehen die Oszillationen hier durch periodisches Quenchen und Wiederanwachsen von GI. Das GI-Quenching resultiert als Folge der signifikanten Produktion von thermischer Energie (Heizung) durch die Ohm'sche Dissipation von magnetischer Energie. Ein qualitativer Übergang findet bei magnetischen Reynoldszahlen von Rm ~ 500 statt. Größere Werte führen zu Zuständen die Ähnlichkeiten mit dem idealen MHD Fall stärkster GI-Aktivität haben.

Chapter 2

Summary

The research, described in this thesis, aims to study the nonlinear state of the gravitational instability (GI, see, e.g., Kratter & Lodato 2016), and GI in combination with the magneto-rotational instability (MRI, see, e.g., Balbus & Hawley 1998), in the context of accretion disks. The main research method is the numerical simulation of accretion disks, in the local shearing-box approximation (see, e.g., Balbus & Hawley 1998). Thereby, only a small part of the disk is considered, that is co-rotating with the disk material, at a fixed fiducial radius. The differential rotation, of the accretion disk, appears as a shear flow in the local, co-rotating system. The advantage of local models is that they allow a more detailed analysis of the turbulence dynamics. In the magnetohydrodynamic (MHD) context, this also includes possible dynamo processes. Summarised here are the three different works, Löhnert, Krätschmer, & Peeters (2020), Löhnert & Peeters (2022), and Löhnert & Peeters (2023). For convenience, the latter three are, in the following, referred to as LPK20, LP22, and LP23, respectively.

The goal of the study LPK20 is to get a better insight into the turbulence structure of GI. Thereby, an effectively two-dimensional, razor-thin setup is used (see, e.g., Gammie 2001), assuming that the vertical disk scale is sufficiently short, in comparison to all dynamically relevant, horizontal length scales. For the simulations, the hydrodynamics code *DiskFlow* is used. Turbulence is often associated with an energy cascade towards ever smaller scales, or an inverse cascade in two dimensions (see, e.g., Frisch 1995; Boffetta & Ecke 2012). The cascade, in the inertial range, leads to a specific power law, in the power spectrum of the turbulent kinetic energy. Whether this is also the case for GI-induced turbulence is not entirely clear (Kratter & Lodato 2016). Hence, in LPK20, the turbulence geometry of GI is studied in more detail. It is observed that the power spectrum of the radial velocity fluctuations, v_x, develops a k_x^{-2} scaling, with the radial wave vector, k_x. It is found that this scaling is consistent with the appearance of hydrodynamic shocks. The velocity profile $v_x(x)$, for a typical shock geometry is analysed, and it is found that the corresponding Fourier transform is consistent with a k_x^{-2} scaling. It is also demonstrated that a simple mixing-length model can be constructed for GI turbulence. The typical length scale is associated with the shock-width, and the typical time scale is given by the inverse growth rate of the most linearly unstable mode.

Often, the disk material (plasma) is sufficiently ionised, so that the magnetic field is frozen into the fluid, necessitating the use of a magnetohydrodynamic description. A small magnetic seed field can then give rise to MRI turbulence. Hence, for some disk systems, both instabilities might be relevant simultaneously. This can, for example, be the case for certain regions of protoplanetary disks (PPDs), with sufficient surface-mass density, and ionisation. And the interplay between GI and MRI may be especially relevant for active galactic nuclei (see, e.g., Menou & Quataert 2001; Goodman 2003). Hence, the question arises how GI and MRI interact. In the context of PPDs, interactions might occur indirectly, with GI, and MRI, operating in different parts of the accretion disk. A

mismatch between the accretion rates (of GI, and MRI), can then lead to non-steady accretion (see, e.g., Armitage, Livio, & Pringle 2001; Zhu, Hartmann, & Gammie 2009; Zhu, Hartmann, & Gammie 2010; Martin & Lubow 2011; Martin et al. 2012). Less clear is the outcome of direct, turbulent interactions. Early, global simulations (Fromang et al. 2004; Fromang 2005) suggested that both instabilities can occur, and that MRI can influence GI. More recent, local simulations (Riols & Latter 2018a; Riols & Latter 2019) suggest that MRI might not be present, replaced by a GI dynamo. A possible GI dynamo is a more general finding of recent simulations (Riols & Latter 2018a; Riols & Latter 2019; Deng, Mayer, & Latter 2020; Riols et al. 2021; Béthune & Latter 2022), including the studies in this thesis. LP22 elaborates more closely on the possibility of direct coexistence between GI and MRI, and concludes that GI-MRI coexistence does occur. The main results of LP22 are briefly summarised, below.

The simulations in the first study, LPK20, discussed previously, are both purely hydrodynamical, as well as two-dimensional. Such a model can be reasonable for GI, and it can lead to significant savings of computational resources. However, the length scales, usually associated with MRI-induced turbulence, are shorter than those associated with GI, and important dynamics may take place over the vertical stratification length of the disk. Therefore, in LP22, a three-dimensional shearing-box setup is applied, whereby the MHD code Athena is used. The evolution of GI, in an MHD regime, is studied by introducing a weak, zero-net-flux (ZNF), magnetic-seed field, into a GI-turbulent state. The main conclusion, in LP22, is that the saturated states of GI-MHD simulations are consistent with a coexistence of both GI and MRI. The observed turbulent stresses can consistently be separated into contributions from GI, and MRI. Moreover, in all cases, the ratio of Maxwell stress to magnetic pressure, $\langle -2B_x B_y \rangle / \langle |\mathbf{B}|^2 \rangle$, is in the $0.3 - 0.4$ range, a value typical for the MRI, as shown in several studies (see, e.g., Hawley, Gammie, & Balbus 1995; Blackman, Penna, & Varnière 2008; Simon, Hawley, & Beckwith 2011; Hawley, Guan, & Krolik 2011; Salvesen et al. 2016). Additionally, the horizontally-averaged, magnetic field component, B_y, as a function of height, and time, shows an oscillating pattern, similar to a butterfly diagram, usually seen in pure-MRI turbulence (see, e.g., Miller & Stone 2000; Turner 2004; Hirose, Krolik, & Stone 2006; Shi, Krolik, & Hirose 2010; Simon, Beckwith, & Armitage 2012; Salvesen et al. 2016). The latter findings mostly concern the MHD-saturated phase. However, shortly after field seeding, MRI is not resolved (indicated by the quality factor, $Q_{\rm mri}$). Yet, a significant field amplification is observed. Hence, it is concluded that GI acts as a dynamo. It is then shown that the dynamo is consistent with an $\alpha - \Omega$-type mechanism, whereby the exact dynamo parameters seem to depend on the vertical elevation.

The third study, LP23, is a follow-up work to LP22. One goal is to further test the influence of GI strength on the nonlinear outcome of the ideal-MHD, GI-MRI combined state. The strength of GI is controlled, by modifying the cooling (heating) law, used in the simulations. That such changes of the cooling (heating) model can influence the GI strength is a direct consequence of the fact that GI saturates via a thermal self-regulation (see, e.g., Gammie 2001). All cases, except the case with strongest GI activity, are consistent with GI-MRI coexistence. Although the turbulent stresses, related to self-gravity, can vary significantly between the simulations, the Maxwell stresses are comparable in all cases. Most prominently, the ratio of Maxwell stress to magnetic pressure is equal to the pure-MRI value, in all cases, despite the GI strength varying up to a factor of two. The weaker GI-cases invariably lead to a clearly visible butterfly diagram. In the case with strongest GI activity, the butterfly diagram takes on a more irregular pattern. The vertical profiles of both the electro-motive forces (EMFs) and the magnetic field components, are mostly consistent with a superposition of GI and MRI contributions, whereby the least coincidence is found for the strong-GI case. All previous simulations were set up in the ideal-MHD limit (grid effects neglected). However, in realistic disk systems, especially in PPDs, non-ideal effects can be important, due to insufficient ionisation (see, e.g., Armitage 2011). Many studies have been dedicated to investigate the evolution of MRI in non-ideal regimes, with the conclusion that MRI might not be possible for all parameters.

The simplest, non-ideal effect is Ohmic resistivity. Similar to the hydrodynamic Reynolds number, Re, one can define a magnetohydrodynamic Reynolds number, Rm, replacing the viscosity by the Ohmic resistivity. If Rm is too small, MRI is not possible, or substantially weakened (see, e.g., Sano & Stone 2002; Ziegler & Rüdiger 2001; Simon & Hawley 2009; Simon, Hawley, & Beckwith 2011). Hence, in LP23, the GI-MRI coexistence state is studied, with a finite Ohmic resistivity. It is found that, for low enough Rm, the GI-MRI coexistence is replaced by a qualitatively new state. This state develops higher magnetic field strengths than GI-MRI coexistence, which we attribute to the GI dynamo, which operates more effectively without MRI. The new state also develops oscillations, though the latter are not obviously connected to a butterfly diagram, and field reversals are absent. It is found that theses oscillations are related to a periodic quenching, and re-emerging of GI. The quenching occurs as a consequence of significant heating, due to Ohmic resistivity. It is then shown that a transition occurs, for Rm ~ 500, with larger values leading to a state that is qualitatively closer to the ideal-MHD cases, and especially the case with the highest GI activity.

Chapter 3

Theoretical Introduction

3.1 Accretion disks

3.1.1 Accretion disks as a phenomenon

Many astrophysical objects take on planar, disk-like shapes, for example, protoplanetary disks, galaxies, or the surrounding areas of black holes. The exact process of disk formation can be different in each case, but first insights can be gained by some general considerations. One can, for example, consider a cloud of gas that contracts under its own gravity (see, e.g., Clarke & Carswell 2007). The cloud likely has a finite angular momentum, with respect to its centre of mass, and this angular momentum is conserved. Hence, as the diameter shrinks, the rotation velocity must increase. Internal energy, on the other hand, can be lost via radiation, to the surrounding regions. Consequently, such a system favours a disk-like shape. Such disks are often associated with the process of accretion, whereby mass is transferred towards a central object (at the disk center), although not by direct radial infall, but rather by a disk-induced inward spiralling of matter (see, e.g., Prendergast & Burbidge 1968; Lynden-Bell 1969; Pringle & Rees 1972). The infalling mass leads to the release of gravitational potential energy, heating the disk material. This, in turn, leads to the local emission of black-body radiation (see, e.g., Shakura 2018). The amount of released energy can be significant. Accretion onto black holes, for example in binary systems, can even lead to X-ray emissions (Prendergast & Burbidge 1968; Pringle & Rees 1972; Shakura & Sunyaev 1973). And also the significant luminosity of the central regions of active galaxies (called active galactic nuclei, or AGN), can be attributed to the significant amount of gravitational potential energy, released by accretion onto a super-massive black hole (Lynden-Bell 1969; Shields 1999), located at the AGN center. The latter examples are mostly accretion disks around black holes (or other compact objects), either in binary systems, or at the centres of AGNs. However, there are other types of accretion disks as well, for example, so-called protostellar, or protoplanetary disks (PPDs) (see, e.g., Armitage 2011). The theorised accretion processes are similar to the previously mentioned cases (Lynden-Bell & Pringle 1974; Bell et al. 1997; D'Alessio et al. 1998), except that the central object is now a young star. The temperatures in PPDs are usually smaller, and additional, more complex processes, can be involved in PPD dynamics. For example, the disk gas (plasma) might decouple from the ambient magnetic field, due to insufficient ionization, the optical and radiative properties can be altered by dust grains, and also planet formation can be involved in the disk dynamics (Armitage 2011). To first approximation, the material inside an accretion disk orbits the central object in nearly Kaplerian motion, with both the angular velocity, $\Omega \propto r^{-3/2}$, and the velocity, $v_\phi = \Omega\, r \propto r^{-1/2}$, decreasing radially outwards. However, the specific angular momentum increases with radius $\Omega\, r^2 \propto r^{1/2}$, which has crucial implications for disk dynamics (see, e.g. Balbus & Hawley 1998). Matter falling inwards looses angular momentum, and as the total angular momentum is conserved, the infalling mass requires angular momentum to

be transported outwards. In modern accretion-disk theory, a main part of this transport is caused by disk turbulence (see, e.g., Balbus & Hawley 1998; Shakura 2018). The role of turbulence is elucidated in upcoming sections.

3.1.2 Structure

Here, the viscous-disk theory is briefly outlined, which is a widely-used approach to model angular momentum transport, in accretion disks (Lynden-Bell & Pringle 1974; Pringle 1981; Balbus & Papaloizou 1999). The conservation of angular momentum requires a transport mechanism for angular momentum, in order to allow mass to move radially inwards. In a fluid description, this would be achieved by introducing viscosity. The latter causes friction between adjacent disk orbits, and initiates an exchange of angular momentum. The problem that arises is that molecular viscosity is far too low, to be reconciled with realistic disk times scales, and, hence, it is now believed that angular momentum transport is primarily driven by dynamical processes, and especially turbulence (see, e.g., Shakura & Sunyaev 1973; Balbus & Hawley 1998; Shakura 2018). In viscous disk theory, the turbulence is assumed to behave similarly to a molecular viscosity, with the stochastic, molecular motions being replaced by chaotic turbulent velocities. Hence, the idea is to assume the Navier-Stokes equation as a model, whereby the small-scale turbulence is not directly included, but rather subsumed into an effective viscosity. This section aims to provide some fundamental understanding of the accretion process, under this premise. The overview follows closely that given in Balbus & Papaloizou (1999) and Shakura (2018).

As the previous considerations suggest, the disk material is assumed to be a fluid, obeying the mass conservation (continuity equation), and the Navier-Stokes equation,

$$\partial_t \rho + \nabla \cdot (\rho \mathbf{u}) = 0 \tag{3.1}$$

$$\partial_t \mathbf{u} + (\mathbf{u} \cdot \nabla)\, \mathbf{u} = -\frac{1}{\rho}\nabla P - \nabla \Phi_\star + \frac{1}{\rho}\nabla \cdot \underline{\sigma}, \tag{3.2}$$

with fluid velocity $\mathbf{u}$, and mass density ρ. The energy balance is, for now, omitted. For reasons of shorter notation, partial derivatives are abbreviated by ∂, for example, $\partial_t \mathbf{u}$ is the partial time derivative. The viscous stress tensor is given by $\underline{\sigma}$. The equation of state is assumed to be that of an ideal gas, $P = n k_B T = \rho R_s T$, with pressure P, particle density n, mass density ρ, temperature T, and mass-specific gas constant R_s [1]. For the following considerations, it is convenient to introduce cylindrical coordinates (r, ϕ, z), with unit basis vectors $(\hat{\mathbf{e}}_r, \hat{\mathbf{e}}_\phi, \hat{\mathbf{e}}_z)$, yielding the velocity components $\mathbf{u} = u_r \hat{\mathbf{e}}_r + u_\phi \hat{\mathbf{e}}_\phi + u_z \hat{\mathbf{e}}_z$. The components of the viscous stress tensor, σ_{ij}, in cylindrical coordinates, are provided in Appendix A, or Shakura (2018). At this point, it is appropriate to shortly introduce the sound speed, since astrophysical fluids can be subject to highly supersonic velocities. Typically, the sound speed (adiabatic sound speed) is defined for constant entropy. For an ideal gas, one then finds $c_s = \sqrt{\gamma P/\rho}$, with γ being the adiabatic index, or the ratio of mass-specific heats, $\gamma = c_P/c_V$ (see, e.g., Regev, Umurhan, & Yecko 2016, or Appendix B). However, in the astrophysical context, one also often uses the isothermal sound speed, defined at constant temperature. For an ideal gas, the latter is given by $c_{s,i} = \sqrt{P/\rho}$, see also Appendix B. However, the deviation, between both values, is only a factor of $\sqrt{\gamma}$, which, for a mono-atomic gas, is given by $\sqrt{5/3}$, see also Appendix B. Hence, for order-of-magnitude comparisons, the latter may be used interchangeably. It is also noted that, for constant temperature, both values $c_{s,i}$ and c_s are constant as well.

In the following, rotational symmetry around the z axis is assumed, that is, all quantities do not depend on ϕ. The gravitational potential of the central object is $\Phi_\star = GM_\star/R$, whereby $M_\star$ is the central objects mass, and $R = \sqrt{r^2 + z^2}$ is the radius in polar coordinates. It is then assumed that, within the disk, the fluid moves around the central object in predominantly circular orbits,

[1] $R_s = k_B/m_p$, with Boltzmann constant k_B, and mass per particle m_p.

with velocity $u_\phi \hat{\mathbf{e}}_\phi$. By neglecting pressure forces, viscous forces, and by setting $u_r = u_z = 0$, Eq. 3.2 reduces to a force balance between the central objects gravity, and the centrifugal force: $u_\phi^2/r = \partial_r \Phi_\star$. The gravitational potential can be simplified, by assuming that the disk is thin, that is, by Taylor-expanding the potential for $|z|/r \ll 1$, see Appendix C. That yields the orbital angular velocity profile

$$\Omega(r) = \sqrt{\frac{GM_\star}{r^3}}, \tag{3.3}$$

which corresponds to the angular velocity of circular, Keplerian orbits, at radius r (see, e.g., Clarke & Carswell 2007). In the z direction, pressure forces are in equilibrium with the vertical component of the central objects gravity, yielding $\partial_z P = -\rho\Omega^2(r)$. It is then assumed, that the disk is vertically isothermal, that is, T does not depend on z. At a given radius, r, this leads to a vertical, Gaussian stratification, of both density and pressure, which is of the form

$$\rho = \rho_0 \exp\left(-\frac{\Omega^2(r) z^2}{2c_{s,i}^2}\right) = \rho_0 \exp\left(-\left(\frac{z}{H}\right)^2\right). \tag{3.4}$$

The density at the mid plane is given by $\rho_0 = \rho(z = 0)$, and the scale-height is defined as

$$H = \frac{\sqrt{2} c_{s,i}}{\Omega}, \tag{3.5}$$

which is a measure for the typical vertical stratification-height of the disk. The thin-disk approximation is often stated, using the scale height, as $H/r \ll 1$ (see, e.g., Balbus & Hawley 1998). To summarise, the fluid is orbiting the central object with a velocity $\Omega\, r\, \hat{\mathbf{e}}_\phi$, whereby the internal pressure establishes a local, vertical equilibrium, with a typical height H. Mass transport, towards the central object, is achieved, by taking viscosity into account. Qualitatively, viscosity causes friction between adjacent radial orbits, due to the inner orbit moving faster than the outer orbit. Hence, the dominant viscous-stress component is (see, e.g., Appendix A, or Shakura 2018)

$$\sigma_{r\phi} = \rho\nu\, r\, \partial_r \Omega, \tag{3.6}$$

with kinematic viscosity ν. It is noted that the specific angular momentum, $\Omega\, r^2 \propto \sqrt{r}$, increases with radius, opposite to the angular velocity Ω, and the velocity $u_\phi = \Omega\, r$. This has significant consequences for radial transport processes (see, e.g., Balbus & Hawley 1998). A fluid parcel on the inner orbit is decelerated, loosing angular momentum, due to the friction. Hence, the parcel moves radially inwards to an even lower orbit. The opposite is true for the outer parcel, with the latter gaining the difference in angular momentum and moving radially outwards. Hence, a mass flux, radially inwards, corresponds to a flux of angular momentum, radially outwards. The net angular momentum is conserved, but redistributed. From this, one can infer that viscosity does lead to a radial drift velocity u_r. The latter can be assumed to be much smaller than the orbital velocity u_ϕ. This follows from the thin-disk approximation, taking into account that velocity perturbations, u_r, can not exceed the sound speed, c_s, by much, as this would cause shocks, dissipating the excess kinetic energy into heat (see, e.g., Shakura & Sunyaev 1973; Balbus & Hawley 1998). Hence, assuming that the velocity perturbation u_r is of the order of the sound speed, one obtains $u_r/u_\phi = c_s/(\Omega r) \sim H/r \ll 1$ [2]. Due to axial symmetry, the angular-momentum conservation can be written in the form (see, e.g., Balbus & Papaloizou 1999; Balbus & Hawley 1998)

$$\partial_t\left(\rho r^2 \Omega\right) + \frac{1}{r}\frac{\partial}{\partial r}\left(r\left[\rho r^2 \Omega u_r - \rho\nu r^2 \partial_r \Omega\right]\right) + \frac{\partial}{\partial z}\left(\rho r^2 \Omega u_z\right) = 0. \tag{3.7}$$

[2] Here, the adiabatic sound speed, $c_s = \sqrt{\gamma} c_{s,i}$, with adiabatic index γ, was used

Taking into account the thin-disk approximation, the equations of motion are integrated over all z. For example, the mass density ρ is replaced by the surface-mass density

$$\Sigma(r,\phi) = \int_{-\infty}^{\infty} \rho(r,\phi,z)\, dz. \tag{3.8}$$

Integrating the continuity equation (mass conservation), as well as the angular momentum conservation, over z, one obtains (see, e.g., Balbus & Papaloizou 1999)

$$\frac{\partial \Sigma}{\partial t} + \frac{1}{r}\frac{\partial}{\partial r}\left(r\Sigma u_r\right) = 0 \tag{3.9a}$$

$$\frac{\partial}{\partial t}\left(\Sigma r^2 \Omega\right) + \frac{1}{r}\frac{\partial}{\partial r}\left(r^3 \Sigma \Omega u_r - \nu \Sigma r^3 \partial_r \Omega\right) = 0 \tag{3.9b}$$

Under stationary conditions, the surface density is constant over time, yielding $r\Sigma u_r = \text{const}$, from Eq. 3.9a. Hence, the flux of mass, across a cylindrical surface, in a given amount of time, is constant for all radii r. Often, this rate of mass drift is referred to as accretion rate (see, e.g., Balbus & Hawley 1998; Balbus & Papaloizou 1999; Shakura 2018):

$$\dot{M} = -2\pi r \Sigma u_r. \tag{3.10}$$

The minus sign indicates that the mass is spiralling inwards, $u_r < 0$. Similar to the mass flux, the angular momentum flux, in Eq. 3.9b, contains a term, proportional to u_r, corresponding to the angular momentum flux of the in-spiralling mass. But there is one additional term, representing outward angular momentum transport. A stationary state requires this angular-momentum flux (the net of both terms) to be constant as well. Together, this yields (see also Pringle 1981; Balbus & Papaloizou 1999)

$$\dot{M}\left(1 - \sqrt{\frac{r_0}{r}}\right) = 3\pi\nu\Sigma, \tag{3.11}$$

whereby r_0 is the inner disk radius, at which the viscous stress is assumed to vanish. This implies that the mass-accretion, $\dot{M}$, rate is proportional to the product of ν and Σ. Hence, a mass flow can be initiated by the introduction of viscous friction. However, viscosity also turns kinetic energy into thermal energy. This viscous heating is one part of the general energy balance of the accretion process. As mass moves radially inwards, it releases gravitational potential energy, which is converted into other energy forms (see, e.g., Shakura 2018). One part of this energy is turned into orbital kinetic energy. That is necessary, because the orbital velocity, Ωr, is larger for smaller radii, in contrast to the angular momentum. Hence, mass spiralling inwards, gains kinetic energy, despite loosing angular momentum. The remaining energy is turned into heat, and the detailed mechanism of this is the viscous dissipation. One can show that the local viscous-heating rate, per area, is given by (see, e.g., Shakura 2018)

$$\sim \Sigma\nu r^2 \left(\frac{\partial\Omega}{\partial r}\right)^2, \tag{3.12}$$

which, depends on the orbital shear rate $\partial_r\Omega$. In order to achieve a stationary state, an additional cooling mechanism must be present, which is, for example, achieved by radiation, leaving the disk. Hence, the partial conversion of gravitational potential energy, into thermal energy, is the main reason why accretion disks are capable of generating luminosity in the first place (Pringle 1981; Balbus & Hawley 1998; Shakura 2018). If it is assumed that the energy is radiated away at the location at which the thermal energy was generated, implying that the thermal energy balance is local, and one can define a surface emission rate, per area (see, e.g., Pringle 1981; Balbus & Hawley 1998)

$$E_{\text{rad}} = \frac{3G\,M\,\dot{M}}{8\pi r^3}\left(1 - \sqrt{\frac{r_0}{r}}\right). \tag{3.13}$$

Integrated over the entire disk, assuming that the disk is large, compared to its inner radius r_0, the total luminosity is given by (see, e.g., Pringle 1981; Balbus & Hawley 1998)

$$L \sim \frac{GM_\star \dot{M}}{2r_0}, \tag{3.14}$$

which corresponds to half the potential energy (of the mass $\dot{M}$, for a given amount of time) at the innermost orbits. This is also theorised to provide the significant luminosities of AGNs (Lynden-Bell 1969).

3.2 Turbulence and transport

3.2.1 Turbulent viscosity, and the α prescription

As mentioned previously, the viscosity was merely introduced as a model for the actual disk turbulence. That raises the question what values for ν one should expect, or how this viscosity relates to turbulence, in general. Historically, this has led to the α prescription of viscous accretion disks (Shakura & Sunyaev 1973), whereby α is a dimensionless viscosity coefficient, derived from the turbulence. To make the similarities to viscosity more explicit, one can start with angular momentum conservation. It is assumed that the z axis is aligned with the axis of angular momentum, $l_z = \rho\, r\, v_\phi$. Note that the velocity $\mathbf{v}$ contains both the orbital velocity, as well as the small-scale turbulent velocities (no rotational symmetry is assumed), in contrast to the previous section. Angular momentum conservation can then be formulated as follows (see, e.g., Balbus & Hawley 1998):

$$\partial_t \left(\rho\, r\, v_\phi\right) + \nabla \cdot \left(\rho\, r\, v_\phi\, \mathbf{v} + P\hat{\mathbf{e}}_\phi\right) = 0. \tag{3.15}$$

Note that no explicit viscosity is used, the latter should rather emerge as a statistical property of the turbulence. One then averages Eq. 3.15 over all angles ϕ, and integrates over all z. For convenience, the abbreviation

$$\langle f \rangle_\phi^z := \frac{1}{2\pi} \int_{-\infty}^{\infty} dz \int f\, d\phi \tag{3.16}$$

is introduced, whereby z appears as an upper case index, to highlight that one integrates over z (not an average). One thus obtains

$$\partial_t \langle r\rho v_\phi \rangle_\phi^z + \frac{1}{r}\partial_r \left(r \langle r\rho v_\phi v_r \rangle_\phi^z\right) = 0. \tag{3.17}$$

The velocity is then separated into an orbital component, and a turbulent part, $\mathbf{v} = r\Omega\, \hat{\mathbf{e}}_\phi + \delta\mathbf{v}$, with $\delta\mathbf{v} = (v_r, \delta v_\phi, v_z)$. That yields

$$\partial_t \langle r\rho v_\phi \rangle_\phi^z + \frac{1}{r}\partial_r \left(r^3\Omega \langle \rho\, v_r \rangle_\phi^z + r^2 \langle \rho\, \delta v_\phi v_r \rangle_\phi^z\right) = 0. \tag{3.18}$$

The latter equation can directly be compared to Eq. 3.9b. It is apparent that $r^3\Omega \langle \rho\, v_r \rangle_\phi^z$ corresponds to $\Sigma r^3 \Omega u_r$, in Eq. 3.9b. Intuitively, the idea of a turbulent viscosity can be understood as the assumption that the term $r^2 \langle \rho\, \delta v_\phi v_z \rangle_\phi^z$, is equivalent to the term $-\Sigma\nu r^3 \partial_r \Omega$, in Eq. 3.9b. Hence, the Reynolds stress, $\langle \rho\, \delta v_\phi v_r \rangle$, is interpreted as an actual viscous stress, via the identification (see, e.g., Shakura 2018)

$$\langle \rho \delta v_\phi v_r \rangle_\phi^z = -\Sigma \nu_t r \partial_r \Omega = \frac{3}{2}\nu_t \Sigma \Omega, \tag{3.19}$$

whereby the last equality follows by assuming a Keplerian profile for $\Omega(r)$. It is important to note, that one usually has $\partial_r \Omega < 0$, and, hence, $\langle \rho \delta v_\phi v_r \rangle_\phi^z > 0$ must hold, for angular momentum to be transported outwards. This is not a trivial point, and the mere presence of turbulence is not

sufficient to guarantee this (see, e.g., Balbus & Hawley 1998). Though for shear-induced turbulence, there is also a qualitative interpretation for the viscosity analogy. Consider a flow, in Cartesian coordinates (x, y), with a x-dependent, large-scale mean velocity $\langle v_y \rangle(x)$ (shear flow, corresponds to $r\Omega$), such that $\frac{\partial \langle v_y \rangle}{\partial x} < 0$. Say, there is a velocity perturbation in the x direction, v_x. In a small amount of time δt, the fluid element travels the distance $\delta x = v_x \, \delta t$. If the fluid element retains its original mean velocity, $\langle v_y \rangle(x)$, then there will be a velocity perturbation, at $x + \delta x$, of the form

$$\delta v_y = \langle v_y \rangle(x) - \langle v_y \rangle(x + \delta x) \sim -(\partial \langle v_y \rangle / \partial x) \, \delta x \tag{3.20}$$

Hence, the Reynolds stress can then be written in the form (see, e.g., Tennekes & Lumley 1972; Shakura 2018)

$$\langle \rho v_x \delta v_y \rangle = -\langle \rho \rangle \langle v_x \, \delta x \rangle \, \frac{\partial \langle v_y \rangle}{\partial x}. \tag{3.21}$$

The latter is positive, as v_x, and δx have the same sign, by construction. One can then ask what meaning δx (or δt) has. In the derivation above, it is assumed that the velocity perturbation in the y direction follows as a consequence of the background-y velocity, being transported with v_x in the x direction. For chaotic motions, it can be guessed that this straight transport is not possible for arbitrarily long time spans δt, before v_x, and δv_y, mix with the surrounding velocities. Hence, one uses a mean correlation length for δx, which is often referred to as mixing length, and which may best be compared to the mean-free path in kinetic gas theory (see, e.g., Tennekes & Lumley 1972). By comparing Eq. 3.21 to Eq. 3.19, one can thus infer that the turbulent viscosity is given by $\nu_t = \langle v_x \, \delta x \rangle$ (see also Shakura 2018). It has turned out that one can construct a convenient, dimensionless measure, from ν_t (Shakura & Sunyaev 1973), mostly referred to as α. One first recalls that the turbulent velocities can be assumed to be at most of the order of the sound speed $|\delta \mathbf{v}| \sim c_s$, as much larger velocities would cause the formation of shocks, dissipating kinetic energy (Shakura & Sunyaev 1973). Similarly, a typical length scale is given by the scale height, $\delta x \sim H \sim c_s / \Omega$. Hence, it is convenient to introduce the parameter α, such that

$$\langle \rho \delta v_\phi v_r \rangle^z_\phi = \Sigma \, \alpha \, c_s^2, \tag{3.22}$$

whereby $c_s^2 = \gamma \langle P \rangle^z_\phi / \Sigma$ is used for the sound speed. That implies:

$$\alpha = \frac{\langle \rho \delta v_\phi v_r \rangle^z_\phi}{c_s^2 \Sigma} = \frac{\langle \rho \delta v_\phi v_r \rangle^z_\phi}{\gamma \langle P \rangle^z_\phi}. \tag{3.23}$$

This definition is commonly used in the context of accretion-disk turbulence. Due to the special form of the Kepler profile, the last term in Eq. 3.19, contains a factor 3/2. Sometimes, the latter is accounted for, by including an additional factor of 2/3, in the definition of α, especially in the context of gravitational, or gravito-turbulence (see, e.g., Gammie 2001). One additional note on the averages: Instead of $\langle f \rangle^z_\phi$ one can use any type of average that is suitable. In the local approximation (discussed in detail later), one uses a simple volume average, there denoted by $\langle f \rangle$, without any further specifications. It is important to note, that the previous considerations assumed that the turbulence is connected to the local shearing rate (see, e.g., Balbus & Hawley 1998). There can be an ambiguity for the direction of transport, if the turbulence was not a direct result of the velocity gradient. An example are convective instabilities that arise as a consequence of thermal gradients, for which the direction of angular momentum transport is not entirely certain (see, e.g., Papaloizou & Lin 1995; Balbus & Hawley 1998; Lesur & Ogilvie 2010). Nevertheless, the viscosity prescription is a very potent approximation, and it allows the development of global disk models, without the need to simulate small scale turbulence. It is also noted, that the involved turbulence must be local (e.g, no waves that transport angular momentum, or energy, over large distances, see, e.g., Balbus & Papaloizou 1999).

Up to now, the presence of turbulence was merely assumed, and no mechanism was provided. One might, at first, assume that disk systems lead to turbulence immediately, as they represent a high-Reynolds-number shear flow. However, there are significant differences to simple shear flows that prevent the sustainance of purely hydrodynamical shearing turbulence (see, e.g., Pringle 1981; Balbus & Hawley 1998). Often, enhanced turbulent transport arises as a consequence of a gradient of some quantity. This can, for example, be the velocity gradient of a shear flow. However, in disks, there is not only a velocity gradient, but also a specific angular momentum gradient, and both point in opposite directions. Hence, there is not immediately a preferred direction of transport, which is related to the hydrodynamical stabilisation (see also Balbus & Hawley 1998). As a consequence, the possibilities for purely hydrodynamical turbulence, are limited. However, other effects, such as magnetic fields, or self-gravity, can cause the disk to become linearly unstable, triggering turbulence. One of the most promising candidates is the so-called magneto-rotational instability (MRI) (see, e.g., Balbus & Hawley 1991; Balbus & Hawley 1998). The latter emerges, if the disk material was sufficiently ionised, such that it can couple to the ambient magnetic field. The interplay between tidal forces and Lorentz-forces can then cause the system to become linearly unstable (Balbus & Hawley 1991). MRI is likely relevant, for a large range of accretion disks, from AGNs, or hot disks in binary systems (Balbus & Hawley 1998; Shakura 2018), to PPDs (see, e.g., Armitage 2011). Another important instability relies on the disk-materials own gravity, often referred to as self-gravity. For sufficiently massive disks, this can lead to the so-called gravitationl instability (GI) (see, e.g., Toomre 1964; Toomre 1981; Kratter & Lodato 2016). The latter is thought to play a major role in AGN disks (see, e.g., Goodman 2003), but can also be relevant for PPD disks (Armitage 2011). MRI is likely the most prominent candidate for disk turbulence, though in PPDs, colder regions, dead zones, can occur, which do not allow the development of MRI (see, e.g., Gammie 1996; Armitage 2011). Hence, other instability mechanisms might be relevant there. These can, for example, include baroclinic instabilities, convective instabilities, or even angular momentum transport due to planet formation (Armitage 2011). Additionally, there may also be transport processes, operating outside the typical viscosity prescription, on global scales. This is, for example, the case for large-scale, spiral waves, related to the disk materials self gravity (see, e.g., Balbus & Papaloizou 1999; Kratter & Lodato 2016), which are very prominent in galactic disks (Lynden-Bell & Kalnajs 1972).

Both the gravitational instability (GI), and the magneto-rotational instability (MRI), are reviewed in more detail, in Sect. 3.3. The latter two instabilities rely on self-gravity, and magnetic fields, respectively. Both contributions lead to additional stresses, besides the Reynolds stress, that were not considered here. Hence, the following two sections briefly introduce the concepts of self-gravity, and magnetohydrodynamics (MHD), in order to provide a motivation for the additional stress contributions.

3.2.2 Self-gravity

The material of the disk itself also has mass, and the latter contributes a gravitational potential, Φ. The mutual attraction of different parts of the disk material, due to this potential, is referred to as self-gravity. For the purposes here, self-gravity can be discussed in the non-relativistic, Newtonian limit. Thereby, it is assumed that mass, and length scales are such that $GM/(c^2 r) \ll 1$ (see, e.g., Schutz 2009), and $|\mathbf{v}| \ll c$ (with the speed of light c). In that case, retardation effects, necessitating the use of a general-relativistic description, are omitted. Hence, the potential of self-gravity, Φ, is linked to the mass density, ρ, via Poisson's equation (see, e.g., Binney & Tremaine 2008)

$$\nabla^2 \Phi = 4\pi G \rho. \tag{3.24}$$

The lack of retardation implies that ρ, at a given location, will change Φ at all other locations, instantaneously. The potential Φ acts on the fluid by exerting a force density $-\rho \nabla \Phi$. The latter

contributes to the right hand side of the Euler equation:

$$\rho\frac{\partial \mathbf{u}}{\partial t} + \rho\left(\mathbf{u}\cdot\nabla\right)\mathbf{u} = -\nabla P - \rho\nabla\Phi^{\star} - \rho\nabla\Phi. \tag{3.25}$$

Instead of using a gradient, this force density can also be represented using a divergence (see Lynden-Bell & Kalnajs 1972),

$$-\rho\nabla\Phi = -\nabla\cdot\underline{\mathbf{G}}, \tag{3.26}$$

whereby the gravitational stress tensor, $\underline{\mathbf{G}}$, was introduced. The components of this tensor are given by

$$G_{ij} = \frac{1}{4\pi G}\left(\partial_i\Phi\,\partial_j\Phi - \frac{1}{2}(\nabla\Phi\cdot\nabla\Phi)\delta_{ij}\right). \tag{3.27}$$

Due to its importance, a derivation of this divergence representation is provided in Appendix D. One can now use this to rewrite the Euler equation in the following, conservative form

$$\frac{\partial \rho\mathbf{u}}{\partial t} + \nabla\cdot\left(\rho\mathbf{u}\mathbf{u} + \underline{\mathbf{G}} + P\underline{\mathbf{I}}\right) = \rho\nabla\Phi^{\star}. \tag{3.28}$$

$\rho\mathbf{u}\mathbf{u}$ (or in components, $\rho u_i u_j$) is the Reynolds stress, and $\underline{\mathbf{I}}$ is the identity matrix. From that representation, it becomes clear that the tensor $\underline{\mathbf{G}}$ enters the divergence term in a way, that is similar to the Reynolds stress. In fact, if one wants to obtain the effective viscosity for local, gravitationally induced turbulence, one has to consider $\underline{\mathbf{G}}$ as an equally important stress contribution (see, e.g., Lynden-Bell & Kalnajs 1972; Gammie 2001). More precisely, the definition of α (see Eq. 3.23), has to be adjusted accordingly, to (see, e.g., Gammie 2001)

$$\alpha = \alpha_r + \alpha_g = \frac{2\langle\rho\delta v_\phi v_r + G_{r\phi}\rangle}{3\gamma\langle P\rangle}. \tag{3.29}$$

It is noted that the self-gravity induced dynamics is not always local, and some disks develop global spiral waves, which can also transport angular momentum (see, e.g., Balbus & Papaloizou 1999; Kratter & Lodato 2016). Here, it is assumed that the disk parameters are such (thin, less massive disks), that a local α prescription is justified (see also Cossins, Lodato, & Clarke 2009; Kratter & Lodato 2016).

3.2.3 Magnetic fields

In many astrophysical systems, the gas is highly ionised, forming a plasma. In such cases, the magnetic fields are coupled to the fluid, whereby magnetic field lines can be carried by the fluid flow (flux freezing), and reversely, the fields can back-react onto the fluid via Lorentz forces (see, e.g., Kulsrud 2005; Jackson 2014; Chiuderi & Velli 2015). In order to retain a description, similar to the hydrodynamical description, the fluid equations are extended to the full magnetohydrodynamic (MHD) equations. Basically, this consists of two steps: One needs to introduce a force term in the Euler equation, accounting for forces due to electric or magnetic fields, and one needs to provide evolution equations for the electric and magnetic fields. Clearly, the latter are the Maxwell equations (see, e.g., Jackson 2014):

$$\begin{aligned} \nabla\cdot\mathbf{E} &= \frac{\rho_c}{\epsilon_0} \qquad & \nabla\times\mathbf{E} &= -\frac{\partial\mathbf{B}}{\partial t} \\ \nabla\cdot\mathbf{B} &= 0 \qquad & \nabla\times\mathbf{B} &= \mu_0\mathbf{J} + \frac{1}{c^2}\frac{\partial\mathbf{E}}{\partial t}. \end{aligned} \tag{3.30}$$

Therein are $\mathbf{E}$ the electric field, $\mathbf{B}$ the magnetic field (magnetic induction), $\mathbf{J}$ the current density, and ρ_c the electric-charge density. The equations are, starting from top left, counter-clock wise, Gauss's law for the electric field, Faraday's law of induction, the source-free condition for the

magnetic field, and Ampere's law. The displacement current, $\partial_t \mathbf{E}/c^2$, is of the order $|\mathbf{v}|^2/c^2 \ll 1$ (see, e.g., Kulsrud 2005; Chiuderi & Velli 2015), and as the systems, discussed here, do not involve relativistic fluids, this term can be discarded. Ampere's law then reduces to $\nabla \times \mathbf{B} = \mu_0 \mathbf{J}$. The back-reaction onto the fluid is considered, by adding the Lorentz-force density, $\mathbf{f}_{\rm mag} = \rho_c \mathbf{E} + \mathbf{J} \times \mathbf{B}$, as a source term in the Euler equation (see, e.g., Biskamp 2003; Kulsrud 2005; Chiuderi & Velli 2015)

$$\rho \frac{\partial \mathbf{u}}{\partial t} + \rho \left(\mathbf{u} \cdot \nabla \right) \mathbf{u} = -\nabla P - \rho \nabla \Phi^\star + \rho_c \mathbf{E} + \mathbf{J} \times \mathbf{B}. \tag{3.31}$$

The electric field acts on the charge density, ρ_c, and the magnetic field exerts a force onto the current density, $\mathbf{J}$. In the context here, the Coulomb contribution, $\rho_c \mathbf{E}$, is usually negligible (Biskamp 2003; Kulsrud 2005; Chiuderi & Velli 2015), as the freely moving charges, within the plasma, establish quasi neutrality. The Lorentz-force density can also be written in a different form, by using Ampere's law[3]:

$$\mathbf{f}_{\rm mag} = \mathbf{J} \times \mathbf{B} = \frac{1}{\mu_0} \mathbf{B} \cdot \nabla \mathbf{B} - \nabla \left(\frac{|\mathbf{B}|^2}{2\mu_0} \right). \tag{3.32}$$

In the last expression, the gradient acts on the magnetic energy density, $|\mathbf{B}|^2/(2\mu_0)$, which introduces a force density that acts similar to a pressure force (see, e.g., Chiuderi & Velli 2015). The term $\mathbf{B} \cdot \nabla \mathbf{B}/\mu_0$ is a restoring force, resulting from the bending of magnetic field lines, and it tries to straighten the field lines (see, e.g., Chiuderi & Velli 2015). Changes of $|\mathbf{B}|$ along the field line, act as an additional, anisotropic pressure, along the field line (see, e.g., Chiuderi & Velli 2015). Similar to the case of self-gravity, the Euler equation can be rewritten in the following, conservative form:

$$\partial_t \left(\rho \mathbf{u} \right) + \nabla \cdot \left(\rho \mathbf{u}\mathbf{u} - \frac{1}{\mu_0} \mathbf{B}\mathbf{B} + \underline{\mathbf{G}} + \left(P + \frac{\mathbf{B}^2}{2\mu_0} \right) \underline{\mathbf{I}} \right) = -\rho \nabla \Phi^\star \tag{3.33}$$

Hence, in addition to the Reynolds stress ($\rho \mathbf{u}\mathbf{u}$), and the gravitational stress ($\underline{\mathbf{G}}$), a magnetic contribution, $-\mathbf{B}\mathbf{B}/\mu_0$, emerges, which is referred to as Maxwell stress (see, e.g., Jackson 2014). This necessitates a third contribution to the dimensionless, turbulent viscosity:

$$\alpha = \alpha_r + \alpha_g + \alpha_m = \frac{2 \langle \rho \delta v_\phi v_r + G_{r\phi} - \frac{1}{\mu_0} B_x B_y \rangle}{3 \gamma \langle P \rangle}. \tag{3.34}$$

Eq. 3.33 further highlights the similarities between the magnetic energy density, $|\mathbf{B}|^2/(2\mu_0)$, and the thermal pressure P. Due to these similarities, one often defines the additional quantities (see, e.g., Biskamp 2003; Kulsrud 2005; Jackson 2014; Chiuderi & Velli 2015):

$$\beta = \frac{P}{|\mathbf{B}|^2/(2\mu_0)}, \quad \mathbf{v}_A = \frac{\mathbf{B}}{\sqrt{\mu_0 \rho}}. \tag{3.35}$$

The so-called plasma-β is a measure for the relative importance of the thermal pressure over the magnetic pressure. The Alfven velocity is defined in accordance to the sound speed, $c_s = \sqrt{\gamma P/\rho}$, but with the thermal pressure replaced by the magnetic pressure.

In principle, the time evolution of the fields is given by the Maxwell equations. However, in an MHD description, one can reduce this time evolution to just one equation for the magnetic field. This is achieved, using Ohm's law (see, e.g., Biskamp 2003; Kulsrud 2005; Chiuderi & Velli 2015),

$$\sigma \left(\mathbf{E} + \mathbf{v} \times \mathbf{B} \right) = \mathbf{J}, \qquad \text{or} \qquad \mathbf{E} + \mathbf{v} \times \mathbf{B} = \eta \mathbf{J}. \tag{3.36}$$

Thereby, σ is the conductivity of the plasma, and $\eta = 1/\sigma$ is the resistivity. One can now use Ohm's law to eliminate the electric field in Faraday's law, $\partial_t \mathbf{B} = -\nabla \times \mathbf{E}$, by solving Eq. 3.36 for

[3] The vector identity $\nabla(\mathbf{A} \cdot \mathbf{B}) = (\mathbf{A} \cdot \nabla)\mathbf{B} + (\mathbf{B} \cdot \nabla)\mathbf{A} + \mathbf{A} \times (\nabla \times \mathbf{B}) + \mathbf{B} \times (\nabla \times \mathbf{A})$ is used (see, e.g., Bronstein et al. 2012).

E. Further replacing the current density, using Ampere's law, one obtains an evolution equation for the magnetic field, the induction equation (Biskamp 2003; Kulsrud 2005; Chiuderi & Velli 2015),

$$\partial_t \mathbf{B} = \nabla \times (\mathbf{v} \times \mathbf{B}) + \frac{\eta}{\mu_0} \nabla^2 \mathbf{B}. \tag{3.37}$$

Hence, considering Eq. 3.33, the full fluid description only requires the induction equation. Technically, the condition $\nabla \cdot \mathbf{B} = 0$, is required as well, but the time evolution, provided by Eq. 3.37, automatically satisfies $\nabla \cdot \mathbf{B} = 0$, given that it is satisfied by the initial condition (see, e.g., Kulsrud 2005). It is apparent, that Eq. 3.37 is almost a conservation law, except that, instead of a divergence, the induction equation contains a curl, indicating that conservation refers to surfaces, and not to volumes. Lets first assume $\eta = 0$, then Eq. 3.37 can be interpreted as follows: The magnetic flux across a given surface [4], that is co-moving with the fluid, is conserved (Alfven Theorem, see, e.g., Kulsrud 2005; Chiuderi & Velli 2015). Hence, one often says that the magnetic field lines are frozen into the fluid flow. The last term in Eq. 3.37 has the form of a diffusive term, and, hence, the factor $\hat{\eta} := \eta/\mu_0$ is often called magnetic diffusivity (see, e.g., Biskamp 2003; Chiuderi & Velli 2015). This term causes deviations from the frozen-in-flux behaviour, as the diffusion allows the field lines to move with respect to the fluid. A dimensionless measure, for the importance of resistivity, is the magnetic Reynolds number (see, e.g., Chiuderi & Velli 2015)

$$\mathrm{Rm} := \frac{UL}{\eta}, \tag{3.38}$$

whereby U is a typical velocity, and L is a typical length scale. For $\mathrm{Rm} \gg 1$, the diffusive term is usually neglected. In the accretion-disk context, the typical velocity is often chosen to be the sound speed, c_s, and the typical length scale is the disk scale height, $H = c_s/\Omega$, yielding $\mathrm{Rm} = c_s^2/(\eta\Omega)$.

It is noted that one can also derive a time-evolution law for the magnetic-energy density, $|\mathbf{B}|^2/(2\mu_0)$. This can, for example, be achieved by multiplying the induction equation by $\mathbf{B}/\mu_0$. Since this magnetic-energy balance is used in Sect. 9 (LP23), a detailed derivation is provided in Appendix F.

3.3 Disk instabilities and turbulence

As was alluded to earlier, the emergence of turbulence, in accretion disks, is not guaranteed, at least not for the purely hydrodynamical case. However, self-gravity and magnetic fields can lead to instabilities, that result in turbulence. Weak magnetic fields allow for the emergence of the so-called magneto-rotational instability (MRI) (Balbus & Hawley 1991). Similarly, in sufficiently massive disks, such as AGNs, PPDs, or galactic disks, self-gravity can cause gravitational instabilities (GI) (see, e.g., Toomre 1964; Goodman 2003; Armitage 2011; Kratter & Lodato 2016). These are two of the more prominent sources for disk turbulence, and the latter are reviewed in more detail, in the following two sections.

3.3.1 Gravitational instability (GI)

One important type of disk instability, is the so-called gravitational instability, in the following often abbreviated by GI. This type of instability relies on the mutual attraction of different parts of the fluid, which is referred to as self-gravity. At first, one might expect that, due to the always attractive nature of gravity, such an instability is inevitable. It turns out though, that this is not the case, and whether stability sets in depends on the exact system parameters. The ability of self-gravity to trigger instabilities is characterised by the dimensionless parameter

$$Q = \frac{c_s \kappa}{\pi G \Sigma}, \tag{3.39}$$

[4] The magnetic flux, through a surface $\mathcal{S}$, is given by $\Phi_m = \int_{\mathcal{S}} \mathbf{B} \cdot \mathbf{n} \, d^2S$, with surface norm $\mathbf{n}$.

depending on the sound speed ($c_s^2 = \gamma P_{(2)}/\Sigma$)[5], the epicyclic frequency ($\kappa^2 = r\partial_r(\Omega^2) + 4\Omega^2$), and the mass surface density (Σ) (see, e.g., Toomre 1964; Binney & Tremaine 2008; Kratter & Lodato 2016). It is noted that, for Keplerian $\Omega(r)$, one simply finds $\kappa = \Omega$. As a first estimate, one obtains that a self-gravitating disk is locally unstable to short-wavelength, axisymmetric perturbations, if $Q < 1$, which is often referred to as the Toomre criterion (see Toomre 1964; Toomre 1969; Binney & Tremaine 2008; Kratter & Lodato 2016). Axisymmetric means that the unstable modes do not depend on the angular coordinate ϕ (ring-like structures), and short wave-length implies that $k_r r \gg 1$, with radial wave vector, k_r. It is noted that the original derivation of Toomre (1964) was concerned with a diks of stars, instead of a fluid disk, whereby the sound speed is then interpreted as the velocity dispersion of the stars. However, the criteria for fluid, and star systems are very similar (see, e.g., Binney & Tremaine 2008). Non-axisymmetric modes lead to density waves with a spiral appearance. A quantity $f(r,\phi)$ may then, for example, be represented as a wave of the form $f(r,\phi) = \hat{f}(r)\exp\left(i\omega\, t - im\phi - i\int_{r_0}^{r} k_r(r')\, dr'\right)$ (see, e.g., Lin & Shu 1964; Binney & Tremaine 2008), with frequency ω, angular wave number m, and radial wave vector $k_r(r)$. For analytical calculations it is often convenient to use the tightly-wound limit (see, e.g., Binney & Tremaine 2008; Kratter & Lodato 2016). Thereby it is assumed that $k_r r \gg 1$, and that the envelope, $f(r)$, varies over a significantly larger, radial distance, than the wave length $2\pi/k_r$ (see, e.g., Binney & Tremaine 2008). One can derive an estimated dispersion relation (Lin & Shu 1964; Binney & Tremaine 2008)

$$(\omega - m\Omega)^2 = c_s^2 k - 2\pi G\Sigma|k_r| + \kappa^2. \tag{3.40}$$

Under the assumption of axisymmetry ($m = 0$), one recovers the criterion, $Q < 1$, for axisymmetric instabilities, with $k_r r \gg 1$ (see, e.g., Kratter & Lodato 2016). Due to its importance for (Löhnert, Krätschmer, & Peeters 2020, see Sect. 7), a detailed derivation of the axisymmetric dispersion relation, is provided in Sect. 10.1. Instead of a global disk, the latter derivation uses the sharing-sheet as a background, see also Sect. 4.1. From the axisymmetric case of Eq. 3.40 ($m = 0$), one can infer that instability will only occur, if the right hand side is negative. Hence, stability depends on the terms on the right hand side. The term $-2\pi G|k_r|$ represents the destabilising effect of the mutual gravitational attraction, the term $c_s^2 k$ represents the stabilising effect of pressure, and the term κ^2 represents stabilisation due to the epicyclic restoring force (see, e.g., Toomre 1964; Binney & Tremaine 2008). Put differently, if the wave length $\lambda = 2\pi/k_r$ of a mode is too small, it will be stabilised by pressure forces, and if λ is too large, the mode is stabilised by inertial forces (see, e.g., Toomre 1964; Binney & Tremaine 2008). Hence, only wave lengths in between are unstable, and $Q < 1$ guarantees that such an interval exists. The criterion $Q < 1$ is not exact though, and it is restricted to axisymmetric cases without additional effects, such as cooling, or viscous heating (see Kratter & Lodato 2016; Lin & Kratter 2016). Non-axisymmetric modes, on global scales, can occur for Q values larger than one as well (see the spiral modes of Hohl 1971). A corresponding dispersion relation was provided by (Lau & Bertin 1978). In addition to Q, stability then also depends on the parameter $\mathcal{J} \propto m\, M_{\rm disk}/M_\star$, whereby $M_{\rm disk}$, refers to the disk mass (see, e.g., Lau & Bertin 1978; Kratter & Lodato 2016). One obtains the above dispersion relation in the limit of small $\mathcal{J}$ (Lau & Bertin 1978; Kratter & Lodato 2016). Large disk mass ratios $M_{\rm disk}/M_\star$, usually yield less spiral arms (low m), whereas small $M_{\rm disk}/M_\star$ ratios yield more spirals, corresponding to tightly wound cases (Cossins, Lodato, & Clarke 2009; Kratter et al. 2010; Kratter & Lodato 2016). Numerical simulations suggest that the most unstable wave lengths are in all cases, of the order of the scale height $k \sim H^{-1}$ (see, e.g., Gammie 2001; Cossins, Lodato, & Clarke 2009; Kratter & Lodato 2016), which implies that the tightly wound limit also corresponds to rather thin disks (see Kratter & Lodato 2016). The introduction of radiative cooling can also destabilise disks (see Lin & Kratter 2016, or Sect. 10.1), by reducing the influence of pressure forces. For some cooling prescriptions, one might even find instability for all values of Q (Lin & Kratter 2016; Löhnert, Krätschmer, & Peeters 2020, or Sect. 10.1). The growth rates for large Q then decrease significantly, though. Another

[5] $P_{(2)}(r,\phi) := \int_{-\infty}^{\infty} P(r,\phi,z)\, dz$

factor, influencing the stability against self-gravity, is the dimensionality of the system. Self-gravity models for disks often consider effectively two-dimensional (razor-thin) systems, see also Sect. 4.5.1. It turns out that three-dimensional effects tend to stabilise disks against self-gravity, as a vertically extended mass distribution tends to soften the gravitational potential (see, e.g., Binney & Tremaine 2008; Kratter & Lodato 2016).

The density waves, in a Toomre unstable system, will not grow indefinitely, and a nonlinear response will eventually develop. This raises the question, how GI saturates. The two main routes to saturation are gravitoturbulence, and clumping (see, e.g., Gammie 2001; Kratter & Lodato 2016). In the following, the latter two outcomes are discussed in more detail. It is noted that the focus is more on the tightly-wound limit, as the latter is also more accessible via local shearing box simulations, which are the main focus of the works Löhnert, Krätschmer, & Peeters (2020) (Sect. 7), Löhnert & Peeters (2022) (Sect. 8), and Sect. 9 (LP23).

GI Turbulence:
Gravitoturbulence usually manifests as a state of self regulation, such that the Toomre parameter is close to the stability threshold, $Q \sim Q_c$, with the critical Toomre parameter $Q_c \gtrsim 1$ (see Paczynski 1978; Gammie 2001). As noted previously, additional physics, not considered in the derivation of Toomre, can destabilise the system, and, hence, Q_c can be slightly larger than one. The self regulation emerges as a balance between heating, due to GI turbulence, and cooling, due to radiation (Paczynski 1978). The velocity perturbations, associated with GI turbulence, are mostly supersonic, indicating that compressibility effects, as well as shocks, can heat up the gas (see, e.g., Gammie 2001; Cossins, Lodato, & Clarke 2009). As a consequence, the Toomre parameter $Q \propto \sqrt{T}$ also rises. Eventually, the larger Q value quenches GI, and the GI-related heat production ceases. Radiative cooling then reduces the thermal energy level again, until Q is low enough to reignite GI. This cycle represents a thermal regulation of the Toomre parameter at $Q \sim Q_c$, with $Q_c \gtrsim 1$. It is pointed out, that two-dimensional simulations often yield values $Q \sim 2$ (see, e.g., Gammie 2001; Vanon 2018; Löhnert, Krätschmer, & Peeters 2020). As noted above, this may be related to the effect that three-dimensional systems tend to be more stable, compared to two-dimensional cases. An important part in the thermal self-regulation is the radiative cooling. A simple, yet easy to interpret, way of modelling radiative cooling, in simulations, is to add a cooling term to the thermal energy balance (see, e.g., Gammie 2001; Rice et al. 2003; Rice et al. 2011),

$$\partial_t E_{th} = ... - \frac{E_{th}}{\tau_c}. \tag{3.41}$$

Therein, τ_c is a typical time scale, associated with the cooling process. The latter is often referred to as a β-cooling prescription, whereby τ_c is connected to the orbital time scale $1/\Omega$, via the dimensionless number $\beta = \tau_c \Omega$ (see, e.g., Kratter & Lodato 2016). Additional heating sources are also often included, accounting for, for example, irradiation from the central object (see Rice et al. 2011). The above defined cooling model is rather simple, and in optically thick regimes, one would have to consider radiative transport, necessitating more complicated cooling models (see, e.g., Boley et al. 2006; Krumholz et al. 2009; Stamatellos & Whitworth 2009; Hirose & Shi 2019). In some cases of AGN disks (accretion near the Eddington limit), radiation pressure may also be important, in addition to the gas (plasma) dynamics (Jiang & Goodman 2011). Nevertheless, the above cooling model is a useful first approximation, which can readily be interpreted, and also implemented in numerical applications. In a stationary sate, this cooling rate must be equal to the net heating rate. Without additional heating sources (e.g. irradiation), this heating rate must originate from the dissipation of turbulent kinetic energy via compression, and shocks. If the turbulent kinetic energy is dissipated locally (and not transported over large distances by waves, see, e.g., Balbus & Papaloizou 1999; Gammie 2001; Cossins, Lodato, & Clarke 2009), then this implies that the net production rate of turbulent kinetic energy equals the net cooling rate. A dimensionless measure

for the rate of turbulent energy production is the dimensionless, turbulent stress α, see Eq. 3.29. The condition for self regulation can be formulated analytically, as follows (see, e.g., Gammie 2001; Kratter & Lodato 2016)

$$\alpha = \left| \frac{r}{\Omega} \frac{d\Omega}{dr} \right|^{-2} \frac{1}{\gamma(\gamma-1)\tau_c \Omega}. \tag{3.42}$$

Hence, there is a direct relation between the cooling efficiency (given by τ_c), and the dimensionless turbulent stress. For a Keplerian $\Omega(r)$, the prefactor reduces to $|(r/\Omega)d\Omega/dr|^{-2} = 4/9$. Analogous expressions, including additional heating sources, also exist (see, e.g. Rice et al. 2011). In global disk simulations, the morphology of GI turbulence appears as a superposition of transient spiral, or density waves (see, e.g., Rice et al. 2003; Boley et al. 2006; Cossins, Lodato, & Clarke 2009; Michael et al. 2012; Kratter & Lodato 2016). The wave length of the dominant Fourier modes is found to be mostly of the order of the disk scale height, $k \sim 1/H$ (see, e.g., Gammie 2001; Cossins, Lodato, & Clarke 2009). For studies of the detailed, small-scale structure of GI turbulence, the so-called local shearing-box approximation is often used (see, e.e., Gammie 2001; Shi & Chiang 2014; Riols, Latter, & Paardekooper 2017; Booth & Clarke 2019; Hirose & Shi 2019; Riols & Latter 2018b; Zier & Springel 2023). These local simulations are also consistent with $k \sim 1/H$. Shearing-box simulations provide the possibility to obtain α values for GI turbulence, in a controlled manner. This is also how Eq. 3.42 was demonstrated, in Gammie (2001). However, there has been doubt, whether angular momentum transport, as well as the dissipation of turbulent energy, are local processes, when self-gravity is involved (Balbus & Papaloizou 1999; Gammie 2001; Cossins, Lodato, & Clarke 2009; Kratter & Lodato 2016). The doubt mostly originates from the fact that gravity is a long range force. Hence, there is the possibility of long-range coherent structures, such as global density waves, that are able to transport angular momentum (Cossins, Lodato, & Clarke 2009). This would also imply, that the turbulent kinetic energy is not necessarily thermlised, at the location it is generated, invalidating the above thermal balance. However, it has also been argued, that such waves would quickly lead to shocks, which prevent the waves from travelling too far from their co-rotation radius (see Balbus & Papaloizou 1999; Cossins, Lodato, & Clarke 2009; Kratter & Lodato 2016). Usually, the transport can be considered to be local for cases of thin disks, and small $M_d/M_\star$ ratios (see, e.g., Cossins, Lodato, & Clarke 2009; Kratter & Lodato 2016).

Clumping:
The sate of GI turbulence requires a balance between radiative cooling, and turbulent heating. However, it is not guaranteed, that such a balance can always be established. Taking the aforementioned β-cooling prescription, one can choose the cooling time, $\beta = \tau_c \Omega$, low enough, such that no stationary state is achievable. At first, one might think that GI is simply stronger then, resulting in a higher value of α (see Eq. 3.42). However, GI can not sustain arbitrarily large values of α. Intuitively one might interpret this such that larger α correspond to larger density perturbations (see Rice, Lodato, & Armitage 2005; Cossins, Lodato, & Clarke 2009; Rice et al. 2011). Eventually, the density perturbations are of the order of the background density ($\delta\Sigma/\Sigma \sim 1$). Hence, given that there is a maximum value of α, then there also is a maximum value of turbulent heating. If cooling is efficient enough, then turbulent heating can not balance the latter, and further gravitational collapse ensues, giving rise to clumping, or fragmentation. This was also demonstrated in early simulations of GI-turbulent systems (Gammie 2001; Johnson & Gammie 2003; Rice, Lodato, & Armitage 2005; Clarke, Harper-Clark, & Lodato 2007). Thereby, Gammie (2001) found a critical cooling time of $\tau_{c,\mathrm{crit}}\Omega \sim 3$, below which clumping ensues. However, later studies found larger values, in the range $\beta \sim 10 - 30$ (Meru & Bate 2012; Paardekooper 2012; Baehr & Klahr 2015; Kratter & Lodato 2016), implying that, to some degree, there is an uncertainty in the exact value. It may even be the case that clumping is a statistical process, whereby one can only say whether fragmentation is more or less likely to occur (Paardekooper 2012). Fragmentation was also studied with more elaborated cooling laws (see, e.g., Boley et al. 2006; Stamatellos & Whitworth 2008; Hirose & Shi 2019). In order to determine the exact fragmentation criteria, it is also relevant

whether the considered model is two- or three-dimensional (see, e.g., Young & Clarke 2015), and the Toomre parameter can be relevant as well (see Boss 2017). Another route to clumping can be a very large mass accretion rate $\dot{M}$, as the latter may not be processable by the maximum possible α of GI (see, e.g., Kratter & Lodato 2016). In summary, one could say that clumping will ensue, if a self-regulated state is not possible for the imposed conditions (see, e.g., Kratter & Lodato 2016).

All works shown here, Löhnert, Krätschmer, & Peeters (2020) (see Sect. 7), Löhnert & Peeters (2022) (see Sect. 8), and Sect. 9, focus on GI-turbulent states, in the local shearing-box approximation. Hence, the cases studied there allow a self-regulated, gravito-turbulent state.

3.3.2 Magneto-rotational instability (MRI)

Another important candidate, for a generation mechanism of disk turbulence, is the magneto-rotational instability (MRI) (Balbus & Hawley 1991; Balbus & Hawley 1992; Hawley & Balbus 1992), which is a magnetohydrodynamic (MHD) instability. The instability is a consequence of the fact, that the magnetic field, in an ideal plasma, is frozen into the fluid. Intuitively, one might say that the magnetic field lines are dragged with the fluid flow (see, e.g., Chiuderi & Velli 2015). The magnetic field, $\mathbf{B}$, back-reacts onto the fluid, by exerting Lorentz forces. The detailed MHD equations are given in Sect. 3.2.3, here, it suffices to say that the Lorentz force density contains a term $(\mathbf{B}\cdot\nabla)\mathbf{B}/\mu_0$ (see, e.g., Biskamp 2003; Kulsrud 2005; Chiuderi & Velli 2015), which is sensitive to the curvature of magnetic field lines. If field lines get bent, a restoring force emerges, trying to straighten the field line. This, in combination with a differential rotation, is what gives rise to MRI (see Balbus & Hawley 1998). In the following, the qualitative instability mechanism is briefly reviewed, whereby the intuitive picture follows closely that, given in Balbus & Hawley (1998). Consider two fluid elements, which, initially, orbit at the same radial, and angular position, but are slightly displaced in the vertical direction. The two fluid elements are chosen such that they are connected via a magnetic field line (e.g. in z direction). Lets then assume that a fluctuation causes a small radial displacement, in the opposite direction, of the two fluid elements. As the magnetic field is frozen into the fluid, the field line gets slightly bent by theses displacements. The Kepler, radial velocity profile resembles a differential rotation, and, hence, the inner element, displaced to a slightly smaller radius, now orbits faster than the other fluid element, displaced to a larger radius. This causes the fluid elements to separate in the angular direction, which also increases the bending of the field line, connecting the fluid elements. The restoring force, due to the bending, tries to reduce the separation. The inner parcel is slightly decelerated, whereas the outer parcel is slightly accelerated. This causes the inner parcel to loose centrifugal support, and it moves radially inwards, whereas the outer parcel gains centrifugal support, and it moves radially outwards. As the fluid elements now have an even larger radial separation, the difference in rotation speeds also increases, causing more field-line bending. This establishes a positive feedback loop, providing an instability mechanism. One can think of the two fluid elements, as being connected via a spring (Balbus & Hawley 1998). It also demonstrates, how MRI is capable of transporting angular momentum: The element moving radially outwards is gaining angular momentum from the fluid element that is moving radially inwards, establishing a transport of angular momentum, outwards. However, this process is not inevitable. Were the magnetic field strong enough, the instability could be prevented (see, e.g., Balbus & Hawley 1998). The fact that, for example, the outer fluid element accelerates further out is due to additional centrifugal forces, arising from the acceleration in angular direction, caused by the restoring forces of the field lines. However, the small radial displacement also means that parts of the field-line bending, back-reacts in the radial direction. Hence, too strong a field can prevent the centrifugal forces from flinging the fluid parcels further out, and the mechanism fails (the spring is too stiff in this case). Formally, this translates into a stability criterion of the form (see, e.g., Balbus & Hawley 1998)

$$(\mathbf{k}\cdot\mathbf{v}_A)^2 > 3\Omega^2, \tag{3.43}$$

with the Keplerian[6] angular velocity Ω, the wave vector $\mathbf{k}$, and the Alfven velocity $\mathbf{v}_A$. The most unstable modes are of the form $\delta\mathbf{B} \propto \exp(ik_z z - i\omega t)$, with an initial field $\mathbf{B} = B_z\hat{\mathbf{e}}_z$ (see also Balbus & Hawley 1998). For Keplerian $\Omega(r)$, the highest growth rate is given by (see, e.g., Balbus & Hawley 1998)

$$g_{\max} = \frac{3}{4}\Omega, \quad \text{with} \quad (\mathbf{k}\cdot\mathbf{v}_A)_{\max} = k_{z,\max}\, v_{A,z} = \frac{\sqrt{15}}{4}\Omega. \tag{3.44}$$

Hence, for a given initial magnetic field, B_z, the most unstable wave length is $\lambda_{z,\max} \sim 2\pi v_{A,z}/\Omega$. A configuration with $\delta\mathbf{B} = \delta B_r\hat{\mathbf{e}}_r$ is also consistent with the intuitive picture above. In most accretions disks, one can consider the gas to be reasonably well coupled to the magnetic field, but in some disks systems, especially PPDs, non-ideal MHD effects can be important (see, e.g., Armitage 2011). Effects of low ionisation can be important, as either the temperatures, in PPDs, are too low for thermal ionisation, or the the disk material prevents ionising radiation to penetrate towards the inner disk regions (Armitage 2011). Ohmic resistivity, tends to dampen the growth rates of MRI (see, e.g, Jin 1996; Sano & Miyama 1999). In the limit $v_{A,z}^2/(\eta\Omega) \ll 1$, with Ohmic resistivity η, Sano & Miyama (1999) find $g_{\max} = 3v_{A,z}^2/(4\eta)$, at $k_{z,\max} = \sqrt{3}v_{A,z}/(2\eta)$. For $v_{A,z}^2/(\eta\Omega) > 1$, Sano & Miyama (1999) recover the ideal-MHD limit, for both the growth rate, and the most unstable wave vector. The growth-rate deviation is estimated by the resistive damping rate, $\sim \eta\, k_z^2$ (see, e.g, Jin 1996; Balbus & Hawley 1998). Low ionisation fractions (as may be the case in some regions of PPDs, see, e.g., Armitage 2011) require a more elaborated approach, such as a separate treatment of the neutral and ion fluids (see Blaes & Balbus 1994). One can still find a stability criterion, similar to Eq. 3.43, but the field is only frozen into the ion fluid, and not the entire fluid-mass density, is contributing to v_A (see Blaes & Balbus 1994; Balbus & Hawley 1998). In order to achieve a sufficient coupling to the entire fluid (ions and neutral), the ion-neutral collision rate must be sufficiently large, compared to the orbital frequency, Ω (see Blaes & Balbus 1994; Balbus & Hawley 1998). In one-fluid MHD, the difference between the ion, and neutral fluids, is often modelled, by introducing an additional, non-ideal term into the induction equation, the ambipolar diffusion (see, e.g., Kunz & Balbus 2004; Desch 2004). Interestingly, ambipolar diffusion can act destabilising, in some circumstances, (Kunz & Balbus 2004; Desch 2004). However, if the ion-neutral collision frequency is lower than the orbital frequency, then the corresponding growth rates can be significantly reduced (Kunz & Balbus 2004). Similarly, the Hall effect can also influence disk instabilities (see Wardle 1999; Balbus & Terquem 2001). In the Hall case, the field geometry can have an influence on the stability, whereby configurations, with $(\mathbf{k}\cdot\mathbf{\Omega})(\mathbf{k}\cdot\mathbf{B}) < 0$ can even act destabilising (see Balbus & Terquem 2001), with wave vector $\mathbf{k}$, and angular-velocity vector, $\mathbf{\Omega}$ (e.g., in z direction). In addition to non-ideal effects, also the vertical disk stratification can influence the occurrence of MRI, as the latter imposes a vertical length scale H onto the system. This is most easily understood from Eq. 3.43, by considering the most unstable case with $\mathbf{k} = k_z\hat{\mathbf{e}}_z$. Take a given value of $v_{A,z0}$, then instability is in principle always possible, one simply has to choose sufficiently low wave numbers. However, the vertical scale H prevents arbitrarily large wave lengths. Moreover, the Alfven velocity may also be height-dependent, $v_A(z)$. For example, considering the vertical structure, Sano & Miyama (1999) found that, with Ohmic resistivity, unstable modes occur for magnetic Reynolds numbers above $\mathrm{Rm} = c_s^2/(\eta\Omega) \sim 1$, with the additional condition of sub-thermal fields, $c_s^2/v_A^2 \gtrsim 1$. The latter can also be written as $\beta \gtrsim 1$, with the plasma-β. The requirement of weak fields is also present in the un-stratified, ideal-MHD case, see the spring analogy above.

Numerical simulations demonstrated that the nonlinear evolution of MRI can lead to self-sustained, three-dimensional turbulence (Balbus & Hawley 1991; Hawley, Gammie, & Balbus 1995; Brandenburg et al. 1995; Matsumoto & Tajima 1995; Stone et al. 1996; Hawley, Gammie, & Balbus 1996). In order to study the turbulence details, one often utilises the so-called local shearing-box approximation (see, e.g., Hawley, Gammie, & Balbus 1995), which introduces a local Cartesian coordinate system ($x = r - r_0$, and $y = r_0(\phi - \Omega(r_0)\, t)$), that is co-rotating at a given point

[6] $(\mathbf{k}\cdot\mathbf{v}_A)^2 > -d\Omega^2/d\ln r$ in the general case (see, e.g., Balbus & Hawley 1998).

$r = r_0, \phi = \Omega(r_0)\, t$ (see Sect. 4.1). Global simulations do exist (see, e.g., Hawley & Krolik 2001; Machida & Matsumoto 2003; De Villiers, Hawley, & Krolik 2003; Fragile & Meier 2009; Beckwith, Armitage, & Simon 2011; Suzuki & Inutsuka 2014; Gressel et al. 2015; Zhu & Stone 2018; Mishra et al. 2020), but the resolution requirements for MRI turbulence are harder to establish in global models, than in local ones (see, e.g., Hawley, Guan, & Krolik 2011). Some global MHD aspects, such as disk winds, or jets, may only be accessible via global simulations though (Suzuki & Inutsuka 2009; Bai & Stone 2013a; Sorathia et al. 2012; Suzuki & Inutsuka 2014; Gressel et al. 2015; Zhu & Stone 2018). The benefit of local simulations is that they allow for a more detailed analysis of the turbulence properties (see, e.g., Fromang & Papaloizou 2007; Guan et al. 2009; Lesur & Longaretti 2011; Simon, Beckwith, & Armitage 2012; Nauman & Blackman 2014; Walker, Lesur, & Boldyrev 2016). For shearing-box simulations alone, a variety of different setups is possible. One differentiating factor is the treatment of vertical gravity. If the vertical component of the central objects gravity ($\sim \Omega_0^2\, z$) was taken into account, then the box is referred to as stratified. Otherwise, the box is un-stratified. Another parameter is the geometry of the initial magnetic field. Possible are cases with zero-net flux (the average of $\mathbf{B}$, over planes of constant x, y, or z, is zero), or cases with a net mean magnetic field. In the latter case, the structure, and strength of turbulence, can depend on the net strength of the mean field, and local winds are often observed (see, e.g., Bai & Stone 2013a; Fromang et al. 2013; Salvesen et al. 2016). The detailed thermal, and radiation physics can also vary between different shearing-box setups. The simplest case is that of an isothermal equation of state, $P = c_{s,i}^2 \rho$, with constant $c_{s,i}$, but often, more elaborated models may be required (see, e.g., Hirose et al. 2014; Hirose 2015). It is pointed out, that the exact requirements for MRI convergence, in local shearing-box simulations, is still debated (Ryan et al. 2017). Especially in unstratified boxes, with a zero-net-flux, the outcome can be resolution dependent (see, e.g., Fromang & Papaloizou 2007). However, a finite mean magnetic field, larger box sizes, or suitable values of both viscosity and Ohmic resistivity might lead to convergence (see, e.g., Simon & Hawley 2009; Guan et al. 2009; Fromang 2010; Simon, Beckwith, & Armitage 2012; Ross, Latter, & Guilet 2016; Shi, Stone, & Huang 2016; Ryan et al. 2017). There is evidence that stratified cases tend to converge (Shi, Krolik, & Hirose 2010; Davis, Stone, & Pessah 2010), but this is not entirely clear for all cases (see Bodo et al. 2014; Ryan et al. 2017). However, a detailed discussion of this is beyond the scope of this thesis. An approximate criterion, for whether MRI is resolved, is the quality factor, $Q_j \sim 2\pi |v_{A,j}|/(\Omega \Delta x_j)$ (Noble, Krolik, & Hawley 2010; Sano et al. 2004; Hawley, Guan, & Krolik 2011). Often, one only considers the Q_z component, which corresponds to the number of discretisation lenghts, Δz, fitting the most unstable wave length $\lambda_{z,\max}$. For MRI to be resolved, one has to demand $Q_z \gg 1$, whereby, more precisely, Sano et al. (2004) finds that $Q_z > 6$ is required. Non-axisymmetric modes, which must occur in turbulent states, may also require sufficiently large Q_y, but for similar resolutions (in both the z and the y direction), the latter is often guaranteed due to the effect of shear, which can generate significant B_y field strengths, by shearing radial fields, B_r, into the y direction (Hawley, Guan, & Krolik 2011). Furthermore, it has turned out that some statistical properties of MRI turbulence are rather universal, and are found in a variety of simulations (see Blackman, Penna, & Varnière 2008). This includes, for example, the ratio of Maxwell stress to magnetic pressure, which is often found in the range (see, e.g., Hawley, Gammie, & Balbus 1995; Blackman, Penna, & Varnière 2008; Simon, Hawley, & Beckwith 2011; Hawley, Guan, & Krolik 2011; Salvesen et al. 2016)

$$r_{sp} := \frac{\langle -B_x B_y \rangle}{\langle |\mathbf{B}|^2/2 \rangle} \sim 0.3 - 0.4. \tag{3.45}$$

Similarly, the Maxwell stress contribution is consistently larger than the Reynolds contribution, by roughly a factor of four, $\langle -B_x B_y/\mu_0 \rangle \sim 4 \langle \rho v_x \delta v_y \rangle$ (see, e.g., Hawley, Gammie, & Balbus 1995; Pessah, Chan, & Psaltis 2006; Hawley, Guan, & Krolik 2011). Moreover, these ratios seem to not depend on the exact system parameters, such as the initial field configuration, whether the box is stratified, or the boundary conditions (Pessah, Chan, & Psaltis 2006; Blackman, Penna, & Varnière 2008).

Also important, for the nonlinear evolution of MRI, is the influence of non-ideal MHD effects. In some of the early non-ideal, unstratified shearing-box simulations, Lesur & Longaretti (2007) and Fromang et al. (2007) found that the turbulent stress α increases, with increasing magnetic Prandtl number, $\mathrm{Pm} = \nu/\eta$ (with viscosity ν, and Ohmic resistivity η). In Fromang et al. (2007), no turbulence was found for $\mathrm{Pm} \lesssim 1$, in zero-net-flux cases. This is not inevitably the case in simulations with a net magnetic flux (see Simon & Hawley 2009), or with vertical-field boundary conditions (Käpylä & Korpi 2011). It also appears that stratification is an additional factor, that allows for turbulence below $\mathrm{Pm} \sim 1$ (see, e.g., Davis, Stone, & Pessah 2010; Oishi & Mac Low 2011), and for large enough Rm (Oishi & Mac Low 2011). There is still debate about the exact behaviour of MRI in the low Pm regime (see, e.g., Meheut et al. 2015). However, an in-depth discussion is beyond the scope of this introduction. More generally, Ohmic resistivity has a dampening effect, and small enough magnetic Reynolds numbers, Rm, can cause MRI turbulence to cease (Sano & Stone 2002; Ziegler & Rüdiger 2001; Simon & Hawley 2009; Simon, Hawley, & Beckwith 2011). For moderate Ohmic resistivity, $\mathrm{Rm} \sim 3200$, Davis, Stone, & Pessah (2010) and Simon, Hawley, & Beckwith (2011), found episodic decay, and eventual regrowth, of turbulence, in stratified simulations. The latter effect may be related to the effect of shear, which eventually generates enough magnetic field strength, B_y, to reignite MRI, even in a resistively damped case (Simon, Hawley, & Beckwith 2011). The influence of other non-ideal MHD effects on MRI have also been tested (see, e.g., Bai & Stone 2011; Bai & Stone 2013b; Simon et al. 2013; Lesur, Kunz, & Fromang 2014; Bai 2015; Simon et al. 2015). Strong ambipolar diffusion ($v_A^2/(\eta_A \Omega) \lesssim 1$, with ambipolar-diffusion coefficient, η_A) tends to dampen MRI (Simon et al. 2013), which is similar to the effects of Ohmic resistivity. The influence of the Hall effect can be more subtle, as the latter also depends on the orientation of the mean magnetic field, and it may actually destabilise configurations that would be stable against ideal MRI (Kunz & Lesur 2013; Lesur, Kunz, & Fromang 2014; Simon et al. 2015). This is in agreement, with the linear stability tests (Balbus & Terquem 2001). Such non-ideal effects are especially important in low-ionisation regimes, in PPD disks (see, e.g., Armitage 2011). Some PPD regions may only provide sufficient radiative ionisation near the top layers, leading to strongly height-dependent ionisation, and the formation of a dead-zone, near the mid-plane (Fleming & Stone 2003; Turner, Sano, & Dziourkevitch 2007; Bai 2015; Simon et al. 2015; Flock et al. 2015).

Finally, another important aspect of MRI is the associated dynamo, that is, the ability of MRI to generate, and sustain, large-scale magnetic fields (see, e.g., Brandenburg et al. 1995; Hawley, Gammie, & Balbus 1996; Johansen & Levin 2008; Vishniac 2009; Shi, Krolik, & Hirose 2010; Gressel 2010; Simon, Hawley, & Beckwith 2011; O'Neill et al. 2011; Salvesen et al. 2016). Simulations demonstrate, that the MRI state is consistent with an $\alpha - \Omega$ dynamo (Guan & Gammie 2011; Simon, Hawley, & Beckwith 2011). The latter refers to the combination of an α-, and an Ω-effect (see, e.g., Brandenburg & Subramanian 2005), whereby the α here has to be distinguished from the dimensionless turbulent viscosity.
The nature of these effects is best explained, using the mean-field approach (see, e.g., Steenbeck, Krause, & Rädler 1966; Biskamp 2003; Brandenburg & Subramanian 2005). Thereby, the fields (including the velocity) are separated into an averaged field, and a fluctuating part, for example, $\mathbf{B} = \langle \mathbf{B} \rangle + \delta\mathbf{B}$, and $\mathbf{v} = \langle \mathbf{v} \rangle + \delta\mathbf{v}$. For brevity, $\langle ... \rangle$ is simply assumed to be some type of average, and δ indicates deviations from the latter. Substituting this separation into the ideal-MHD induction equation, one obtains an equation for the averaged field (see, e.g., Brandenburg & Subramanian 2005)

$$\partial_t \langle \mathbf{B} \rangle \quad = \quad \nabla \times (\langle \mathbf{v} \rangle \times \langle \mathbf{B} \rangle) + \nabla \times \langle \mathcal{E} \rangle, \tag{3.46}$$

whereby the electromotive force, or EMF, $\mathcal{E} = \delta\mathbf{v} \times \delta\mathbf{B}$ was introduced. Assuming, for simplicity,

that the mean velocity satisfies $\nabla \cdot \langle \mathbf{v} \rangle = 0$, one finds[7].

$$\partial_t \langle \mathbf{B} \rangle = \underbrace{(\langle \mathbf{B} \rangle \cdot \nabla) \langle \mathbf{v} \rangle}_{(1)} - \underbrace{(\langle \mathbf{v} \rangle \cdot \nabla) \langle \mathbf{B} \rangle}_{(2)} + \underbrace{\nabla \times \langle \mathcal{E} \rangle}_{(3)} . \tag{3.47}$$

The (2)-term simply means that the mean flow, $\langle \mathbf{v} \rangle$, transports a certain field distribution, $\langle \mathbf{B} \rangle$, past a given location, say $\mathbf{x}$, contributing to $\partial_t \langle \mathbf{B} \rangle$, at this location. The term (1) is more subtle. It's effect is best understood by considering a shear flow in Cartesian coordinates, for example, $\langle \mathbf{v} \rangle = sx\,\hat{\mathbf{e}}_y$, with shear rate s. In that case, term (1) only contributes to the y component, yielding $\partial_t \langle B_y \rangle = s \langle B_x \rangle$. Hence, the shear generates a mean field in the y direction, out of a mean field in the x direction. Such situations are relevant in the astrophysical context, as differential rotation, with spatially varying $\Omega(r)$, can lead to to this effect, which is, therefore, often referred to as Ω-effect (see, e.g., Brandenburg & Subramanian 2005). What remains is the α-effect, and the latter is related to term (3). Thereby, the EMF is represented in terms of the mean field, $\langle \mathcal{E}_j \rangle = \alpha_{jk} \langle B_k \rangle + \eta_{jkl} \partial_k \langle B_l \rangle$ (see, e.g., Moffatt 1978; Biskamp 2003; Brandenburg & Subramanian 2005; Chiuderi & Velli 2015). Depending on the analytical model, the α_{jk}, and η_{jkl} may be condensed to single numbers, yielding $\langle \mathcal{E} \rangle = \alpha_{\rm dyn} \langle \mathbf{B} \rangle - \eta_{\rm dyn} \langle \mathbf{J} \rangle$ (see, e.g., Brandenburg & Subramanian 2005). Thereby, the dynamo-coefficient $\alpha_{\rm dyn}$ allows for field amplification, whereas $\eta_{\rm dyn}$ represents a form of turbulent diffusivity. Depending on the closure model, one can derive expressions for $\alpha_{\rm dyn}$, and $\eta_{\rm dyn}$. Neglecting the back-reaction via Lorentz forces (kinematic dynamo), one can derive $\alpha_{\rm dyn} = -(1/3)\tau H_k$, with kinetic helicity $H_k = \langle \delta\mathbf{v} \cdot \nabla \times \delta\mathbf{v} \rangle$, and $\eta_{\rm dyn} = (1/3)\tau \langle \delta\mathbf{v}^2 \rangle$, whereby τ is a typical correlation time (see Biskamp 2003; Brandenburg & Subramanian 2005). For stronger fields, the back-reaction of the field, onto the turbulence, can be important, and generalisations also take into account the current helicity, $H_c = \langle \delta\mathbf{v}_A \cdot \nabla \times \delta\mathbf{v}_A \rangle$, yielding $\alpha_{\rm dyn} \propto (-H_k + H_c)$, with the perturbed Alfven velocity, $\delta\mathbf{v}_A$ (see, e.g., Pouquet, Frisch, & Léorat 1976; Blackman & Field 2002; Biskamp 2003; Brandenburg & Subramanian 2005). The exact form may also be modified by an inverse cascade of magnetic helicity $\langle \mathbf{B} \cdot \mathbf{A} \rangle$, with $\mathbf{B} = \nabla \times \mathbf{A}$ (see, e.g., Müller, Malapaka, & Busse 2012; Teissier & Müller 2021). More specifically, in the context of MRI turbulence, the importance of current helicity, H_c, was explored by Gressel (2010). The MRI dynamo is not a typical kinematic dynamo, in the sense that the magnetic field is not passive with respect to the fluid flow. Lorentz forces are important a-priori, as they are responsible for the instability mechanism in the first place (see, e.g., Balbus & Hawley 1998). It is noted that vertical motions may also be involved in the MRI dynamo, as MRI turbulence often exhibits periodic patterns in time, so-called butterfly diagrams (see, e.g., Brandenburg et al. 1995; Stone et al. 1996; Miller & Stone 2000; Shi, Krolik, & Hirose 2010; Simon, Beckwith, & Armitage 2012; Salvesen et al. 2016). The latter appear as a consequence, of magnetic energy, leaving the mid-plane region, moving vertically upwards. Whether this phenomenon is related to buoyancy, or other mechanisms is not entirely clear (see, e.g., Gressel 2010). The exact mechanisms, involved in both MRI turbulence and dynamo, are still an active area of research.

[7] The identity $\nabla \times (\mathbf{A} \times \mathbf{B}) = (\mathbf{B} \cdot \nabla)\mathbf{A} - (\mathbf{A} \cdot \nabla)\mathbf{B} + \mathbf{A}(\nabla \cdot \mathbf{B}) - \mathbf{B}(\nabla \cdot \mathbf{A})$ is used (see, e.g., Bronstein et al. 2012).

Chapter 4

Methods and Numerical Schemes

4.1 The local shearing-box approximation

The model that is used, in the works Löhnert, Krätschmer, & Peeters (2020) (Sect. 7), Löhnert & Peeters (2022) (Sect. 8), and Sect. 9, is the so-called local shearing-box approximation (see, e.g., Hawley, Gammie, & Balbus 1995; Balbus & Hawley 1998). The goal of this section is to motivate how this local model can be constructed. Starting point is the Euler equation in the following form:

$$\frac{\partial \mathbf{u}}{\partial t} + (\mathbf{u} \cdot \nabla)\,\mathbf{u} = -\frac{1}{\rho}\nabla P - \nabla \Phi^{\star} + \frac{1}{\rho}\mathbf{f}_{\mathrm{ext}}. \tag{4.1}$$

Thereby, ρ is the mass density, $\mathbf{u}$ is the fluid velocity, P is the thermal pressure, and $\Phi^{\star}$ is the gravitational potential of the central object. For now, $\mathbf{f}_{\mathrm{ext}}$ is simply a dummy force density, summarising all additional forces that may be relevant (e.g., Lorentz forces, or self-gravity). The Euler equation, as given above, is rather general, and may directly by applied to a global disk model. In order to study the turbulence details, a local model can often be convenient, as this limits the range of length scales that need to be resolved (see, e.g., the review Balbus & Hawley 1998). Thereby, one assumes that the typical wavelengths, λ_{typ}, connected to the turbulent motions, are reasonably small, compared to the global disk scale, $\lambda_{\mathrm{typ}}/r \ll 1$. More precisely, the goal is to attach a local, co-rotating, Cartesian coordinate system to the disk material (see also Goldreich & Lynden-Bell 1965; Toomre 1981; Binney & Tremaine 2008; Balbus & Hawley 1998). The idea of this frame is sketched in Fig. 4.1. In order to construct such a frame, one can start with global, cylindrical coordinates (r, ϕ, z). Then, a fiducial radius, say r_0, is selected, with a corresponding Kepler orbital frequency $\Omega_0 = \Omega(r_0)$. One then transforms to a cylindrical coordinate system, $(\tilde{r} = r, \tilde{\phi} = \phi - \Omega_0\, t, \tilde{z} = z)$, that co-rotates with Ω_0, at $r = r_0$. Finally, in order to obtain a local, Cartesian coordinate system, one introduces the coordinates (see, e.g., Goldreich & Lynden-Bell 1965; Toomre 1981; Binney &

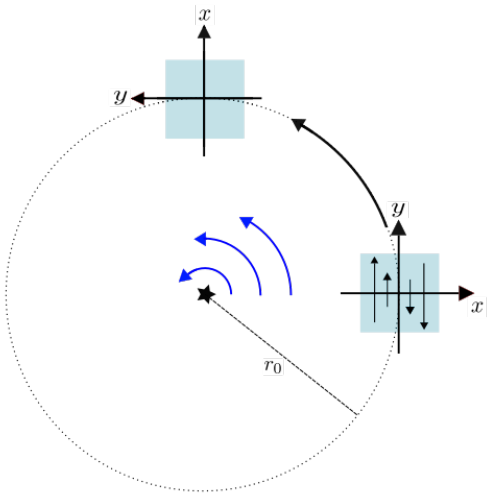

Figure 4.1: Conceptual visualisation of the local shearing-box approximation.

Tremaine 2008; Balbus & Hawley 1998)

$$x = r - r_0, \quad y = r_0\tilde{\phi}, \quad z, \tag{4.2}$$

whereby it is assumed that $|x|/r_0 = |y|/r_0 \ll 1$. It is furthermore assumed that the disk is thin, that is, $|z|/r_0 \ll 1$, or $H \ll 1$. One can show that the Euler equation, in this frame of reference, is of the form

$$\frac{\partial \mathbf{v}}{\partial t} + (\mathbf{v}\cdot\nabla)\,\mathbf{v} = -\frac{1}{\rho}\nabla P + \frac{1}{\rho}\mathbf{f}_{\rm ext} - 2\boldsymbol{\Omega}_0 \times \mathbf{v} + 3\Omega_0^2 x\hat{\mathbf{e}}_x + \Omega_0^2 z\hat{\mathbf{e}}_z, \tag{4.3}$$

which is often referred to as the local Hill approximation (see, e.g., Binney & Tremaine 2008). A more detailed derivation, of Eq. 4.3, is provided in Appendix H. This reference frame is not an inertial frame, and additional, fictitious force terms appear on the right hand side. One of these terms is the specific Coriolis force, $-2\boldsymbol{\Omega}_0 \times \mathbf{v}$, while the term $3\Omega_0^2 x\hat{\mathbf{e}}_x$ represents the net force of the central objects gravity (in radial direction), and the centrifugal force, due to the non-inertial frame. Finally, the term $\Omega_0^2 z\hat{\mathbf{e}}_z$ is the Taylor-expanded z component of the central objects gravity. Technically, Eq. 4.3 can be used for arbitrary values of x and y (often referred to as a shearing sheet, see, e.g., Goldreich & Lynden-Bell 1965; Binney & Tremaine 2008), but one has to keep in mind that this coordinate system is intended for a local approximation only. In Fig. 4.1, this is illustrated by the blue-shaded region.

Lets now assume a sate where both ρ and P are horizontally homogeneous, that is, ρ and P do not depend on (x, y). In the vertical direction, gravitational, and pressure forces give rise to density stratification. The corresponding force balance follows from the vertical component of Eq. 4.3, yielding $\rho\Omega_0^2 z - \partial_z P + f_{{\rm ext},z} = 0$. One can then show that Eq. 4.3 has the stationary solution

$$\mathbf{v}_0 = -(3\Omega_0/2)\, x\,\hat{\mathbf{e}}_y = -q\Omega_0 x\,\hat{\mathbf{e}}_y. \tag{4.4}$$

This solution represents a shear flow in y direction, centred at $x = 0$. It is noted that one could have also obtained this result, by expanding the Kepler orbital velocity difference, $r\Omega - r_0\Omega_0$, for small $x = r - r_0$ (see, e.g., Balbus & Hawley 1998). Often, the shearing pre-factor is abbreviated by q, here $q = 3/2$, as, for Keplerian orbits, one finds $\Omega(r) \propto r^{-3/2}$ (see also Balbus & Hawley 1998). In Fig. 4.1, the shear flow is depicted by the black arrows inside the blue-shaded region. In the shearing box approximation, this shear flow represents the Kepler background velocity, and turbulent velocities are interpreted as deviations from this background flow. Hence, the velocity is in general of the form $\mathbf{v} = q\Omega_0 x\hat{\mathbf{e}}_y + \delta\mathbf{v}$, with $\delta\mathbf{v} = (v_x, \delta v_y, v_z)$ (the delta is omitted in v_x, and v_z, as the latter are, by definition, perturbations).

4.2 Summary of all three-dimensional equations of motion

Listed below, is the full set of equations, used in the local shearing-box approximation (see, e.g., Stone & Gardiner 2010; Clarke & Carswell 2007; Balbus & Hawley 1998):

$$\partial_t \rho + \nabla\cdot(\rho\mathbf{v}) = 0 \tag{4.5}$$

$$\partial_t(\rho\mathbf{v}) + \nabla\cdot\left(\rho\mathbf{v}\mathbf{v} - \frac{1}{\mu_0}\mathbf{B}\mathbf{B} + \left(P + \frac{\mathbf{B}^2}{2\mu_0}\right)\underline{\mathbf{I}} + \underline{\mathbf{G}}\right) = -2\rho\boldsymbol{\Omega}_0\times\mathbf{v} + 3\rho\Omega_0^2 x\mathbf{e}_x - \rho\Omega_0^2 z\mathbf{e}_z \tag{4.6}$$

$$\partial_t\mathbf{B} - \nabla\times(\mathbf{v}\times\mathbf{B}) = \frac{\eta}{\mu_0}\nabla^2\mathbf{B} \tag{4.7}$$

$$\partial_t E + \nabla\cdot\left(\left(E + P + \frac{\mathbf{B}^2}{2\mu_0}\right)\mathbf{v} - \mathbf{B}(\mathbf{B}\cdot\mathbf{v})\right) = -\rho\mathbf{v}\cdot\nabla\Phi + 2\Omega_0^2 x v_x - \Omega_0^2 z v_z + \rho\dot{q} \tag{4.8}$$

$$\nabla^2\Phi = 4\pi G\rho. \tag{4.9}$$

Eq. 4.5 represents mass conservation (continuity equation), whereby ρ and $\mathbf{v}$ are the mass density and fluid velocity, respectively. Eq. 4.6 is essentially Eq. 4.3, except that it was rewritten in conservative form (momentum conservation). Hence, changes of the momentum ($\rho\mathbf{v}$) are due to fluxes through the boundaries (expressions inside the divergence term), or momentum sources (terms on the right hand side). Note that the additional terms, containing the magnetic field, $\mathbf{B}$, and the gravitational stress tensor, $\underline{\mathbf{G}}$ (see also Lynden-Bell & Kalnajs 1972), were previously summarised in the dummy force density $\mathbf{f}_{\text{ext}}$. Eq. 4.7 is the induction equation, which provides the time evolution of the magnetic field, including Ohmic resistivity, η. The time evolution of the total energy density,

$$E = \frac{1}{2}\rho\mathbf{v}^2 + E_{\text{th}} + \frac{1}{2\mu_0}\mathbf{B}^2, \tag{4.10}$$

is given by Eq. 4.8, whereby potential energies, due to gravity, are not included in E, and appear as source terms on the right hand side. Separate equations for the kinetic, and magnetic energy densities can be obtained by multiplying Eq. 4.6 with $\mathbf{v}$, and Eq. 4.7 with $\mathbf{B}/\mu_0$, respectively. What then remains, in order to obtain Eq. 4.8, is an evolution law for the thermal energy density. More details about how such an equation can be obtained are provided in Appendix I. Most of the source terms of Eq. 4.8 can directly be identified with source terms of Eq. 4.6, though there is one extra term, $\rho\dot{q}$. The latter is referred to as cooling (heating) term, and accounts for radiative cooling, or additional sources of heating, besides turbulent heat production (see, e.g., Gammie 2001; Rice et al. 2011). More details about this term are provided in Sect. 4.5.3, and Appendix I. The Poisson equation, Eq. 4.9, determines the potential of self-gravity, for a given mass density ρ. The equation of state is assumed to be that of an ideal gas, $P = nk_BT$, whereby P is the pressure, T is the temperature, and n is the number density of particles. The thermal energy density is then given by $E_{th} = (f/2)nk_BT = nk_BT/(\gamma - 1)$, whereby f is the number of degrees of freedom ($f = 3$ for a mono-atomic gas in three dimensions), and $\gamma = 1 + 2/f$ is the adiabatic index (5/3 for the mono-atomic case) (see, e.g., Regev, Umurhan, & Yecko 2016). Using this, the equation of state can be written as $P = (\gamma - 1)E_{th}$, linking the pressure (appearing in the Euler equation) to the thermal energy density.

4.3 A numerical scheme for the local shearing-box model

The goal of this section is to motivate a scheme for the local shearing-sheet approximation, that can be implemented numerically, and that was used in Löhnert, Krätschmer, & Peeters (2020), Löhnert & Peeters (2022), and Sect. 9. Such a scheme is the shearing-box method, suggested in Hawley, Gammie, & Balbus (1995). The main points of the shearing-box method rely only on the horizontal coordinates, x and y. How z is taken into account depends on other details. In Löhnert, Krätschmer, & Peeters (2020) (Sect. 7), the simulations are two-dimensional. However, in Löhnert & Peeters (2022) (Sect. 8), and Sect. 9, fully three-dimensional simulations are studied, whereby the disks stratification is established in the z direction. A discussion of the vertical direction is postponed to below. Here, z is merely kept, and the focus is on x, and y. Starting point is a local, Cartesian coordinate system, (x, y, z), co-rotating at $r = r_0$, see Sect. 4.1. The simulation domain is a rectangular grid, centred at $x = y = z = 0$, with dimensions L_x, L_y, and L_z. Hence, the possible coordinate values are in the range $-L_x/2 \leq x \leq L_x/2$, and similar for y, and z.

Of central importance, for the shearing-box method, are the boundary conditions in the x and y direction. The model is local, and one assumes the surrounding regions to be of a composition, similar to the simulation volume itself. Hence, one is inclined to use periodic boundary conditions in x, and y. Periodicity would enforce that the surrounding region is tiled with boxes, identical to the simulation domain. Periodicity is certainly possible for the y boundaries, though for the radial, x, boundaries, a periodic continuation is problematic. As noted in Sect. 4.1, the local equations of motion give rise to a shear flow, $\mathbf{v}_0 = -q\Omega_0 x\hat{\mathbf{e}}_y$, as the homo-

geneous equilibrium solution (Keplerian differential rotation). The shear velocity depends on x explicitly, and is certainly not periodic, conflicting with periodic boundaries in the x direction. This is circumvented by using so-called shearing-periodic boundary conditions in the x-direction (see Hawley, Gammie, & Balbus 1995; Balbus & Hawley 1998). To understand the idea, it is convenient to first consider two additional boxes, identical to the initial simulation domain. One then demands that the additional boxes are radially adjacent to the original box, with coordinate centres, located at $x_c^{\pm} = \pm L_x$. Hence, one box connects to the inner x boundary of the original box (x_c^-), and the other box connects to the outer x boundary (x_c^+). Extrapolating the shear flow to theses center locations, one obtains, $v_{y,c}^{\pm} = \mp q\Omega_0 L_x$, for $x_c^{\pm} = \pm L_x$. The idea is now that the inner box moves past the original simulation domain with velocity $v_{y,c}^-$, and the outer box moves past the original box with velocity $v_{y,c}^+$. It is best to visualise the procedure, using the surface mass density, Σ, obtained from a GI simulation with *DiskFlow*, see Fig. 4.2. The yellow lines indicate the boundaries of the initial simulation domain, and the blue boundaries correspond to surrounding copies of this domain. The coordinate centres of the original domain ($x_c = 0$), and two radially adjacent domains (x_c^-, and x_c^+), are highlighted in white. The boundaries in y direction are strictly periodic, whereas the x boundaries are almost periodic, except that the inner and outer boundaries are shifted with respect to each other, and the amount of shift is a function of time. Say $f(x, y, z)$ is some dummy variable, then the (x, y) boundary conditions are realised as follows (see, e.g., Balbus & Hawley 1998):

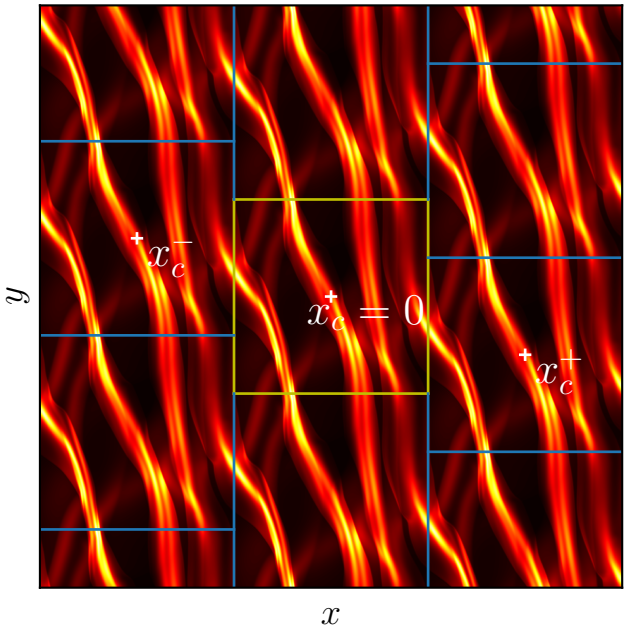

Figure 4.2: Surface density, Σ, evaluated for a GI-turbulent state, obtained with *DiskFlow*. The initial shearing box (yellow boundaries), is surrounded by identical boxes, passing by (blue boundaries). Boxes to the left move upwards, and boxes to the right move downwards.

$$\begin{aligned} f(x \pm L_x, y \mp q\Omega_0 L_x\, t, z) &= f(x, y, z) \\ f(x, y \pm L_y, z) &= f(x, y, z). \end{aligned} \tag{4.11}$$

The second equation refers to the periodic boundary conditions in y direction, and the first equation refers to the shearing-periodic boundary conditions. From the latter two equations, one can see that a radial displacement of one box length, $\pm L_x$, is always connected to a y displacement of $\mp q\Omega_0 L_x\, t$. These boundary conditions hold for all variables $f \in \{\rho, P, \mathbf{B}, \Phi, v_x, v_z\}$, except the toroidal velocity v_y. The latter is in general of the form $v_y = -q\Omega_0 x + \delta v_y$, with δv_y representing the deviation from the shear flow. Hence, the y boundary can be handled equally to the former variables, but for the x boundaries, one has to consider the relative velocity, $v_{y,c}^{\pm} = \mp q\Omega_0 L_x$, of the adjacent boxes. As a consequence, the boundary conditions for the toroidal velocity are as follows (see Hawley, Gammie,

& Balbus 1995; Balbus & Hawley 1998)

$$\begin{aligned} v_y(x \pm L_x, y \mp q\Omega_0 L_x\, t, z) &= v_y(x,y,z) \mp q\Omega_0 L_x \\ v_y(x, y \pm L_y, z) &= v_y(x,y,z) \end{aligned} \tag{4.12}$$

The additional term $\mp q\Omega_0 L_x$ is a boost that accounts for the fact that the radiallay-adjacent boxes pass by the original box. If only the deviation δv_y was considered, then the boundary conditions in Eq. 4.12 would reduce to the form of Eq. 4.11. Numerically, this implies that a fluid parcel, leaving the box at the left boundary, enters the box at the right boundary, but at a shifted location. All properties of the parcel retain their original value, including δv_y, but an additional boost in y direction is required, because the shear is antisymmetric with respect to $x = 0$, and the velocity must have a jump from the left ot the right boundary. Finally, the time-dependence of Eqs. 4.11, and 4.12, that is, the t in $y \mp q\Omega_0 L_x\, t$, requires a short discussion. Obviously, the absolute amount of shift, $|q\Omega_0 L_x\, t|$, increases linearly with time. This is rather inconvenient for longer simulations. However, one can see from Fig. 4.2 that, as the neighbouring boxes pass by, the setup periodically returns to a state where the boxes align perfectly. More precisely, this happens at times t_p, when $|q\Omega_0 L_x\, t_p| = M\, L_y$, with $M \in \mathbb{N}$. Put differently, perfect alignment happens at time points $t_p\Omega_0 = M\, \Delta t_p$, with $\Delta t_p = qL_x/L_y$ (see Balbus & Hawley 1998). Note that the boundary conditions (Eqs. 4.11, and 4.12) reduce to strictly periodic boundary conditions, in this case. Hence, the time Δt_p is often referred to as periodic time (Hawley, Gammie, & Balbus 1995; Balbus & Hawley 1998). This allows a more convenient handling in simulations, by introducing a new time counter that is reset to zero, after a time Δt_p has past. This counter is then used for t, in Eqs. 4.11, and 4.12.

4.4 Self-gravity prescription in the local shearing box

The Poisson equation, $\nabla^2\Phi = 4\pi G\rho$ (see, e.g., Binney & Tremaine 2008), is markedly different from the other evolution laws, such as the induction equation for the magnetic field (see Sect. 4.2), as it does not contain time derivatives. It is non-local, in the sense that there is no retardation. A change of the mass density, ρ, at point A, causes an immediate response of the potential, Φ, at point B. Put differently, the value of Φ, at a given grid point, depends on the ρ values, at all other grid locations (see also Binney & Tremaine 2008; Balbus & Papaloizou 1999). Moreover, since a form of periodic boundary conditions is used, it is implied that there is also mass outside of the actual simulation volume, which also contributes to the Φ values, within the simulation domain. This suggests a different numerical method, to solve the Poisson equation. The method used here was inspired by the scheme, proposed in Koyama & Ostriker (2009) and Shi, Krolik, & Hirose (2010), though with minor modifications. This is a Fourier-based method that takes advantage of the periodicity. The Poisson solvers are essential for the works Löhnert, Krätschmer, & Peeters (2020) (Sect. 7), Löhnert & Peeters (2022) (see Sect. 8), and Sect. 9. Moreover, the above method was not implemented in the base-Poisson solver, provided by Athena (Athena is used in the works Löhnert & Peeters (2022), and Sect. 9), and the latter had to be modified accordingly. Hence, it is appropriate to discuss the approach, used to solve the Poisson equation, in more detail. The following two subsections aim to provide a very general overview. Details about the numerical implementation follow in Sects. 4.5.5, and 4.6.4.

4.4.1 General considerations

The naive approach, to obtain the potential, at point P, would be to sum up the contributions from all other grid points. Say there are N_V grid points within the simulation volume V, then this would require to sum over N_V grid points (Note that this does not account for mass outside of V). Since one wants to know the potential at each grid point, this requires N_V^2 operations in total. The linearity of the Poisson equation, with respect to the potential Φ, suggests a Fourier approach,

thereby utilising the efficiency of the Fast-Fourier transform (Cooley & Tukey 1965). By utilising Fast-Fourier transforms (FFTs), the required number of operations can be reduced, to be of the order of $N_V \log(N_V)$ operations (see, e.g., Landau et al. 2008). A discrete Fourier transform (DFT), and its numerical instantiation, the FFT, assume the boundary conditions to be periodic (see, e.g., Binney & Tremaine 2008; Bronstein et al. 2012). Hence, using three-dimensional FFTs, to solve the Poisson equation, assumes that ρ, and Φ repeat infinitely, outside of the simulation domain. This is problematic for the z direction, because stratification implies that ρ falls off with increasing $|z|$, and there is essentially no mass outside of the simulation volume. Hence, the procedure is to use Fourier transforms along x, and y, but to keep the z-coordinate separate. Technically, due to shearing-periodicity, the x direction is also problematic, though this is addressed in Sect. 4.4.2. In this section, no direct reference is made to the bounded shearing-box, as defined in Sect. 4.3, and it is assumed that the shearing sheet extends to infinity in directions x and y. And, correspondingly, Fourier transforms (see, e.g., Bronstein et al. 2012) over the entire (x, y) plane are used.

As a starting point, the potential is represented as a Fourier-transform in the directions x and y only[1]

$$\Phi(x, y, z) = \frac{1}{4\pi^2} \int_{\mathbb{R}^2} dk_x dk_y \, \hat{\Phi}(k_x, k_y, z) \, e^{ik_x x + ik_y y} = \frac{1}{4\pi^2} \int_{\mathbb{R}^2} d^2k \, \hat{\Phi}(\mathbf{k}, z) \, e^{i\mathbf{k}\cdot\mathbf{x}_{(2)}}. \tag{4.13}$$

For reasons of shorter notation, the abbreviations $\mathbf{k} = (k_x, k_y)$, $\mathbf{x}_{(2)} = (x, y)$, and $k = |\mathbf{k}|$ were introduced. The mass density can be represented in a similar way:

$$\rho(x, y, z) = \frac{1}{4\pi^2} \int_{\mathbb{R}^2} d^2k \, \hat{\rho}(\mathbf{k}, z) \, e^{i\mathbf{k}\cdot\mathbf{x}_{(2)}}. \tag{4.14}$$

One then substitutes Eqs. 4.13, and 4.14 into the Poisson equation. The resulting equation then contains integrals of the form $\int_{\mathbb{R}^2}(...)dk_x \, dk_y$. The integrations can be eliminated by projecting onto $e^{i\mathbf{k}\cdot\mathbf{x}_{(2)}}$[2], yielding:

$$-k^2\hat{\Phi}(\mathbf{k}, z) + \partial_z^2\hat{\Phi}(\mathbf{k}, z) = 4\pi G\hat{\rho}(\mathbf{k}, z). \tag{4.15}$$

The Fourier representation of the mass density, $\hat{\rho}(\mathbf{k}, z)$, can be an arbitrary function of z. One can construct the general solution $\hat{\Phi}(\mathbf{k}, z)$, by first considering the simpler mass distribution $\hat{\rho} = \delta(z - z')$, with the Diract-$\delta$ function (see, e.g., Bronstein et al. 2012), representing a situation in which the entire mass is concentrated in an infinitely thin plane at $z = z'$. Say the solution for this mass distribution is $G_\Phi(\mathbf{k}, z, z')$ (z' is a parameter), then one has to solve

$$-k^2 G_\Phi + \partial_z^2 G_\Phi = 4\pi G\delta(z - z'). \tag{4.16}$$

Hence, $G_\Phi(\mathbf{k}, z, z')$ is a Green's function (see, e.g., Jackson 2014). At this point, a distinction between the cases $k \neq 0$ and $k = 0$ is required.

Case $k \neq 0$:
At first, Eq. 4.16 is solved for $z \neq z'$, and, hence, the right hand side of Eq. 4.16 vanishes, yielding

$$\partial_z^2 G_\Phi = k^2\hat{\Phi}. \tag{4.17}$$

This has solutions of the form

$$G_\Phi = A^{\pm} \exp(k\,(z - z')) + B^{\pm} \exp(-k\,(z - z')). \tag{4.18}$$

[1] The intergral $\int_{\mathbb{R}^2} dk_x dk_y ...$ is over all k_x and k_y. The factor $1/4\pi^2$ originates from two factors $1/2\pi$ for each direction.

[2] Projection here means that one applies $\int_{\mathbb{R}^2}(...)e^{-i\mathbf{k}'\cdot\mathbf{x}_{(2)}} \, d^2x_{(2)}$, to both sides of the equation.

The superscript $\pm$ differentiates between the solutions for $z - z' > 0$ and $z - z' < 0$, respectively. Demanding that $G_\Phi \to 0$, for $|z| \to \infty$, leads to

$$G_\Phi = \begin{cases} B^+ \exp(-k\,(z - z')) & \text{for} \quad z - z' > 0 \\ A^- \exp(k\,(z - z')) & \text{for} \quad z - z' < 0, \end{cases} \tag{4.19}$$

with $A^+ = B^- = 0$. As the solution is mirror-symmetric, with respect to z', one finds $A^- = B^+ =: A$, yielding

$$G_\Phi = A \exp(-k\,|z - z'|). \tag{4.20}$$

Hence, the solution is continuous at $z = z'$, and one can simply read off the solution for $z = z'$, by taking $z = 0$. The value of A is determined by a jump condition, for the first z derivative of G_Φ, at $z = z'$. In order to see that, Eq. 4.16 is integrated over $z \in [z' - \epsilon, z' + \epsilon]$, with $\epsilon \in \mathbb{R}^+$, and the previous result for G_Φ is substituted:

$$\begin{aligned} -k^2 \int_{z'-\epsilon}^{z'+\epsilon} G_\Phi \, dz + \left[\frac{\partial G_\Phi}{\partial z} \right]_{z'-\epsilon}^{z'+\epsilon} &= 4\pi G \\ \Rightarrow -k^2 \int_{z'-\epsilon}^{z'+\epsilon} G_\Phi \, dz - 2Ak \exp(-k\epsilon) &= 4\pi G. \end{aligned} \tag{4.21}$$

Next, the limit $\epsilon \to 0$ is taken. As G_ϕ is continuous at $z = z'$, the fist term (integral over G_ϕ) vanishes, yielding $A = -2\pi G/k$. Hence, Green's function for the potential is of the form

$$G_\Phi(\mathbf{k}, z, z') = -\frac{2\pi G}{k} \exp(-k\,|z - z'|), \tag{4.22}$$

for $k \neq 0$.

Case $k = 0$:
Similar to the first case, Eq. 4.16 is first solved for $z \neq z'$, that is

$$\partial_z^2 G_\Phi = 0. \tag{4.23}$$

Hence, Green's function is curvature-free, and has the form

$$G_\Phi = A + Bz, \tag{4.24}$$

in each interval ($z \lessgtr z'$), respectively. Due to mirror symmetry, with respect to $z = z'$, the solution for the whole domain, $-\infty < z < \infty$, can be written as

$$G_\Phi = \begin{cases} A + B(z - z') & \text{for} \quad z \geq z' \\ A - B(z - z') & \text{for} \quad z < z'. \end{cases} \tag{4.25}$$

Since G_ϕ represents a potential, we are free to add a constant to the solution. Hence, one can demand $A = 0$, and the solution can be expressed more compactly as

$$G_\Phi = B|z - z'| \tag{4.26}$$

The constant B can be determined by applying the jump condition at $z = z'$. The jump condition is obtained by integrating Eq. 4.16, over the interval $z \in [z' - \epsilon, z' + \epsilon]$, with $\epsilon \in \mathbb{R}^+$, see also the calculation in Eq. 4.21. One then finds

$$2B' = 4\pi G. \tag{4.27}$$

Hence,

$$G_\Phi(\mathbf{k}, z, z') = 2\pi G|z - z'|, \quad \text{for} \quad k = 0. \tag{4.28}$$

Both cases combined ⇒ Algorithm for Φ:
Both cases together yield the following expression for Green's function:

$$G_\Phi(\mathbf{k}, z, z') = 2\pi G \begin{cases} -\frac{1}{k}\exp(-k|z - z'|) & \text{for} \quad k \neq 0 \\ |z - z'| & \text{for} \quad k = 0 \end{cases}. \tag{4.29}$$

From that, the Fourier representation $\hat{\Phi}(\mathbf{k}, z)$ (see Eq. 4.13), for an arbitrary density stratification $\hat{\rho}(\mathbf{k}, z)$, can be constructed via the convolution[3]

$$\hat{\Phi}(\mathbf{k}, z) = \int_{-\infty}^{\infty} dz'\, \hat{\rho}(\mathbf{k}, z') G_\Phi(\mathbf{k}, z, z'). \tag{4.30}$$

An inverse, two-dimensional Fourier transform finally yields the gravitational potential in real space:

$$\Phi(x, y, z) = \frac{1}{4\pi^2} \int_{\mathbb{R}^2} d^2k \left(\exp(i\mathbf{k} \cdot \mathbf{x}_{(2)}) \int_{-\infty}^{\infty} dz'\, \hat{\rho}(\mathbf{k}, z') G_\Phi(\mathbf{k}, z, z') \right). \tag{4.31}$$

To summarise, one first applies a two-dimensional Fourier transform to $\rho(x, y, z)$, yielding $\hat{\rho}(\mathbf{k}, z)$. The latter is then convolved with Green's function, to obtain $\hat{\Phi}(\mathbf{k}, z)$. Finally, an inverse Fourier transform is applied, yielding the potential in real space, $\Phi(x, y, z)$. That is the basis for the numerical Poisson solvers, that were used in Löhnert, Krätschmer, & Peeters (2020), Löhnert & Peeters (2022), and Sect. 9.

4.4.2 Density remapping

The Fourier representation of the potential, outlined in the previous Sect. 4.4.1, does not refer to any type of boundary condition. Instead, the shearing sheet is assumed to extend to infinity, and a continuous Fourier transform is applied. In the bounded shearing box, one would wish to replace the Fourier transform by a Fourier series, or, more precisely, a DFT. One problem arises, as DFTs (or FFTs) require the simulation domain to be periodic (here, in directions x and y). The shearing box does comply with this requirement, in the y direction, though the time-dependent shearing-periodicity, in the x direction, is more problematic. The aim of this section is to demonstrate how this is circumvented, whereby the method, proposed in Gammie (2001), is used. Starting point is the Fourier representation of the gravitational potential, Eq. 4.13. One can now decide to evaluate this equation in a new coordinate system, called (x', y', z), whereby the z coordinate remains separate, and unchanged. The new coordinate y' is defined such that the effect of shearing is removed: $y = -q\Omega_0 x t + y'$. Hence, the new coordinates are time-dependent and essentially remove the shear. The x coordinate is left unchanged, and one defines (see, also Gammie 2001):

$$x' = x \qquad y' = y + q\Omega_0 x t. \tag{4.32}$$

If this coordinate transformation was applied to the shearing box, defined in Sect. 4.3, then this box would be periodic, in both directions x' and y'. This already indicates that FFTs are permitted in this coordinate system. The question then arises how Eqs. 4.30 and 4.31 translate into this

[3] This immediately follows from the fact that $G_\Phi(\mathbf{k}, z, z')$ is the solution for $\hat{\rho} = \delta(z - z')$ (see also Jackson 2014, for Green's functions in general).

new coordinates system. As a first step, the Fourier representation of the potential, Eq. 4.13, is evaluated in the primed coordinates, yielding:

$$\begin{aligned}\Phi'(x',y',z) &= \Phi(x=x', y=y'-q\Omega_0 t x', z) \\ &= \frac{1}{4\pi^2}\int_{\mathbb{R}^2} d^2k\, \hat{\Phi}(k_x,k_y,z)\, e^{ik_x x' + ik_y(y'-q\Omega_0 t x')}\end{aligned} \tag{4.33}$$

Note that Φ' is simply Φ, except that it is represented as a function of the primed coordinates. The imaginary exponent can be rewritten as $i(k_x + q\Omega_0 t k_y)x' + ik_y y$. This is a new wave vector, whereby the x component depends linearly on time (see also Goldreich & Lynden-Bell 1965). At a given instance of time, one can apply a coordinate transformation, in Fourier space, of the following form:

$$k'_x = k_x - q\Omega_0 t\, k_y \qquad k'_y = k_y. \tag{4.34}$$

This is substituted into Eq. 4.33, replacing the (k_x, k_y) integral by an integration over the (k'_x, k'_y) plane:

$$\begin{aligned}\Phi'(x',y',z) &= \frac{1}{4\pi^2}\int_{\mathbb{R}^2} d^2k'\, \det(\underline{\underline{\mathbf{J}}})\, \hat{\Phi}(k'_x + q\Omega_0 t\, k'_y, k'_y, z)\, e^{ik'_x x' + ik'_y y'} \\ &= \frac{1}{4\pi^2}\int_{\mathbb{R}^2} d^2k'\, \hat{\Phi}'(k'_x,k'_y,z)\, e^{ik'_x x' + ik'_y y'}.\end{aligned} \tag{4.35}$$

The Jacobian determinant is one, $\det(\underline{\underline{\mathbf{J}}}) = 1$, as the shear does not change the area of a surface element. The function $\hat{\Phi}'$ is $\hat{\Phi}$, evaluated in the new coordinates, k'_x and k'_y. The last equation implies that $\hat{\Phi}'(k'_x, k'_y, z)$ is the xy-Fourier transform of $\Phi'(x', y', z)$. This results is not restricted to Φ, but is a general statement about the behaviour of Fourier transforms, in coordinate systems of the form Eq. 4.32, and 4.34. More precisely, this calculation is equally valid for the mass density $\rho(x, y, z)$. Say the coordinate transformations, Eqs. 4.32 and 4.34, are abbreviated by $\mathcal{KO}_x$, and $\mathcal{KO}_k$, respectively, and the Fourier transform is abbreviated by $\mathcal{FT}$, then the previous results can be summarised as follows:

$$\begin{array}{ccc} \Phi(x,y,z),\ \rho(x,y,z) & \xrightarrow{\mathcal{FT}} & \hat{\Phi}(k_x,k_y,z),\ \hat{\rho}(k_x,k_y,z) \\ \mathcal{KO}_x \downarrow & & \mathcal{KO}_k \downarrow \\ \Phi'(x',y',z),\ \rho'(x',y',z) & \xrightarrow{\mathcal{FT}} & \hat{\Phi}'(k'_x,k'_y,z),\ \hat{\rho}'(k'_x,k'_y,z) \end{array} \tag{4.36}$$

What remains is the relationship between $\hat{\Phi}'$ and $\hat{\rho}'$. The latter can be found by evaluating Eq. 4.30 in the primed coordinates (similar to Eqs. 4.33, and 4.35):

$$\hat{\Phi}'(k'_x,k'_y,z) = \int_{-\infty}^{\infty} dz'\, \hat{\rho}'(k'_x,k'_y,z') G_\Phi(k'_x + q\Omega_0 t\, k'_y, k'_y, z, z'). \tag{4.37}$$

The main difference between the last expression, and Eq. 4.30, is that G_Φ is here evaluated at the sheared wave vector $(k'_x + q\Omega_0 t\, k'_y, k'_y)$, which has to be considered, when Eq. 4.29 is used. Nevertheless, this provides a new algorithm: One first remaps the mass density ρ to ρ', using $\mathcal{KO}_x$. Afterwards, a two-dimensional Fourier transform is applied, to get $\hat{\rho}'$. Then, Eq. 4.37 is used, yielding $\hat{\Phi}'$. Next, an inverse-Fourier transform is applied, to obtain Φ'. Finally, one has to back-map the potential, using the inverse of $\mathcal{KO}_x$, to obtain Φ. This may be summarised as follows:

$$\begin{array}{ccccc} \rho(x,y,z) & \xrightarrow{\mathcal{KO}_x} & \rho'(x',y',z) & \xrightarrow{\mathcal{FT}} & \hat{\rho}'(k'_x,k'_y,z) \\ & & & & \downarrow \text{Eq. 4.37} \\ \Phi(x,y,z) & \xleftarrow{\mathcal{KO}_x^{-1}} & \Phi'(x',y',z) & \xleftarrow{\mathcal{FT}^{-1}} & \hat{\Phi}'(k'_x,k'_y,z) \end{array} \tag{4.38}$$

Hence, this method is similar to the algorithm in Sect. 4.4.1, and only the first step ($\mathcal{KO}_x$), and the last step ($\mathcal{KO}_k^{-1}$) are additional. However, this is worth the effort, because in the primed coordinate system one can use FFTs, due to periodicity being established, in both horizontal directions.

4.5 Two-dimensional simulations of GI turbulence, with *DiskFlow*

The simulations in Löhnert, Krätschmer, & Peeters (2020), see Sect. 7, were carried out, using the self-gravity hydrodynamics code *DiskFlow*[4]. The code *DiskFlow* was originally developed by Stephan Krätschmer, in 2018, then at the group of theoretical physics 5. *DiskFlow* is aimed for shearing-box simulations of GI turbulence, in the two-dimensional, razor-thin limit (see Sect. 4.5.1). The original implementation turned out to be prone to numerical instabilities, during the nonlinear phase. Hence, in order to obtain the simulations, shown in Löhnert, Krätschmer, & Peeters (2020), modifications to *DiskFlow* were required. A major modification was the implementation of the wave-vector shift, $q\Omega_0 k_y t$, required for the density-remapping algorithm, see Sect. 4.4.2. Also implemented was a variable time step, based on a CFL criterion (see Sect. 4.5.2). In order to save computational resources, the ghost-zone method (see, e.g., Balbus & Hawley 1998) was implemented. The latter adds N_{ghost} additional grid cells at each boundary. The corresponding grid values are obtained, by applying the boundary conditions. This allows an easier calculation of derivatives, as the boundary conditions do not have to be checked at each derivative call. Also implemented was additional heating, used in the cooling law, detailed in Sect. 4.5.3. The following sections aim to provide an overview over the numerical methods of *DiskFlow*.

4.5.1 The razor-thin limit

It is first noted that *DiskFlow* only includes self-gravity, and magnetic fields are omitted. For studying gravitational instabilities (see also Sect. 3.3.1), it is often convenient to take the so-called razor-thin limit, as was done in the seminal shearing-box simulations of Gammie (2001). In this limit, the system is effectively two-dimensional. Thereby, the goal is to formulate height-integrated versions of Eqs. 4.5 - 4.9, whereby the variables are also replaced by height-integrated versions. For example, one wants to use the surface density, Σ, and the height-integrated pressure, $P_{(2)}$, which are defined as follows:

$$\Sigma(x,y) = \int_{-\infty}^{\infty} \rho(x,y,z)\, dz \qquad P_{(2)}(x,y) = \int_{-\infty}^{\infty} P(x,y,z)\, dz. \tag{4.39}$$

It is then assumed, that the vertical stratification is fast enough to be instantaneous, with respect to the horizontal motions. Hence, for the fluid properties, the vertical direction is neglected completely, leading to an Ansatz of the form

$$\rho(x,y,z) = \Sigma(x,y)\,\delta(z) \qquad P(x,y,z) = P_{(2)}(x,y)\,\delta(z), \tag{4.40}$$

with the Diract-δ function. The two-dimensional, thermal energy density follows from the corresponding pressure, $U := P_{(2)}/(\gamma_{(2)} - 1)$. Since the new description is effectively two-dimensional, the value of γ needs to be adjusted consistently. One reason for this is that horizontal compressions can cause a vertical response (Goldreich, Goodman, & Narayan 1986; Ostriker, Shu, & Adams 1992), that is not captured by $\rho, P \propto \delta(z)$. One can relate the two-dimensional adiabatic index $\gamma_{(2)}$, to the three-dimensional adiabatic index $\gamma_{(3)}$, via $\gamma_{(2)} = (3\gamma_{(3)} - 1)/(\gamma_{(3)} + 1)$ (Goldreich, Goodman, & Narayan 1986; Ostriker, Shu, & Adams 1992; Gammie 2001). For strongly self-gravity-dominated systems, one finds $\gamma_{(2)} = 3 - 2/\gamma_{(3)}$ (see Gammie 2001). Assuming $\gamma_{(3)} = 5/3$, we set the two-dimensional adiabatic index to $\gamma_{(2)} = 2$ (in accordance with Gammie 2001). It is noted, that this is also consistent with a purely two-dimensional, monoatomic gas[5]. One then substitutes this ansatz into the three-dimensional equations of motion, Eqs. 4.5, 4.6, and 10.122. The resulting

[4] `https://bitbucket.org/astro_bayreuth/accretion-disk-flow/src/master/` (as of 25.05.2023)

[5] Assuming two degrees of freedom, one obtains $\gamma = 1 + 2/f = 1 + 2/2 = 2$.

equations are then integrated over all z, yielding (see also Gammie 2001)

$$\partial_t \Sigma + \nabla \cdot (\Sigma \, \mathbf{v}) = 0 \tag{4.41}$$

$$\partial_t (\Sigma \, \mathbf{v}) + \nabla \cdot \left(\Sigma \, \mathbf{v}\mathbf{v} + P_{(2)} \underline{\mathbf{I}} \right) = -2\Sigma \, \Omega_0 \times \mathbf{v} + 3\Sigma \, \Omega_0^2 x \hat{\mathbf{e}}_x - \Sigma \, \nabla \Phi(x, y, z = 0) \tag{4.42}$$

$$\partial_t U + \nabla \cdot (U \mathbf{v}) = -P_{(2)} (\nabla \cdot \mathbf{v}) + \Sigma \dot{q}. \tag{4.43}$$

An example derivation is provided for the momentum equation in Appendix J. It is noted that, in the above three equations, the nabla operator is only two-dimensional, $\nabla = (\partial_x, \partial_y)$. Since magnetic fields are absent here, the total energy balance equation, given in Sect. 4.2, is here replaced by only the time evolution of the thermal energy density. As noted in Sect. 4.2, the kinetic-energy balance follows from the the momentum conservation, by multiplying the latter with $\mathbf{v}$. A model for the cooling (heating) term, $\Sigma \dot{q}$, is provided in Sect. 4.5.3. Special care must be taken for the evaluation of the gravitational potential. The fluid may be restricted to the mid plane, but the gravitational field still extends to the regions, above and below the mid plane. However, the force density, appearing in Eq. 4.42, is only evaluated at $z = 0$. This originates from the z integration that was applied to obtain Eq. 4.42, and the fact that the mass density was assumed to be proportional to $\delta(z)$ (see also Appendix J).

4.5.2 Numerical method of the hydrodynamical solver

DiskFlow is a solver for the hydrodynamical equations of motion, in the two-dimensional, razor-thin approximation, including self-gravity (a setup, similar to that in Gammie 2001). Hence, *DiskFlow* solves the equations of motion, provided in Sect. 4.5.1. The Poisson solver is discussed separately in Sect. 4.5.5. All flux and source terms are calculated using a finite difference scheme. Spatial derivatives are of the central-difference type, and are accurate to within second order of the discretisation length (see, e.g., Toro 2009). The time-integration is achieved, using a Runge-Kutta forth-order method (see, e.g., Toro 2009). The time-step, Δt, is variable, and updated, at each time point, via:

$$\Delta t = \mathrm{CFL} \cdot \frac{\min(\Delta x, \Delta y)}{\max(|v_x|) + \max(|v_y|)}. \tag{4.44}$$

CFL is chosen to be a positive, real number, smaller than one. Essentially, CFL represents the Courant-Friedrichs-Lewy number (see, e.g., Courant, Friedrichs, & Lewy 1928; Toro 2009), although the stability criterion here is simplified, in the sense that only the fastest velocity, within the simulation domain, is considered. The discretisation lengths are defined as $\Delta x = L_x / N_x$ and $\Delta y = L_y / N_y$, whereby the smallest of both values is chosen. The max() function, in the denominator, implies that the highest, absolute velocity value, within the simulation domain, is selected. The boundary conditions are periodic in the y direction, and shearing-periodic in the x direction, see Sect. 4.3. This is realised with the help of so-called ghost zones (see, e.g., Hawley, Gammie, & Balbus 1995; Balbus & Hawley 1998). The latter are additional grid zones, added at the boundaries of the active simulation domain. The values, assigned to theses ghost zones, are obtained, using Eqs. 4.11, and 4.12. The shift, $q \Omega_0 L_x t$, used in the x boundary condition, varies continuously with time, and does not always align with a ghost grid-point. Hence, in those cases, a linear interpolation is applied, to obtain the ghost-cell values. The solver requires at least two ghost zones, in order to calculate second-order derivatives, at the boundaries.

4.5.3 Cooling prescription

Important for simulations of GI turbulence is the cooling (heating) model. A corresponding term, $\Sigma \dot{q}$, enters the evolution law for the thermal energy density U, see Eq. 4.43. The cooling model,

used here, is based on the cooling prescriptions, provided in Gammie (2001) and Rice et al. (2011)

$$\Sigma\dot{q} = \frac{U - U_0}{\tau_c} = -\frac{U}{\tau_c} + \frac{U_0}{\tau_c}. \tag{4.45}$$

The first term, $-U/\tau_c$, represents radiative cooling, and is equivalent to that used in Gammie (2001). Thereby, τ_c refers to a typical cooling time scale, regulating how efficient cooling operates, see also Appendix K. The second term, U_0/τ_c, is an additional heating term, accounting for heating sources, other than turbulent heating (Rice et al. 2011). This can, for example, represent irradiation heating (e.g., radiation from the central star in a PPD Kratter, Murray-Clay, & Youdin 2010; Rice et al. 2011; Kratter & Lodato 2016), or even heating, due to embedded stars (or other objects), inside AGN disks (see, e.g., Rice et al. 2011; Goodman 2003). Depending on whether a disk is optically thick, or optically thin, the processes, involved in radiative cooling (heating), can be rather complex (see, e.g., Shakura 2018). Thermal energy may be produced close towards the disk mid plane, but radiation, leaves the disk at the surface, and an accurate description would require to solve a detailed radiation transport model (see, e.g., Hirose & Shi 2019). Here, the focus is more on the dynamics of turbulence, and less on the detailed radiation physics. Hence, a very simple cooling model is considered to be sufficient.
If turbulence was absent, the above cooling (heating) prescription would relax the system to a target thermal energy density, U_0. This is slightly different from the cooling law, used in Rice et al. (2011), which is of the form

$$\Sigma\dot{q} = -\frac{\Sigma(c_s^2 - c_{s,0}^2)}{\gamma(\gamma-1)\tau_c} = -\frac{U}{\tau_c} + \frac{\Sigma c_{s,0}^2}{\gamma(\gamma-1)\tau_c}, \tag{4.46}$$

with $c_s^2 = \gamma(\gamma-1)U/\Sigma$. The cooling terms are exactly equal, though the heating terms are slightly different. In the form of Eq. 4.46, the cooling (heating) law relaxes the system towards a constant temperature, or sound speed, $c_{s,0}$, and not a constant thermal energy density, U_0. Mostly used, in Löhnert, Krätschmer, & Peeters (2020), is the heating model in Eq. 4.45. However, in *DiskFlow*, a switch has been implemented, such that one can use both models, as well as arbitrary linear combinations between the two. The latter is achieved by introducing a continuous parameter, $\xi \in [0, 1]$, which is detailed in the context of the linear-stability analysis, in Sect. 10.1. Estimates for the dimensionless cooling time, $\tau_c\Omega$, were, for example, provided in Kratter, Murray-Clay, & Youdin (2010), for the case of a PPD disk, as a function temperature, T. $\tau_c\Omega$ values can vary over orders of magnitude, depending on the temperature, and the location within the disk. Numerical simulations show that self-regulated, gravito-turbulent states might not be possible for $\tau_c\Omega < 3 - 10$ (clumping, see, e.g., Gammie 2001; Kratter & Lodato 2016, or Sect. 3.3.1). The values, used here, in Löhnert, Krätschmer, & Peeters (2020) (Sect. 7), Löhnert & Peeters (2022) (Sect. 8), and Sect. 9, are typically in the range $\tau_c\Omega_0 \sim 10 - 20$.

4.5.4 Mechanisms for numerical stabilisation

In states of GI turbulence, the velocity fluctuations can be highly supersonic, leading to shocks (see also Gammie 2001; Cossins, Lodato, & Clarke 2009). In *DiskFlow*, it has turned out that this necessitates additional, stabilising mechanisms. This is achieved using artificial viscosity, and artificial viscous pressure. The latter two methods are discussed below.

Artificial viscosity:
Artificial viscosity is an explicit viscosity, added to each of the evolution laws. More precisely, for $f \in \{\Sigma, U, \mathbf{v}\}$, the evolution laws (Eqs. 4.41 - 4.43) are modified as follows (see also Löhnert, Krätschmer, & Peeters 2020):

$$\partial_t f = ... + D_{(2)}\Delta x \nabla^2 f. \tag{4.47}$$

The damping coefficient $D_{(2)}$ is usually chosen to be in the interval $0.07 - 0.8$, (see also Löhnert, Krätschmer, & Peeters 2020). Additionally, $D_{(2)}$ can be made time-dependent. In the latter case, $D_{(2)}$ varies between a highest and lowest value, depending on the highest velocity in the grid domain. More precisely,

$$D_{(2)}(t) = D_{\min} + (1/2)(D_{\max} - D_{\min})(1 + \tanh\left[C\left(\max(|v_x|) - v_0\right)\right]), \tag{4.48}$$

whereby $D_{\min}$, $D_{\max}$, C, and v_0 are free parameters. Artificial viscosity is especially important for the transition, between the linear, and the nonlinear phases of GI. The most unstable GI modes can reach rather large amplitudes, before they break up into turbulence, leading to a violent transition. Due to the large velocities at this point, the value of $D_{(2)}(t)$ reaches its maximum then. After the transition, $D_{(2)}(t)$ returns to its low state again.

Artificial viscous pressure:
In order to capture the effects of shock dissipation, an additional, artificial viscous pressure is added (see, e.g., Gammie 2001):

$$P_{\text{vis}} = \left[\zeta\Sigma(\nabla\cdot\mathbf{v})^2\right]\Theta\left(-\nabla\cdot\mathbf{v}\right), \quad \text{with} \quad \Theta\left(-\nabla\cdot\mathbf{v}\right) = \begin{cases} 1 \text{ for } \nabla\cdot\mathbf{v} < 0 \\ 0 \text{ else} \end{cases} . \tag{4.49}$$

Thereby, the coefficient ζ is a free parameter. The term P_{vis} is included as an additional pressure contribution in the Euler equation, and there is also a corresponding source term in the thermal energy equation, which is of the form $-P_{\text{vis}}\left(\nabla\cdot\mathbf{v}\right)$. The Heaviside function, $\Theta\left(-\nabla\cdot\mathbf{v}\right)$, indicates that the artificial viscous pressure only operates, in cases of fluid compression. Moreover, P_{vis} is proportional to the square of the divergence, and, hence, it operates especially in cases with strong compression, which is, for example, the case in the strongly localised regions of shock fronts. The net effect is to alleviate numerical instabilities, and to capture the heat, dissipated by the shocks, via the additional term in the thermal energy balance. For the simulations, shown in Löhnert, Krätschmer, & Peeters (2020) (see Sect. 7), $\zeta \sim 6 \cdot 10^{-3}$ was found to be a suitable value, for this purpose. Thereby it is noted that, in code units, densities, velocities, and length scales are of the order unity.

4.5.5 Implementation of the Poisson solver in *DiskFlow*

The Poisson solver, used in *DiskFlow*, is based on the analytical foundations, detailed in Sect. 4.4. As *DiskFlow* solves the equations of hydrodynamics, in the razor-thin approximation, the mass density is of the form $\rho(x,y,z) = \Sigma(x,y)\,\delta(z)$, with surface-mass density $\Sigma(x,y)$. Hence, the Fourier-transformed mass density (see Eq. 4.14) is of a similar form, $\hat{\rho}(\mathbf{k},z) = \hat{\Sigma}(\mathbf{k})\delta(z)$, with $\mathbf{k} = (k_x, k_y)$. Although the mass is restricted to the mid plane, its gravitational potential extends to the regions above, and below the mid plane, as well. However, as can be seen from Eq. 4.42, in Sect. 4.5.1, for the hydrodynamical equations of motion, only the potential at $z = 0$ is relevant. This can significantly simplify the steps, detailed in Sect. 4.4.1. With Eqs. 4.30, and 4.29, one finds

$$\hat{\Phi}(\mathbf{k}, z=0) = \hat{\Sigma}(\mathbf{k})G_{\Phi}(\mathbf{k},0,0) = \begin{cases} -\frac{2\pi G}{k}\hat{\Sigma}(\mathbf{k}) & \text{for} \quad k \neq 0 \\ 0 & \text{for} \quad k = 0 \end{cases}, \tag{4.50}$$

with $k = \sqrt{k_x^2 + k_y^2}$. The potential, at $z = 0$, then follows by applying an inverse Fourier transform. Numerically, FFTs are used, to obtain both $\hat{\Sigma}(\mathbf{k})$ and $\Phi(x,y,0)$. However, the shearing box is not periodic in the x direction, and one has to first apply the density remapping, outlined in Sect. 4.4.2:

$$\Sigma(x,y) \xrightarrow{\mathcal{KO}_x} \Sigma'(x',y') \xrightarrow{\text{FFT}} \hat{\Sigma}'(k_x',k_y') \xrightarrow{\text{Eq. 4.50}} \hat{\Phi}'(k_x',k_y',0) \xrightarrow{\text{FFT}^{-1}} \Phi'(x',y',0) \xrightarrow{\mathcal{KO}_x^{-1}} \Phi(x,y,0)$$

Additional remarks:

▷ In the original version of *DiskFlow*, $\sqrt{k_x^2 + k_y^2}$ was used for k. Hence, in order to account for the shearing transformation, $\mathcal{KO}_x$, the sheared wave vectors had to be implemented, $k = \sqrt{(k'_x + q\Omega_0 t k'_y)^2 + k'^2_y}$.

▷ Following Gammie (2001), a cut-off wave vector, $k_{\max} = (1/\sqrt{2})\min(\pi N_x/L_x, \pi N_y/L_y)$, is applied, whereby all Fourier amplitudes with $k = |\mathbf{k}| > k_{\max}$ are set to zero. This aims to prevent small-scale inhomogeneities (see Gammie 2001). The factor $1/\sqrt{2}$ arises, because an initially rectangular $\mathbf{k}$ grid gets sheared into a parallelogram, with a maximum tilting angle of 45°, after one periodic time Δt_p. Assuming an edge length of one, then the maximum radius of a circle, fitting the parallelogram, is $1/\sqrt{2}$. Also here, for the calculation of k, the wave-vector shearing has to be considered.

▷ The transformation $\mathcal{KO}_x$, and its inverse, do not necessarily transform one grid point onto another grid point. In such cases, the values are linearly interpolated.

4.6 Three-dimensional, MHD simulations of GI

For the simulations, shown in Löhnert & Peeters (2022) (see Sect. 8), and Sect. 9 (LP23), the MHD code Athena was used[6]. Athena is a hydrodynamics, and MHD code, aimed for astrophysical applications, and the principal methods, used in Athena, are detailed in Stone et al. (2008). The Athena code was not developed by our group, at theoretical physics 5. Hence, the MHD solver is here only summarised, see Sect. 4.6.1, below. The main goal of the simulations, put forward in Löhnert & Peeters (2022), and Sect. 9, is to study GI-turbulent states, in a regime with additional magnetic fields. Hence, besides the MHD solver, one also requires a Poisson solver for self-gravity. Athena offers simple Poisson solvers, for strictly periodic domains, though these solvers are not directly applicable to stratified shearing boxes. For the latter, the approach, presented in Sect. 4.4.1, is convenient, yet this requires significant modifications to the basic Athena Poisson solver. Since the implementation of this solver is central for Löhnert & Peeters (2022), and Sect. 9, the solver is discussed in detail, in see Sect. 4.6.4.

4.6.1 Athena settings for the MHD solver

MHD-solver - The general method:
Athena solves the full set of MHD equations (see Stone et al. 2008), whereby the exact equations depend on the additional-physics options that are included. In the works Löhnert & Peeters (2022), and Sect. 9, the equations solved are those, provided in Sect. 4.2. In general, Athena is a finite-volume solver, using higher-order Godunov methods (see, e.g., Stone et al. 2008; Toro 2009). More precisely, the algorithm is of the corner transport upwind (CTU) type (Gardiner & Stone 2008; Stone et al. 2008). The method was first proposed by Colella (1990) and Saltzman (1994), for hyperbolic conservation laws (Gardiner & Stone 2008). The method for three-dimensional systems, outlined in Saltzman (1994), requires twelve intermediate applications of a Riemann solver. Thereby, the complete, three-dimensional problem is dimensionally split into three sub-problems. In the case of MHD, the splitting can lead to conflicts, as flux gradients in one direction may not be independent from flux gradients in other directions (Gardiner & Stone 2008). Hence, magnetic flux gradients, $\partial_j B_j$, can be interdependent, due to the additional constraint $\nabla \cdot \mathbf{B} = 0$. In order to reduce the number of additional source terms, required to account for the interdependence, a less complex method is described in Gardiner & Stone (2008), using only six Riemann-solver calls, though requiring a stability criterion of CFL ≤ 0.5. The update of the magnetic fields is achieved using the constraint transport (CT) method (Evans & Hawley 1988; Gardiner & Stone 2008). A major part of the CT method is the way, by which the electro-motive force (EMF), $\mathcal{E} = \mathbf{v} \times \mathbf{B}$,

[6] `https://princetonuniversity.github.io/Athena-Cversion/` (as of 25.05.2023)

is reconstructed. It is first noted that, in the case of Athena, conserved fluid variables (ρ, E, $\rho\mathbf{v}$) are stored at cell-centres, whereas fluxes, such as the magnetic field (flux) $\mathbf{B}$, are stored at the interfaces, between cells (Stone et al. 2008). The EMFs are stored at the cell edges (see Gardiner & Stone 2008; Stone et al. 2008). In the following the general integrator is referred to as CTU+CT. In order to calculate the fluxes at the cell interfaces, a spatial reconstruction scheme, and a Riemann solver are required (see, e.g., Toro 2009). The Athena option, used for the spatial reconstruction, is the third-order accurate, piecewise-parabolic reconstruction (PPM, see Colella & Woodward 1984; Stone et al. 2008). For the Riemann solver, Roe's method (see Roe 1981) is used. Instead of approximating the fluxes, Roe's method tries to find exact fluxes for linearly approximated equations (see, e.g., Roe 1981; Stone et al. 2008).

The shearing-box:
Among other geometries, Athena allows simulations in the local shearing-box approximation (Stone & Gardiner 2010). As noted in Sects. 4.1, and 4.2, the non-inertial frame of reference gives rise to additional source terms, in both the momentum equation (Eq. 4.6), and the energy equation (Eq. 4.8). In Athena, a Crank-Nicolson time-differencing scheme (Crank & Nicolson 1947) is used to incorporate the shearing-box source terms, in the final time update (Stone & Gardiner 2010). As the CTU+CT algorithm requires intermediates steps with half time steps ($\delta t/2$), the additional source terms need to be considered there as well. For the momentum conservation, Eq. 4.6, this is the case for the reconstruction of the primitive variables (velocities) at the interface states, the calculation of the flux gradients in the CTU algorithm, and the reconstruction of the EMF in the CT algorithm (Stone & Gardiner 2010). For the energy balance, Eq. 4.8, a correction is only required for the flux gradients in the CTU algorithm (Stone & Gardiner 2010). In all the former half-steps, a forward-Euler time differencing is used for the source terms (Stone & Gardiner 2010). Note also that the vertical, gravitational potential energy is not part of the total energy, E. Though E is still conserved to machine precision, as the vertical-gravity source term is added in such a way, that a volume average leads to exact cancellation of all contributions, except at the boundaries (Stone & Gardiner 2010). For the vertical component of the central objects gravity, the potential $\Phi_{\text{vert}} = (1/2)\Omega_0^2 z^2$ is provided, and the corresponding source term is obtained by using finite differencing, in the vertical direction (Stone & Gardiner 2010). Additionally, for the simulations in Löhnert & Peeters (2022) (Sect. 8), and Sect. 9, the FARGO algorithm (Masset 2000) is used. To summarise, FARGO (fast advection in rotating gaseous objects), separates the velocity into a background flow, and a deviation, $\mathbf{v} = \mathbf{v}_0 + \delta\mathbf{v}$. Here, $\mathbf{v}_0 = -q\Omega_0 x\,\hat{\mathbf{e}}_y$ is the shear flow, see Sect. 4.1. The set of MHD equations is thereby separated into two sets of equations. One of these sets only contains the perturbation $\delta\mathbf{v}$, and the remaining set summarises all terms, containing $\mathbf{v}_0$ (Stone & Gardiner 2010). The perturbed equations can be solved using the CTU-CT method, and the remaining set can be solved by applying a direct advection with $\mathbf{v}_0$ (and potentially additional source terms). The net result is that the shear flow does not contribute to the CFL condition, which can lead to significant increases in efficiency, especially for larger boxes, spanning many scale heights in the x direction (Stone & Gardiner 2010).

Additional numerical stabilisation:
A common feature of GI-turbulent states in the emergence of shocks. It has turned out that the introduction of shock capturing (H-correction, see Sanders, Morano, & Druguet 1998), provided as an option in Athena, can greatly reduce the tendency to numerical instabilities. H-correction enters the CTU+CT algorithm, after the fluxes have been updated for a $\delta t/2$ time step (Stone et al. 2008). For the projects in Löhnert & Peeters (2022), and Sect. 9, additional stabilisation mechanisms were implemented. A minimum for the mass density, ρ, was introduced, whereby the density minimum is of the order of $\rho_{\min} = \rho_0 \cdot 10^{-4}$, with mid-plane density ρ_0. A corresponding minimum for the pressure is also introduced, $P_{\min} = c_{si,0}^2 \rho_{\min}$, whereby $c_{si,0}$ is the initial, isothermal sound speed. Especially during the linear-nonlinar transition, and in the low-density regimes near the vertical boundaries, this can be beneficial. The transition between the linear and the nonlinear state can be

rather violent, and the minima were introduced to prevent the density, or the pressure from falling below zero, locally.

4.6.2 Boundary conditions

Horizontal boundaries:
In the horizontal directions (x, y), periodic, and shearing-periodic boundary conditions are used (see, e.g., Hawley, Gammie, & Balbus 1995; Balbus & Hawley 1998; Stone & Gardiner 2010). More precisely, the boundaries are periodic in the y direction, and shearing-periodic in the x direction, see also Sect. 4.3. Hence, in the horizontal directions, the boundary conditions are equivalent to those, used in *DiskFlow*.

Vertical direction:
The vertical direction requires a different approach, due to the density stratification. To see how stratification is established, one can consider a typical initial condition. One might, for example, assume a horizontally constant density, $\rho = \rho(z)$, and pressure, $P = P(z)$. The corresponding velocity is the simple shear flow, $\mathbf{v} = -q\Omega_0 x\,\hat{\mathbf{e}}_y$. Eq. 4.6 then reduces to a vertical force balance of the form

$$\rho\Omega_0^2 z - \partial_z P - \rho\partial_z\Phi = 0. \tag{4.51}$$

Thereby, it is assumed that magnetic fields are, initially, so weak (or absent) that they are not relevant. In principle, stratification only requires the vertical component of the central objects gravity, $-\partial_z\Phi^\star \sim -\Omega_0^2 z$, which would lead to a Gaussian density profile, $\rho(z)$, as given by Eq. 3.4. However, the point where GI turbulence can occur ($Q \sim 1$) also corresponds to the regime, where self-gravity can have an influence on the vertical stratification (see, e.g., Kratter & Lodato 2016). With that, the force balance is less trivial to solve. Though one can assume that the disk is, initially, vertically isothermal, and use the Poisson equation, to express both $P(z)$ and $\Phi(z)$, as a function of $\rho(z)$. What follows is a second order, differential equation for $\rho(z)$ (see also Koyama & Ostriker 2009). For the cases shown in this work, a Runge-Kutta fourth-order method was implemented, to solve this equation once at the start of a new simulation, see Appendix L for a detailed description of the method.
Athena provides a set of default boundary conditions, appropriate for vertically stratified simulations. However, as the density can yield very low values at the vertical boundaries, the boundary conditions were slightly modified. In general, the vertical boundary conditions are of the outflow type. For the mass density, $\partial_z\rho = 0$, is demanded, at the vertical boundaries, and, hence, the mass density is extrapolated constantly into the ghost zones. Then, it is demanded that $\partial_z c_s = 0$, that is, the sound speed (or the temperature) is also extrapolated constantly into the ghost zones. The ghost-zone pressure then follows from $P = c_{s,i}^2\rho$. The horizontal velocity components, v_x and v_y, are also extrapolated, assuming $\partial_z v_x = \partial_z v_y = 0$. The only deviation is the vertical velocity, v_z, whereby for the latter, $\partial_z v_z = 0$ will only be used if $v_z\,\mathrm{sign}(z) \geq 0$, and v_z is set to zero in the ghost zones, if $v_z\,\mathrm{sign}(z) < 0$, that is, if the velocity points towards the mid plane. For the magnetic field, vertical field (VF) boundary conditions are used (see, e.g., Käpylä & Korpi 2011). This boundary condition was also pre-implemented in Athena. VF boundaries assume, as the name suggests, that the magnetic field is vertical to the boundary plane. Here, this implies that $B_x = B_y = 0$, at the vertical boundaries. For the z component of the magnetic field, $\partial_z B_z = 0$ is assumed, that is, B_z is extrapolated constantly into the ghost zones. The boundary conditions for the potential of self-gravity, Φ, are discussed separately, below.

Boundary conditions for the potential of self-gravity:
In the horizontal directions, the potential, Φ, due to self-gravity, is treated equally to all other variables. That is, shearing-periodicity is assumed in the x direction, and simple periodicity in the y direction. Only the vertical, z direction is special. Here, so-called vacuum boundary conditions (see, e.g., Binney & Tremaine 2008; Koyama & Ostriker 2009) are used. Thereby, it is assumed

that the mass density vanishes ($\rho = 0$), outside of the simulation domain, and the Poisson equation reduces to the Laplace equation, $\nabla^2\Phi = 0$. This is a reasonable approach for vertically stratified systems, as the mass density falls of significantly, with increasing distance from the mid plane, $|z|$. Given that the boundary conditions, in directions x and y, have been applied first, the ghost-cell values, at the z boundaries, can be obtained, by solving $\partial_z^2\Phi = -\partial_x^2\Phi - \partial_y^2\Phi$. In the following, $\Phi_{k,j,i}$ abbreviates the value of Φ, at the discrete grid location $(x_{\min} + i\,dx, y_{\min} + j\,dy, z_{\min} + k\,dz)$, whereby $(x_{\min}, y_{\min}, z_{\min})$ are the lower coordinate boundaries, including the buffer zone due to the ghost zones. In central-difference form (see, e.g., Toro 2009), the Laplace equation can be written as

$$\frac{\Phi_{k+1,j,i} - 2\Phi_{k,j,i} + \Phi_{k-1,j,i}}{\delta z^2} = -\frac{\Phi_{k,j,i+1} - 2\Phi_{k,j,i} + \Phi_{k,j,i-1}}{\delta x^2} - \frac{\Phi_{k,j+1,i} - 2\Phi_{k,j,i} + \Phi_{k,j-1,i}}{\delta y^2}. \tag{4.52}$$

Solving for $\Phi_{k+1,j,i}$, yields:

$$\Phi_{k+1,j,i} = 2\Phi_{k,j,i} - \Phi_{k-1,j,i} - \left(\frac{\Phi_{k,j,i+1} - 2\Phi_{k,j,i} + \Phi_{k,j,i-1}}{\delta x^2} + \frac{\Phi_{k,j+1,i} - 2\Phi_{k,j,i} + \Phi_{k,j-1,i}}{\delta y^2}\right)\delta z^2. \tag{4.53}$$

Hence, in order to determine the potential at the z index $k+1$ (i.e., $\Phi_{k+1,j,i}$), one only requires grid values with z indices $k' < k+1$. All ghost-cell values, at the upper vertical boundary, can thus be calculated successively. One starts by calculating the first ghost-cell value, followed by the second ghost-cell value, up to $N_{\rm ghost}$, whereby $N_{\rm ghost}$ is the total number of ghost cells. The lower vertical boundary can be handled similarly. Instead of solving Eq. 4.52 for $\Phi_{k+1,j,i}$, one solves for $\Phi_{k-1,j,i}$. One can then apply the same method, as for the upper boundary, by successively calculating the ghost-cell values, at the lower, vertical boundary. It is noted that the finite difference form of the second order spatial derivative, at an index l, needs two neighbouring indices, $l-1$ and $l+1$. Hence, this can be problematic for the ghost zones at the outermost, horizontal boundaries. Say, for example, that there are N_x grid points in x direction. Including the ghost-zones, those are $N_x + 2N_{\rm ghost}$ grid points. Then, the total index of a grid location, in x direction, is in the $(0 \leq i < N_x + 2N_{\rm ghost})$-range. One can then consider the index $i = 0$. The latter grid point has no left successor, since the ghost zones are already included. Hence, one can not calculate the second derivative in x direction, at this point. Here, this is solved by taking the second derivative, evaluated at the next index $i = 1$. If, on the other hand, the original index was $i = N_x + 2N_{\rm ghost} - 1$, one would use the second derivative at the index $N_x + 2N_{\rm ghost} - 2$. The procedure in the y direction is equivalent. At the horizontal box corners, one may also apply the method to both x, and y, simultaneously.

It is noted that the above-described, successive integration into the ghost zones is rather simple. This scheme might, for larger iteration numbers, be unstable, and deviate from the desired analytical solution. Here, this is less problematic, as the extrapolation is only used to assign reasonable values, to the small number of ghost zones.

4.6.3 Cooling model

In order to study stationary, GI-turbulent states, using Athena, a cooling model, similar to that used in *DiskFlow* (see Sect. 4.5.3), was implemented. More precisely, the volumetric cooling (heating) rate, in Eq. 4.8, is here defined as follows

$$\rho\dot{q} = -\frac{E_{th}}{\tau_c} + \frac{\rho\, c_{s,0}^2}{\gamma(\gamma-1)\tau_c}. \tag{4.54}$$

This is the exact cooling law, used in Rice et al. (2011), except that E_{th}, and ρ are now volumetric densities, instead of surface densities. The first term, $-E_{th}/\tau_c$, represents direct cooling, and

the second term is an additional heating term. The heating term is density-dependent, and is chosen such that, without further turbulence, the balance between heating and cooling establishes an equilibrium state, with $c_s(x,y,z) = c_{s,0} = \text{const}$. It is noted that this can have numerical advantages, as without additional heating, every possible initial state, with $c_{s,0} > 0$, is necessarily out of equilibrium. The heating term allows for an equilibrium, even without turbulence. This equilibrium state, $(\rho, c_{s,0})$, also corresponds to a Toomre parameter,

$$Q_0 = \frac{c_{s,0}\Omega_0}{\pi G\Sigma} = \frac{c_{s,0}\Omega_0}{\pi G\langle\rho\rangle L_z}, \tag{4.55}$$

whereby $\langle\rho\rangle$ is the volume-averaged mass density, and L_z is the vertical box height. For $Q_0 < Q_c$, with $Q_c \gtrsim 1$, this cooling-heating equilibrium is unstable to GI (see, e.g., Kratter & Lodato 2016, or Sect. 3.3.1). This can be regulated by selecting appropriate input values for $\langle\rho\rangle$, and $c_{s,0}$. Mostly $c_{s,0} = 1$ is used, which amounts to a definition of units, such that, together with $\Omega_0 = 1$, all lengths are in units of $H = c_{s,0}/\Omega_0$.

4.6.4 Implementation of the Poisson solver

General method

As shown in Sect. 4.4, the potential in a vertically stratified shearing box can be determined, using two-dimensional Fourier transforms, and a convolution in the vertical direction. This method was inspired by the ansatz used in Koyama and Ostriker 2009, but with slight modifications. Koyama & Ostriker (2009) provided a methodical overview, but in order to implement the modified solver, it was required to redo the detailed analytical calculations. As the Poisson solver is essential for the projects shown here, the calculation steps are outlined in detail, below.

Using continuous variables, the method is completely summarised by Eqs. 4.13, 4.30, and 4.31, in Sect. 4.4. As the goal is to apply FFTs, it is convenient to directly define the variables on a computational grid. The real-space grid is here defined as follows:

$$\begin{aligned}&(x_\mu, y_\nu, z_\sigma) \in \left[-\frac{L_x}{2}, \frac{L_x}{2}\right] \times \left[-\frac{L_y}{2}, \frac{L_y}{2}\right] \times \left[-\frac{L_z}{2}, \frac{L_z}{2}\right], \\ &\text{with } \mu \in [0, N_x - 1],\ \ \nu \in [0, N_y - 1],\ \ \sigma \in [0, N_z - 1].\end{aligned} \tag{4.56}$$

The spatial-discretisation lengths, in each direction, are defined as $\delta i = L_i/N_i$, with $i \in \{x, y, z\}$. The next step is to replace all continuous, two-dimensional Fourier transforms, in Eqs. 4.13, and 4.31, with DFTs, that is (see, e.g., Binney & Tremaine 2008),

$$\int_{\mathbb{R}^2} f(x,y)\, d^2\mathbf{x} e^{-i\mathbf{k}\cdot\mathbf{x}_{(2)}} \quad \rightarrow \quad \sum_{a=0}^{N_x-1} \sum_{b=0}^{N_y-1} f_{\mu\nu}\, e^{-2\pi i\left(\frac{\mu m}{N_x} + \frac{\nu n}{N_y}\right)} \tag{4.57}$$

$$\left(\frac{1}{2\pi}\right)^2 \int_{\mathbb{R}^2} \hat{f}(k_x, k_y)\, d^2k e^{i\mathbf{k}\cdot\mathbf{x}_{(2)}} \quad \rightarrow \quad \frac{1}{N_x N_y} \sum_{m=0}^{N_x-1} \sum_{n=0}^{N_y-1} \hat{f}_{mn}\, e^{2\pi i\left(\frac{\mu m}{N_x} + \frac{\nu n}{N_y}\right)}, \tag{4.58}$$

for the forward and backward Fourier transforms, respectively. Thereby, $f_{\mu\nu}$ is the field f, evaluated on the grid position (x_μ, y_ν), and $\hat{f}_{mn}$ is the Fourier transform, evaluated at the Fourier-grid position $\mathbf{k} = (k_{x,m}, k_{y,n})$. The z dependence is omitted, because the DFTs, considered here, are two-dimensional, and z merely acts as a parameter for the latter. For real input data, $f_{\mu\nu} \in \mathbb{R}$, one finds $\hat{f}_{mn} = \hat{f}^\star_{N_x-m, N_y-n}$, whereby the star represents the complex-conjugate (see, e.g., Bronstein et al. 2012). Related to this is the wave-number ordering. The wave vectors, $(k_{x,m}, k_{y,n})$, corresponding

to the DFT indices, (m,n), flip sign for $m > N_x/2$, $n > N_y/2$[7]:

$$k_{i,n} = \begin{cases} \frac{2\pi n}{L_i} & \text{for} \quad n \in \{0, ..., \frac{N_i}{2}\} \\ \frac{2\pi(n-N_i)}{L_i} & \text{for} \quad n \in \{\frac{N_i}{2}+1, ..., N_i-1\} \end{cases}, \quad \text{with } i \in \{x, y\}. \tag{4.59}$$

For simplicity, the abbreviation

$$k_{mn} = |\mathbf{k}| = \sqrt{(k_{x,m})^2 + (k_{y,n})^2}, \tag{4.60}$$

is introduced, for the absolute value of the wave vector, at Fourier-grid position (m,n). It is noted that a special technique is applied to calculate the absolute values, k_{mn}, avoiding a case separation for the indices m, and n. The technique is explained in more detail in Appendix M. With these definitions, one can now represent the potential, using a discrete version of Eq. 4.31 (see also Koyama & Ostriker 2009)

$$\Phi(x_\mu, y_\nu, z_\sigma) = \frac{\delta_z}{N_x N_y} \sum_{m=0}^{N_x-1} \sum_{n=0}^{N_y-1} \sum_{j=0}^{N_z-1} e^{2\pi i \left(\frac{\mu m}{N_x} + \frac{\nu n}{N_y}\right)} \hat{\rho}_{mn}(z_j) G_{mn}(z_\sigma, z_j), \tag{4.61}$$

whereby

$$\hat{\rho}_{mn}(z_j) = \sum_{a=0}^{N_x-1} \sum_{b=0}^{N_z-1} e^{-2\pi i \left(\frac{\mu m}{N_x} + \frac{\nu n}{N_y}\right)} \rho(x_\mu, y_\nu, z_j), \tag{4.62}$$

is the two-dimensional, forward DFT of the mass density, evaluated at the vertical elevation z_j. Similarly,

$$G_{mn}(z_\sigma, z_j) = 4\pi G \begin{cases} -\frac{1}{2k_{mn}} \exp(-k_{mn}|z_\sigma - z_j|) & \text{for} \quad k_{mn} \neq 0 \\ \frac{1}{2}|z_\sigma - z_j| & \text{for} \quad k_{mn} = 0 \end{cases}, \tag{4.63}$$

is the discrete version of the Green's function (see, Eq. 4.29, or Koyama & Ostriker 2009), evaluated at the discrete elevations (z_σ, z_j), and the horizontal wave numbers (m,n). In Eq. 4.61, the (m,n) summations correspond to the two-dimensional, backward DFT, whereas the j summation represents the convolution over z, and the latter is also the reason why the vertical discretisation length, δ_z, enters Eq. 4.61.

Note: The analytical convolution integral, in Eq. 4.30, covers the entire z axis, $-\infty < z < \infty$, whereas the summation in Eq. 4.61 only covers grid points within the confines of the simulation domain, $\{z_j | \, 0 \leq j < N_z\}$. Hence, using Eq. 4.61 implicitly assumes that the mass density, or, more precisely, the DFT $\hat{\rho}_{mn}(z_j)$, is zero outside of the vertical boundaries. Essentially, this represents a boundary condition for the potential (at the vertical boundaries), which is often referred to as vacuum boundary conditions (see, e.g., Binney & Tremaine 2008; Koyama & Ostriker 2009; Shi & Chiang 2014, or Sect. 4.6.2). Here, this is a reasonable assumption, due to the vertical density stratification.

As can be seen from Eq. 4.63, G_{mn} depends on z_σ, and z_j only in the from of a difference, and one can write $G_{mn}(z_\sigma, z_j) = G_{mn}(\hat{z}_{\sigma j})$, whereby the abbreviation $\hat{z}_{\sigma j} = z_\sigma - z_j = (\sigma - j)\delta_z$ was introduced. Hence, G_{mn} only requires one argument, which can take on the values (see also Koyama & Ostriker 2009)

$$-L_z < \hat{z}_{\sigma j} < L_z, \quad \text{and} \quad -N_z + 1 < (\sigma - j) < N_z - 1. \tag{4.64}$$

These are $2N_z - 2$ values, which can be inconvenient for the following calculations. As G_{mn} is an analytical expression, one is always free to simply evaluate G_{mn} at one further grid point, for

[7] By substituting $m \to N_x - m$ (and similar for the y direction), one can check that $\exp(2\pi i \mu m/N_x) \to \exp(2\pi i \mu(N_x - m)/N_x) = \exp(-2\pi i \mu m/N_x)$.

example, including the lower value $\sigma - j = -N_z$. Hence, $G_{mn}(\hat{z}_{\sigma j})$ is now evaluated on a grid, with size $N_x \times N_y \times (2N_z - 1)$. For reasons of shorter notation, one can also introduce the index p, such that $\sigma - j = -N_z + p$, with $0 \leq p \leq 2N_z - 1$, and, correspondingly, one can introduce $\hat{z}_p = \hat{z}_{\sigma j} = (p - N_z)L_z/N_z$. One is also free to calculate the DFT of the values $G_{mn}(\hat{z}_p)$, along the $\hat{z}_p$ direction (see also Koyama & Ostriker 2009):

$$G_{mnl} = \sum_{p=0}^{2N_z-1} e^{-2\pi i \frac{(p-N_z)l}{2N_z}} G_{mn}\left(\hat{z}_p\right). \tag{4.65}$$

It is pointed out that the index shift of $-N_z$, occurring in the complex exponential, is unusual for a DFT, as one would expect the running index to yield values in the interval $[0, 2N_z - 1]$, and not $[-N_z, N_z - 1]$. Clearly, this originates from the definition $p - N_z = \sigma - j$, and, as may become clear later, that is a deliberate choice (see also Koyama & Ostriker 2009). However, this shift, by one half of the total number of values, only leads to an additional factor of $e^{i\pi l} = e^{-i\pi l} = (-1)^l$, which is not problematic, as long as one considers the shift in the backward transform as well. Moreover, this transform is here only required for the analytical derivation, and is not numerically calculated by the algorithm, that is set up in this section. Taking into account the shifted index, the backwards transform is given by

$$G_{mn}(\hat{z}_p) = \frac{1}{2N_z} \sum_{l=0}^{2N_z-1} e^{2\pi i \frac{(p-N_z)l}{2N_z}} G_{mnl} = \frac{1}{2N_z} \sum_{l=0}^{2N_z-1} e^{2\pi i \frac{(\sigma-j)l}{2N_z}} G_{mnl}. \tag{4.66}$$

The last step makes clear why the index-shift is deliberate, as the convolution over z, see Eq. 4.61, requires two indices (σ, j), and not only one index p. Moreover, this indexing scheme allows for an easier comparison to Koyama & Ostriker (2009), as the latter also used this indexing scheme.
More generally, the reason why $G_{mn}(\hat{z}_p)$ is represented by an inverse DFT of G_{mnl} is that the additional sum, which is thus introduced, can later be used to write the potential as one three-dimensional, inverse DFT. Conveniently, as $G_{mn}(\hat{z}_p)$ is an analytical expression (see Eq. 4.63), the values G_{mnl} can also be represented analytically, which is detailed in the following cases.

Case one, $k_{nn} \neq 0$:
An analytical expression for G_{mnl} can be obtained, by substituting the expression for $G_{mn}(\hat{z}_p)$ (see Eq. 4.63) into Eq. 4.65, first for the case $k_{nn} \neq 0$:

$$\begin{aligned}
G_{mnl} &= \frac{-4\pi G}{2k_{mn}} \sum_{p=0}^{2N_z-1} \exp\left(-2\pi i \frac{(p-N_z)l}{2N_z} - k_{mn}\left|\frac{(p-N_z)L_z}{N_z}\right|\right) \\
&= \frac{-4\pi G}{2k_{mn}} \left\{ \sum_{p=0}^{N_z-1} \exp\left(-\frac{i\pi lp}{N_z} + i\pi l - k_{mn}L_z + k_{mn}\frac{L_z}{N_z}p\right) \right. \\
&\quad \left. + \sum_{p=N_z}^{2N_z-1} \exp\left(-\frac{i\pi lp}{N_z} + i\pi l + k_{mn}L_z - k_{mn}\frac{L_z}{N_z}p\right) \right\} \\
&= \frac{-4\pi G\, e^{i\pi l}}{2k_{mn}} \left\{ e^{-k_{mn}L_z} \sum_{p=0}^{N_z-1} \left(e^{\frac{-i\pi l + k_{mn}L_z}{N_z}}\right)^p + e^{k_{mn}L_z} \sum_{p=N_z}^{2N_z-1} \left(e^{\frac{-i\pi l - k_{mn}L_z}{N_z}}\right)^p \right\} \\
&= \frac{-4\pi G\, e^{i\pi l}}{2k_{mn}} \left\{ e^{-k_{mn}L_z} S_1 + e^{k_{mn}L_z} S_2 \right\}.
\end{aligned} \tag{4.67}$$

In the last step, the summations were abbreviated by S_1 and S_2, whereby both can be represented

as a geometric series (see, e.g., Bronstein et al. 2012). For S_1, that works out as follows:

$$\begin{aligned} S_1 &= \sum_{p=0}^{N_z-1} \left(e^{\frac{-i\pi l+k_{mn}L_z}{N_z}}\right)^p = \frac{1-\left(e^{\frac{-i\pi l+k_{mn}L_z}{N_z}}\right)^{N_z}}{1-e^{\frac{-i\pi l+k_{mn}L_z}{N_z}}} \\ &= \frac{1-e^{-i\pi l+k_{mn}L_z}}{1-e^{\frac{-i\pi l}{N_z}+k_{mn}\delta_z}}. \end{aligned} \tag{4.68}$$

The same procedure can be applied to S_2, except that one first has to shift the index of summation. S_2 sums all terms from $p = N_z$ to $p = 2N_z - 1$. That is equivalent to a summation from $p = 0$ to $p = N_z - 1$, by replacing $p \to N_z + p$. Applying the latter replacement, one obtains

$$S_2 = e^{-i\pi l-k_{mn}L_z}\frac{1-e^{-i\pi l-k_{mn}L_z}}{1-e^{\frac{-i\pi l}{N_z}-k_{mn}\delta_z}}. \tag{4.69}$$

Due to its frequent occurrence, the term $\exp(-i\pi l/N_z)$ is in the following abbreviated by c_l. It is also noted that $c_{-l} = c_l^\star$. Now, S_1, and S_2 are substituted back into the full expression for G_{mnl}, yielding

$$\begin{aligned} G_{mnl} &= \frac{-4\pi G}{2k_{mn}}\left\{\frac{e^{i\pi l-k_{mn}L_z}-1}{1-e^{\frac{-i\pi l}{N_z}+k_{mn}\delta_z}} + \frac{1-e^{-i\pi l-k_{mn}L_z}}{1-e^{\frac{-i\pi l}{N_z}-k_{mn}\delta_z}}\right\} \\ &= -4\pi G\frac{1-e^{-i\pi l-k_{mn}L_z}}{2k_{mn}}\left\{\frac{-1}{1-c_l e^{k_{mn}\delta_z}} + \frac{1}{1-c_l e^{-k_{mn}\delta_z}}\right\} \\ &= -4\pi G\,\frac{1-e^{-i\pi l-k_{mn}L_z}}{2k_{mn}}\,\frac{c_l(e^{-k_{mn}\delta_z}-e^{k_{mn}\delta_z})}{1+c_l^2-c_l(e^{k_{mn}\delta_z}+e^{-k_{mn}\delta_z})} \\ &= -4\pi G\,\frac{1-e^{-i\pi l-k_{mn}L_z}}{2k_{mn}}\,\frac{-2c_l\sinh(k_{mn}\delta_z)}{1+c_l^2-2c_l\cosh(k_{mn}\delta_z)} \\ &= 4\pi G\,\frac{1-e^{-i\pi l}e^{-k_{mn}L_z}}{k_{mn}}\,\frac{\sinh(k_{mn}\delta_z)}{2\cos(\frac{\pi l}{N_z})-2\cosh(k_{mn}\delta_z)}. \end{aligned} \tag{4.70}$$

In the last step, c_l has been factored out of the nominator, yielding $1/c_l + c_l = c_{-l} + c_l = 2\cos(\pi l/N_z)$, in the nominator. Eq. 4.70 now provides an analytical representation of G_{mnl}, for $k_{mn} \neq 0$.

Case two, $k_{mn} = 0$:
One way of calculating G_{mnl}, for $k_{mn} = 0$, is by directly substituting Eq. 4.63, into Eq. 4.65, similar to the case $k_{mn} \neq 0$. This is demonstrated in Appendix N. However, there is a faster alternative. The result is also obtained by taking the limit $k_{mn} \to 0$, of Eq. 4.70. One can not simply substitute $k_{mn} = 0$, as that would require a division by zero, though one can Taylor expand $\sinh(k_{mn}\delta_z) \sim k_{mn}\delta_z$, and $\cosh(k_{mn}\delta_z) \sim 1$, to obtain

$$G_{mnl} = \frac{4\pi G\,\delta_z}{2}\,\frac{1-e^{i\pi l}}{\cos\left(\frac{\pi l}{N_z}\right)-1}. \tag{4.71}$$

It is noted that the Taylor expansion does not mean that this result is an approximation, it is rather the exact limit, for $k_{mn} \to 0$.

Combining the cases $k_{mn} \neq 0$, and $k_{mn} = 0$, one obtains

$$G_{mnl} = 4\pi G\begin{cases} \frac{1-e^{-i\pi l}e^{-k_{mn}L_z}}{k_{mn}}\,\frac{\sinh(k_{mn}\delta_z)}{2\cos(\frac{\pi l}{N_z})-2\cosh(k_{mn}\delta_z)} & \text{for } k_{mn} \neq 0 \\ \frac{\delta_z}{2}\,\frac{1-e^{i\pi l}}{\cos(\frac{\pi l}{N_z})-1} & \text{for } k_{mn} = 0. \end{cases} \tag{4.72}$$

It is noted that this result is slightly different from the expression used in Koyama & Ostriker (2009). However, if one uses the above expression, and Taylor expands for $l/N_z, k_{mn}\delta_z \ll 1$, one recovers the outcome in Koyama & Ostriker (2009).

One can now substitute the analytical result for G_{mnl} into the expression for the potential, Eq. 4.61, using Eq. 4.66

$$\begin{aligned} \Phi(x_\mu, y_\nu, z_\sigma) &= \frac{\delta_z}{N_x N_y (2N_z)} \sum_{m=0}^{N_x-1} \sum_{n=0}^{N_y-1} \sum_{j=0}^{N_z-1} \sum_{l=0}^{2N_z-1} T \\ \text{with } T &:= \exp\left[2\pi i \left(\frac{\mu m}{N_x} + \frac{\nu n}{N_y} + \frac{(\sigma - j)l}{2N_z}\right)\right] G_{mnl}\, \hat{\rho}_{mn}(z_j). \end{aligned} \tag{4.73}$$

Note that the summation index j only occurs in the complex exponent, and in $\hat{\rho}_{mn}(z_j)$. Hence, one can rewrite the last equation as follows

$$\Phi(x_\mu, y_\nu, z_\sigma) = \frac{4\pi G \delta_z}{N_x N_y (2N_z)} \sum_{m=0}^{N_x-1} \sum_{n=0}^{N_y-1} \sum_{l=0}^{2N_z-1} \left\{ \mathcal{K}_{mnl}\, \hat{\rho}^{\rm mod}_{mnl}\, \exp\left(2\pi i \left[\frac{\mu m}{N_x} + \frac{\nu n}{N_y} + \frac{\sigma l}{2N_z}\right]\right)\right\}. \tag{4.74}$$

Thereby, the Fourier-kernel,

$$\mathcal{K}_{mnl} := \frac{\left(1 - e^{i\pi l} e^{-k_{mn} L_z}\right)}{2k_{mn}} \frac{\sinh(k_{mn}\delta_z)}{\cos(\frac{\pi l}{N_z}) - \cosh(k_{mn}\delta_z)}, \tag{4.75}$$

and the modified mass density (see also Koyama & Ostriker 2009),

$$\hat{\rho}^{\rm mod}_{mnl} = \sum_{j=0}^{N_z-1} \exp\left(-2\pi i \frac{jl}{2N_z}\right) \hat{\rho}_{mn}(z_j), \tag{4.76}$$

have been defined. The important point, for the numerical implementation, is that Eq. 4.74 is a three-dimensional, backward DFT, of size $N_x, N_y, 2N_z$. The analytical form of $\hat{\rho}^{\rm mod}_{mnl}$ almost resembles a forward DFT, but the number of possible indices does not match, $j \in [0, N_z - 1]$, and $l \in [0, 2N_z - 1]$. This can be resolved, by separating between even, and odd l. An even index l can be represented as $l = 2q$, with integer $q \in [0, N_z - 1]$. The complex exponent, in $\hat{\rho}^{\rm mod}_{mnl}$, then becomes

$$\exp\left(-2\pi i \frac{jl}{2N_z}\right) = \exp\left(-2\pi i \frac{jq}{N_z}\right). \tag{4.77}$$

Similarly, for an odd index, one can write $l = 2q + 1$, and the complex exponent is given by

$$\exp\left(-2\pi i \frac{jl}{2N_z}\right) = \exp\left(2\pi i \frac{jq}{N_z}\right) \exp\left(-i\pi \frac{j}{N_z}\right). \tag{4.78}$$

Substitution into $\hat{\rho}^{\rm mod}_{mnl}$, yields, separated into even and odd contributions,

$$\begin{aligned} \hat{\rho}^{\rm mod}_{mn(2q)} &= \sum_{j=0}^{N_z-1} \exp\left(-2\pi i \frac{jq}{N_z}\right) \hat{\rho}_{mn}(z_j) \\ \hat{\rho}^{\rm mod}_{mn(2q+1)} &= \sum_{j=0}^{N_z-1} \exp\left(-2\pi i \frac{jq}{N_z}\right) \left[\exp\left(-i\pi \frac{j}{N_z}\right) \hat{\rho}_{mn}(z_j)\right]. \end{aligned} \tag{4.79}$$

Hence, considered separately, the even and odd contributions each correspond to a one-dimensional, forward DFT. One can now express $\hat{\rho}_{mn}(z_j)$, in terms of $\rho(x_\mu, y_\nu, z_j)$, yielding

$$\hat{\rho}^{\rm mod}_{mn(2q)} = \sum_{\mu=0}^{N_x-1}\sum_{\nu=0}^{N_y-1}\sum_{j=0}^{N_z-1}\rho(x_\mu,y_\nu,z_j)\exp\left(-2\pi i\left[\frac{\mu m}{N_x}+\frac{\nu n}{N_y}+\frac{jq}{N_z}\right]\right) \tag{4.80}$$

$$\hat{\rho}^{\rm mod}_{mn(2q+1)} = \sum_{a=0}^{N_x-1}\sum_{b=0}^{N_y-1}\sum_{j=0}^{N_z-1}\left\{\exp\left(-i\pi\frac{j}{N_z}\right)\rho(x_\mu,y_\nu,z_j)\right\}\exp\left(-2\pi i\left[\frac{\mu m}{N_x}+\frac{\nu n}{N_y}+\frac{jq}{N_z}\right]\right).$$

Those are two, three-dimensional DFTs. The full array for $\hat{\rho}^{\rm mod}_{mnl}$ can then be obtained by zipping the even, and odd contributions together

$$\text{ZIP}\left(\hat{\rho}^{\rm mod}_{mn(2q)},\hat{\rho}^{\rm mod}_{mn(2q+1)}\right)\rightarrow\hat{\rho}^{\rm mod}_{mnl}. \tag{4.81}$$

It is noted that this representation, using three-dimensional, forward FFTs, deviates from the method, used in Koyama & Ostriker (2009). The latter calculated two-dimensional FFTs, for each elevation z, and afterwards used one-dimensional FFTs to obtain $\hat{\rho}^{\rm mod}_{mnl}$.

To summarise: The previous analytical considerations suggest that one can calculate the potential, $\Phi(x_\mu, x_\nu, x_\sigma)$, by applying two three-dimensional, forward FFTs (each of size N_x, N_y, N_z), and one three-dimensional, backward FFT (of size $N_x, N_y, 2N_z$). The advantage of using FFTs is that the required number of operations scales as $N\log(N)$, in contrast to N^2, whereby N is the total number gird points, within the simulation volume (see, e.g., Landau et al. 2008). Note that, in the local shearing box, one also has to apply the density-mapping routine, detailed in Sect. 4.4.2. The latter is applied to $\rho(x_\mu, y_\nu, z_\sigma)$, before the forward FFTs are applied. And the density-mapping is reversed, after the inverse FFT is applied. Athena provides a pre-defined remapping routine, "RemapVar(Grid, ρ, dt)", which is also used in Löhnert & Peeters (2022), and Sect. 9.

Self-gravity source terms

In the discussion above, the method, used to obtain $\Phi(x_\mu, y_\nu, z_\sigma)$, is presented. What then remains is to include the source terms, corresponding to self-gravity, in both the momentum and energy conservation equations. This step is pre-implemented in Athena. In Athena, self-gravity enters the momentum equation, via a flux divergence, $\nabla\cdot\underline{\mathbf{G}}$ (see Eq. 4.6), allowing for the conservation of momentum, up to machine precision. Thereby, the exact form of the gravitational stress tensor, $\underline{\mathbf{G}}$, is given by Eq. 3.27 (or see Lynden-Bell & Kalnajs 1972). However, in the equation for energy conservation, self-gravity in included as a source term (see Eq. 4.8). Hence, the energetic influence of self-gravity is not captured to exact round-off error[8].

[8] see also `https://princetonuniversity.github.io/Athena-Cversion/AthenaDocsUGGravity` (as of 25.05.2023)

Chapter 5

About this Thesis

The previous sections provide a brief introduction into the general research area, and introduce the methods that are used. The following sections (Sects. 7 - 10) discuss the actual research, summarised by this thesis. The goal of his section is to provide an overview, and to explain both the order and the format, in which the results are presented. All published, and submitted articles are listed in Sect. 6.

Sect. 7 has been published in the journal Astronomy & Astrophysics (Löhnert, Krätschmer, & Peeters 2020, in the following abbreviated by LPK20). The work focuses on numerical simulations of gravitoturbulence (or GI turbulence, see also Sect. 3.3.1), in the local shearing-box approximation (see also Sects. 4.1, and 4.5). For the vertical direction, a razor-thin setup is used (see Sect. 4.5.1). The turbulence structure is analysed in more detail, by evaluating Fourier spectra of the turbulent fluctuations, and the importance of velocity discontinuities (shocks), for determining the spectral power law, is highlighted. Additionally, a simple mixing-length model, for the turbulent viscosities, is developed. The model is based on properties of the linear-instability phase of GI.

Sect. 8 has been published in Astronomy & Astrophysics, as well (Löhnert & Peeters 2022, in the following abbreviated by LP22). LP22 also studies numerical simulations of gravitoturbulence, in the local shearing-box approximation. In contrast to the hydrodynamical simulations in LPK20, the GI simulations in LP22 include magnetic fields (ideal MHD), and are three-dimensional. The simulations were run using the MHD code Athena (see also Sect. 4.6). The procedure is to start with a GI-turbulent state, and to introduce a small magnetic-seed field into that state. The subsequent time evolution is then studied. Since such systems are known to give rise to MRI (see Sect. 3.3.2), one goal, in LP22, is to test the possibility of a coexistence between GI- and MRI-related turbulence. Also tested are the dynamo properties of the GI, or GI-MRI-turbulent state.

Sect. 9 has been published in Astronomy & Astrophysics (Löhnert & Peeters 2023), and is, in the following, referred to as LP23. The latter is a follow-up study to LP22, also utilising three-dimensional MHD simulations of GI turbulence. The focus in LP23 is on behaviour of GI-MRI coexistence, under changes of a variety of system parameters. Tested are two major regimes. First, additional, ideal-MHD simulations are provided, and the influence of GI strength is tested by modifying the cooling law. The second regime are non-ideal MHD simulations, including Ohmic resistivity. A scan over different values of Ohmic resistivity is provided, and the possibility of a phase transition is demonstrated.

Finally, Sect. 10 provides additional results, related to the previously summarised works, that have not been published, but are thematically related. Sect. 10.1 contributes a detailed analytical derivation of the linear stability analysis, used in LPK20. Sect. 10.2 derives an analytical expression

for the Fourier transform of a generic shock profile, which is also used in LPK20. Since the special variant of the Athena Poisson solver, used here (see also Sect. 4.6.4), had to be implemented, Sect. 10.3 provides additional tests, and demonstrations of the solver accuracy. Sect. 10.4 is a detailed analytical derivation of the dynamo-oscillations frequency, used in LP22. Finally, Sect. 10.5 is an additional analysis of the electromotive forces (EMFs), for the ideal-MHD simulations, shown in LP23.

References

Armitage, Philip J. (2011). "Dynamics of protoplanetary disks". In: *Annual Review of Astronomy and Astrophysics* 49, pp. 195–236.

Armitage, Philip J., Mario Livio, and James E. Pringle (2001). "Episodic accretion in magnetically layered protoplanetary discs". In: *Monthly Notices of the Royal Astronomical Society* 324.3, pp. 705–711.

Baehr, Hans and Hubert Klahr (2015). "The role of the cooling prescription for disk fragmentation: Numerical convergence and critical cooling parameter in self-gravitating disks". In: *The Astrophysical Journal* 814.2, p. 155.

Bai, Xue-Ning (2015). "Hall effect controlled gas dynamics in protoplanetary disks. II. Full 3D simulations toward the outer disk". In: *The Astrophysical Journal* 798.2, p. 84.

Bai, Xue-Ning and James M. Stone (2011). "Effect of ambipolar diffusion on the nonlinear evolution of magnetorotational instability in weakly ionized disks". In: *The Astrophysical Journal* 736.2, p. 144.

— (2013a). "Local study of accretion disks with a strong vertical magnetic field: Magnetorotational instability and disk outflow". In: *The Astrophysical Journal* 767.1, p. 30.

— (2013b). "Wind-driven accretion in protoplanetary disks. I. Suppression of the magnetorotational instability and launching of the magnetocentrifugal wind". In: *The Astrophysical Journal* 769.1, p. 76.

Balbus, Steven A. and John F. Hawley (1991). "A powerful local shear instability in weakly magnetized disks. I-Linear analysis. II-Nonlinear evolution". In: *The Astrophysical Journal* 376, pp. 214–233.

— (1992). "Is the Oort A-value a universal growth rate limit for accretion disk shear instabilities?" In: *The Astrophysical Journal* 392, pp. 662–666.

— (1998). "Instability, turbulence, and enhanced transport in accretion disks". In: *Reviews of modern physics* 70.1, p. 1.

Balbus, Steven A. and John C. B. Papaloizou (1999). "On the dynamical foundations of alpha disks". In: *The Astrophysical Journal* 521.2, p. 650.

Balbus, Steven A. and Caroline Terquem (2001). "Linear analysis of the Hall effect in protostellar disks". In: *The Astrophysical Journal* 552.1, p. 235.

Beckwith, Kris, Philip J. Armitage, and Jacob B. Simon (2011). "Turbulence in global simulations of magnetized thin accretion discs". In: *Monthly Notices of the Royal Astronomical Society* 416.1, pp. 361–382.

Bell, K. R. et al. (1997). "The structure and appearance of protostellar accretion disks: Limits on disk flaring". In: *The Astrophysical Journal* 486.1, p. 372.

Béthune, William and Henrik Latter (2022). "Gravitoturbulent dynamo in global simulations of gaseous disks". In: *Astronomy & Astrophysics* 663, A138.

Binney, James and Scott Tremaine (2008). *Galactic dynamics*. 2nd ed. Princeton University Press.

Biskamp, Dieter (2003). *Magnetohydrodynamic turbulence*. Cambridge University Press.

Blackman, Eric G. and George B. Field (2002). "New dynamical mean-field dynamo theory and closure approach". In: *Physical Review Letters* 89.26, p. 265007.

Blackman, Eric G., Robert F. Penna, and Peggy Varnière (2008). "Empirical relation between angular momentum transport and thermal-to-magnetic pressure ratio in shearing box simulations". In: *New Astronomy* 13.4, pp. 244–251.

Blaes, Omer M. and Steven A. Balbus (1994). "Local shear instabilities in weakly ionized, weakly magnetized disks". In: *The Astrophysical Journal* 421, pp. 163–177.

Bodo, G. et al. (2014). "On the convergence of magnetorotational turbulence in stratified isothermal shearing boxes". In: *The Astrophysical Journal Letters* 787.1, p. L13.

Boffetta, Guido and Robert E. Ecke (2012). "Two-dimensional turbulence". In: *Annual review of fluid mechanics* 44, pp. 427–451.

Boley, Aaron C. et al. (2006). "The thermal regulation of gravitational instabilities in protoplanetary disks. III. Simulations with radiative cooling and realistic opacities". In: *The Astrophysical Journal* 651.1, p. 517.

Booth, Richard A. and Cathie J. Clarke (2019). "Characterizing gravito-turbulence in 3D: turbulent properties and stability against fragmentation". In: *Monthly Notices of the Royal Astronomical Society* 483.3, pp. 3718–3729.

Boss, Alan P. (2017). "The Effect of Protoplanetary Disk Cooling Times on the Formation of Gas Giant Planets by Gravitational Instability". In: *The Astrophysical Journal* 836.1, p. 53.

Brandenburg, Axel and Kandaswamy Subramanian (2005). "Astrophysical magnetic fields and nonlinear dynamo theory". In: *Physics Reports* 417.1-4, pp. 1–209.

Brandenburg, Axel et al. (1995). "Dynamo-generated turbulence and large-scale magnetic fields in a Keplerian shear flow". In: *The Astrophysical Journal* 446, p. 741.

Bronstein, Ilja N. et al. (2012). *Taschenbuch der Mathematik*. 8th ed. Harri Deutsch.

Chiuderi, Claudio and Marco Velli (2015). *Basics of Plasma Astrophysics*. Springer.

Clarke, C. J., E. Harper-Clark, and G. Lodato (2007). "The response of self-gravitating protostellar discs to slow reduction in cooling time-scale: the fragmentation boundary revisited". In: *Monthly Notices of the Royal Astronomical Society* 381.4, pp. 1543–1547.

Clarke, Cathie and Bob Carswell (2007). *Principles of astrophysical fluid dynamics*. Cambridge University Press.

Colella, Phillip (1990). "Multidimensional upwind methods for hyperbolic conservation laws". In: *Journal of Computational Physics* 87.1, pp. 171–200.

Colella, Phillip and Paul R. Woodward (1984). "The piecewise parabolic method (PPM) for gas-dynamical simulations". In: *Journal of Computational Physics* 54.1, pp. 174–201.

Cooley, James W. and John W. Tukey (1965). "An algorithm for the machine calculation of complex Fourier series". In: *Mathematics of computation* 19.90, pp. 297–301.

Cossins, Peter, Giuseppe Lodato, and C. J. Clarke (2009). "Characterizing the gravitational instability in cooling accretion discs". In: *Monthly Notices of the Royal Astronomical Society* 393.4, pp. 1157–1173.

Courant, Richard, Kurt Friedrichs, and Hans Lewy (1928). "Über die partiellen Differenzengleichungen der mathematischen Physik". In: *Mathematische annalen* 100.1, pp. 32–74.

Crank, John and Phyllis Nicolson (1947). "A practical method for numerical evaluation of solutions of partial differential equations of the heat-conduction type". In: *Mathematical proceedings of the Cambridge philosophical society*. Vol. 43. 1. Cambridge University Press, pp. 50–67.

D'Alessio, Paola et al. (1998). "Accretion disks around young objects. I. The detailed vertical structure". In: *The Astrophysical Journal* 500.1, p. 411.

Davis, Shane W., James M. Stone, and Martin E. Pessah (2010). "Sustained magnetorotational turbulence in local simulations of stratified disks with zero net magnetic flux". In: *The Astrophysical Journal* 713.1, p. 52.

De Villiers, Jean-Pierre, John F. Hawley, and Julian H. Krolik (2003). "Magnetically driven accretion flows in the Kerr metric. I. Models and overall structure". In: *The Astrophysical Journal* 599.2, p. 1238.

Deng, Hongping, Lucio Mayer, and Henrik Latter (2020). "Global simulations of self-gravitating magnetized protoplanetary disks". In: *The Astrophysical Journal* 891.2, p. 154.

Desch, S. J. (2004). "Linear analysis of the magnetorotational instability, including ambipolar diffusion, with application to protoplanetary disks". In: *The Astrophysical Journal* 608.1, p. 509.

Evans, Charles R. and John F. Hawley (1988). "Simulation of magnetohydrodynamic flows - A constrained transport method". In: *The Astrophysical Journal* 332, pp. 659–677.

Fleming, Timothy and James M. Stone (2003). "Local magnetohydrodynamic models of layered accretion disks". In: *The Astrophysical Journal* 585.2, p. 908.

Flock, M. et al. (2015). "Gaps, rings, and non-axisymmetric structures in protoplanetary disks-From simulations to ALMA observations". In: *Astronomy & Astrophysics* 574, A68.

Fragile, P. Chris and David L. Meier (2009). "General relativistic magnetohydrodynamic simulations of the hard state as a magnetically dominated accretion flow". In: *The Astrophysical Journal* 693.1, p. 771.

Frisch, Uriel (1995). *Turbulence - The legacy of AN Kolmogorov*. Cambridge University Press.

Fromang, Sébastien (2005). "The effect of MHD turbulence on massive protoplanetary disk fragmentation". In: *Astronomy & Astrophysics* 441.1, pp. 1–8.

— (2010). "MHD simulations of the magnetorotational instability in a shearing box with zero net flux: the case Pm= 4". In: *Astronomy & Astrophysics* 514, p. L5.

Fromang, Sébastien and John Papaloizou (2007). "MHD simulations of the magnetorotational instability in a shearing box with zero net flux-I. The issue of convergence". In: *Astronomy & Astrophysics* 476.3, pp. 1113–1122.

Fromang, Sébastien et al. (2004). "Evolution of self-gravitating magnetized disks. II. Interaction between magnetohydrodynamic turbulence and gravitational instabilities". In: *The Astrophysical Journal* 616.1, p. 364.

Fromang, Sébastien et al. (2007). "MHD simulations of the magnetorotational instability in a shearing box with zero net flux-II. the effect of transport coefficients". In: *Astronomy & Astrophysics* 476.3, pp. 1123–1132.

Fromang, Sébastien et al. (2013). "Local outflows from turbulent accretion disks". In: *Astronomy & Astrophysics* 552, A71.

Gammie, Charles F. (1996). "Layered accretion in T Tauri disks". In: *The Astrophysical Journal* 457, p. 355.

— (2001). "Nonlinear outcome of gravitational instability in cooling, gaseous disks". In: *The Astrophysical Journal* 553.1, p. 174.

Gardiner, Thomas A. and James M. Stone (2008). "An unsplit Godunov method for ideal MHD via constrained transport in three dimensions". In: *Journal of Computational Physics* 227.8, pp. 4123–4141.

Goldreich, Peter, Jeremy Goodman, and Ramesh Narayan (1986). "The stability of accretion tori–I. Long-wavelength modes of slender tori". In: *Monthly Notices of the Royal Astronomical Society* 221.2, pp. 339–364.

Goldreich, Peter and D. Lynden-Bell (1965). "II. Spiral arms as sheared gravitational instabilities". In: *Monthly Notices of the Royal Astronomical Society* 130.2, pp. 125–158.

Goodman, Jeremy (2003). "Self-gravity and quasi-stellar object discs". In: *Monthly Notices of the Royal Astronomical Society* 339.4, pp. 937–948.

Gressel, Oliver (2010). "A mean-field approach to the propagation of field patterns in stratified magnetorotational turbulence". In: *Monthly Notices of the Royal Astronomical Society* 405.1, pp. 41–48.

Gressel, Oliver et al. (2015). "Global simulations of protoplanetary disks with ohmic resistivity and ambipolar diffusion". In: *The Astrophysical Journal* 801.2, p. 84.

Guan, Xiaoyue and Charles F. Gammie (2011). "Radially extended, stratified, local models of isothermal disks". In: *The Astrophysical Journal* 728.2, p. 130.

Guan, Xiaoyue et al. (2009). "Locality of mhd turbulence in isothermal disks". In: *The Astrophysical Journal* 694.2, p. 1010.

Hawley, John F. and Steven A. Balbus (1992). "A powerful local shear instability in weakly magnetized disks. III Long-term evolution in a shearing sheet, IV Nonaxisymmetric perturbations". In: *The Astrophysical Journal* 400, pp. 595–609.

Hawley, John F., Charles F. Gammie, and Steven A. Balbus (1995). "Local three-dimensional magnetohydrodynamic simulations of accretion disks". In: *The Astrophysical Journal* 440, p. 742.

— (1996). "Local three-dimensional simulations of an accretion disk hydromagnetic dynamo". In: *The Astrophysical Journal* 464, p. 690.

Hawley, John F., Xiaoyue Guan, and Julian H. Krolik (2011). "Assessing quantitative results in accretion simulations: from local to global". In: *The Astrophysical Journal* 738.1, p. 84.

Hawley, John F. and Julian H. Krolik (2001). "Global MHD simulation of the inner accretion disk in a pseudo-Newtonian potential". In: *The Astrophysical Journal* 548.1, p. 348.

Hirose, Shigenobu (2015). "Magnetic turbulence and thermodynamics in the inner region of protoplanetary discs". In: *Monthly Notices of the Royal Astronomical Society* 448.4, pp. 3105–3120.

Hirose, Shigenobu, Julian H. Krolik, and James M. Stone (2006). "Vertical structure of gas pressure-dominated accretion disks with local dissipation of turbulence and radiative transport". In: *The Astrophysical Journal* 640.2, p. 901.

Hirose, Shigenobu and Ji-Ming Shi (2019). "Non-linear outcome of gravitational instability in an irradiated protoplanetary disc". In: *Monthly Notices of the Royal Astronomical Society* 485.1, pp. 266–285.

Hirose, Shigenobu et al. (2014). "Convection causes enhanced magnetic turbulence in accretion disks in outburst". In: *The Astrophysical Journal* 787.1, p. 1.

Hohl, Frank (1971). "Numerical experiments with a disk of stars". In: *The Astrophysical Journal* 168, p. 343.

Jackson, John David (2014). *Klassische Elektrodynamik*. 3rd ed. de Gruyter.

Jiang, Yan-Fei and Jeremy Goodman (2011). "Star Formation in a Quasar Disk". In: *The Astrophysical Journal* 730.1, p. 45.

Jin, Liping (1996). "Damping of the shear instability in magnetized disks by Ohmic diffusion". In: *The Astrophysical Journal* 457, p. 798.

Johansen, Anders and Yuri Levin (2008). "High accretion rates in magnetised Keplerian discs mediated by a Parker instability driven dynamo". In: *Astronomy & Astrophysics* 490.2, pp. 501–514.

Johnson, Bryan M. and Charles F. Gammie (2003). "Nonlinear outcome of gravitational instability in disks with realistic cooling". In: *The Astrophysical Journal* 597.1, p. 131.

Käpylä, Petri J. and Maarit J. Korpi (2011). "Magnetorotational instability driven dynamos at low magnetic Prandtl numbers". In: *Monthly Notices of the Royal Astronomical Society* 413.2, pp. 901–907.

Koyama, H. and E. C. Ostriker (2009). "Gas properties and implications for galactic star formation in numerical models of the turbulent, multiphase interstellar medium". In: *The Astrophysical Journal* 693, pp. 1316–1345.

Kratter, Kaitlin and Giuseppe Lodato (2016). "Gravitational Instabilities in Circumstellar Disks". In: *Annual review of astronomy and astrophysics* 54.1, pp. 271–311.

Kratter, Kaitlin M., Ruth A. Murray-Clay, and Andrew N. Youdin (2010). "The runts of the litter: Why planets formed through gravitational instability can only be failed binary stars". In: *The Astrophysical Journal* 710.2, p. 1375.

Kratter, Kaitlin M. et al. (2010). "On the role of disks in the formation of stellar systems: a numerical parameter study of rapid accretion". In: *The Astrophysical Journal* 708.2, p. 1585.

Krumholz, Mark R. et al. (2009). "The formation of massive star systems by accretion". In: *Science* 323.5915, pp. 754–757.

Kulsrud, R. M. (2005). *Plasma Physics for Astrophysics*. Princeton University Press.

Kunz, Matthew W. and Steven A. Balbus (2004). "Ambipolar diffusion in the magnetorotational instability". In: *Monthly Notices of the Royal Astronomical Society* 348.1, pp. 355–360.

Kunz, Matthew W. and Geoffroy Lesur (2013). "Magnetic self-organization in Hall-dominated magnetorotational turbulence". In: *Monthly Notices of the Royal Astronomical Society* 434.3, pp. 2295–2312.

Landau, Rubin H. et al. (2008). *A survey of computational physics: introductory computational science*. Princeton University Press.

Lau, Y. Y. and G. Bertin (1978). "Discrete spiral modes, spiral waves, and the local dispersion relationship". In: *The Astrophysical Journal* 226, pp. 508–520.

Lesur, G. and P.-Y. Longaretti (2007). "Impact of dimensionless numbers on the efficiency of magnetorotational instability induced turbulent transport". In: *Monthly Notices of the Royal Astronomical Society* 378.4, pp. 1471–1480.

Lesur, Geoffroy, Matthew W. Kunz, and Sébastien Fromang (2014). "Thanatology in protoplanetary discs-The combined influence of Ohmic, Hall, and ambipolar diffusion on dead zones". In: *Astronomy & Astrophysics* 566, A56.

Lesur, Geoffroy and P.-Y. Longaretti (2011). "Non-linear energy transfers in accretion discs MRI turbulence-I. Net vertical field case". In: *Astronomy & Astrophysics* 528, A17.

Lesur, Geoffroy and Gordon I. Ogilvie (2010). "On the angular momentum transport due to vertical convection in accretion discs". In: *Monthly Notices of the Royal Astronomical Society: Letters* 404.1, pp. L64–L68.

Lin, C. C. and Frank H. Shu (1964). "On the Spiral Structure of Disk Galaxies." In: *The Astrophysical Journal* 140, p. 646.

Lin, Min-Kai and Kaitlin M. Kratter (2016). "On the Gravitational Stability of Gravito-turbulent Accretion Disks". In: *The Astrophysical Journal* 824.2, p. 91.

Löhnert, L., S. Krätschmer, and A. G. Peeters (2020). "Saturation mechanism and generated viscosity in gravito-turbulent accretion disks". In: *Astronomy & Astrophysics* 640, A53.

Löhnert, L. and A. G. Peeters (2022). "Combined dynamo of gravitational and magneto-rotational instability in irradiated accretion discs". In: *Astronomy and Astrophysics* 663, A176.

— (2023). "The persistence of magneto-rotational turbulence in gravitationally turbulent accretion disks". In: *Astronomy and Astrophysics* 677, A173.

Lynden-Bell, D. and A. J. Kalnajs (1972). "On the generating mechanism of spiral structure". In: *Monthly Notices of the Royal Astronomical Society* 157.1, pp. 1–30.

Lynden-Bell, Donald (1969). "Galactic nuclei as collapsed old quasars". In: *Nature* 223, pp. 690–694.

Lynden-Bell, Donald and Jim E. Pringle (1974). "The evolution of viscous discs and the origin of the nebular variables". In: *Monthly Notices of the Royal Astronomical Society* 168.3, pp. 603–637.

Machida, Mami and Ryoji Matsumoto (2003). "Global three-dimensional magnetohydrodynamic simulations of black hole accretion disks: X-ray flares in the plunging region". In: *The Astrophysical Journal* 585.1, p. 429.

Martin, Rebecca G. and Stephen H. Lubow (2011). "The gravo-magneto limit cycle in accretion disks". In: *The Astrophysical Journal Letters* 740.1, p. L6.

Martin, Rebecca G. et al. (2012). "Dead zones around young stellar objects: FU Orionis outbursts and transition discs". In: *Monthly Notices of the Royal Astronomical Society* 423.3, pp. 2718–2725.

Masset, F. (2000). "FARGO: A fast eulerian transport algorithm for differentially rotating disks". In: *Astronomy & Astrophysics Supplement Series* 141.1, pp. 165–173.

Matsumoto, R. and T. Tajima (1995). *Magnetic viscosity by localized shear flow instability in magnetized accretion disks*. Tech. rep. Texas Univ., Austin, TX (United States). Inst. for Fusion Studies.

Meheut, Heloise et al. (2015). "Angular momentum transport and large eddy simulations in magnetorotational turbulence: the small Pm limit". In: *Astronomy & Astrophysics* 579, A117.

Menou, Kristen and Eliot Quataert (2001). "Ionization, magnetorotational, and gravitational instabilities in thin accretion disks around supermassive black holes". In: *The Astrophysical Journal* 552.1, p. 204.

Meru, Farzana and Matthew R. Bate (2012). "On the convergence of the critical cooling time-scale for the fragmentation of self-gravitating discs". In: *Monthly Notices of the Royal Astronomical Society* 427.3, pp. 2022–2046.

Michael, Scott et al. (2012). "Convergence studies of mass transport in disks with gravitational instabilities. I. The constant cooling time case". In: *The Astrophysical Journal* 746.1, p. 98.

Miller, Kristen A. and James M. Stone (2000). "The formation and structure of a strongly magnetized corona above a weakly magnetized accretion disk". In: *The Astrophysical Journal* 534.1, p. 398.

Mishra, Bhupendra et al. (2020). “Strongly magnetized accretion discs: structure and accretion from global magnetohydrodynamic simulations”. In: *Monthly Notices of the Royal Astronomical Society* 492.2, pp. 1855–1868.

Moffatt, Henry K. (1978). *Field generation in electrically conducting fluids*. Cambridge University Press.

Müller, Wolf-Christian, Shiva Kumar Malapaka, and Angela Busse (2012). “Inverse cascade of magnetic helicity in magnetohydrodynamic turbulence”. In: *Physical Review E* 85.1, p. 015302.

Nauman, Farrukh and Eric G. Blackman (2014). “On characterizing non-locality and anisotropy for the magnetorotational instability”. In: *Monthly Notices of the Royal Astronomical Society* 441.3, pp. 1855–1860.

Noble, Scott C., Julian H. Krolik, and John F. Hawley (2010). “Dependence of inner accretion disk stress on parameters: the schwarzschild case”. In: *The Astrophysical Journal* 711.2, p. 959.

Oishi, Jeffrey S. and Mordecai-Mark Mac Low (2011). “Magnetorotational turbulence transports angular momentum in stratified disks with low magnetic Prandtl number but magnetic Reynolds number above a critical value”. In: *The Astrophysical Journal* 740.1, p. 18.

O’Neill, Sean M. et al. (2011). “Low-frequency oscillations in global simulations of black hole accretion”. In: *The Astrophysical Journal* 736.2, p. 107.

Ostriker, Eve C., Frank H. Shu, and Fred C. Adams (1992). “Near-resonant excitation and propagation of eccentric density waves by external forcing”. In: *The Astrophysical Journal* 399, pp. 192–212.

Paardekooper, Sijme-Jan (2012). “Numerical convergence in self-gravitating shearing sheet simulations and the stochastic nature of disc fragmentation”. In: *Monthly Notices of the Royal Astronomical Society* 421.4, pp. 3286–3299.

Paczynski, B. (1978). “A model of selfgravitating accretion disk”. In: *Acta Astronomica* 28.2, pp. 91–109.

Papaloizou, J. C. B. and D. N. C. Lin (1995). “Theory of accretion disks I: Angular momentum transport processes”. In: *Annual Review of Astronomy and Astrophysics* 33.1, pp. 505–540.

Pessah, Martin E., Chi-kwan Chan, and Dimitrios Psaltis (2006). “The signature of the magnetorotational instability in the Reynolds and Maxwell stress tensors in accretion discs”. In: *Monthly Notices of the Royal Astronomical Society* 372.1, pp. 183–190.

Pouquet, A., U. Frisch, and J. Léorat (1976). “Strong MHD helical turbulence and the nonlinear dynamo effect”. In: *Journal of Fluid Mechanics* 77.2, pp. 321–354.

Prendergast, K. H. and G. R. Burbidge (1968). “On the nature of some galactic X-ray sources”. In: *The Astrophysical Journal* 151, p. L83.

Pringle, J. E. and M. J. Rees (1972). “Accretion disc models for compact X-ray sources”. In: *Astronomy & Astrophysics* 21, p. 1.

Pringle, James E. (1981). “Accretion discs in astrophysics”. In: *Annual Review of Astronomy and Astrophysics* 19.1, pp. 137–160.

Regev, Oded, Orkan M. Umurhan, and Philip A. Yecko (2016). *Modern fluid dynamics for physics and astrophysics*. Springer.

Rice, W. K. M., Giuseppe Lodato, and Philip J. Armitage (2005). “Investigating fragmentation conditions in self-gravitating accretion discs”. In: *Monthly Notices of the Royal Astronomical Society: Letters* 364.1, pp. L56–L60.

Rice, W. K. M. et al. (2003). "The effect of cooling on the global stability of self-gravitating protoplanetary discs". In: *Monthly Notices of the Royal Astronomical Society* 339.4, pp. 1025–1030.

Rice, W. K. M. et al. (2011). "Stability of self-gravitating discs under irradiation". In: *Monthly Notices of the Royal Astronomical Society* 418.2, pp. 1356–1362.

Riols, A. and H. Latter (2018a). "Magnetorotational instability and dynamo action in gravito-turbulent astrophysical discs". In: *Monthly Notices of the Royal Astronomical Society* 474.2, pp. 2212–2232.

— (2018b). "Spiral density waves and vertical circulation in protoplanetary discs". In: *Monthly Notices of the Royal Astronomical Society* 476.4, pp. 5115–5126.

— (2019). "Gravitoturbulent dynamos in astrophysical discs". In: *Monthly Notices of the Royal Astronomical Society* 482.3, pp. 3989–4008.

Riols, A., H. Latter, and S.-J. Paardekooper (2017). "Gravitoturbulence and the excitation of small-scale parametric instability in astrophysical discs". In: *Monthly Notices of the Royal Astronomical Society* 471.1, pp. 317–336.

Riols, A. et al. (2021). "Gravito-turbulence and dynamo in poorly ionized protostellar discs–I. Zero-net-flux case". In: *Monthly Notices of the Royal Astronomical Society* 506.1, pp. 1407–1426.

Roe, Philip L. (1981). "Approximate Riemann solvers, parameter vectors, and difference schemes". In: *Journal of Computational Physics* 43.2, pp. 357–372.

Ross, Johnathan, Henrik N. Latter, and Jerome Guilet (2016). "The stress–pressure relationship in simulations of MRI-induced turbulence". In: *Monthly Notices of the Royal Astronomical Society* 455.1, pp. 526–539.

Ryan, Benjamin R. et al. (2017). "Resolution dependence of magnetorotational turbulence in the isothermal stratified shearing box". In: *The Astrophysical Journal* 840.1, p. 6.

Saltzman, Jeff (1994). "An unsplit 3D upwind method for hyperbolic conservation laws". In: *Journal of Computational Physics* 115.1, pp. 153–168.

Salvesen, Greg et al. (2016). "Accretion disc dynamo activity in local simulations spanning weak-to-strong net vertical magnetic flux regimes". In: *Monthly Notices of the Royal Astronomical Society* 457.1, pp. 857–874.

Sanders, Richard, Eric Morano, and Marie-Claude Druguet (1998). "Multidimensional dissipation for upwind schemes: stability and applications to gas dynamics". In: *Journal of Computational Physics* 145.2, pp. 511–537.

Sano, Takayoshi and Shoken M. Miyama (1999). "Magnetorotational instability in protoplanetary disks. I. On the global stability of weakly ionized disks with ohmic dissipation". In: *The Astrophysical Journal* 515.2, p. 776.

Sano, Takayoshi and James M. Stone (2002). "The effect of the Hall term on the nonlinear evolution of the magnetorotational instability. II. Saturation level and critical magnetic Reynolds number". In: *The Astrophysical Journal* 577.1, p. 534.

Sano, Takayoshi et al. (2004). "Angular momentum transport by magnetohydrodynamic turbulence in accretion disks: gas pressure dependence of the saturation level of the magnetorotational instability". In: *The Astrophysical Journal* 605.1, p. 321.

Schutz, Bernard F. (2009). *A first course in general relativity*. 2nd ed. Cambridge University Press.

Shakura, N. (2018). *Accretion flows in astrophysics*. Ed. by N. Shakura. Vol. 454. Springer.

Shakura, N. I. and Rashid Alievich Sunyaev (1973). "Black holes in binary systems. Observational appearance." In: *Astronomy & Astrophysics* 24, pp. 337–355.

Shi, Ji-Ming and Eugene Chiang (2014). "Gravito-turbulent disks in three dimensions: Turbulent velocities versus depth". In: *The Astrophysical Journal* 789.1, p. 34.

Shi, Ji-Ming, James M. Stone, and Chelsea X. Huang (2016). "Saturation of the magnetorotational instability in the unstratified shearing box with zero net flux: convergence in taller boxes". In: *Monthly Notices of the Royal Astronomical Society* 456.3, pp. 2273–2289.

Shi, Jiming, Julian H. Krolik, and Shigenobu Hirose (2010). "What is the numerically converged amplitude of magnetohydrodynamics turbulence in stratified shearing boxes?" In: *The Astrophysical Journal* 708.2, p. 1716.

Shields, Gregory A. (1999). "A brief history of active galactic nuclei". In: *Publications of the Astronomical Society of the Pacific* 111.760, p. 661.

Simon, Jacob B., Kris Beckwith, and Philip J. Armitage (2012). "Emergent mesoscale phenomena in magnetized accretion disc turbulence". In: *Monthly Notices of the Royal Astronomical Society* 422.3, pp. 2685–2700.

Simon, Jacob B. and John F. Hawley (2009). "Viscous and resistive effects on the magnetorotational instability with a net toroidal field". In: *The Astrophysical Journal* 707.1, p. 833.

Simon, Jacob B., John F. Hawley, and Kris Beckwith (2011). "Resistivity-driven state changes in vertically stratified accretion disks". In: *The Astrophysical Journal* 730.2, p. 94.

Simon, Jacob B. et al. (2013). "Turbulence in the outer regions of protoplanetary disks. I. Weak accretion with no vertical magnetic flux". In: *The Astrophysical Journal* 764.1, p. 66.

Simon, Jacob B. et al. (2015). "Magnetically driven accretion in protoplanetary discs". In: *Monthly Notices of the Royal Astronomical Society* 454.1, pp. 1117–1131.

Sorathia, Kareem A. et al. (2012). "Global simulations of accretion disks. I. Convergence and comparisons with local models". In: *The Astrophysical Journal* 749.2, p. 189.

Stamatellos, Dimitris and Anthony P. Whitworth (2008). "Can giant planets form by gravitational fragmentation of discs?-Radiative hydrodynamic simulations of the inner disc region (40 AU)". In: *Astronomy & Astrophysics* 480.3, pp. 879–887.

— (2009). "The role of thermodynamics in disc fragmentation". In: *Monthly Notices of the Royal Astronomical Society* 400.3, pp. 1563–1573.

Steenbeck, Max, Fritz Krause, and K.-H. Rädler (1966). "Berechnung der mittleren Lorentz-Feldstärke für ein elektrisch leitendes Medium in turbulenter, durch Coriolis-Kräfte beeinflußter Bewegung". In: *Zeitschrift für Naturforschung A* 21.4, pp. 369–376.

Stone, James M. and Thomas A. Gardiner (2010). "Implementation of the shearing box approximation in Athena". In: *The Astrophysical Journal Supplement Series* 189.1, p. 142.

Stone, James M. et al. (1996). "Three-dimensional magnetohydrodynamical simulations of vertically stratified accretion disks". In: *The Astrophysical Journal* 463, p. 656.

Stone, James M. et al. (2008). "Athena: a new code for astrophysical MHD". In: *The Astrophysical Journal Supplement Series* 178.1, p. 137.

Suzuki, Takeru K. and Shu-ichiro Inutsuka (2009). "Disk winds driven by magnetorotational instability and dispersal of protoplanetary disks". In: *The Astrophysical Journal Letters* 691.1, p. L49.

Suzuki, Takeru K. and Shu-ichiro Inutsuka (2014). "Magnetohydrodynamic simulations of global accretion disks with vertical magnetic fields". In: *The Astrophysical Journal* 784.2, p. 121.

Teissier, Jean-Mathieu and Wolf-Christian Müller (2021). "Inverse transfer of magnetic helicity in direct numerical simulations of compressible isothermal turbulence: scaling laws". In: *Journal of Fluid Mechanics* 915, A23.

Tennekes, Hendrik and John Leask Lumley (1972). *A first course in turbulence*. MIT press.

Toomre, Alar (1964). "On the Gravitational Stability of A Disk of Stars". In: *The Astrophysical Journal* 139, pp. 1217–1238.

— (1969). "Group velocity of spiral waves in galactic disks". In: *The Astrophysical Journal* 158, p. 899.

— (1981). "What amplifies the spirals". In: *Structure and evolution of normal Galaxies*. Cambridge University Press, pp. 111–136.

Toro, Eleuterio F. (2009). *Riemann solvers and numerical methods for fluid dynamics: a practical introduction*. 3rd ed. Springer.

Turner, N. J. (2004). "On the Vertical Structure of Radiation-dominated Accretion Disks". In: *The Astrophysical Journal* 605.1, p. L45.

Turner, N. J., T. Sano, and N. Dziourkevitch (2007). "Turbulent mixing and the dead zone in protostellar disks". In: *The Astrophysical Journal* 659.1, p. 729.

Vanon, Riccardo (2018). "The role of zonal flows in disc gravito-turbulence". In: *Monthly Notices of the Royal Astronomical Society* 477.3, pp. 3683–3693.

Vishniac, Ethan T. (2009). "The saturation limit of the magnetorotational instability". In: *The Astrophysical Journal* 696.1, p. 1021.

Walker, Justin, Geoffroy Lesur, and Stanislav Boldyrev (2016). "On the nature of magnetic turbulence in rotating, shearing flows". In: *Monthly Notices of the Royal Astronomical Society: Letters* 457.1, pp. L39–L43.

Wardle, Mark (1999). "The Balbus-Hawley instability in weakly ionized discs". In: *Monthly Notices of the Royal Astronomical Society* 307.4, pp. 849–856.

Young, Matthew D. and Cathie J. Clarke (2015). "Dependence of fragmentation in self-gravitating accretion discs on small-scale structure". In: *Monthly Notices of the Royal Astronomical Society* 451.4, pp. 3987–3994.

Zhu, Zhaohuan, Lee Hartmann, and Charles Gammie (2009). "Nonsteady accretion in protostars". In: *The Astrophysical Journal* 694.2, p. 1045.

— (2010). "Long-term evolution of protostellar and protoplanetary disks. II. Layered accretion with infall". In: *The Astrophysical Journal* 713.2, p. 1143.

Zhu, Zhaohuan and James M. Stone (2018). "Global evolution of an accretion disk with a net vertical field: coronal accretion, flux transport, and disk winds". In: *The Astrophysical Journal* 857.1, p. 34.

Ziegler, Udo and Günther Rüdiger (2001). "Shear rate dependence and the effect of resistivity in magneto-rotationally unstable, stratified disks". In: *Astronomy & Astrophysics* 378.2, pp. 668–678.

Zier, Oliver and Volker Springel (2023). "Gravito-turbulence in local disc simulations with an adaptive moving mesh". In: *Monthly Notices of the Royal Astronomical Society* 520.2, pp. 3097–3116.

Chapter 6

List of all Publications

Listed here are all my works, published in, or submitted to scientific journals.

▷ Löhnert, L., Krätschmer, S. & Peeters, A. G., 2020, Astronomy & Astrophysics, 640, A53
Title: "Saturation Mechanism and Generated Viscosity in Gravito-turbulent Accretion Disks"

URL: `https://www.aanda.org/articles/aa/abs/2020/08/aa38023-20/aa38023-20.html` (as of 25.05.2023)

See LPK20, Sect. 7.

▷ Löhnert, L. & Peeters, A. G., 2022, Astronomy & Astrophysics, 663, A176
Title: "Combined Dynamo of Gravitational and Magneto-Rotational Instability in Irradiated Accretion Disks"

URL: `https://doi.org/10.1051/0004-6361/202142121` (as of 25.05.2023)

See LP22, Sect. 8.

▷ Löhnert, L. & Peeters, A. G., 2023, Astronomy & Astrophysics, 677, A173
Title: "The Persistence of Magneto-Rotational Turbulence in Gravitationally-turbulent Accretion Disks"

URL: `https://doi.org/10.1051/0004-6361/202244608` (as of 14.10.2023)

See LP23, Sect. 9.

Chapter 7

Saturation Mechanism and Generated Viscosity in Gravito-Turbulent Accretion Disks

L. Löhnert, S. Krätschmer, and A. G. Peeters

This chapter has been published in the journal Astronomy & Astrophysics:

Credit: Löhnert, L., Krätschmer, S. & Peeters, A. G., Astronomy & Astrophysics, 640, A53, 2020, reproduced with permission © ESO
URL: `https://www.aanda.org/articles/aa/abs/2020/08/aa38023-20/aa38023-20.html`
(as of 25.05.2023)

A&A 640, A53 (2020)
https://doi.org/10.1051/0004-6361/202038023

Astronomy & Astrophysics

Saturation mechanism and generated viscosity in gravito-turbulent accretion disks

L. Löhnert[1], S. Krätschmer[2], and A. G. Peeters[1]

[1] Physics Department of Bayreuth, Universitätsstraße 30, Bayreuth, Germany
e-mail: lucas.loehnert@uni-bayreuth.de
[2] Alfred Wegener Institute, Helmholtz Centre for Polar and Marine Research, Bremerhaven, Germany

Received 25 March 2020 / Accepted 6 June 2020

ABSTRACT

Here, we address the turbulent dynamics of the gravitational instability in accretion disks, retaining both radiative cooling and irradiation. Due to radiative cooling, the disk is unstable for all values of the Toomre parameter, and an accurate estimate of the maximum growth rate is derived analytically. A detailed study of the turbulent spectra shows a rapid decay with an azimuthal wave number stronger than k_y^{-3}, whereas the spectrum is more broad in the radial direction and shows a scaling in the range k_x^{-3} to k_x^{-2}. The radial component of the radial velocity profile consists of a superposition of shocks of different heights, and is similar to that found in Burgers' turbulence. Assuming saturation occurs through nonlinear wave steepening leading to shock formation, we developed a mixing-length model in which the typical length scale is related to the average radial distance between shocks. Furthermore, since the numerical simulations show that linear drive is necessary in order to sustain turbulence, we used the growth rate of the most unstable mode to estimate the typical timescale. The mixing-length model that was obtained agrees well with numerical simulations. The model gives an analytic expression for the turbulent viscosity as a function of the Toomre parameter and cooling time. It predicts that relevant values of $\alpha = 10^{-3}$ can be obtained in disks that have a Toomre parameter as high as $Q \approx 10$.

Key words. accretion, accretion disks – protoplanetary disks – hydrodynamics – instabilities – turbulence

1. Introduction

Self-gravity in accretion disks can lead to gravitational instability (GI), which was originally studied in the context of galaxies (Toomre 1964; Lin & Shu 1964; Lynden-Bell & Kalnajs 1972), but is relevant also for accretion disks around young stellar objects and protoplanetary disks (YSOs; PPDs) (Gammie 2001; Kratter & Lodato 2016). The gravitational instability sets in when the Toomre parameter,

$$Q = \frac{c_s \kappa}{\pi G \Sigma}, \tag{1}$$

is smaller than one ($Q < 1$) (Toomre 1964). Here, c_s is the sound speed, Σ is the mass surface density, and κ is the epicyclic frequency, or the angular frequency ($\kappa = \Omega_0$) in the case of a Keplerian disk. The Toomre parameter expresses that a higher temperature (or equivalently a higher sound speed) will stabilize the disk, whereas a higher surface density (Σ) has a destabilizing effect (Kratter & Lodato 2016; Lin & Kratter 2016). Additional physics has been considered since the original derivation, and it has been shown that radiative cooling and viscosity can destabilize the disk for $Q > 1$ (Lin & Kratter 2016).

Numerical simulations have clarified some aspects of the nonlinear evolution of the gravitational instability. In the case of sufficiently fast cooling, fragmentation occurs (Johnson & Gammie 2003; Rice et al. 2003, 2005; Kratter & Murray-Clay 2011; Booth & Clarke 2019), which may be relevant for the formation of massive exoplanets. If the cooling is less efficient, a gravito-turbulent state is obtained, in which the radiation losses are compensated by the heating of the disk through dissipation in shocks (Gammie 2001; Kratter & Lodato 2016). Hence, cooling strongly effects the nonlinear saturation of the gravitational instability (Cossins et al. 2009), and different implementations of the cooling prescription have been tested. These include the so-called β cooling prescription (Gammie 2001), an irradiated version of this latter model (Rice et al. 2011; Baehr & Klahr 2015), and also the solution of the full radiative transfer problem (Hirose & Shi 2019).

One major quality of gravito-turbulence is its ability to transport angular momentum, leading to accretion. A common measure for the angular momentum transport through turbulence is the α-parameter (Shakura & Sunyaev 1973). In a stationary state, the turbulent dissipation connected with the effective viscosity described by the α parameter is then balanced by the energy loss through radiation ($\langle U \rangle / \tau_c$, where τ_c is the cooling timescale on which the thermal energy is lost), yielding (Gammie 2001; Rice et al. 2011)

$$\alpha \approx \frac{4}{9\gamma(\gamma-1)\tau_c \Omega_0}\left(1 - \frac{U_0}{\langle U \rangle}\right), \tag{2}$$

where γ is the adiabatic index, U_0 the stationary energy density obtained in the absence of turbulence through the combination of irradiation and radiation loss, and $\langle U \rangle$ is the averaged energy density in the presence of turbulence. Although the relation above is a powerful restriction on α, it does not allow a direct prediction because the averaged energy density $\langle U \rangle$ is not a priori known. As $U_0/\langle U \rangle \approx Q_0^2/\langle Q \rangle^2$, a prediction of α is possible when the Toomre parameter of the saturated turbulent state ($\langle Q \rangle$) is known. It is generally accepted that saturation occurs close to marginal stability $\langle Q \rangle \approx 1$ (Kratter & Lodato 2016). However, simulations suggest saturated values higher than one ($1 \lesssim \langle Q \rangle \lesssim 2$) (Rice et al. 2011; Vanon 2018), and those are

often associated to the effects of nonaxisymmetric instabilities (Kratter & Lodato 2016; Vanon & Ogilvie 2016; Vanon 2018).

The goal of this paper is to study the nonlinear gravito-turbulent state, and to develop an analytic prediction for $\langle Q \rangle$ and α in the case of an irradiated disk. In Sect. 2 the basic model equations and assumptions used for the study are outlined. Section 3 presents a linear stability analysis, and Sect. 4 gives a short overview of the numerical tool *DiskFlow* including certain benchmarks. Section 5 analyses the nonlinear state, after which the analytic model based on a mixing length approach is introduced in Sect. 6. Section 7 derives some predictions of the analytic model, and conclusions are drawn in Sect. 8.

2. The model

The evolution of the disk is described with the local two-dimensional shearing sheet approximation (Goldreich & Lynden-Bell 1965; Balbus & Hawley 1998; Gammie 2001). The model equations consist of the continuity equation, Euler's equation, the evolution equation for the internal energy density (U), and a Poisson equation for the gravitational potential (Φ) due to the mass density in the disk:

$$\partial_t \Sigma + \nabla \cdot (\Sigma \boldsymbol{v}) = 0 \tag{3a}$$

$$\partial_t \boldsymbol{v} + (\boldsymbol{v} \cdot \nabla)\, \boldsymbol{v} = -\frac{1}{\Sigma} \nabla P - 2\boldsymbol{\Omega}_0 \times \boldsymbol{v} + 3\Omega_0^2 x \boldsymbol{e}_x - \nabla \Phi \tag{3b}$$

$$\partial_t U + (\boldsymbol{v} \cdot \nabla)\, U = -\gamma U\, (\nabla \cdot \boldsymbol{v}) - \frac{U - U_0}{\tau_c} \tag{3c}$$

$$\nabla^2 \Phi = 4\pi G \Sigma \cdot \delta(z). \tag{3d}$$

In the equations above, $\boldsymbol{v}$ is the fluid velocity, G is the gravitational constant, and P is the pressure, with the latter linked to the internal energy density (U) through the equation of state

$$P = (\gamma - 1) U. \tag{4}$$

The shearing box coordinates (x, y) used in the equations above represent the radial x and azimuthal y direction. The forces per unit mass on the right hand side of the Euler equation, Eq. (3b), include the pressure gradient and the Coriolis, tidal, and self-gravitational forces in that order. The equilibrium is given by a uniform surface mass density (Σ_0) and uniform internal energy density (U_0). This equilibrium incorporates the shear in the Keplerian velocity profile $\boldsymbol{v}_0 = -3\Omega_0 x \boldsymbol{e}_y/2$, which develops through a balance of the Coriolis ($-2\boldsymbol{\Omega}_0 \times \boldsymbol{v}$) and tidal ($3\Omega_0^2 x \boldsymbol{e}_x$) force.

For consistency with the literature (e.g., Gammie 2001) the adiabatic index is chosen as $\gamma = 2$, which agrees with the two-dimensional nature of the system. A model equation for the internal energy rather than an adiabatic closing relation for the pressure ($P = \text{const.} \cdot \Sigma^\gamma$) is necessary, because the β-cooling prescription to mimic the loss of thermal energy due to radiation (Gammie 2001) is applied. Therein, $\beta = \tau_c \Omega_0$ is the dimensionless cooling timescale. The cooling term incorporates a fiducial thermal energy density, U_0, that the system would obtain in the absence of turbulence. Here, U_0 is motived by the irradiation of the disk by the young star (see e.g., Rice et al. 2011), which, in combination with the radiation losses from the disk, leads to a floor in the thermal energy density.

The equilibrium values Σ_0 and U_0 also define initial values for the Toomre parameter (Q_0) and sound speed $c_{s,0}$, defined as

$$c_s^2 = \gamma \frac{P}{\Sigma} = \gamma(\gamma - 1) \frac{U}{\Sigma}. \tag{5}$$

3. Linear stability in the presence of cooling

The Toomre stability criterion $Q > 1$ was derived assuming the gas behaves adiabatically or barotropically, and expresses the fact that the gas pressure has a stabilizing effect. It is therefore natural to assume that radiative cooling leads to further destabilization and indeed this has been found (see e.g., Lin & Kratter 2016). As the linear instability plays a role for the nonlinear saturated state, it is investigated in some detail in this section.

The model equations of the previous section are linearised around the equilibrium $(\Sigma_0, U_0, \boldsymbol{v}_0 = -(3/2)\Omega_0 x \boldsymbol{e}_y), \Phi = 0$,

$$U = U_0 + \tilde{U}, \tag{6a}$$

$$\Sigma = \Sigma_0 + \tilde{\Sigma}, \tag{6b}$$

$$\boldsymbol{v} = -\frac{3}{2}\Omega_0 x \boldsymbol{e}_y + \tilde{v}_x \boldsymbol{e}_x + \tilde{v}_y \boldsymbol{e}_y, \tag{6c}$$

$$\Phi = \tilde{\Phi}, \tag{6d}$$

whereby the tilde denotes a perturbed quantity. Neglecting all quadratic terms in the perturbations then gives a set of equations for the evolution of the perturbations:

$$\partial_t \tilde{\Sigma} + \Sigma_0 \partial_x \tilde{v}_x = 0, \tag{7a}$$

$$\partial_t \tilde{v}_x + \frac{\gamma - 1}{\Sigma_0} \partial_x \tilde{U} - 2\Omega_0 \tilde{v}_y + \partial_x \tilde{\Phi} = 0, \tag{7b}$$

$$\partial_t \tilde{v}_y + \frac{\Omega_0}{2} \tilde{v}_x = 0, \tag{7c}$$

$$\partial_t \tilde{U} + \gamma U_0 \partial_x \tilde{v}_x + \frac{\tilde{U}}{\tau_c} = 0, \tag{7d}$$

where the perturbations have been assumed to be axisymmetric. Substituting $\tilde{f} = \hat{f} \cdot \exp(gt + ikx)$ for all perturbed quantities (f) yields a set of algebraic equations from which the dispersion relation is obtained:

$$g^2 = -\Omega_0^2 + \frac{2 c_{s,0} \Omega_0}{Q_0} k - \frac{c_{s,0}^2 \tau_c g}{1 + \tau_c g} k^2. \tag{8}$$

The dispersion relation is similar to that found by Lin & Kratter (2016). Solutions for the growth rate as function of the wave vector for different values of Q_0 and a normalized cooling time, $\beta \equiv \tau_c \Omega_0 = 10$, are shown in Fig. 1.

Taking the limit $\beta = \tau_c \Omega_0 \to \infty$ fully recovers the classical Toomre case with the known stability limit $Q_0 > 1$. However, for finite β it follows from the dispersion relation that unstable modes occur for all values of Q_0. The k domain is divided into two regions, with instability only occurring for $k > Q_0/2$ as larger structures (smaller wave numbers) are stabilized by the Coriolis force. One might expect large wave numbers (small structures) to be stabilized as well because the critical Jeans mass cannot be met. However, the cooling extracts the excess thermal energy that is generated by the compression of the fluid, and exponential growth is obtained on timescales that are sufficiently long for this cooling to be effective. This is expressed in Eq. (8) through the occurrence of $\tau_c g$ in the stabilizing term connected with the pressure response. Therefore, the observation that the value of the Toomre parameter of the saturated turbulent state is larger than one ($\langle Q \rangle > 1$) does not imply linear stability. Although, it should be mentioned that the instability for Q_0 might sensitively depend on the exact choice of the cooling model (see Lin & Kratter 2016, and the discussion in Sect. 7).

The fastest growing mode can be obtained by taking the partial derivative of the dispersion relation towards k and setting

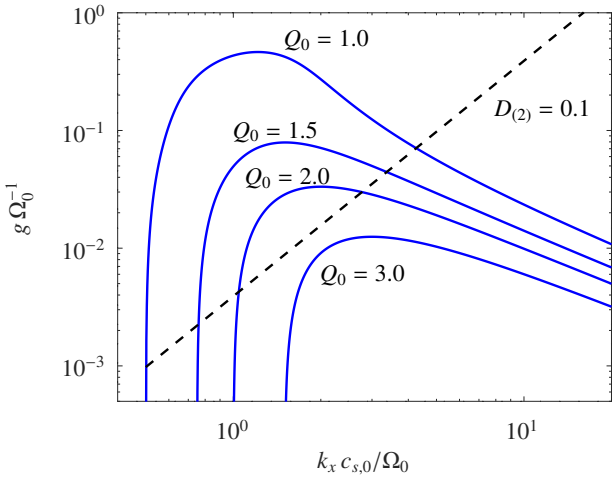

Fig. 1. Linear growth rate g as a function of the radial wave number k_x for different equilibrium Toomre values Q_0 and a cooling time $\beta = \tau_c\Omega_0 = 10$. The straight dotted line gives the damping rate in numerical simulations ($\propto k^2$) for a damping coefficient $D_{(2)} = 0.1$ (see Sect. 4).

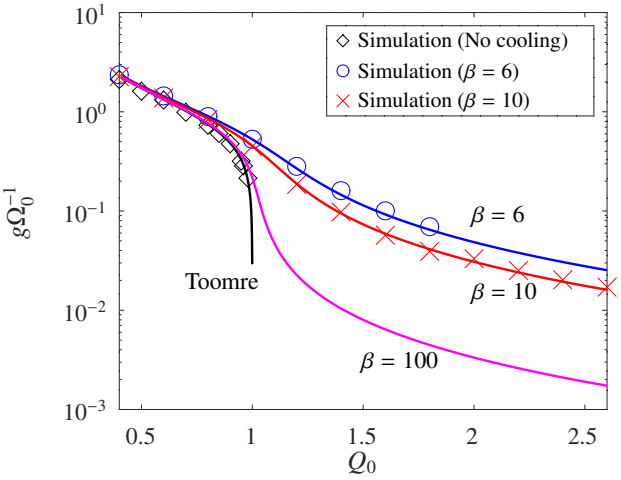

Fig. 2. Analytically obtained growth rates of the most unstable modes, depicted as solid lines. The symbols ∘, ×, and ⋄ correspond to simulations with $\beta = \tau_c\Omega_0 = 6, 10$ and no cooling respectively. The classical Toomre case (no cooling) prevents stability for $Q_0 > 1$. The cooled cases are unstable for all Q_0.

$\partial g/\partial k = 0$ to obtain

$$\frac{k_M c_{s0}}{\Omega_O} = \frac{1+\tau_c g}{Q_0 \tau_c g}. \tag{9}$$

Substituting this back into Eq. (8) leads to a cubic polynomial in g only

$$\left(\frac{g}{\Omega_0}\right)^3 - \left(\frac{1}{Q_0^2} - 1\right)\frac{g}{\Omega_0} - \frac{1}{\beta Q_0^2} = 0. \tag{10}$$

Solutions of this equation are shown as solid lines in Fig. 2 for cooling times $\beta \in \{6, 10, 100, \infty\}$. The last case ($\beta \to \infty$) is the classical Toomre criterion without cooling. The analytic expression of the solution $g(k)$ is somewhat extensive, but here the interest is mostly for cases with $Q_0 > 1$ for which the growth rate is relatively small. In this case, the first term in Eq. (10) can be neglected against the second, and one readily obtains

$$\frac{g}{\Omega_0} = \frac{1}{\beta}\frac{1}{Q_0^2 - 1} \qquad \frac{k_M c_{s0}}{\Omega_0} = Q_0, \tag{11}$$

where the maximum wave vector is obtained by inserting the estimate for the growth rate in Eq. (9). The result of Eq. (11) is relatively simple and therefore an easy-to-use estimate of the growth rate that works well for $Q \gtrsim 1.2$. The wave vector is surprising as one usually finds $kc_{s0}/\Omega_0 = 1/Q_0$ according to the classical Toomre criterion in the absence of cooling. The latter is equivalent to a Jeans criterion, stating that for smaller mass densities (larger Q_0) one needs a larger volume (size $\propto 1/k$) to reach the critical mass. In fact, the result in Eq. (11) is assumed to hold for small g. It turns out that for $g\beta >> 1$ one actually finds $kc_{s0}/\Omega_0 = 1/Q_0$ as for the case without cooling. This backs up the above given interpretation that, for a given Q_0, the growth rate is sufficiently small in comparison to $1/\beta$ to allow further collapse.

4. Code and benchmarking

The simulations presented here use the code *DiskFlow*[1] which is a grid-based finite-difference code. The equations solved are the two-dimensional compressible fluid equations outlined above. The fluid equations are integrated using a fourth-order Runge-Kutta method. *DiskFlow* assumes shearing periodic boundary conditions, with the box being periodic in azimuthal y-direction and sheared periodic in the radial x-direction (see e.g., Balbus & Hawley 1998). The Poisson equation for self-gravity is solved using a Fourier transform (Gammie 2001). At each time-step the surface density Σ is transformed to Fourier space $\hat{\Sigma}_{\boldsymbol{k}}$, and the Fourier amplitude of the gravitational potential ($\hat{\Phi}$) is updated through

$$\hat{\Phi}_{\boldsymbol{k}} = -\frac{2\pi G}{k}\hat{\Sigma}_{\boldsymbol{k}}, \tag{12}$$

where $k := |\boldsymbol{k}|$ and $\boldsymbol{k} = (k_x, k_y)$ is the two-dimensional wave vector. The gravitational potential in real space is then obtained through a backward transformation. To avoid difficulties with the Fourier transform in combination with the shearing periodic boundary conditions, a back mapping of the surface mass density, undoing the effect of the shearing and ensuring the solution is periodic in both directions, is performed before the Fourier transform is calculated. Furthermore, a cut-off wave vector $|\boldsymbol{k}|_{\max} = \frac{1}{\sqrt{2}}\min(\frac{\pi N_x}{L_x}, \frac{\pi N_y}{L_y})$ is introduced, following (Gammie 2001). The cut-off acts as a smoothing factor for small-scale gravity. Although this is possibly problematic for cases with clumping (see e.g., Young & Clarke 2015) it has been shown to work well for the gravito-turbulent state.

An artificial viscous pressure is included in *DiskFlow* to guarantee numerical stability

$$P_{\text{vis}} = \zeta\Sigma(\nabla\cdot\boldsymbol{v})^2. \tag{13}$$

This artificial viscous pressure is especially useful in the case of shocks (see e.g., Gammie 2001), as it acts as a viscosity that responds to volumetric changes in the fluid. Moreover, it does not extract energy from the system, as the dissipated kinetic energy is consistently transferred to thermal energy. For the simulations shown here, $\zeta = 0.006$ is chosen.

The code also provides the possibility of using artificial viscosity, which is implemented as a second-order diffusion scheme. More precisely, all of the Eqs. (3a)–(3c) contain an additional dissipative term (second spatial derivatives):

$$\partial_t f + \cdots = \cdots + D_{(2)}(\triangle x)\nabla^2 f, \tag{14}$$

[1] For more details as well as the source code see https://bitbucket.org/astro_bayreuth/accretion-disk-flow/src/master/

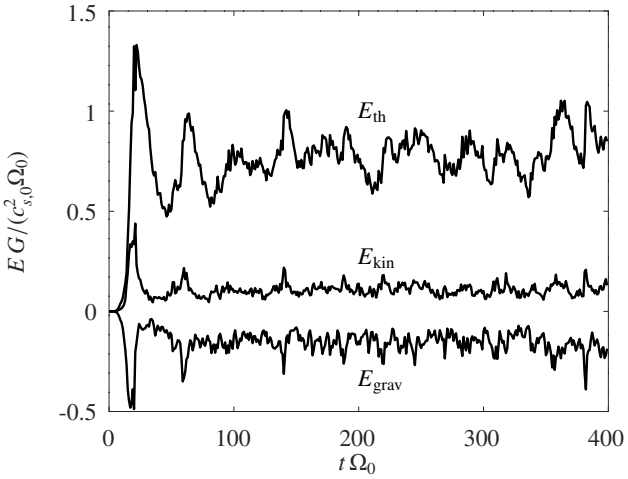

Fig. 3. Temporal evolution of the averaged perturbed energy densities for a simulation with $Q_0 = 1$ and $\beta = 10$. Shown are the mean thermal energy density $E_{\rm th}$, the mean kinetic energy density $E_{\rm kin}$, and the mean gravitational potential energy density $E_{\rm grav}$, as defined in Eq. (16).

with a damping coefficient $D_{(2)}$ and resolution $\triangle x = L/N$. Typical values used for the simulations are $D_{(2)} \sim \{0.07{-}0.8\}$. Empirically, it is found that $D_{(2)} \leq 0.1$ is problematic as small-scale perturbations cannot be damped sufficiently and the simulation might eventually become numerically unstable. The coefficient $D_{(2)}$ is made variable in time in order to capture the violent transition from the linear growth phase to the nonlinearly saturated state. In this latter state, the damping coefficient is kept as low as possible. By construction, the damping predominantly acts on small scales (i.e., roughly grid-scale).

All quantities have been made dimensionless using the angular frequency (Ω_0), the sound speed at initialisation (c_{s0}), and the gravitational constant G. With this choice the surface mass density is normalized with $\Sigma_{\rm ch} = c_{s,0}\Omega_0/G$, the internal energy density with $U_{\rm ch} = c_{s,0}^2\Omega_0/G$, and the gravitational potential with $\Phi_{\rm ch} = c_{s,0}^2$. Furthermore, the characteristic length scale $L_{\rm ch} = c_{s,0}/\Omega_0$ is equal to the disk scale height, $L_{\rm ch} = H$, that would be obtained if the vertical force balance were considered. Timescales are normalized with the characteristic time $t_{\rm ch} = \Omega_0^{-1}$, which is consistent with the dimensionless cooling parameter, $\beta \equiv \tau_c\Omega_0$, used before. Unless stated otherwise, all quantities below are dimensionless.

As one of the code benchmarks, the growth rate of the most unstable mode is calculated as a function of the Toomre parameter (Q_0) for different normalized cooling times (β). The numerical results, shown in Fig. 2, are in excellent agreement with the analytic formula obtained in Sect. 3. The simulations use a box size comparable to the analytically derived wavelength of the fastest growing mode and are initialised with random density perturbations. The growth rates are then determined for an interval of exponential growth $t_1 < t < t_2$, using

$$g = \frac{\ln\left(\frac{\langle\tilde{\Sigma}_2^2\rangle}{\langle\tilde{\Sigma}_1^2\rangle}\right)}{2(t_2 - t_1)}. \tag{15}$$

Figure 3 shows that a stationary turbulent state is obtained in the simulations and gives the time evolution of the box-averaged perturbed kinetic, gravitational, and thermal energy densities:

Table 1. Specifications of the example simulation.

Quantity-name	Value
N (grid points)	768
$L_x H^{-1} = L_y H^{-1}$ (box length)	30
Q_0 (Toomre at initialisation)	1.0
$\beta = \tau_c\,\Omega_0$ (cooling time)	10

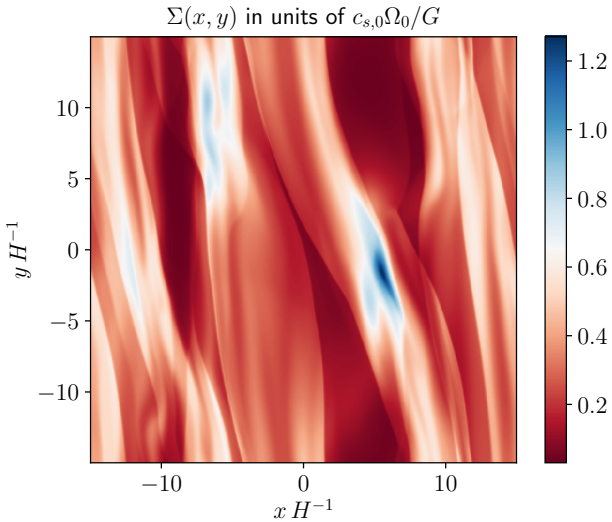

Fig. 4. Snapshot of the surface density $\Sigma(x, y)$ at time $t = 200$ for a simulation with $Q_0 = 1$ and $\beta = 10$.

$$E_{\rm kin} = \frac{1}{2}\langle\Sigma(\tilde{v_x}^2 + \tilde{v_y}^2)\rangle \tag{16}$$
$$E_{\rm th} = \langle U - U_0\rangle = \langle U\rangle - U_0 = \tilde{U}$$
$$E_{\rm grav} = \frac{1}{2}\langle\Sigma\cdot\phi\rangle.$$

The corresponding simulation parameters are specified in Table 1. The corresponding surface density $\Sigma(x, y)$ and radial velocity $v_x(x, y)$ at $t = 200$ for this simulation are shown in Figs. 4 and 5, respectively. As can be inferred from the images, the system is subject to shock formation. The shocks provide the mechanism for dissipating kinetic energy and to increase the thermal energy which is then lost through radiative cooling.

The α parameter is directly linked to the xy-component of the total stress (S_{xy}). Here, the definition of Ref. (Gammie 2001) is used

$$\alpha = \frac{2\langle S_{xy}\rangle}{3\langle\Sigma c_s^2\rangle} = \frac{2\langle S_{xy}\rangle}{3\gamma(\gamma-1)\langle U\rangle}, \tag{17}$$

where the average $\langle\ldots\rangle$ is over both the simulation domain and time. The total stress consists of the Reynolds and Gravitational stress $S_{xy} = S_{xy}^{(R)} + S_{xy}^{(G)}$, with

$$S_{xy}^{(R)} = \Sigma\,\tilde{v}_x\tilde{v}_y \quad \text{(Reynolds)}, \tag{18}$$
$$S_{xy}^{(G)} = \frac{1}{4\pi}\int_{-\infty}^{\infty}(\partial_x\Phi\cdot\partial_y\Phi)\,{\rm d}z \quad \text{(gravitation)}$$
$$= \sum_{\boldsymbol{k}}\frac{k_x\,k_y}{4\pi|\boldsymbol{k}|}|\hat{\Phi}_{\boldsymbol{k}}|^2.$$

(For a derivation of the gravitational stress, see e.g., Lynden-Bell & Kalnajs 1972). A stringent benchmark for the nonlinear

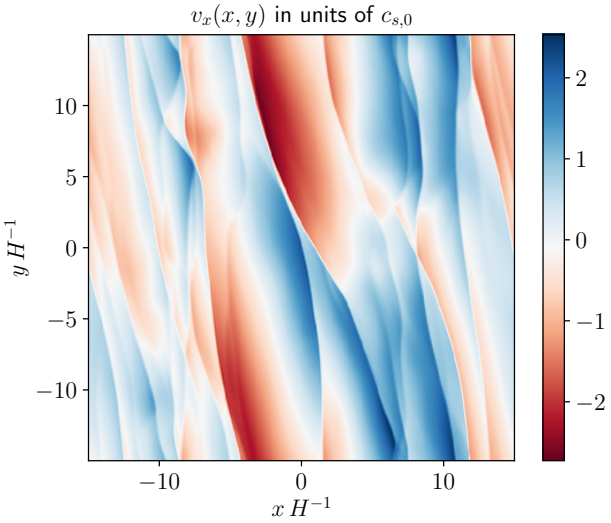

Fig. 5. Snapshot of the radial velocity $v_x(x, y)$ at time $t = 200$ for a simulation with $Q_0 = 1$ and $\beta = 10$.

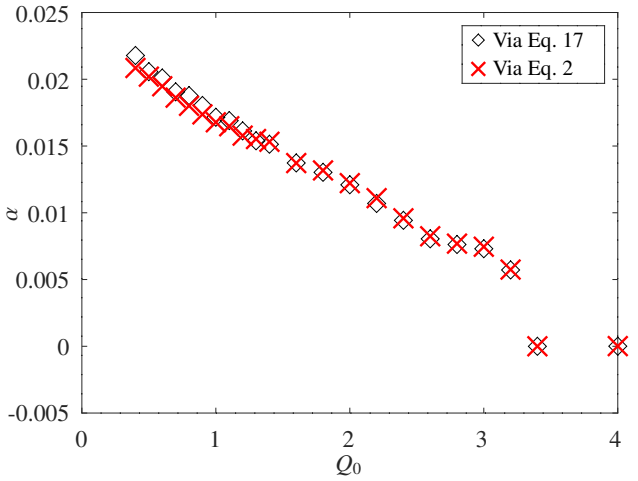

Fig. 6. α-values obtained via two different approaches. Values of α directly obtained from the simulations via averaging of the stresses over both the box and time, according to Eq. (17) ($\diamond$). The values of α were obtained via Eq. (2) ($\times$). All simulations use $\beta = 10$ and the sizes of time averaging intervals are chosen in the range 100–400.

saturated stated is then provided by Eq. (2), which links α to the averaged internal energy $\langle U \rangle$, which can be directly measured in the simulations. The two methods are compared in Fig. 6, which shows that they agree very well. As Eq. (2) is derived from energy conservation, the agreement between the two methods of determining α shows that energy conservation is adequately satisfied numerically.

5. Nonlinear state

To better understand the nature of the gravito-turbulent state, in this section, the nonlinear saturated state is investigated in some detail. Important insights can be obtained through the study of the power spectra in Fourier space. The power spectrum of the perturbed mass surface density $|\hat{\Sigma}(k_x, k_y)|^2$, where $\hat{\Sigma}(k_x, k_y)$ is the Fourier amplitude, is shown in Fig. 7 as a function of the wave vector $\boldsymbol{k} = (k_x, k_y)$. This spectrum is obtained by averaging over a time interval of $\Delta t = 400$ of the fully developed turbulent state.

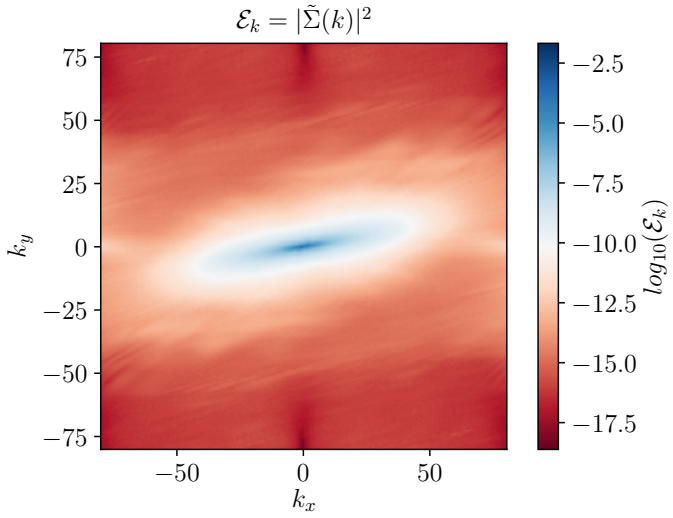

Fig. 7. Two-dimensional power spectrum of the surface density $\mathcal{E}_k(k_x, k_y)$ for the case $Q_0 = 2.2$, $\beta = 10$, $L_x = L_y = 20$, $N = 512$. The image was obtained by averaging all time-snapshots over an interval of orbits $\triangle t = 400$.

The parameters of the simulation are: $Q_0 = 2.2$ and $\beta = 10$, and a 512×512 grid is used with box sizes $L_x = L_y = 20$. Although the surface mass density spectrum is shown here, the spectrum of the kinetic energy is qualitatively similar.

As can be seen in Fig. 7, the spectrum is not isotropic in the (k_x, k_y) plane. Contours of constant intensity are tilted ellipses, with the spectrum being more extended in the x- than in the y-direction. A similar result has been found Lesur & Longaretti (2011), Mamatsashvili et al. (2014), and Gogichaishvili et al. (2017) for the case of magnetohydrodynamic turbulence. The anisotropy can be explained through the equilibrium flow which sets a unique direction to the system. More specifically, due to the equilibrium shear flow, each structure with a finite k_y develops ever smaller wavelengths in the x-direction or, in other words, the x-component of the wave vector (k_x) is time dependent,

$$k_x = k_{x,0} + \frac{3}{2} k_y\, t, \tag{19}$$

(see e.g., Lesur & Longaretti 2011; Goldreich & Lynden-Bell 1965). It has been shown for the case of incompressible magnetohydrodynamic turbulence that the shearing can lead to an anomalous energy transfer in Fourier space in the direction of larger radial wave vectors (Lesur & Longaretti 2011).

In order to study the dependency on k_x (k_y), the spectra are projected onto the k_x (k_y) axis by integrating over k_y (k_x)

$$\mathcal{P}_x \mathcal{E}_k(k_x^{(i)}) \equiv \sum_{j=0}^{N-1} \mathcal{E}_k(k_x^{(i)}, k_y^{(j)}). \tag{20}$$

Depicted in Fig. 8 are the $\mathcal{P}_x$-projections of the power spectra for the kinetic energy density per mass $|\hat{\boldsymbol{v}}(k)|^2$ and the surface density $|\hat{\Sigma}(k)|^2$, for both $Q_0 = 1.2$ and $Q_0 = 2.4$. As expected, the turbulent intensity drops with increasing Q_0. However, the qualitative shape of the spectrum remains unaltered. The spectra appear to obey a scaling law for the range of radial wave numbers $3 \lesssim k_x \lesssim 30$. Depending on whether one studies the surface density or the kinetic energy density per mass, the scaling is between k^{-2} and k^{-3}, as can be seen in Fig. 8. The $\mathcal{P}_y$ projection is shown for comparison in Fig. 9 for an initial Toomre

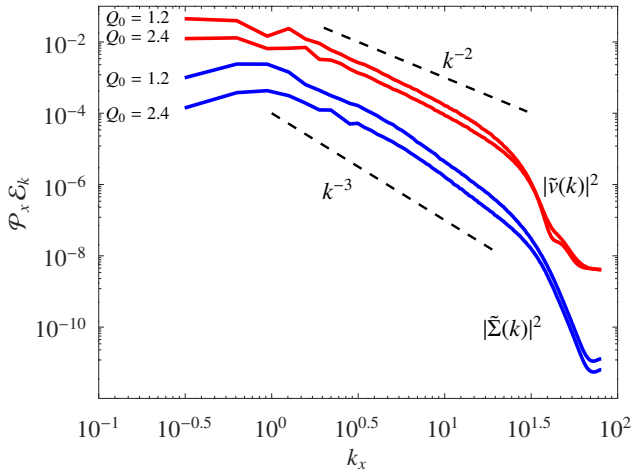

Fig. 8. Projections $\mathcal{P}_x$ of the two-dimensional power spectra onto the k_x-axis for $\mathcal{E}_k = |\hat{\boldsymbol{v}}(k)|^2$ and $\mathcal{E}_k = |\hat{\Sigma}(k)|^2$ respectively. Each of the latter is shown for $Q_0 \in \{1.2, 2.4\}$. Furthermore, the scaling laws k^{-2} and k^{-3} are shown for comparison.

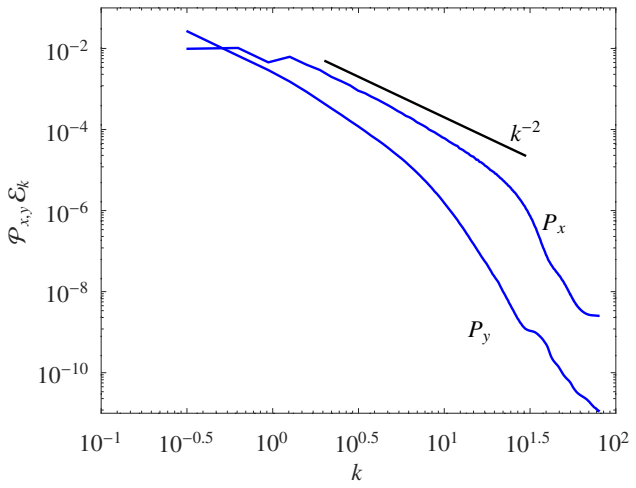

Fig. 9. Projections $\mathcal{P}_x$ and $\mathcal{P}_y$ of the kinetic energy per mass power spectrum onto the k_x and k_y-axis respectively. As can be observed, the $\mathcal{P}_y$-projection drops significantly faster than the $\mathcal{P}_x$-projection. The spectra are shown for $Q_0 = 2.0$.

parameter $Q_0 = 2.0$. It can be seen that the projection $\mathcal{P}_y$ drops significantly faster with increasing k_y than $\mathcal{P}_x$ with increasing k_x. The anisotropy therefore increases with increasing wave vectors (we note that the small-scale behavior might differ from that in case of a three-dimensional system (Riols et al. 2017; Booth & Clarke 2019). Furthermore, in contrast to $\mathcal{P}_x$ it is not obvious that $\mathcal{P}_y$ obeys a scaling law.

As the scaling of the x-projections is close to k^{-3}, it is tempting to connect the scaling with the enstrophy cascade of two-dimensional incompressible turbulence (see e.g., Boffetta & Ecke 2012). However, the velocity field of the gravito-turbulence is not incompressible, and in combination with the nonadiabatic response, neither enstrophy nor potential vorticity are conserved. Furthermore, the turbulence is strongly anisotropic. The strong decay of $\mathcal{P}_y \mathcal{E}_k$ with k_y (stronger than k^{-3}) shows that there is no strong cascade in the y-direction. This, together with the increasing anisotropy of the turbulence with increasing wave vector, shows that the velocity nonlinearity, although important, does not completely dominate the dynamics. The gravito-turbulent

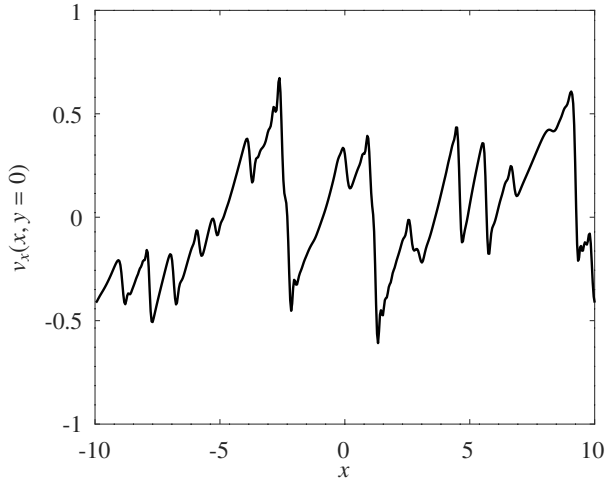

Fig. 10. Slice ($y = 0$) for the radial velocity v_x of a simulation with $Q_0 = 2.8, \beta = 10$. One characteristic of the radial velocity snapshots is the appearance of shocks or velocity discontinuities.

state is consequently not a strongly turbulent system. At the wave vectors where dissipation becomes important (which can be seen from the change in slope of the spectrum), the energy in the k_y modes is negligible compared to the energy in the k_x modes, and kinetic energy is transferred to internal energy through the dynamics in the radial direction. The wider spectrum in the radial direction is partly due to the shearing that leads to a temporal increase in the radial wave vector given by Eq. (19). However, the scaling of $\mathcal{P}_x \mathcal{E}_k$ with k_x is not entirely consistent with the steep decrease in $\mathcal{P}_y \mathcal{E}_k$ with k_y, when only shearing over a fixed time interval is considered. Additional physics is therefore expected to further broaden the spectrum in the radial direction.

Further insights can be drawn by investigating the radial velocity profiles. Depicted in Fig. 10 is a slice $y = 0$ of the radial velocity $v_x(x, y = 0)$ from a simulation with $Q_0 = 2.8$. The radial velocity in the turbulent state consists of a chaotic superposition of several shocks, where the velocity is discontinuous. These shocks have different widths and heights, and are almost axisymmetric, as can be seen from Fig. 5, reflecting the strong anisotropy in the spectrum. We note that, although the velocity is of the order of the sound speed (i.e., of the order of 1 due to the normalization to the sound speed), almost all the shocks have a step in velocity smaller than the sound speed. Furthermore, at smaller Q_0 the steps are larger and can considerably exceed the sound speed. The shocks that form are not directly due to the Mach number exceeding one in the frame of the computational grid.

The radial profile of the radial velocity is in agreement with the nonlinear wave steepening obtained in Burgers' turbulence (see e.g., Bec & Khanin 2007):

$$\partial_t v_x + v_x \partial_x v_x = 0. \tag{21}$$

An initially unstable sine profile of the radial velocity, $v_x = v_0 \sin(k_x x)$, develops through the nonlinearity with the two adjacent maxima (positive and negative) approaching each other and eventually coalescing. In this process, the original sine profile will change its morphology to a structure similar to those seen in the small image in Fig. 11.

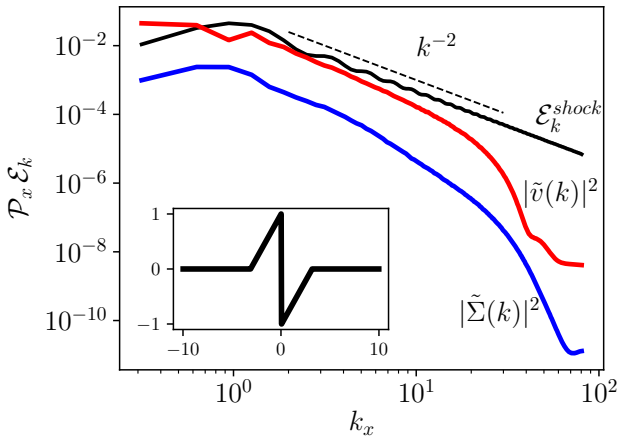

Fig. 11. Comparison of the power spectrum for a single shock $c \cdot |\psi^{\mu}_{\sigma}(k_x)|^2$ with the power spectra for $\mathcal{E}_k = |\hat{\Sigma}(k)|^2$ and $\mathcal{E}_k = |\hat{v}_x(k)|^2$. The shock width is chosen to be $\lambda = 2\pi$ corresponding to $k = 1$ and is depicted in the small subfigure. The constant c is chosen such that the shock spectrum is more comparable to the simulated spectra.

Taking the shock to have a generic form,

$$\Psi^{\mu}_{\lambda}(x) = \begin{cases} \frac{2\mu}{\lambda}(x + \frac{\lambda}{2}) & -\lambda/2 \le x \le 0 \\ \frac{2\mu}{\lambda}(x - \frac{\lambda}{2}) & 0 < x \le \lambda/2 \\ 0 & \text{else,} \end{cases} \tag{22}$$

the Fourier transform can be shown to be

$$\Psi^{\mu}_{\lambda}(k) = i\frac{4\mu}{\lambda} e^{ikx_0} \frac{1}{k}\left(\frac{\lambda}{2} - \frac{\sin(k\lambda/2)}{k}\right). \tag{23}$$

Therefore, the Fourier spectrum of the shock depicted in Fig. 11 scales as

$$\mathcal{E}_k^{\text{shock}} = f(k_x, \mu, \lambda) \cdot k_x^{-2}, \tag{24}$$

where f modulates the k^{-2} scaling. As the power spectra suggest, most of the energy resides in modes with $k_x \approx 1$. Hence, one might use a width of the shock $\lambda = 2\pi/k \approx 2\pi$. The power spectrum of the shock with this assumption is shown in Fig. 11. The shock spectrum has been scaled vertically for better comparison with the spectra obtained from the simulations. The shock shows a k^{-2} law and the nonlinear spectra of the turbulent state differ only slightly from that scaling. It is noted here that the k^{-2}-scaling is relatively independent of the actual shock width λ and height μ and therefore a chaotic superposition of shocks does not qualitatively alter the appearance of the spectra. Deviations between the shock spectrum and the simulated spectra occur for large values of k_x, suggesting that the deviations are likely due to the artificial viscosity which dominates at larger wave vectors.

The picture that emerges from the studies presented in this section is that the velocity nonlinearity mainly leads to wave steepening in the radial direction. The process continues until a shock forms, with the small radial length scales associated with the shock allowing for efficient dissipation. Modes that are initially growing saturate through the dissipation that occurs when shocks are present.

6. Analytic model

In this section, we develop an analytic model that predicts α for the gravito-turbulent state of an irradiated disk. The model combines a mixing length approach with elements from linear theory. Using the definition of α provided in Eq. (17), and linking the stress to the turbulent viscosity (ν_t) yields

$$\langle S_{xy}\rangle = -\langle\Sigma\rangle\nu_t\frac{\partial\langle v_y\rangle}{\partial x} = \frac{3}{2}\langle\Sigma\rangle\nu_t, \tag{25}$$

where a Keplerian velocity profile in the local approximation $\partial\langle v_y\rangle/\partial x = -3/2$ is used. The kinematic viscosity of the nonlinear state can be estimated using a mixing length approach Shakura (2018). Consider the two dimensional (x, y) shear flow in the local shearing box approximation. A turbulent velocity $\tilde{v}_x$ will move a fluid parcel in the radial direction over a distance δ_x, with the parcel keeping its original y-component of the velocity v_y. Hence, the y-velocity perturbation δv_y is (see Shakura 2018)

$$\delta v_y = \langle v_y\rangle(x) - \langle v_y\rangle(x + \delta_x) \approx -\delta_x\frac{\partial\langle v_y\rangle}{\partial x}. \tag{26}$$

The averaging brackets $\langle\ldots\rangle$ are assumed to be spatial and temporal averages (more technically, one can also assume them to be ensemble averages, see e.g., Shakura 2018). Using the equation above in the stress yields

$$\langle\Sigma v_x\delta v_y\rangle \approx -\langle\Sigma\rangle\cdot\langle\delta_x v_x\rangle\cdot\frac{\partial\langle v_y\rangle}{\partial x}, \tag{27}$$

and comparison with equation (25) then gives the mixing length estimate of the kinematic viscosity

$$\nu_t = \langle\delta_x v_x\rangle = \langle\delta_x^2/\delta_t\rangle, \tag{28}$$

where in the second step the radial velocity is expressed through a typical timescale of $v_x = \delta_x/\delta_t$.

In order to predict α, Eq. (2) is used to eliminate $\langle U\rangle$ in Eq. (17), yielding

$$\alpha = \frac{2}{3\gamma(\gamma-1)}\langle S_{xy}\rangle\frac{1 - \frac{9}{4}\gamma(\gamma-1)\beta\alpha}{U_0}. \tag{29}$$

Subsequently, expressing the stress in the kinematic viscosity using Eq. (25), gives

$$\alpha = \frac{\nu_t}{1 + \frac{9}{4}\gamma(\gamma-1)\beta\nu_t} = \frac{\nu_t}{1 + \frac{\nu_t}{\alpha_0}}, \tag{30}$$

whereby $\alpha_0 \equiv 4/(9\gamma(\gamma-1)\beta)$ is used for the last step. We would like to point out that $\nu_t \neq \alpha$, as ν is normalized with the background sound speed $c_{s,0}$ rather than saturated speed of sound $\langle c_s\rangle$. Using the mixing length model for ν_t in the equation above gives an expression for α.

As discussed in Sect. 5, saturation occurs through the nonlinear steepening of radial waves. Since the maximum (minimum) of the wave has to move over roughly a quarter wavelength to generate the observed shock structures, the mixing length can be taken to be a quarter wavelength of the dominant radial mode:

$$\delta_x = \frac{\lambda}{4} = \frac{\pi}{2}k^{-1}. \tag{31}$$

The spectra of the nonlinear state decrease in amplitude with increasing Q_0, but the functional dependence on k_x remains nearly unaltered. Therefore, the typical wave vector appearing in the mixing length estimate is relatively nonsensitive to the Q_0 value, and a typical value can be obtained by averaging over the spectrum:

$$\langle k_x\rangle_k = \frac{\int|\hat{\Sigma}(k)|^2 k_x\,\mathrm{d}^2\boldsymbol{k}}{\int|\hat{\Sigma}(k)|^2\,\mathrm{d}^2\boldsymbol{k}}. \tag{32}$$

This procedure yields

$$\bar{k} \approx \frac{3}{2} \tag{33}$$

as a typical value for $\bar{k}$. It then follows that $\bar{\lambda} = 2\pi/\bar{k} \approx 4$, which fits with the average distance between two shock fronts in Fig. 5, and agrees with the results of previous work (e.g., Kratter & Lodato 2016; Cossins et al. 2009) showing that dissipation occurs at wave numbers $\bar{k} \approx 1$ through sonic shocks.

The typical timescale can be argued to be linked to the growth rate. Although, for many turbulent systems, linear theory is not particularly relevant, we show in the previous section that the nonlinear state of the gravito-turbulence is not strongly turbulent. The relevance of linear theory can be further justified by the following observations.

- There must be a mechanism providing an ongoing exchange of energy from the background (shear flow) to the actual turbulent motion of the fluid. A linear instability is a candidate for this mechanism. Indeed, the strength of turbulence drops with increasing values of Q_0 as can be seen in Fig. 8 in agreement with the dependence of the linear growth rate g on Q_0.
- The relevance of linear theory for the nonlinear state can be further assessed by investigating cases close to the threshold of the linear instability. With radiative cooling, the disk is analytically unstable for all values of the Toomre parameter. However, due to the added dissipation, this is not necessarily the case in the numerical simulations. This is illustrated in Fig. 6, where it can be seen that for $Q_0 > 3$ the disk is stable when a diffusion coefficient $D_{(2)} = 0.1$ is used. Indeed, numerical simulations with $Q_0 > 3.2$ ($D_{(2)} = 0.1$) show no turbulent state even when initialised with a turbulent state obtained for $Q_0 < 3$. Although there is a window in Q_0 where turbulence can be maintained despite linear stability, at least for some time, this window is small. Therefore, in summary, the development of gravito-turbulence requires a linear instability to be present.

The relevance of the linear drive suggests that the growth rate plays a role in the determination of the typical timescale. Consequently $\delta_t^{-1} = g$ is used as the typical inverse timescale. Using that and Eq. (33), one finds an analytical expression for the turbulent kinematic viscosity:

$$\nu_t = \left(\frac{\pi}{2}\right)^2 \frac{g}{\bar{k}^2} = \left(\frac{\pi}{3}\right)^2 g. \tag{34}$$

We note that something similar is often used in fusion plasma physics in the context of turbulent transport (Weiland 2016).

The analytic result of Eq. (34) can subsequently be used to predict α according to Eq. (30). Indeed, g depends on both the Toomre parameter Q and the cooling timescale β.

7. Predictions of the analytic model

Analytic linear growth rates were obtained for an equilibrium without turbulence and are therefore a function of Q_0. The saturated Toomre parameter of the turbulent state $\langle Q \rangle$, with $\langle ... \rangle$ denoting averages over the computational domain as well as time, is found to be larger than one and close to $\langle Q \rangle \approx 2$ in two-dimensional systems (see e.g., Vanon 2018). The simulations of this paper confirm this observation but nevertheless show that saturation can occur at values considerably larger than 2, and that $\langle Q \rangle$ is a function of irradiation as well as cooling time. The turbulent saturation values obtained from the simulations are depicted as crosses in Fig. 12. The average was calculated in the following way:

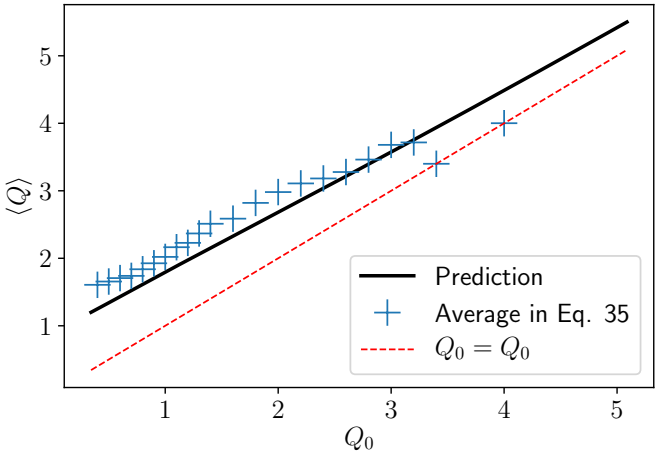

Fig. 12. Toomre parameter at turbulent saturation $\langle Q \rangle$ plotted as a function of irradiation equilibrium Q_0. Crosses: values derived from simulations by averaging the turbulent state over both box and time according to Eq. (35). Solid line: analytical prediction via Eqs. (36) and (37).

$$\langle Q \rangle = \frac{\Omega_0}{\pi G} \sqrt{\frac{\gamma(\gamma-1)\langle U \rangle}{\langle \Sigma \rangle^3}}. \tag{35}$$

The relevant timescale in the mixing length model is set by the linear growth rate. However, the latter must describe the growth in the saturated turbulent state. Consequently, the growth rate must be considered a function of $\langle Q \rangle$ and $\delta_t^{-1} = g(\langle Q \rangle, \beta)$.

As $\langle Q \rangle > 1$, the approximate growth rate from Eq. (11) is used and substituted into Eq. (34):

$$\nu_t = \left(\frac{\pi}{3}\right)^2 \frac{1}{\beta} \frac{1}{\langle Q \rangle^2 - 1} \tag{36}$$
$$\alpha = \frac{\nu_t}{1 + \nu_t/\alpha_0},$$

where $\bar{k} = 3/2$ is used. This latter equation relates α with $\langle Q \rangle$. The prediction is completed using Eq. (2), which provides a relation between α and $\langle U \rangle$ and consequently $\langle Q \rangle$ as well. For the purpose here, it is convenient to rewrite Eq. (2) in terms of ν_t

$$\left(\frac{\langle Q \rangle}{Q_0}\right)^2 = \left(1 - \frac{\alpha}{\alpha_0}\right)^{-1} \tag{37}$$
$$\langle Q \rangle = Q_0 \sqrt{1 + \frac{\nu_t}{\alpha_0}},$$

where $\langle U \rangle / U_0 = \langle Q \rangle^2 / Q_0^2$ is used. Hence, one can now predict both α and $\langle Q \rangle$ depending on the irradiation equilibrium Q_0.

The prediction of $\langle Q \rangle$ as derived above is shown as the black solid line in Fig. 12. One conclusion that can be drawn directly from Eq. (37) is that $\langle Q \rangle > Q_0$ always holds. Furthermore, as $g \to 0$ for $\langle Q \rangle \to \infty$, we conclude that $\langle Q \rangle \to Q_0$ for $Q_0 \to \infty$ by considering Eq. (36). The prediction for α depending on Q_0 is shown in Fig. 13.

The predictions seem to fit the data well except for values of $Q_0 > 3.2$. This discrepancy is due to the above-mentioned numerical damping, which prevents a turbulent state from being sustained as the linear driving is compromised. More precisely, the simulations for $Q_0 = 3.4$ and 4.0 could not maintain a turbulent state. The corresponding values for α and $\langle Q \rangle$ are obtained by averaging the decaying turbulence, in the absence of a persistent nonlinear state.

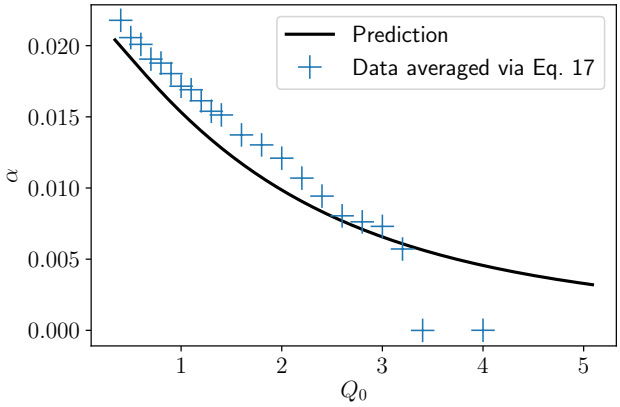

Fig. 13. Comparison of the analytical mixing length prediction with the simulation data. Crosses: α values derived by averaging the simulation data over both box and time according to Eq. (17). Black curve: prediction from the mixing length argument in Eqs. (36) and (37).

We note that the analytic model predicts comparatively large α values for high background Toomre parameters Q_0. To see that, one can approximate Eq. (30) assuming small growth rates,

$$\alpha = \left(\frac{\pi}{3}\right)^2 \frac{1}{\beta} \frac{1}{Q_0^2 - 1}, \tag{38}$$

whereby $\langle Q \rangle \approx Q_0$ for large Q_0. Assuming $\beta = 10$, a relevant value $\alpha = 10^{-3}$ is obtained for $\langle Q \rangle \approx 10$, that is, an order of magnitude above the Toomre stability criterion. Of course, shorter cooling times lead to larger values of α at fixed $\langle Q \rangle$. However, shorter cooling may also lead to clumping (Johnson & Gammie 2003; Rice et al. 2003, 2005, 2011; Kratter & Murray-Clay 2011). The effects of clumping are beyond the scope of this work but a study of this effect at the higher values of $\langle Q \rangle$ obtained in this paper when compared with the literature is worthy of further study.

It is noted that the prediction of $\alpha > 10^{-3}$ for $\langle Q \rangle \approx 10$ is connected with the stability analysis in Sect. 3. The latter might depend on the cooling model that is applied. Here, the fiducial cooling level is a constant background thermal energy density U_0. Alternatively, one can choose the reference cooling level to be density dependent, leading to a cooling term (Rice et al. 2011)

$$-\frac{\Sigma(c_s^2 - c_{s0}^2)}{\gamma(\gamma-1)\tau_c} = -\frac{U}{\tau_c} + \frac{\Sigma c_s^2}{\gamma(\gamma-1)\tau_c}. \tag{39}$$

Linearization leads to an additional term $\propto \tilde{\Sigma}$ (see e.g., Lin & Kratter 2016), when compared with the analysis of Sect. 3. This additional term has stabilizing effects as locally compressed areas are cooled less efficiently than locally expanding areas. Indeed, linear stability analysis reveals that the cooling model presented in Eq. (39) yields positive growth rates only for $Q_0 < \sqrt{\gamma}$ or in the case discussed here: $Q_0 \lesssim 1.4$. Nevertheless, the β-cooling description is a strong simplification and one could argue for both cooling models. To fully elucidate the problem, one would have to solve the full radiative transfer equation.

8. Conclusion

In this paper, the gravito-turbulent state of a razor-thin irradiated disk is studied in detail. We show that, depending on the cooling prescription, a linear instability occurs for all values of the equilibrium Toomre parameter Q_0, and we derive an accurate analytic estimate of the maximum growth rate for $Q_0 > 1$. A detailed study of the spectra reveals that the gravito-turbulent state is not strongly turbulent. The spectra are anisotropic with the anisotropy increasing with the wave vector. The spectra drop off rapidly with k_y (stronger than k_y^{-3}) and show no clear power-law scaling with k_y. This suggests that no cascade in the y-direction takes place and saturation is connected with dynamics in the radial direction. In contrast, the spectrum as a function of the radial wave vector does show a power law with a scaling in the range $k^{-2} - k^{-3}$, which can be explained through the existence of shocks. The radial velocity profile as a function of the radial coordinate is consistent with Burgers' turbulence, consisting of several shocks of different height. The observations suggest that linearly unstable modes grow in amplitude until the nonlinearity is strong enough, leading to wave steepening and shock formation. The small radial scales connected with the shock then allow for efficient dissipation and, consequently, saturation of the mode.

Using these observations, a mixing length model is developed using a quarter wave length as the radial step length and the growth rate of the most unstable mode as the typical time. This model gives an analytic prediction of the viscosity parameter α as a function of the Toomre parameter and cooling time, and it compares very well with the numerical simulations. The model predicts relevant values of $\alpha = 10^{-3}$ for Toomre parameters an order of magnitude larger than the original Toomre limit (i.e., $\langle Q \rangle \approx 10$). It is noted that this result can change when using a different cooling description and more accurate models with radiative transfer would be useful here.

References

Baehr, H., & Klahr, H. 2015, ApJ, 814, 155
Balbus, S. A., & Hawley, J. F. 1998, Rev. Mod. Phys., 70, 1
Bec, J., & Khanin, K. 2007, Phys. Rep., 447, 1
Boffetta, G., & Ecke, R. E. 2012, Ann. Rev. Fluid Mech., 44, 427
Booth, R. A., & Clarke, C. J. 2019, MNRAS, 483, 3718
Cossins, P., Lodato, G., & Clarke, C. J. 2009, MNRAS, 393, 1157
Gammie, C. F. 2001, ApJ, 553, 174
Gogichaishvili, D., Mamatsashvili, G., Horton, W., Chagelishvili, G., & Bodo, G. 2017, ApJ, 845, 70
Goldreich, P., & Lynden-Bell, D. 1965, MNRAS, 130, 125
Hirose, S., & Shi, J.-M. 2019, MNRAS, 485, 266
Johnson, B. M., & Gammie, C. F. 2003, ApJ, 597, 131
Kratter, K., & Lodato, G. 2016, ARA&A, 54, 271
Kratter, K. M., & Murray-Clay, R. A. 2011, ApJ, 740, 1
Lesur, G., & Longaretti, P.-Y. 2011, A&A, 528, A17
Lin, C., & Shu, F. 1964, ApJ, 140, 646
Lin, M.-K., & Kratter, K. M. 2016, ApJ, 824, 91
Lynden-Bell, D., & Kalnajs, A. J. 1972, MNRAS, 157, 1
Mamatsashvili, G. R., Gogichaishvili, D. Z., Chagelishvili, G. D., & Horton, W. 2014, Phys. Rev. E, 89, 043101
Rice, W. K. M., Armitage, P. J., Bate, M. R., & Bonnell, I. A. 2003, MNRAS, 339, 1025
Rice, W. K. M., Lodato, G., & Armitage, P. J. 2005, MNRAS, 364, L56
Rice, W. K. M., Armitage, P. J., Mamatsashvili, G. R., Lodato, G., & Clarke, C. J. 2011, MNRAS, 418, 1356
Riols, A., Latter, H., & Paardekooper, S.-J. 2017, MNRAS, 471, 317
Shakura, N. 2018, Accretion Flows in Astrophysics, Astrophys. Space Sci. Libr., 454 (Springer)
Shakura, N. I., & Sunyaev, R. A. 1973, A&A, 24, 337
Toomre, A. 1964, ApJ, 139, 1217
Vanon, R. 2018, MNRAS, 477, 3683
Vanon, R., & Ogilvie, G. I. 2016, MNRAS, 463, 3725
Weiland, J. 2016, Plasma Phys. Rep., 42, 502
Young, M. D., & Clarke, C. J. 2015, MNRAS, 451, 3987

Chapter 8

Combined Dynamo of Gravitational and Magneto-Rotational Instability in Irradiated Accretion Discs

L. Löhnert, and A. G. Peeters

This chapter has been published in the journal Astronomy & Astrophysics:

Credit: Löhnert, L. & Peeters, A. G., Astronomy & Astrophysics, 663, A176, 2022, reproduced with permission © ESO
URL: https://doi.org/10.1051/0004-6361/202142121 (as of 25.05.2023)

A&A 663, A176 (2022)
https://doi.org/10.1051/0004-6361/202142121

Astronomy & Astrophysics

Combined dynamo of gravitational and magneto-rotational instability in irradiated accretion discs

L. Löhnert and A. G. Peeters

Physics Department of Bayreuth, Universitätsstraße 30, Bayreuth, Germany
e-mail: lucas.loehnert@uni-bayreuth.de

Received 31 August 2021 / Accepted 3 April 2022

ABSTRACT

Aims. We aim to assess whether magneto-rotational instability (MRI) can exist in a turbulent state generated by gravitational instability (GI). We investigated the magnetic field saturation and elucidated the ability of GI turbulence to act as a dynamo.
Methods. The results were obtained by numerical simulations using the magnetohydrodynamics code *Athena*. A sub-routine to solve the Poisson equation for self-gravity using three-dimensional Fourier transforms was implemented for that purpose. A GI-turbulent state was then restarted, with a zero-net-flux type magnetic seed field being introduced. The seed field was chosen with $\beta \approx 10^{10}$ to make sure that the magnetic field of the stationary state is exclusively generated by the dynamo.
Results. Shortly after introducing the magnetic seed field, a significant field amplification is observed, despite MRI not being active. This shows that GI acts as a kinematic dynamo. The growing magnetic field allows MRI to become active, which leads to the emergence of a butterfly diagram. The turbulent stress of the saturated state is found to be consistent with the superposition of GI stresses and MRI stresses. Moreover, the ratio of magnetic stress to magnetic pressure is found to lie in the 0.3−0.4 range, which is typical for MRI turbulence. Furthermore, it is found that the magnetic energy significantly decreases if self-gravity is turned off. This indicates, in accordance with the initial field amplification, that GI provides the dominant dynamo contribution and that MRI is not simply added but rather grows on the magnetic field provided by GI turbulence. Finally, it is shown that the combined GI-MRI-dynamo is consistent with an $\alpha-\Omega$ model and that the observed oscillation frequency of the butterfly diagram roughly agrees with the model prediction.

Key words. accretion, accretion disks – protoplanetary disks – magnetic fields – instabilities – turbulence – dynamo

1. Introduction

The process of accreting matter towards the central object in an accretion disc requires angular momentum to be transported outwards (Lynden-Bell 1969; Shakura & Sunyaev 1973; Lynden-Bell & Pringle 1974; Balbus & Hawley 1998). Molecular viscosity is insufficient to generate the required angular momentum transport and, hence, turbulence is considered the source of the required stresses (see e.g., Shakura & Sunyaev 1973; Balbus & Hawley 1998). Various candidates for instabilities providing the necessary turbulence have been considered. Two prominent candidates are magneto-rotational instability (MRI; see e.g., Balbus & Hawley 1991, 1998; Hawley et al. 1995; Brandenburg et al. 1995) and gravitational instability (GI; Toomre 1964; Lynden-Bell & Kalnajs 1972; Gammie 2001; Kratter & Lodato 2016).

Magneto-rotational instability is proposed as a mechanism for generating turbulence in sufficiently ionised discs (Balbus & Hawley 1991; Blaes & Balbus 1994; Hawley et al. 1995) including accretion discs of binary objects (black holes, neutron stars, white dwarfs), active galactic nuclei (Balbus & Hawley 1998), and sufficiently ionised regions of protoplanetary discs (Armitage 2011). MRI relies on the coupling of adjacent fluid elements by magnetic field lines producing the necessary mechanism for outward angular momentum transport (see e.g., Balbus & Hawley 1998). The linear and nonlinear properties of MRI are studied in various numerical simulations and for a variety of different configurations (Hawley et al. 1995; Brandenburg et al. 1995; Stone et al. 1996; Suzuki & Inutsuka 2009; Guan & Gammie 2011; Shi et al. 2009; Simon et al. 2011; Bai & Stone 2013; Fromang et al. 2013; Bodo et al. 2014).

The GI plays an important role in galactic discs, contributing to the spiral structure (see e.g., Toomre 1964; Lin & Shu 1964; Lynden-Bell & Kalnajs 1972; Kratter & Lodato 2016), and it is also relevant for active galactic nuclei (Menou & Quataert 2001; Goodman 2003) and for sufficiently massive protoplanetary discs (see e.g., Armitage 2011; Kratter & Lodato 2016). A measure of stability is provided by the Toomre parameter (Toomre 1964):

$$Q = \frac{c_s \Omega_0}{\pi G \Sigma}, \tag{1}$$

with the sound speed c_s, *Kepler* orbital frequency Ω_0, and mass surface density Σ. The system is gravitationally unstable for $Q < 1$ (see e.g., Toomre 1964). It is noted that this holds for the thin-disc limit, and three-dimensional effects can alter the stability criterion, typically stabilising the disc (Kratter & Lodato 2016; Binney & Tremaine 1987). Furthermore, turbulent viscosities and radiation physics can have an influence (Lin & Kratter 2016). Simulation studies address gravito-turbulence in both two-dimensional setups (Gammie 2001; Rice et al. 2011; Paardekooper 2012; Young & Clarke 2015; Löhnert et al. 2020) and three-dimensional configurations (see e.g., Rice et al. 2003; Lodato & Rice 2004; Boley et al. 2006; Stamatellos & Whitworth 2008; Cossins et al. 2009; Shi & Chiang 2014; Riols et al. 2017; Riols & Latter 2018b; Booth & Clarke 2019; Hirose & Shi 2019. The instability saturates in

Article published by EDP Sciences

a nonlinear state that is a statistical balance between radiative cooling on the one hand and thermal energy production due to shocks generated by gravitational turbulence on the other hand (Gammie 2001; Kratter & Lodato 2016).

In addition to the ability to transport angular momentum, the disc's ability to sustain large-scale magnetic fields via a dynamo is also attributed to turbulent properties (see e.g., Moffatt 1978; Brandenburg & Donner 1997; Vishniac & Brandenburg 1997; Balbus & Hawley 1998; Rüdiger & Pipin 2000). Magneto-rotational turbulence is often considered as a dynamo mechanism, sustaining large-scale magnetic fields (see e.g., Brandenburg et al. 1995; Balbus & Hawley 1998; Ziegler & Rüdiger 2000; Lesur & Ogilvie 2008; Gressel 2010; Guan & Gammie 2011; Käpylä & Korpi 2011). It was recently suggested that GI can also provide the means to sustain a dynamo (see e.g., Riols & Latter 2019).

The interplay of magneto-rotational and gravitational turbulence has previously been considered in the context of gravito-magneto limit cycles (see Armitage et al. 2001; Zhu et al. 2010; Martin & Lubow 2011; Martin et al. 2012), suggesting that the heating due to GI may enhance the ionisation level and in turn trigger MRI. A few studies also exist on the direct interplay of GI with magnetic fields or MRI (Fromang et al. 2004; Fromang 2005), and more recently Riols & Latter (2018a, 2019) investigated the interaction of GI and MRI more directly in the context of local shearing box simulations with a β-cooling prescription. A possible dynamo-mechanism is provided in Riols & Latter (2019). A global simulation for the interaction of both is provided by Deng et al. (2020).

The present study is intended to address the question of MRI and GI coexistence for ideal magnetohydrodynamic (MHD) cases with zero-net-flux initial conditions and for irradiated discs in the local shearing-box approximation.

This paper is structured as follows. In Sect. 2, the model equations are discussed and important quantities and averages are defined. In Sect. 3, the numerical scheme is described, as well as the boundary conditions, initial conditions and the method used to solve the Poisson equation for self-gravity. Section 4 briefly discusses benchmark simulations for magneto-rotational turbulence as well as gravitational-turbulence. Simulations including both self-gravity and MHD are studied in Sect. 5. The time evolution of field amplitudes, energy densities, and the saturated turbulent stresses are analysed in detail. In Sect. 6, we explain why a superposition of gravitational and magneto-rotational turbulence is likely to be present. The influence of irradiation is addressed in Sect. 7, thereby making a comparison to Riols & Latter (2018a, 2019). The importance of self-gravity in the dynamo mechanism is highlighted in Sect. 8. In Sect. 9, it is then shown that the findings are consistent with an α–Ω model for the dynamo. The main results are summarised in Sect. 11.

2. The model

The model consists of the MHD equations of motion in the local shearing box approximation, retaining the effect of self-gravity as well as a cooling (heating) term:

$$\partial_t \rho + \nabla \cdot (\rho \boldsymbol{v}) = 0, \tag{2a}$$

$$\partial_t(\rho \boldsymbol{v}) + \nabla \cdot \left(\rho \boldsymbol{v}\boldsymbol{v} - \frac{1}{\mu_0}\mathbf{B}\mathbf{B} + (P + \frac{\mathbf{B}^2}{2\mu_0})\underline{\mathbf{I}} + \underline{\mathbf{G}}\right), \tag{2b}$$

$$= -2\rho\Omega_0 \mathbf{e}_z \times \boldsymbol{v} + 3\rho\Omega_0^2 x\, \mathbf{e}_x - \rho\Omega_0^2 z\, \mathbf{e}_z$$

$$\partial_t \mathbf{B} - \nabla \times (\boldsymbol{v} \times \mathbf{B}) = \eta \nabla^2 \mathbf{B}, \tag{2c}$$

$$\partial_t E + \nabla \cdot \left((E + P + \frac{\mathbf{B}^2}{2\mu_0})\boldsymbol{v} - \mathbf{B}(\mathbf{B} \cdot \boldsymbol{v})\right) = -\rho \boldsymbol{v} \cdot \nabla\Phi, \tag{2d}$$

$$+ 3\Omega_0^2 x\, v_x - \Omega_0^2 z\, v_z + \rho\dot{q}.$$

$$\nabla^2 \Phi = 4\pi G\rho, \tag{2e}$$

$$\nabla \times \mathbf{B} = \mu_0 \mathbf{J}. \tag{2f}$$

In the equations above, ρ is the mass-density, $\boldsymbol{v}$ the fluid velocity, P the thermal pressure, $\mathbf{B}$ the magnetic field, E the total energy density, $\mathbf{J}$ the current density, and $\underline{\mathbf{G}}$ the gravitational stress tensor. The $\underline{\mathbf{G}}$-tensor is given by

$$\underline{\mathbf{G}} = \frac{1}{4\pi G}\left(\nabla\Phi\nabla\Phi - \frac{1}{2}(\nabla\Phi \cdot \nabla\Phi)\underline{\mathbf{I}}\right) \tag{3}$$

(see e.g., Lynden-Bell & Kalnajs 1972), with the potential of self-gravity Φ. The first term is a dyadic product and the second term contains the identity-matrix $\underline{\mathbf{I}}$. The total energy density is defined by

$$E = \frac{\rho \mathbf{v}^2}{2} + \frac{P}{\gamma - 1} + \frac{\mathbf{B}^2}{2\mu_0}. \tag{4}$$

The cooling (heating) model $\rho\dot{q}$ includes both pure radiative cooling and a heating source:

$$\rho\dot{q} = -\frac{P}{(\gamma - 1)\tau_c} + \frac{\rho\, c_{s,0}^2}{\gamma(\gamma - 1)\tau_c}, \tag{5}$$

where $c_{s,0}$ is the background sound speed. The first term on the right hand side corresponds to a simple β-cooling prescription with cooling timescale τ_c. The second term is the heating-source due to irradiation (e.g., from the central star). In general, the sound speed is defined here as $c_s = \sqrt{\gamma P/\rho}$, with adiabatic index γ. Unless stated otherwise, $\gamma = 1.64$ is used. In the absence of turbulence, the interplay of cooling and heating generates a stationary, stratified state with $\rho = \rho(z)$, $P = P(z)$, and $c_s = c_{s,0} = \sqrt{\gamma P(z)/\rho(z)} = \text{const}$. Hence, irradiation heating would balance radiative cooling such that the disc settles into a state with constant temperature in the vertical direction. It is noted that in turbulent states, one may find $\langle\rho\rangle_{xy} \neq \rho(z)$ and $\langle P\rangle_{xy} \neq P(z)$, with a horizontal average $\langle\ldots\rangle_{xy}$ and $\sqrt{\gamma\langle P\rangle_{xy}/\langle\rho\rangle_{xy}} \neq c_{s,0}$ in general.

To investigate turbulent states, averages of different types are used. Spatial averages are denoted by $\langle\rangle_i$, whereby the identifier i defines the average region; for example, $\langle f\rangle_{xy}$ averages f over horizontal planes $z = \text{const}$, and the average is thus a function of z only. Without further designation, $\langle f\rangle$ is an average over the entire box-volume. Time averages are indicated by $\langle f\rangle_t$. A statement of the form $\langle\langle f\rangle\rangle_t$ then means that f is first averaged over the volume and the resulting values are then averaged over time.

To quantify the strength of gravitational instability, the Toomre-parameter is used (see e.g., Toomre 1964; Kratter & Lodato 2016; Gammie 2001):

$$Q = \frac{c_s \Omega_0}{\pi G \Sigma}, \tag{6}$$

where Σ is the averaged mass surface density, $\Sigma = \langle\rho\rangle L_z$, $\langle\rho\rangle$ is the volume-averaged mass density, and L_z is the vertical extend of the box volume. In the following discussions, two different definitions for the Toomre parameter are used, Q_0 and $\langle Q\rangle$. The difference arises due to different choices for the sound-speed.

For Q_0, the irradiation value is used ($c_s = c_{s,0}$), and for $\langle Q \rangle$, the volume average is used ($c_s = \langle c_s \rangle$). Hence,

$$Q_0 = \frac{c_{s,0}\Omega_0}{\pi G \Sigma}, \quad \langle Q \rangle = \frac{\langle c_s \rangle \Omega_0}{\pi G \langle \Sigma \rangle}, \quad \langle c_s \rangle = \sqrt{\gamma \frac{\langle P \rangle}{\langle \rho \rangle}}. \tag{7}$$

Another frequently used quantity is the Alfven speed: $v_A = \sqrt{B^2/(\mu_0 \rho)}$ (see e.g., Jackson 2014; Balbus & Hawley 1998). When applying a volume average, $\langle v_A \rangle = \sqrt{\langle B^2 \rangle / (\mu_0 \langle \rho \rangle)}$ is used.

The dimensionless turbulent stress parameter α (see Shakura & Sunyaev 1973) is defined by

$$\alpha = \frac{2\langle S_{xy} \rangle}{3\gamma \langle P \rangle}. \tag{8}$$

The additional factor $2/(3\gamma)$ is frequently used in the context of gravitational turbulence (see e.g., Gammie 2001) and is also used here. The turbulent stress is comprised of three contributions, the Reynolds stress, the Maxwell stress, and the gravitational stress:

$$S_{xy} = \rho v_x \delta v_y - \frac{1}{\mu_0} B_x B_y + \frac{1}{4\pi G} \partial_x \Phi \, \partial_y \Phi. \tag{9}$$

In dimensionless form (Eq. (8)), the corresponding stresses are referred to as α_r, α_m, and α_g, respectively.

In the simulations and plots, all quantities f are made dimensionless by using characteristic scales f_{ch}, yielding $f = \hat{f} f_{ch}$, with $\hat{f}$ being dimensionless. Times are made dimensionless using the fiducial orbital angular frequency, that is, $t_{ch} = \Omega_0^{-1}$. Velocities scale with the background speed of sound $v_{ch} = c_{s,0}$. Lengths are made dimensionless by using the scale height $H = c_{s,0}/\Omega_0$ and $l_{ch} = H$. It is noted that the exact definition of H varies in the literature as the additional factors $\sqrt{\gamma}$ or $\sqrt{2}$ may arise and H should rather be understood as a typical scale. Mass densities are made dimensionless by using $\rho_{ch} = \Omega_0^2/G$, and from there a typical pressure of $P_{ch} = c_{s,0}^2 \rho_{ch}$ immediately follows. A typical magnetic field is conveniently defined as $B_{ch} = \sqrt{\mu_0 P_{ch}}$. Finally, the characteristic gravitational potential is $\Phi_{ch} = c_{s,0}^2$.

3. Method and code

3.1. Code and algorithm

For all simulations shown here, the MHD code Athena [1] is used (see Stone et al. 2008). The Riemann solver applied here is the Roe solver (Roe 1981), and the spatial reconstruction is third order (Colella & Woodward 1984). The integrator used is the corner transport upwind (CTU) integrator (see Colella 1990). The equations solved are Eqs. (2a)–(2f) (Stone & Gardiner 2010). The fast advection in rotating gaseous objects (FARGO) algorithm is also enabled (see Masset 2000; Stone & Gardiner 2010). The latter separates the velocity into background shear and perturbation $\boldsymbol{v} = -(3\Omega_0/2) x \mathbf{e}_y + \delta \boldsymbol{v}$. The equations are then solved for the perturbation and the shear advection separately, and the shear advection is added to the perturbations afterwards. In boxes spanning many scale heights in radial direction, the shear velocities can become large near the boundaries, and FARGO can therefore reduce the required time step. As velocities are expected to reach supersonic values, especially in self-gravitating cases, shock-capturing H correction is enabled (see Sanders et al. 1998).

[1] See https://princetonuniversity.github.io/Athena-Cversion/

The problem generator used builds upon the stratified-shearing-sheet generator that is based on the setup in Hawley & Balbus (1992), Stone et al. (1996). The time step is mediated via the Courant–Friedrichs–Lewy (CFL) number (see e.g., Courant et al. 1928), with a CFL value of 0.06.

3.2. Boundary conditions

All variables (velocities without background shear flow) are periodic in the y direction and shearing-periodic in the x direction. In the vertical direction, outflow boundary conditions are used for hydrodynamical variables, that is, the ghost-zone velocities are set to zero for inward motion and extrapolated constantly into the ghost zones otherwise. Mass density and pressure are extrapolated constantly into the ghost zones, whereby the pressure in the ghost zones is isothermally linked to the density. For the magnetic field, we utilised vertical field boundary conditions at the vertical boundaries. Hence, $B_x = B_y = 0$ and $\partial_z B_z = 0$ (see e.g., Brandenburg et al. 1995; Ziegler & Rüdiger 2001; Käpylä & Korpi 2011; Oishi & Low 2011) at the vertical boundaries ($B_{x,y}$ is set to zero in the ghost zones and B_z is extrapolated constantly into the ghost zones). The mass density can be very small near the vertical boundaries, and in order to limit the time step, a lower boundary for the density is introduced (similarly to Shi & Chiang 2014). The limit is chosen as $\rho_0(t = 0) \times 10^{-4}$, with ρ_0 being the mid-plane density at initialisation, or $\rho_0 = 1.0$ for restarted simulations.

3.3. Initial conditions

The background equilibrium consists of a density and pressure distribution $(\rho(z), P(z))$, whereby the z dependence accounts for the vertical stratification. The background velocity is the *Kepler* shear flow, $\boldsymbol{v}_0 = -(3\Omega_0/2) x \mathbf{e}_y$. Density and pressure are linked by $P = \rho c_{si,0}^2$, assuming a constant isothermal speed of sound, $c_{si,0} = c_{s,0}/\sqrt{\gamma} = \text{const}$. This does not imply that an isothermal equation of state is used, and the condition is only imposed at the start of the simulation. It is noted that $c_{s,0}$ corresponds to the irradiation value in Eq. (5), as this must be the case if the initial state is an equilibrium. With that, one finds $\langle Q \rangle = Q_0$ for the initial state. The equilibrium is then perturbed by random density perturbations that are introduced at the start of the simulation. Depending on the exact purpose, a seed magnetic field can also be introduced, which we describe in more detail in the respective sections.

The exact form of the stratification profile $(\rho(z), P(z))$ depends on whether self-gravity is used or not. Without self-gravity, the initialised equilibrium profile for density and pressure is Gaussian ($\rho = \rho_0 \exp\left(-\Omega_0^2 z^2/(2c_{s,i}^2)\right)$). Therein, ρ_0 (P_0 for the pressure) is the mid-plane value at $z = 0$.

With self-gravity, the stratification profile is given by the vertical force balance (see e.g., Shi & Chiang 2014):

$$-\frac{1}{\rho}\partial_z P - \partial_z \Phi - \partial_z \Phi^\star = 0, \tag{10}$$

whereby Φ is the gravitational potential due to self-gravity and $\Phi^\star = 0.5\Omega_0^2 z^2$ is the vertical contribution from the central star's potential. Considering that the stratification is initially isothermal, one can rewrite the force balance, yielding

$$\partial_z^2 \rho = \frac{1}{\rho}(\partial_z \rho)^2 - \frac{4\pi G}{c_{s,i}^2}\rho^2 - \frac{\Omega_0^2}{c_{s,i}^2}\rho. \tag{11}$$

The latter equation is solved once at the start of the simulation using a Runge–Kutta fourth-order method.

3.4. Poisson solver for self-gravity

Athena provides a self-gravity solver based on fast Fourier transforms (FFTs) that can be used in three-dimensional shearing-box calculations. Though, the latter only allows for periodic (shearing periodic in x) boundary conditions in all directions. In order to simulate stratified cases, major changes to the method of solving the Poisson equation are thus required. A possible solution is provided in Koyama & Ostriker (2009), Shi & Chiang (2014). We adopted the code structure provided in Athena and implemented the method outlined in Koyama & Ostriker (2009). Here, a brief analytical explanation of the ansatz is provided, while more details about the numerical implementation are given in Appendix A. One starts by applying a Fourier transform only over (x, y), leaving z unchanged:

$$\rho(x,y,z),\ \Phi(x,y,z) \rightarrow \hat{\rho}(\mathbf{k},z),\ \hat{\Phi}(\mathbf{k},z) \tag{12}$$
$$\mathbf{k} = (k_x, k_y)^T \quad \text{and} \quad k = \sqrt{k_x^2 + k_y^2}.$$

The Poisson equation then takes on the form

$$-k^2\hat{\Phi} + \partial_z^2\hat{\Phi} = 4\pi G\hat{\rho}. \tag{13}$$

Solving Eq. (13) for $\hat{\Phi}$, assuming a mass density $\hat{\rho} = \delta(z - z')$ yields Green's function for the vertical direction (see also Koyama & Ostriker 2009):

$$G(k,(z-z')) = 2\pi G \begin{cases} -\frac{1}{k}\exp(-k|z-z'|) & \text{for } k \neq 0 \\ |z-z'| & \text{for } k = 0. \end{cases} \tag{14}$$

The solution for arbitrary $\hat{\rho}(\mathbf{k}, z)$ can then be obtained by applying a convolution $\hat{\Phi}(\mathbf{k},z) = \int \hat{\rho}(\mathbf{k},z')\, G(k,(z-z'))\,\mathrm{d}z'$. The potential in real space then is

$$\Phi(x,y,z) = \frac{1}{4\pi^2}\int\left(\int_{-\infty}^{\infty}\hat{\rho}(\mathbf{k},z')G(k,(z-z'))\mathrm{d}z'\right) \ldots \exp(ik_x x + ik_y y)\,\mathrm{d}^2\mathbf{k}. \tag{15}$$

As is described in more detail in Appendix A, the convolution integral can be evaluated such that only three-dimensional FFTs of sizes $N_x \times N_y \times N_z$ and $N_x \times N_y \times (2N_z)$ occur. In order to evaluate the convolution for a finite domain size in z, vacuum boundary conditions (see Koyama & Ostriker 2009; Shi & Chiang 2014) are assumed. This implies that the mass density vanishes outside the vertical boundaries. The values in the vertical boundary cells are calculated by explicitly integrating $\nabla^2\Phi = 0$ in the z direction. Finally, it is noted that this method is different from the method used in Riols & Latter (2018a). Both agree up to Eq. (13), but differences arise in the treatment of the z dependence. Instead of using Green's function and convolutions, Riols & Latter (2018a) applied a finite difference scheme in order to solve Eq. (13) for all z values.

4. MRI and SG benchmarks

4.1. MRI turbulence

Pure MHD simulations were prepared as a benchmark for magneto-rotational instability. We solved Eqs. (2a)–(2f) without the self-gravity term $\underline{\mathbf{G}}$ in the Euler-equation and with the energy evolution equation (Eq. (2e)) replaced by an isothermal equation of state $P = \rho c_{\mathrm{s},i}^2$ ($c_{\mathrm{s},i} = 0.780869$ is set at simulation start). The initial condition for the magnetic field is a zero-net-flux type ($\mathbf{B}(t = 0) = B_0 \sin(2\pi x/L_x)\,\mathbf{e}_z$), with the field pointing in the z direction (similarly to Simon et al. 2011). The initial field amplitude is defined by the ratio of thermal-to-magnetic pressure β_0 at the start of the simulation. Hence, $B_0 = \sqrt{2\mu_0 P_0/\beta_0}$, whereby P_0 is the mid-plane value of the initial Gaussian pressure stratification. Instability is initiated by adding small random perturbations to the mass density and the thermal pressure.

Table 1. MRI-benchmark simulations.

	20pHbeta100	30pHbeta100	20pHbeta200
L_x, N_x	$2H$, 40	$2H$, 60	$2H$, 40
L_y, N_y	$4H$, 80	$4H$, 120	$4H$, 80
L_z, N_z	$8H$, 170	$8H$, 240	$8H$, 170
β_0	100	100	200
$\langle Q_{\mathrm{MRI},z}\rangle_t$	7.4	11.6	8.0
$\langle Q_{\mathrm{MRI},y}\rangle_t$	30.7	44.7	32.8
$\langle Q_{\mathrm{MRI},x}\rangle_t$	10.1	16.3	10.7
α_{m}	0.0195	0.020	0.021
α_{r}	0.0052	0.0053	0.0058
$\alpha_{\mathrm{m}}^{(0)}$	0.0047	0.0048	0.0052
$\alpha_{\mathrm{r}}^{(0)}$	0.0013	0.0013	0.0014
r_{sp}	0.34	0.36	0.33
$\alpha_{\mathrm{m}}/\alpha_{\mathrm{r}}$	3.75	3.77	3.62

Notes. The box dimensions in direction i are given by L_i in scale heights and N_i in grid points. The variables $\langle Q_{\mathrm{MRI},z}\rangle_t$, $\langle Q_{\mathrm{MRI},y}\rangle_t$, $\langle Q_{\mathrm{MRI},x}\rangle_t$, α_{m}, α_{r}, and r_{sp} are determined by averaging over a time interval of $500\Omega_0^{-1}$ starting $100\Omega_0^{-1}$ after initialisation. For determining the stresses $\alpha_{m,r}$, Eq. (8) is used, but the factor $2/(3\gamma)$ is excluded. The values $\alpha_{m,r}^{(0)}$ are determined the same way, only the normalisation is close to the mid-plane-pressure at the start of the simulation $P_0(t = 0)$ instead of the averaged pressure.

Three different configurations varying in resolution and β_0 are chosen (20pHbeta100, 30pHbeta100, and 20pHbeta200). The simulation specifics are listed in the first four lines of Table 1. All configurations share the same box size, whereby 20pHbeta100 and 20pHbeta200 are resolved by ∼20 points per scale height in all three directions and 30pHbeta100 by ∼30 points. The physical box size in the (x, y)-plane is chosen as equal to that used in Simon et al. (2011), Riols & Latter (2018a). The vertical domain size is $8H$, which has turned out to reasonably capture the vertical disc structure. The vertical resolution in 20pHbeta100 is chosen similar to that used for GI (see Sect. 4.2) and is also similar to the (x, y)-resolution. It is noted that an additional constraint arises as the total number of processors used has to be divisible by 20 (see Appendix C).

All simulations immediately develop a butterfly diagram, as can be seen for 20pHbeta100 in Fig. 1, showing the horizontally averaged toroidal magnetic-field component $\langle B_y\rangle_{xy}$. This is a common feature in zero-net-flux MRI simulations (see e.g., Brandenburg et al. 1995; Brandenburg & Donner 1997; Miller & Stone 2000; Davis et al. 2010; Gressel 2010; Simon et al. 2011).

We also tested whether the magneto-rotational instability is resolved in the chosen configurations. An approximate criterion for this is given by the ratio of the most unstable MRI wavelength ($\sim 2\pi v_{\mathrm{A},i}/\Omega_0$, see e.g., Balbus & Hawley 1998) to the discretisation length of the grid ($\delta x_i = L_i/N_i$). The index i refers to the ith Cartesian component. The resulting quality factor is

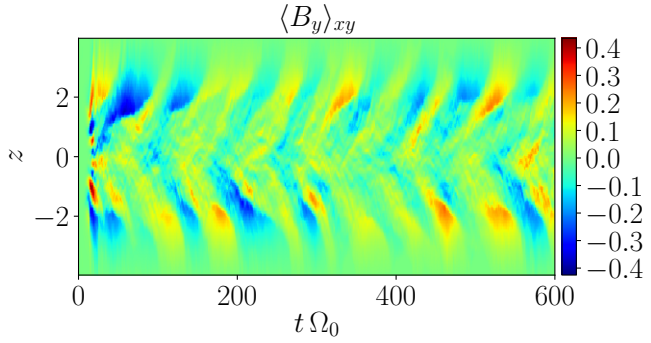

Fig. 1. (z, t)-diagram of the horizontally averaged toroidal magnetic field component $\langle B_y \rangle_{xy}$ for simulation 20pHbeta100. A butterfly pattern emerges shortly after the start of the simulation.

often referred to as Q_{MRI} (see e.g., Noble et al. 2010; Simon et al. 2011):

$$Q_{\mathrm{MRI},i} = \frac{2\pi v_{\mathrm{A},i}}{\Omega_0 \delta x_i} = \frac{2\pi N_i}{\Omega_0 L_i} \sqrt{\frac{\langle B_i^2 \rangle}{\langle \rho \rangle}}. \tag{16}$$

Hence, $Q_{\mathrm{MRI},i} > 1$ is required for the MRI to be resolved. Sano et al. (2004) found $Q_{\mathrm{MRI},z} \gtrsim 6$ as a criterion for MRI to be fully resolved. Time-averaged values $\langle Q_{\mathrm{MRI},i} \rangle_t$ are shown for all three configurations in Table 1. In all cases, one finds $\langle Q_{\mathrm{MRI},y} \rangle_t > \langle Q_{\mathrm{MRI},x} \rangle_t > \langle Q_{\mathrm{MRI},z} \rangle_t$. The lowest value is $\langle Q_{\mathrm{MRI},z} \rangle_t = 7.4$, observed for 20pHbeta100 and above the threshold found by Sano et al. (2004). Furthermore, as a clearly visible butterfly diagram emerges, the simulations are considered sufficiently resolved.

In MRI calculations, the turbulent stress has two contributions, the Maxwell part and the Reynolds part, see Eqs. (8) and (9). Time-averaged values of the stress contributions α_{r} (Reynolds), α_{m} (Maxwell), and $\alpha = \alpha_{\mathrm{r}} + \alpha_{\mathrm{m}}$ are listed in Table 1. For incompressible and isothermal MRI simulations, the factor $(2/(3\gamma))$ in Eq. (8) is often not considered. Hence, for better comparison with other MRI-related literature, that additional factor is not used for the values listed in Table 1. Also, the stresses are sometimes normalised by the mid-plane pressure instead of the volume-averaged pressure. Hence, values normalised by the mid-plane pressure at the start of the simulation $P_0(t = 0)$ are additionally provided in Table 1, designated $\alpha^{(0)}_{m,r}$. The obtained values agree well with previous studies. Stone et al. (1996) found ($\alpha_{\mathrm{m}} = 0.0044$, $\alpha_{\mathrm{r}} = 0.00125$) for run 'IZ1' (compared to values $\alpha^{(0)}_{m,r}$ in Table 1) and Simon et al. (2011) found ($\alpha_{\mathrm{m}} = 0.022$, $\alpha_{\mathrm{r}} = 0.0058$) for run '32Num' (compared to values $\alpha_{m,r}$ in Table 1).

In all three configurations, one finds Maxwell-to-Reynolds stress ratios in the $\alpha_{\mathrm{m}}/\alpha_{\mathrm{r}} \approx 3.6 - 3.8$ (Table 1) range. This is typical for magneto-rotational turbulence and is often observed in simulations (see e.g., Hawley et al. 1995; Blackman et al. 2008; Simon et al. 2011; Riols & Latter 2018a).

Another quantity that is found to yield typical values for MRI turbulence is the ratio of Maxwell stress to magnetic pressure: $r_{\mathrm{sp}} = \langle \langle -B_x B_y \rangle / \langle B^2/2 \rangle \rangle_t$ (Hawley et al. 1995; Blackman et al. 2008; Simon et al. 2011; Hawley et al. 2011). Observed values often lie in the 0.3–0.4 range. For all three cases studied here, one finds a value of $r_{\mathrm{sp}} \sim 0.35$ (see Table 1), which agrees well with the expected range for MRI. As we show below, this also holds for the GI-MRI combined state.

Table 2. Hydrodynamical benchmark simulations with self-gravity.

	GI058	GI072	GI087	GI095
L_x, N_x	$20H$, 440	–	–	–
L_y, N_y	$20H$, 440	–	–	–
L_z, N_z	$8H$, 170	–	–	–
γ	1.64	–	–	–
$\tau_{\mathrm{c}}\Omega_0$	10	–	–	–
$\langle Q_0 \rangle_t$	0.58	0.72	0.87	0.95
$\langle \langle Q \rangle \rangle_t$	1.06	1.06	1.13	1.19
α_{r}	0.0128	0.0079	0.0051	0.0040
α_{g}	0.0176	0.0143	0.0104	0.0083
α	0.0304	0.0222	0.0155	0.0123
α_p	0.0296	0.0225	0.0176	0.0157
F_{g}	1.38	1.80	2.03	2.05

Notes. The four configurations differ in their background Toomre value Q_0 (contained mass), with the latter values appearing in the respective designation. The variables $\langle Q_0 \rangle_t$, $\langle \langle Q \rangle \rangle_t$, and $\alpha_{\ldots}$, are time-averaged over an interval of $120\Omega_0^{-1}$ beginning $40\Omega_0^{-1}$ after the start of the simulation. The Maxwell-to-Reynolds stress-ratio, $F_{\mathrm{g}} = \alpha_{\mathrm{g}}/\alpha_{\mathrm{r}}$, was calculated from the averages. Box sizes, as well as γ and $\tau_{\mathrm{c}}\Omega_0$, are equal for all simulations.

4.2. GI turbulence

In order to study purely gravito-turbulent states in stratified shearing box systems, Eqs. (2a)–(2f) are solved with $\mathbf{B} = \mathbf{J} = 0$. The cooling (heating) model used is that in Eq. (5), with the first term representing radiative cooling with cooling time τ_{c} and the second term accounting for irradiation heating with irradiation temperature $\propto c_{\mathrm{s},0}$. It is noted that in code units, $c_{\mathrm{s},0} = 1$ (see Sect. 2).

We discuss four different configurations, which are shown as columns in Table 2. The four configurations differ in the total mass contained in the box volume. A convenient dimensionless measure for the mass content is the background Toomre value Q_0, Table 2. Background here means that the constant value $c_{\mathrm{s},0}$ (irradiation) is used in Q_0 instead of c_{s}, and, hence, Q_0 only depends on the volume-averaged mass density $\langle \rho \rangle$ (see also Sect. 2). The vertical boundary conditions allow mass to leave the box, causing Q_0 to slightly evolve over time. As the latter effect is small, a time average $\langle Q_0 \rangle_t$ over an interval of $120\Omega_0^{-1}$ is provided in Table 2. Listed separately from the background value is the saturated Toomre value $\langle \langle Q \rangle \rangle_t$. The inner average $\langle Q \rangle$ is over the volume and calculated according to Eq. (7). The obtained values are then averaged over the respective time interval (outer brackets). It is noted that, in contrast to Q_0, $\langle Q \rangle$ also depends on the saturated sound speed $\langle c_{\mathrm{s}} \rangle$ and is therefore also sensitive to the saturation level of the thermal energy density.

The box dimensions are the same for all four simulations and are listed in the first three rows of Table 2. Box dimensions of $20H$ in both horizontal directions turned out to be reasonable for GI, avoiding bursting behaviour due to unstable modes fitting the box size as well as being reasonable in terms of computational effort. The horizontal box size is also similar to that used in Riols & Latter (2018a). The corresponding number of grid points is a compromise between computational accessibility and resolution, whereby the z resolution is chosen to be similar to the horizontal. Hence, the resolution is also comparable to (slightly higher than) that used for 20pHbeta100. Similar to the MRI cases, one has to take into account that the total number of processors used to parallelise over (x, y) is ideally divisible by 20. Hence, 440 points in both horizontal directions is a convenient choice (see

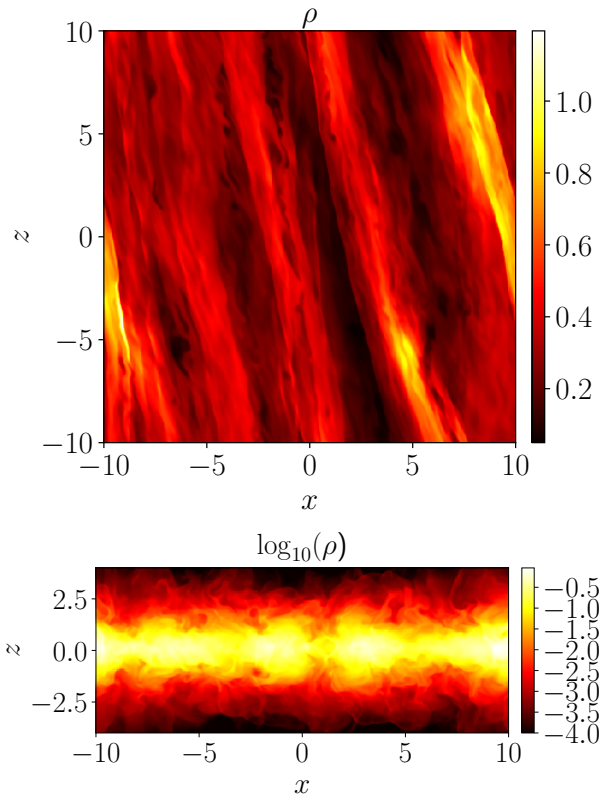

Fig. 2. Mass-density slices for GI072 in fully developed turbulence, $40\Omega_0^{-1}$ after restart. *First image*: horizontal slice $\rho(x, y, z = 0)$. *Second image*: vertical slice $\log_{10}(\rho)(x, y = 0, z)$. The logarithm is used in the bottom image as the latter provides a more convenient visual guide for the vertical density profile.

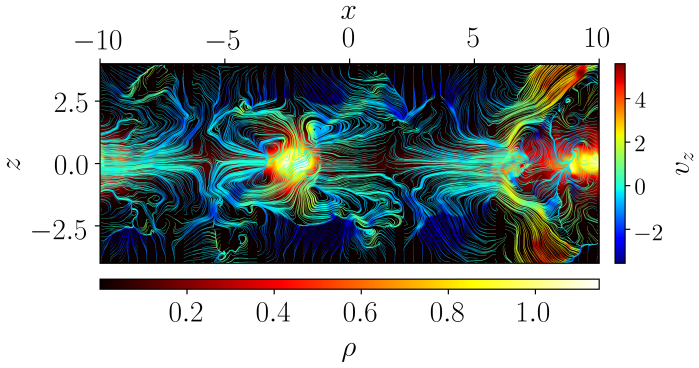

Fig. 3. Poloidal mass-density slice $\rho(x, y = 0, z)$ with stream lines traced in the (x, z) plane. Stream-line colours are mapping the vertical velocity component away from the mid-plane ($\mathrm{sign}(z)\, v_z$). The stream lines are traced for one fixed point in time (t = const.) and by considering only the velocity components (v_x, v_z).

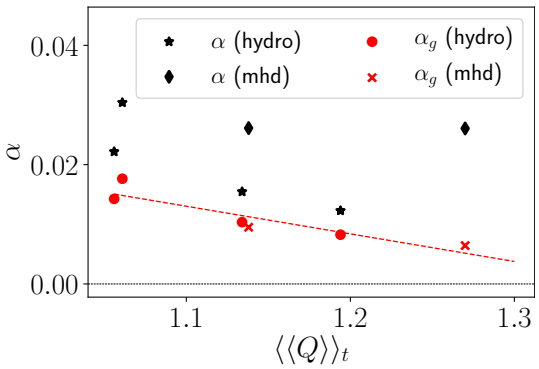

Fig. 4. Time-averaged dimensionless turbulent stresses (Eqs. (8) and (9)) as function of the volume and time-averaged Toomre parameter $\langle\langle Q\rangle\rangle_t$. Each data point corresponds to one simulation. The black stars show the sum total of Reynolds and gravitational stress $\alpha = \alpha_\mathrm{r} + \alpha_\mathrm{g}$ for the hydrodynamical simulations (GI058, GI072, GI087, GI095). The corresponding contributions from the gravitational stress α_g are hown as red dots. Depicted as black diamonds and red crosses are α and α_g for the MHD simulations sg-mhd-1 and sg-mhd-2 (discussed in the following sections). In MHD cases, one has $\alpha = \alpha_\mathrm{r}+\alpha_\mathrm{g}+\alpha_\mathrm{m}$, with Maxwell contribution α_m. The red dashed line is a guide to the eye (linear fit) for the trend in α_g.

also Appendix C). The chosen CFL number in all cases is 0.06. All simulations listed in Table 2 are restarted from an initial simulation that has been brought into the nonlinear state. At the restart time, the mass densities have been rescaled to yield different total box masses ($\Rightarrow$ different Q_0; see Appendix B).

Mass-density snapshots for simulation GI072 are visualised in Fig. 2, with the first image showing a horizontal slice (x, y) and the second image depicting a vertical slice (x, z). In the bottom image, the base-ten logarithm of the mass density is used in order to provide a more convenient visual representation. In the (x, y) slice, one can see density waves and also shocks, separating the waves from lower density regions. Similarly to the findings in Riols & Latter (2018b), vortical motions above and below density waves are also observed. This is captured well in Fig. 3, which depicts an (x, z) slice of the mass density and the vertical stream lines for a fixed time point in the turbulent state of GI058. One can clearly observe four eddies symmetrically oriented around the density maximum near the centre of the image. The stream lines are traced only in the (x, z) plane, that is, neglecting the velocity component v_y. The line colouring is such that motion away from the mid-plane is positive and motion towards the mid-plane is negative ($\mathrm{sign}(z)\, v_z$).

In hydrodynamic, self-gravitating cases, the turbulent stress has two contributions: a Reynolds-part and a gravitational-part (see Eqs. (8)–(9)). Time averages of the dimensionless stress contributions α_r (Reynolds), α_g (gravitational), and $\alpha = \alpha_\mathrm{r} + \alpha_\mathrm{g}$ are provided in Table 2. The obtained values for α and α_g are shown as a function of the saturated Toomre parameter $\langle\langle Q\rangle\rangle_t$ in Fig. 4, whereby red dots correspond to α_g and black stars correspond to α. The time averages for both $\alpha_{...}$ and $\langle Q\rangle$ were taken over an interval of $120\Omega_0^{-1}$ in the fully developed turbulent state of each simulation. The MHD simulations sg-mhd-1 and sg-mhd-2 that will be discussed in later sections are shown as diamonds and crosses. The red dashed line is a guide for the eye (linear fit) for the trend in α_g.

The energy balance is also tested in the nonlinear state. The only way the system can lose or gain energy is by extracting kinetic energy from the background shear flow (*Kepler*) or by radiative cooling and irradiation heating (Eq. (5)). Minor losses over the vertical boundaries may also occur. In a stationary state, the kinetic energy extracted from the *Kepler* shear (related to α) is balanced by net cooling and irradiation (related to $\langle\rho\dot{q}\rangle$). The balance can be used to derive a relation between the cooling rate and the dimensionless turbulent stress α (see Gammie 2001; Rice et al. 2011). For the cooling-model used here, this is

$$\alpha = \frac{4}{9\gamma(\gamma-1)\tau_\mathrm{c}\Omega_0}\left(1 - \frac{\langle\rho\rangle\, c_{\mathrm{s},0}^2}{\gamma(\gamma-1)\langle E_\mathrm{th}\rangle}\right), \tag{17}$$

with $P = (\gamma - 1)E_{\rm th}$. The values $\alpha_{\rm p}$ calculated via Eq. (17) are also shown in Table 2. As can be seen, for all simulations the $\alpha_{\rm p}$ are in good agreement with the values α obtained via Eq. (8), proving that the energy balance between turbulent dissipation and cooling is statistically satisfied with a high level of accuracy.

5. MHD simulations including self-gravity and irradiation heating

5.1. Initial conditions

To investigate interactions of the gravito-turbulent state with magnetic fields, a simulation with fully developed gravito-turbulence but no magnetic field is restarted introducing a magnetic seed field (see also the method used in Riols & Latter 2018a, 2019). The initial field is seeded into the turbulent state of GI072, $40\Omega_0^{-1}$ after the start of the simulation. This corresponds to the density slices shown in Fig. 2. It is noted that, unless stated otherwise, the time axes in all subsequent plots start at $t\Omega_0 = 120$, which is due to the fact that GI072 is restarted from an initial simulation (see Appendix B) and $t\Omega_0 = 120$ corresponds to the absolute time point when the seed field is introduced.

For simplicity, the aforementioned combined simulation is referred to as sg-mhd-1 in the following. The magnetic seed field is chosen such that $\beta \sim 10^{10}$, to make sure that no artefacts from the initial conditions arise. The initial seed-field configuration is of zero-net-flux type, with the field pointing in the z direction:

$$\mathbf{B}_0 = B_0 \sin(2\pi\, x/L_x)\, \mathbf{e}_z \tag{18}$$

$$B_0 = 10^{-5} \leftrightarrow \langle\beta\rangle = 2\langle P\rangle/\langle B^2\rangle \approx 2.66 \times 10^{10}. \tag{19}$$

All hydrodynamic simulation parameters of GI072 are passed on to sg-mhd-1. This includes the radiative cooling model of Eq. (5), with a cooling-time of $\tau_{\rm c}\Omega_0 = 10$.

5.2. Observed time evolution

This section is used to report on some prominent features that are observed in the self-gravitating MHD simulations. More detailed discussions of some of the aspects are provided in subsequent sections.

The time evolution of the box-averaged magnetic energy density for sg-mhd-1 can be seen in the first image of Fig. 5 as the dashed and dotted lines, corresponding to the left abscissa. Most of the energy is in the y component ($\langle B_y^2\rangle$, dotted line), followed by minor contributions from the x component ($\langle B_x^2\rangle$, dashed line) and the z component ($\langle B_z^2\rangle$, dash-dotted line). The system enters a growth phase immediately after initialisation, with the magnetic energy density increasing between five and eight orders of magnitude within $120 \lesssim t\Omega_0 \lesssim 400$. The growth then stagnates for $t\Omega_0 \gtrsim 400$. In the latter phase, the volume-averaged magnetic field components are oscillating (see e.g., $\langle B_y\rangle$ as the black solid line in the first image of Fig. 5). The simulation sg-mhd-2 (red solid line) is discussed in more detail in the last paragraph of this section. $\langle B_y\rangle$ yields significantly larger oscillation amplitudes than the other components, and, during maxima, ∼30% of the total magnetic energy is assigned to $\langle B_y\rangle^2/2$.

In order to asses whether MRI can be active, one can calculate the $Q_{{\rm MRI},j}$ parameters (Eq. (16)) for each field component, B_j, using the time evolution of the magnetic energy densities. First considered is the initial phase, $120 \leq t\Omega_0 \lesssim 400$.

Table 3. $\langle Q_{{\rm MRI},j}\rangle_t$ for sg-mhd-1. The values are calculated according to Eq. (16) and averaged over the respective time interval.

	$Q_{{\rm MRI},x}$	$Q_{{\rm MRI},y}$	$Q_{{\rm MRI},z}$
$120 \leq t\Omega_0 \leq 200$	0.089	0.208	0.060
$200 \leq t\Omega_0 \leq 300$	1.211	2.953	0.812
$300 \leq t\Omega_0 \leq 400$	5.765	15.660	3.697

Similarly to the energy densities, the $Q_{{\rm MRI},j}$ also increase with time, and it is found that $Q_{{\rm MRI},y} \geq Q_{{\rm MRI},x} \geq Q_{{\rm MRI},z}$. Time averages over three different intervals in the initial phase are shown in Table 3.

As can be seen, $Q_{{\rm MRI},z} < 1$, except for the last interval. The z contribution is important as the Alfven component $v_{{\rm A},z}$ is connected to the most unstable MRI mode (see e.g., Sano et al. 2004). It was pointed out in Sano et al. (2004) that $Q_{{\rm MRI},z} < 6$ can lead to the decay of turbulence or significantly lower saturation levels (see also Sect. 1). In Simon et al. (2011), stratified, resistive, and viscous simulations are studied, and it is found that certain parameter regimes lead to time intervals of low turbulent activity. It is also mentioned that those intervals coincide with periods of unresolved poloidal magnetic fields, and turbulence sets back in once the shear has generated enough toroidal field strength B_y to restart turbulence. Hence, one concludes that MRI is, at maximum, marginally resolved in the early phases of sg-mhd-1. Especially in the interval $120 \leq t\Omega_0 \leq 200$, all $Q_{{\rm MRI},j}$ are significantly lower than one, and MRI is almost certainly absent. Further hints for this are also given in Sect. 6. Nevertheless, significant field amplifications are observed in that time period, as can be seen from the energy densities in Fig. 5. However, in the last image of Fig. 6 it is also observed that the ratio

$$\left\langle \frac{F^B_{x,y}}{F^{\rm SG}_{x,y}} \right\rangle_{xy} = \left\langle \frac{\sqrt{(\mathbf{B}\cdot\nabla B_x)^2 + (\mathbf{B}\cdot\nabla B_y)^2}}{\sqrt{(\rho\partial_x\Phi)^2 + (\rho\partial_y\Phi)^2}} \right\rangle_{xy}, \tag{20}$$

relating horizontal forces due to the field line being bent to horizontal forces due to self-gravity, is significantly lower than one for $t\Omega_0 \lesssim 400$. Here, the values shown in Fig. 6 are horizontal averages. It is noted that the field-line bending forces are also an important part of MRI. Weak magnetic pressure forces are guaranteed by the high initial thermal-to-magnetic pressure ratio $\beta \sim 10^{10}$. Hence, one concludes that MRI is most likely absent from the initial phase, and Lorentz forces in general are negligible compared to self-gravity forces. Consequently, one has to assume that the system would be stable without GI and the initial field amplifications must then be caused by kinematic effects of GI turbulence. This suggests that GI provides a possible dynamo mechanism. Additionally, in contrast to the low initial $Q_{{\rm MRI},j}$ values, the saturation level of the $Q_{{\rm MRI},j}$ is roughly two-to-three times larger than for the pure MRI simulations. For the toroidal component, this yields $Q_{{\rm MRI},y} \sim 50{-}90$ for $t\Omega_0 \gtrsim 600$.

The second image in Fig. 5 shows the turbulent stresses normalised by the volume-averaged pressure, following Eqs. 8 and 9. It is noted that both $\alpha_{\rm r}$ and $\alpha_{\rm m}$ significantly fluctuate with time and are therefore smoothed by folding the time series with a Gaussian distribution (standard deviation $\sigma = 3\Omega_0^{-1}$).

Similarly to the magnetic energy, the Maxwell contribution to the stress ($\alpha_{\rm m}$) is also increasing significantly and even becomes the dominant stress contribution for $t\Omega_0 \gtrsim 700$. This is in contrast to Riols & Latter (2018a), in which $\alpha_{\rm g}$ is the dominant contribution.

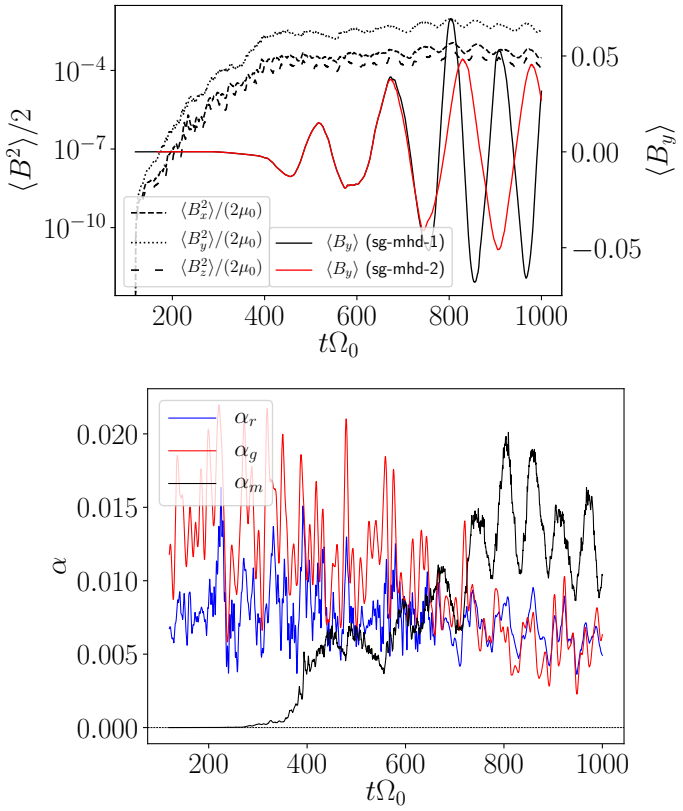

Fig. 5. Time evolution for a selection of volume-averaged quantities, whereby the first image shows quantities related to the magnetic field and the second image depicts the turbulent stresses. *First image:* left axis, dashed and dotted lines: box-averaged magnetic energy densities for B_x, B_y, and B_z. Right axis, solid lines: box-averaged toroidal field component $\langle B_y\rangle$ for simulations sg-mhd-1(black) and sg-mhd-2(red). Simulation sg-mhd-2 is discussed in the last paragraph of this section. *Second image*: turbulent stresses normalised by pressure sorted for α_r (Reynolds), α_g (gravity), and α_m (Maxwell). The stresses (α_r, α_g) are smoothed using a Gaussian convolute (standard deviation $\sigma = 3\Omega_0^{-1}$).

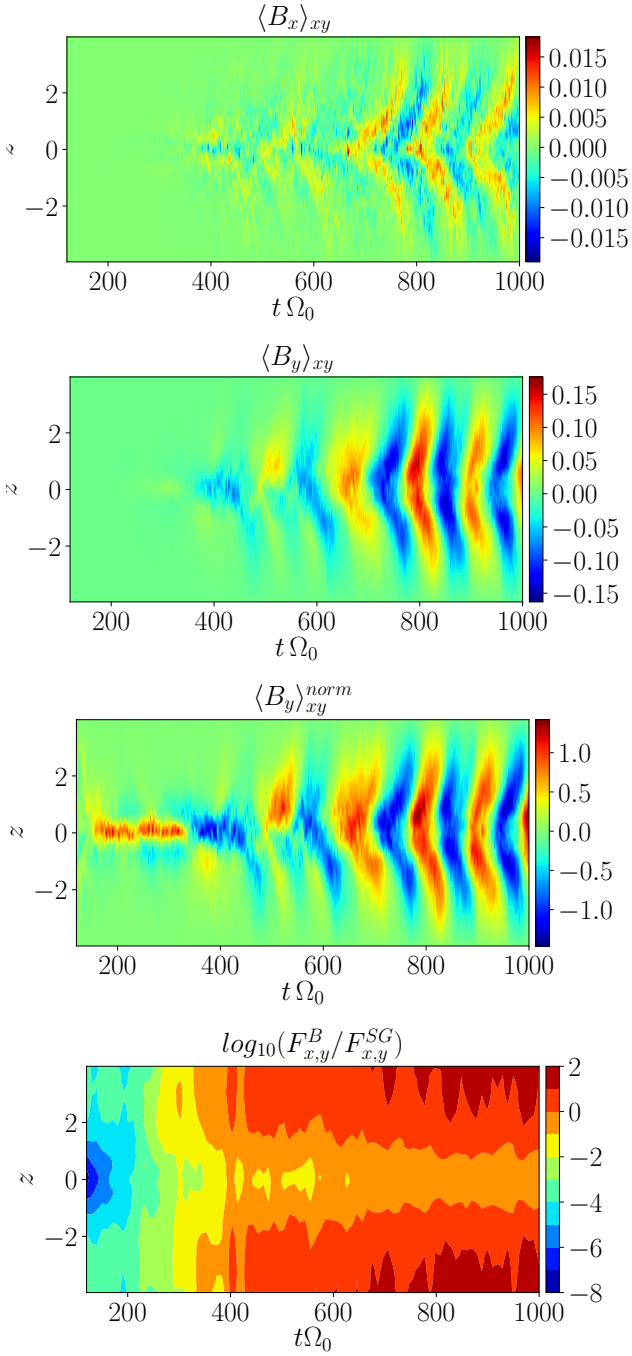

Fig. 6. (z, t) diagrams for different horizontally averaged quantities in sg-mhd-1. The first two images show the magnetic field components $\langle B_x\rangle_{xy}$ and $\langle B_y\rangle_{xy}$, respectively. The third image shows $\langle B_y\rangle_{xy}^{\rm norm} = \langle B_y\rangle_{xy}/\sqrt{\langle B^2\rangle}$. The last image shows the ratio of field-line bending forces to gravitational forces in the horizontal direction (see text and Sect. 6 for more details).

The volume-averaged toroidal field component $\langle B_y\rangle$ for sg-mhd-1 is shown in the first image of Fig. 5 as the solid black curve. For $t\Omega_0 \gtrsim 400$, clear oscillations with growing amplitude can be observed. We only show the y component, though the same oscillation occurs for the $\langle B_x\rangle$ component as well. This can also be seen in the horizontally averaged field components $\langle B_x\rangle_{xy}$ and $\langle B_y\rangle_{xy}$, which are shown in the first two images of Fig. 6. The oscillations appear as a clearly regular pattern that closely resembles that of a butterfly diagram, similar to MRI turbulence (see e.g., Gressel 2010; Davis et al. 2010; Simon et al. 2011). Field reversals are also found in Riols & Latter (2018a), although they are much less regular and more concentrated to the mid-plane, especially for cooling times $t\Omega_0 \lesssim 20$. The pattern obtained here appears to be more akin to that found in the global simulations of Deng et al. (2020).

The first of the bottom two images in Fig. 6 shows $\langle B_y\rangle_{xy}$, except that the averaged field components are normalised by the root-mean-squared field, which is averaged over the entire box volume at that particular time point: $\langle B_{x,y}\rangle_{xy}/\sqrt{\langle B^2\rangle}$. From that, one can see that the initial phase $t\Omega_0 \lesssim 400$ is qualitatively different from later times. One field reversal near the mid-plane is observed shortly before $t\Omega_0 = 400$, though this may already be a first manifestation of the emerging butterfly diagram. Also, the magnetic activity seems to be concentrated closer to the mid-plane, which is clearly in contrast to the butterfly-diagram that develops later. This initial state appears to be qualitatively closer to the state observed in Riols & Latter (2018a), where most of the activity is near the mid-plane and field reversals occur less regularly.

The last image in Fig. 6 shows the ratio of horizontal field-line bending forces, $\sqrt{(\mathbf{B}\cdot\nabla B_x)^2 + (\mathbf{B}\cdot\nabla B_y)^2}$, to horizontal self-gravity forces, $\sqrt{(\rho\,\partial_x\Phi)^2 + (\rho\,\partial_y\Phi)^2}$, whereby the base-ten

logarithm of the values is depicted. For $t\Omega_0 \lesssim 400$, self-gravity clearly dominates (see also the discussion above), whereas for later times, forces due to field-line bending can significantly exceed self-gravity above and below the mid-plane (see also Sect. 6).

The total mass in the simulation volume ($M = \langle\rho\rangle L_x L_y L_z$) starts to decrease once the magnetic field becomes more dominant $t\Omega_0 \gtrsim 400$. This trend is shown for the volume-averaged mass density $\langle\rho\rangle$ by the blue declining curve in Fig. 7. We interpret this as an increased wind activity at the vertical box boundaries. Something similar is also observed for the global simulations in Deng et al. (2020). One can take advantage of this by restarting sg-mhd-1 at a given time point (here $t\Omega_0 = 600$) and holding the total mass in the box volume constant from then on. This restarted simulation is referred to as sg-mhd-2 in the following. Consequently, sg-mhd-1 and sg-mhd-2 can really only be compared for $t\Omega_0 > 600$. Simulation sg-mhd-1 for $t\Omega_0 > 600$ and simulation sg-mhd-2 are exactly equal, with the only difference being that the total mass contained in the box volume is held constant in sg-mhd-2. Hence, the volume-averaged mass density $\langle\rho\rangle$ stays constant in sg-mhd-2, whereas it slowly decreases in sg-mhd-1 (see the dashed blue lines in Fig. 7). Clearly, at $t\Omega_0 = 600$ the values for $\langle\rho\rangle$ are exactly equal in sg-mhd-1 and sg-mhd-2. This reflects on the Toomre values $\langle\langle Q\rangle\rangle_t$ and the latter split at $t\Omega_0 = 600$ with $\langle Q\rangle$ increasing for sg-mhd-1 and $\langle Q\rangle$ staying roughly constant for sg-mhd-2 (see the solid black lines in Fig. 7). This allows one to study the dependence of various quantities on the Toomre parameter in the presence of magnetic fields. For example, one now has two data points for MHD cases in Fig. 4 instead of only one. The last point is elaborated on in more detail in the next section. The replenishing is achieved by calculating the total box mass at each moment and comparing it to the original value (here at $t\Omega_0 = 600$). Once the mass deviates by more than 1%, the latter is restored to its original value by adding a density correction $\delta\rho$ at each grid point, such that the integral yields exactly the missing mass, $\int \delta\rho \, \mathrm{d}V = \triangle M$. Thereby, the density correction is distributed homogeneously over (x, y) and has a Gaussian profile in the z direction. Here, $\delta\rho = (\triangle M \exp(-0.5\,(z/h)^2)/(\sqrt{2\pi}\, h\, L_x L_y))$ with $h = 0.5$ is chosen. Between sg-mhd-1 and sg-mhd-2, no qualitative changes are observed, with the butterfly diagram, for instance, being unchanged. The box-averaged toroidal field component $\langle B_y\rangle$ for sg-mhd-2 is shown as the red, solid curve in Fig. 5, and it can be seen that no qualitative changes occur, except slight changes in frequency and amplitude. However, quantitative changes in the time-averaged stresses can be observed between sg-mhd-1 and sg-mhd-2. This is discussed in more detail in the next section.

6. GI-MRI coexistence

6.1. Testing the presence of MRI

Table 4 lists important quantities averaged over both volume and time for simulations sg-mhd-1 and sg-mhd-2. For sg-mhd-1, two different time intervals are considered for the average, $120 \le t\Omega_0 \le 320$, left column, and $700 \le t\Omega_0 \le 1000$, middle column. The first time interval corresponds to the previously discussed initial phase, where the most unstable MRI mode is significantly under-resolved and where MRI is therefore most likely absent. This is further backed up below. Listed in the third column are time averages for sg-mhd-2 (mass held constant) using the second time interval ($700 \le t\Omega_0 \le 1000$).

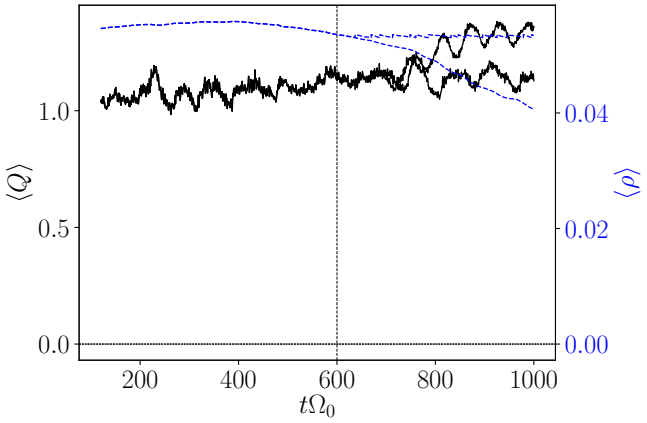

Fig. 7. Saturated Toomre parameter $\langle Q\rangle$ (solid black, left axis) and box-averaged mass density $\langle\rho\rangle$ (dashed blue, right axis). At $t\Omega_0 = 600$, sg-mhd-1 was restarted, with $\langle\rho\rangle$ held constant from then on (sg-mhd-2). Therefore, the values of $\langle\rho\rangle$ start to deviate between sg-mhd-1 and sg-mhd-2 at $t\Omega_0 = 600$. Similarly, the values of $\langle Q\rangle$ also begin to deviate at $t\Omega_0 = 600$. For sg-mhd-1, $\langle Q\rangle$ slightly increases, and for sg-mhd-2, $\langle Q\rangle$ stays almost constant.

In sg-mhd-1, the time-averaged α_m is dominant for $700 \le t\Omega_0 \le 1000$, whereas α_g has decreased by roughly 50% compared to the $120 \le t\Omega_0 \le 320$ interval. The Reynolds contribution α_r is also reduced by ∼20%, which is significantly less than the reduction of α_g. The total stress ($\alpha = \alpha_\mathrm{r} + \alpha_\mathrm{g} + \alpha_\mathrm{m}$) increases from the first to the second time interval by ∼14%, which can be attributed to the emergence of α_m for $t\Omega_0 \gtrsim 400$. Also shown in Table 4 is the predicted total stress, α_p, calculated from the energy balance between turbulent production and radiative cooling (heating) (Eq. (17)). In the low stress interval ($120 \le t\Omega_0 \le 320$) of sg-mhd-1, both α and α_p are in good agreement, indicating that most of the energy extracted from the background is eventually lost through radiative cooling. In the second interval ($700 \le t\Omega_0 \le 1000$) of sg-mhd-1, the α_p-value did not change, but the total stress α increased by ∼14%. This agrees with the observed loss of mass, as the generation of a wind will also lead to an additional energy flux that is not accounted for by radiative cooling. Hence, the most dominant effect of introducing magnetic fields is that the gravitational stress α_g is decreasing, whereas the Maxwell stress α_m is increasing and also overcompensating the reductions of both α_g and α_r.

As it turns out, the reduction of α_g in sg-mhd-1 from the first to the second time interval is related to an increase in the saturated Toomre parameter, $\langle Q\rangle$. The reason for changes in $\langle Q\rangle$ is twofold. The dominant reason in sg-mhd-1 is that, as discussed in Sect. 4, winds at the vertical boundaries lead to a sinking mass in the box volume, thereby increasing both the irradiation-Toomre Q_0 as well as the saturated value $\langle Q\rangle$ (see Table 4). The second reason includes changes in the saturated thermal energy density. The irradiation value Q_0 does only react to changes in mass as the irradiation temperature is held constant ($c_{\mathrm{s},0} = \text{const.}$), but the saturated value $\langle Q\rangle$ can change due to thermal energy changes as it also depends on the saturated sound-speed $\langle c_\mathrm{s}\rangle$. Hence, the $\langle\langle Q\rangle\rangle_t$-difference between sg-mhd-2 and sg-mhd-1 is in part due to the higher mass in sg-mhd-2 (mass held constant), but also due to the slightly different saturation levels of the thermal energy density (see Table 4).

Regardless of the exact changing mechanism, the difference of $\langle\langle Q\rangle\rangle_t$ between sg-mhd-1 and sg-mhd-2 allows one to investigate the dependence of α_g on the saturated Toomre-parameter

Table 4. Selection of volume- and time-averaged quantities for simulations sg-mhd-1,2.

Variable	sg-mhd-1	sg-mhd-1	sg-mhd-2
Time interval	$120 \leq t\Omega_0 \leq 320$	$700 \leq t\Omega_0 \leq 1000$	$700 \leq t\Omega_0 \leq 1000$
$\langle Q_0 \rangle_t$	0.7204 ± 0.004	0.860 ± 0.07	0.74646 ± 0.0005
$\langle\langle Q \rangle\rangle_t$	1.064 ± 0.03	1.270 ± 0.07	1.138 ± 0.02
$\langle E_{\rm th} \rangle_t$	0.1150 ± 0.007	0.098 ± 0.01	0.1182 ± 0.003
$\langle E_{\rm kin} \rangle_t$	0.0205 ± 0.006	0.0087 ± 0.002	0.01350 ± 0.0009
$\langle E_{\rm mag} \rangle_t$	$2.3 \times 10^{-5} \pm 4 \times 10^{-5}$	0.0063 ± 0.001	0.00506 ± 0.0007
$\alpha_{\rm r}$	0.0081 ± 0.001	0.00658 ± 0.0006	0.00739 ± 0.0004
$\alpha_{\rm m}$	$4.7 \times 10^{-5} \pm 8 \times 10^{-5}$	0.0130 ± 0.002	0.0092 ± 0.001
$\alpha_{\rm g}$	0.0142 ± 0.001	0.0064 ± 0.001	0.00951 ± 0.0007
α	0.0223 ± 0.002	0.0261 ± 0.002	0.0261 ± 0.001
$\alpha_{\rm pred}$	0.0229 ± 0.001	0.0229 ± 0.001	0.02408 ± 0.0005

Notes. The respective time intervals, used for the time average, are given in the top row. As sg-mhd-2 is restarted from sg-mhd-1 at $t\Omega_0 = 600$, the first time-interval ($120 \leq t\Omega_0 \leq 320$) is only evaluated for sg-mhd-1. The first interval is chosen such that the magnetic energy densities are negligibly weak ($\sim 10^{-5}$). The standard deviation is calculated by dividing each time interval into five sub-intervals and determining the dispersion. The double average in $\langle\langle Q \rangle\rangle_t$ indicates that Q is first averaged over the volume (Eq. (7)) and afterwards averaged over time.

$\langle\langle Q \rangle\rangle_t$ for the MHD cases. It turns out that the reduction of the time-averaged $\alpha_{\rm g}$ from the first to the second time interval is only 33% for sg-mhd-2 compared to 50% for sg-mhd-1 (see Table 4). A possible trend can be directly analysed using Fig. 4. The dimensionless gravitational stresses $\alpha_{\rm g}$ are shown for sg-mhd-1,2 ($700 \leq t\Omega_0 \leq 1000$) via the two red crosses in Fig. 4, whereby the lower $\alpha_{\rm g}$ value corresponds to sg-mhd-1 (see also Table 4). These values can then be compared to $\alpha_{\rm g}$, obtained from the purely hydrodynamical GI-simulations and shown as red dots. One can clearly see a trend for $\alpha_{\rm g}$ as a function of $\langle\langle Q \rangle\rangle_t$. The data point obtained for sg-mhd-2 is especially close to a hydrodynamical simulation (GI087). It is stressed at this point that sg-mhd-1 (and therefore sg-mhd-2) is restarted initially from GI072 by introducing a seed field. Hence, it appears that the newly formed turbulent states with magnetic fields lead to significantly different values in both $\langle\langle Q \rangle\rangle_t$ and $\alpha_{\rm g}$; though, the dependence $\alpha_{\rm g}(\langle\langle Q \rangle\rangle_t)$ remains similar to the hydrodynamical states. This is clearly not the case for the total stress $\alpha = \alpha_{\rm r} + \alpha_{\rm g} + \alpha_{\rm m}$. From Fig. 4, one can see that simulations sg-mhd-1,2 (black diamonds) deviate significantly from the trend observed for the purely hydrodynamical cases (black stars). This is of course attributed to the emergence of a strong magnetic stress contribution $\alpha_{\rm m}$ (see also Table 4). Despite $\alpha_{\rm g}$ being larger for sg-mhd-2 compared with sg-mhd-1, one can see from Table 4 that the total stress ($\alpha = \alpha_{\rm r} + \alpha_{\rm g} + \alpha_{\rm m}$) for sg-mhd-2 is exactly equal to that found for sg-mhd-1. Consequently, $\alpha_{\rm m}$ is found to be lower in sg-mhd-2 compared to sg-mhd-1. What this suggests is that GI with magnetic fields is qualitatively similar to purely hydrodynamic GI; though, the presence of magnetic fields may have an influence on the Toomre-parameter and thereby on the absolute strength of GI, as measured in $\alpha_{\rm g}$.

It then remains to be tested whether the magnetic stress-contribution $\alpha_{\rm m}$ originates from MRI-turbulence. As shown by the previous considerations, the introduction of magnetic fields did not change the turbulence characteristics of GI, although the absolute values $\langle\langle Q \rangle\rangle_t$ and $\alpha_{\rm g}$ can change. Therefore, a simple superposition may be assumed and the turbulent stress is separated into two contributions: $\alpha = \alpha({\rm GI}) + \alpha({\rm MRI})$. The magnetic part $\alpha_{\rm m}$ then originates from MRI and the gravitational stress $\alpha_{\rm g}$ originates from GI. The Reynolds part has contributions from both MRI and GI. Hence, the following separation of α is suggested:

$$\begin{aligned} \alpha &= \alpha({\rm GI}) + \alpha({\rm MRI}) \\ &= \alpha_{\rm g} + \alpha_{\rm r}({\rm GI}) + \alpha_{\rm r}({\rm MRI}) + \alpha_{\rm m}. \end{aligned} \tag{21}$$

Therein, the Reynolds stress has the contributions $\alpha_{\rm r} = \alpha_{\rm r}({\rm GI}) + \alpha_{\rm r}({\rm MRI})$. One then determines the relations of ($\alpha_{\rm m}$ with $\alpha_{\rm r}$) and ($\alpha_{\rm g}$ with $\alpha_{\rm r}$) for pure MRI and pure-GI states, respectively. More precisely, the ratios $F_{\rm m} = \alpha_{\rm m}/\alpha_{\rm r}$ for MRI and $F_{\rm g} = \alpha_{\rm g}/\alpha_{\rm r}$ for GI are defined. It is noted that this assumes the ratios $F_{\rm g}$ and $F_{\rm m}$ to be set independently from each other. Hence, the presence of MRI does not affect $F_{\rm g}$ and GI does not affect $F_{\rm m}$. It is again noted that this is supported by the previous considerations, showing that the hydrodynamical trend for $\alpha_{\rm g}$ can be extended to the MHD cases as well. To see whether the combined states, sg-mhd-1 and 2, are consistent with the independently set values of $F_{\rm m}$ and $F_{\rm g}$, one first determines the ratio $F_{\rm g}$ from GI simulations and then calculates the resulting $F_{\rm m}$. Simulations of magneto-rotational instability suggest typical values of $3.6 \lesssim F_{\rm m} \lesssim 4.0$ (see Sect. 4.1 and Sect. 8 below). Values for $F_{\rm g}$ are obtained from the pure GI simulations discussed in Sect. 4 and are listed in the last row of Table 2. One could have started with $F_{\rm m}$ and derived $F_{\rm g}$ from that, but $F_{\rm m}$ is rather a fixed (typical) value, whereas $F_{\rm g}$ can depend on the mass content measured by Q_0, as can be seen in Table 2. As Table 2 provides $F_{\rm g}$ for simulations with different total box masses and therefore different values of $\langle Q_0 \rangle_t$, one can estimate the $F_{\rm g}$ for sg-mhd-1 (reduced mass) and sg-mhd-2 (constant mass) by interpolating between the values in Table 2. For sg-mhd-1 one thereby finds $\langle Q_0 \rangle_t = 0.86$ leading to $F_{\rm g} \approx 2.0$ and for sg-mhd-2 it is $\langle Q_0 \rangle_t = 0.75$ leading to $F_{\rm g} \approx 1.85$.

In the combined state, one has $F_{\rm g} = \alpha_{\rm g}/(\alpha_{\rm r}({\rm GI}))$ and as $\alpha_{\rm r} = \alpha_{\rm r}({\rm MRI}) + \alpha_{\rm r}({\rm GI})$, one finds $\alpha_{\rm r}({\rm MRI}) = \alpha_{\rm r} - \alpha_{\rm g}/F_{\rm g}$. This is then substituted in $F_{\rm m} = \alpha_{\rm m}/(\alpha_{\rm r}({\rm MRI}))$, yielding

$$F_{\rm m} = \frac{F_{\rm g}\,\alpha_{\rm m}}{F_{\rm g}\,\alpha_{\rm r} - \alpha_{\rm g}}. \tag{22}$$

Applying Eq. (22) to the values for sg-mhd-1 and sg-mhd-2 (second and third column in Table 4), one finds

$$F_{\rm m} = \begin{cases} 3.85 & \text{For sg}-\text{mhd}-1 \\ 4.09 & \text{For sg}-\text{mhd}-2. \end{cases} \tag{23}$$

Hence, the values are in very good agreement with the expectation for MRI turbulence. This also demonstrates that the combined state is consistent with a coexistence of GI and MRI,

whereby the ratios F_g and F_m are set independently from each other. For comparison, one can also evaluate F_m for the initial phase $120 \leq t\Omega_0 \leq 320$ of simulation sg-mhd-1 (first column in Table 4). There, one finds $\langle Q_0 \rangle_t \sim 0.72$, which is expected, as sg-mhd-1 is restarted from GI072 and the initial magnetic fields are weak. From Table 2 then follows $F_g = 1.8$. Using the time averages in Table 4 and applying Eq. (22), one obtains $F_m = 0.223 \ll 4$. This is further proof supporting the argument in Sect. 5.2 that MRI is absent from the initial phase of sg-mhd-1. It also shows that, even when GI is corrected for, the kinematic stress contributions dominate the magnetic contribution and the fields are likely passive in the initial phase. This further strengthens the picture that the initial field amplification is caused by GI turbulence. This is of course significantly different from the saturated state primarily studied in this section.

Similarly to the pure MRI simulations, one can also check for the ratio of Maxwell stress to magnetic pressure $r_{sp} = \langle \langle -B_x B_y \rangle / \langle B^2/2 \rangle \rangle_t$. For sg-mhd-1, we find $r_{sp} = 0.32$, and for sg-mhd-2 $r_{sp} = 0.34$, whereby the time averages are evaluated for $700 \leq t\Omega_0 \leq 1000$. Hence, the ratio also agrees well with the ratios obtained for the pure MRI simulations (see Sect. 4.1).

The coexistence hypothesis is further backed up by the last image in Fig. 6, depicting the ratio of horizontal field-line bending forces to horizontal forces of self-gravity $\langle F^B_{x,y} / F^{SG}_{x,y} \rangle_{xy}$, evaluated for sg-mhd-1. As can be observed in Fig. 6, values of $\langle F^B_{x,y} / F^{SG}_{x,y} \rangle_{xy} > 1$ occur for $t\Omega_0 \gtrsim 400$. The ratio increases with $|z|$, and for higher altitudes one even finds values up to ~100 and the bending forces clearly dominate. Only near the mid-plane ($|z| \lesssim 1H$) does one find self-gravity forces to be significantly larger than field-line bending. Since the instability mechanism of MRI relies on field-line bending forces (see e.g., Balbus & Hawley 1998), this is a strong indication that the latter is active, at least for higher altitudes.

6.2. Discussion and comparison to previous studies

At this point, it is useful to present a short discussion about the interpretation of the previously obtained results and also to give a comparison to the findings for the non-irradiated cases studied in Riols & Latter (2018a). First, an overview of similarities and differences to the setup of the SGMRI simulations in Riols & Latter (2018a) is given. The similarities are discussed first. One of them is the horizontal box size, which is $20H$ in both the x and the y direction. The horizontal resolutions are also similar, whereby Riols & Latter (2018a) used ~26 points per H, and here, 22 points per H are used. This is true for the vertical resolution as well, which is ~21 point per H in both cases. The boundary conditions are also similar for both setups. These are outflow-type boundaries for the velocity and vertical-field boundary conditions for the magnetic field. An important difference is the cooling model. In addition to a pure cooling function, the model used here also includes a heating term (see the second term in Eq. (5)). The latter is not used in Riols & Latter (2018a). Additionally, the vertical box size used here ($-4H < z < 4H$) is slightly larger than the size used in Riols & Latter (2018a) ($-3H < z < 3H$). The comparison provided here especially refers to the SGMRI-(...) simulations in Riols & Latter (2018a), as they also introduced a magnetic seed field into a gravito-turbulent state. It is noted that Riols & Latter (2018a) also provided simulations starting with an MRI state and introducing self-gravity, whereby no significant differences are observed.

Now, differences in the simulation outcomes are elucidated. One difference is the saturation level of the turbulent stresses. Here, it is found that α_m is the dominant contribution in both simulations sg-mhd-1 and 2 and the stresses α_g and α_r are of the same order of magnitude. This is in contrast to SGMRI-10 ($\tau_c\Omega_0 = 10$) in Riols & Latter (2018a). There, α_m and α_r are of the same order of magnitude and α_g is the dominant contribution. Moreover, the relative strength of α_m is even weaker for higher cooling times. Differences are also observed in both the time evolution and the vertical structure of the magnetic field. Our simulations sg-mhg-1 and 2 both develop butterfly diagrams with clearly distinguishable field oscillations (see Fig. 6). Furthermore, magnetic activity extends to higher altitudes. This is a distinguishing feature of Riols & Latter (2018a), in which more irregular field reversals were found, and for cooling times $\tau_c\Omega_0 < 100$ the magnetic activity is mainly confined to the mid-plane region. It is noted that the concentration of magnetic activity near the mid-plane is also found here, though this is only in the early phases $t\Omega_0 \lesssim 400$ where MRI is not resolved or fully developed. We agree with Riols & Latter (2018a) that GI provides a dynamo (see the initial field amplification between $120\Omega_0^{-1}$ and $400\Omega_0^{-1}$). However, it is found that this does not imply suppression of MRI for efficient cooling ($\tau_c\Omega_0 = 10$), but rather that the saturated state is characterised by a coexistence of both.

It is noted at this point that the previously discussed simulations do include the effect of irradiation heating (second term in Eq. (5)), which is not the case in Riols & Latter (2018a). Whether the differences are due to the influence of irradiation is elucidated in Sect. 7 below. The boundary conditions used here are comparable to those used in Riols & Latter (2018a); hence, the differences are unlikely to arise from boundary artefacts.

From the previously derived results, one concludes that the turbulent states of simulations sg-mhd-1 and 2 consist of a coexistence between MRI and GI. However, this does not mean that the stresses can simply be added, as is also pointed out in Riols & Latter (2018a). Equation (21) may seem to do that, but it is noted that the saturation value of the Toomre-parameter $\langle Q \rangle$ also changes with the introduction of magnetic fields. Hence, this is different than adding MRI stresses to the GI stress before magnetic fields have been introduced, as the presence of magnetic fields has an influence on the overall energy balance. Here, the changes in $\langle Q \rangle$ are in part due to mass changes, but even with constant mass, the additional Maxwell stress $-B_x B_y$ provides additional means to extract energy from the background flow and thereby to change the saturation level of thermal energy.

Finally, it is noted that the results obtained here are more akin to the findings in the global simulations of Deng et al. (2020). There, hints for field-oscillations reminiscent of a butterfly diagram are found as well. Furthermore, the 'grvmhd1' simulation in Deng et al. (2020) develops a Maxwell stress in excess of the other stress contributions, which is also a common feature of the simulations presented here.

7. The influence of irradiation-heating

All previous simulations include irradiation heating (second term in Eq. (5)), which is not the case for the simulations in Riols & Latter (2018a). As notable differences arise in the previous chapters, the influence of irradiation will be elucidated in more detail here. For that purpose, restarts are conducted from sg-mhd-1 at $t\Omega_0 = 920$. For the restarts, irradiation is turned off and the total mass held constant. Two different restarts are run, with the first changing the cooling time to $\tau_c\Omega_0 = 20$ (sg-mhd-noirrad-20) (a more detailed discussion is provided for that cooling time in Riols & Latter 2018a) and the second keeping the original cooling time $\tau_c\Omega_0 = 10$ (sg-mhd-noirrad-10).

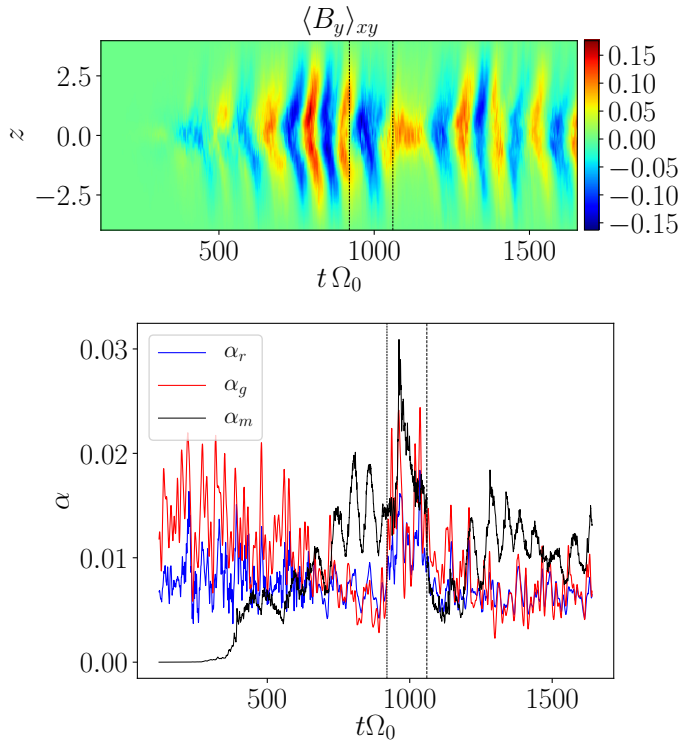

Fig. 8. Time evolutions of the vertical magnetic field structure and the dimensionless turbulent stresses for simulation sg-mhd-noirrad-20. *First image*: horizontally averaged field component $\langle B_y \rangle_{xy}$ as function of (z, t). *Second image*: dimensionless turbulent stresses $(\alpha_r, \alpha_g, \alpha_m)$. Stresses (α_r, α_g) were smoothed using a Gaussian convolute (standard deviation $\sigma = 3\Omega_0^{-1}$).

The restart of sg-mhd-noirrad-20 is done in two steps. At $t\Omega_0 = 920$, irradiation is turned off, and later, at $t\Omega_0 = 1060$, the cooling time is set to $\tau_c\Omega_0 = 20$.

The horizontally averaged toroidal field component $\langle B_y \rangle_{xy}$ is depicted for sg-mhd-noirrad-20 as functions of z and t in the first image of Fig. 8. As can be seen, the butterfly diagram is at first disrupted but eventually returns. The resulting state is qualitatively different from that found for SGMRI-20 in Riols & Latter (2018a). It is noted that for sg-mhd-noirrad-10, the field oscillations become more irregular near the mid-plane ($|z| \lesssim 1H$), but the butterfly is still visible for higher altitudes. The second image of Fig. 8 depicts the dimensionless turbulent stresses α_r, α_g, and α_m as a function of time. Averaging the stresses over time, starting at $t\Omega_0 = 1100$ yields the values listed in the first line of Table 5. The corresponding values found in Riols & Latter (2018a) (SGMRI-20) are shown in the second line. The same is also shown for sg-mhd-noirrad-10 (third line) and the respective SGMRI-10 simulation of Riols & Latter (2018a) (fourth line).

The stresses for SGMRI-20 and SGMRI-10 were obtained by applying Eqs. (8) and (9) to the values provided in Riols & Latter (2018a) (see also Appendix D). In addition to the stresses, the ratio of Maxwell stress to magnetic pressure $r_{sp} = \langle\langle -B_x B_y \rangle / \langle B^2/2 \rangle\rangle_t$ is provided in the last column.

As one can see, all stress contributions (α_r, α_g and α_m) in sg-mhd-noirrad-10 are comparable to those obtained in SGMRI-10. Regarding the ratio r_{sp}, both simulations yield values from 0.3−0.4, which is also typical of MRI. The situation is different for sg-mhd-noirrad-20 and SGMRI-20, with the stresses differing significantly. The Reynolds-contribution α_r is mostly similar in both cases, but the Maxwell and gravitational contributions switch places. In sg-mhd-noirrad-20, the Maxwell part α_m is dominant whereas in SGMRI-20 the gravitational contribution α_g is dominant. Also, the magnetic stress-to-pressure ratio for sg-mhd-noirrad-20 is $r_{sp} \sim 0.32$, which is also MRI typical, but for SGMRI-20 it is found to be $r_{sp} \sim 0.28$, which is considerably lower than all other values. We also analysed the sum total stress α for both cooling times. One first notices that the cases of Riols & Latter (2018a) and our simulations agree in that their α values differ by roughly a factor of two between $\tau_c\Omega_0 = 10$ and $\tau_c\Omega_0 = 20$. This finding is reasonable, considering that the total stress α is a measure of the rate at which energy is drawn from the Kepler flow and that the cooling timescale is a measure of how fast the system can lose thermal energy. Assuming a steady state, the extracted energy must be balanced by the losses. Reducing the $\tau_c\Omega_0$ by a factor of two means doubling the energy-loss rate, which correlates with a doubling of turbulent energy production α. However, considering each cooling time separately, the α values found in Riols & Latter (2018a) and the values found here differ by ∼10%. One likely reason for the differences in α might be different rates of wind cooling. It may also be speculated that this is related to the other differences observed for $\tau_c\Omega_0 = 20$ as well. This is also supported by the observed butterfly pattern, as the latter is characterised by magnetic activity rising to higher altitudes. Hence, this is likely an interesting route for future investigations.

One concludes that for $\tau_c\Omega_0 = 10$ we can partly reproduce the results obtained in Riols & Latter (2018a), especially that the turbulent stresses are comparable. Although, for $\tau_c\Omega_0 = 20$, significant differences arise. Although we currently have no clear explanation for the latter differences, one might speculate that they are related to wind activity at higher altitudes. Furthermore, we come to a different conclusion regarding the coexistence of GI and MRI. Similarly to the irradiated cases, the ratio of Maxwell stress to magnetic pressure is typical of MRI in both cases, and for $\tau_c\Omega_0 = 20$ one finds a clearly visible butterfly pattern. Hence, a GI–MRI coexistent state can also be sustained without irradiation, and MRI is not suppressed.

Table 5. Time-averaged, dimensionless, turbulent stresses for cases without irradiation: sg-mhd-noirrad-10 ($\tau_c\Omega_0 = 10$, first line) and sg-mhd-noirrad-20, ($\tau_c\Omega_0 = 20$, second line).

	α_r	α_g	α_m	α	r_{sp}
sg-mhd-noirrad-20	0.0065	0.0072	0.0102	0.0239	0.3231
SGMRI-20	0.0056	0.012	0.0028	0.020	0.28
sg-mhd-noirrad-10	0.0126	0.0197	0.0111	0.0434	0.3578
SGMRI-10	0.011	0.017	0.012	0.04	0.34

Notes. In both cases, the time average starts at $t\Omega_0 = 1100$ and covers an interval of $\gtrsim 500\Omega_0^{-1}$. The corresponding cases in Riols & Latter (2018a), SGMRI-10 and SGMRI-20, are shown in the second and fourth lines, respectively. The magnetic stress-to-pressure ratio is $r_{sp} = \langle\langle -B_x B_y \rangle / \langle B^2/2 \rangle\rangle_t$.

8. Turning off self-gravity

To elaborate on the role of self-gravity, the simulation sg-mhd-1 is restarted at $t\Omega_0 = 920$, with the influence of self-gravity being effectively removed. For that purpose, the gravitational

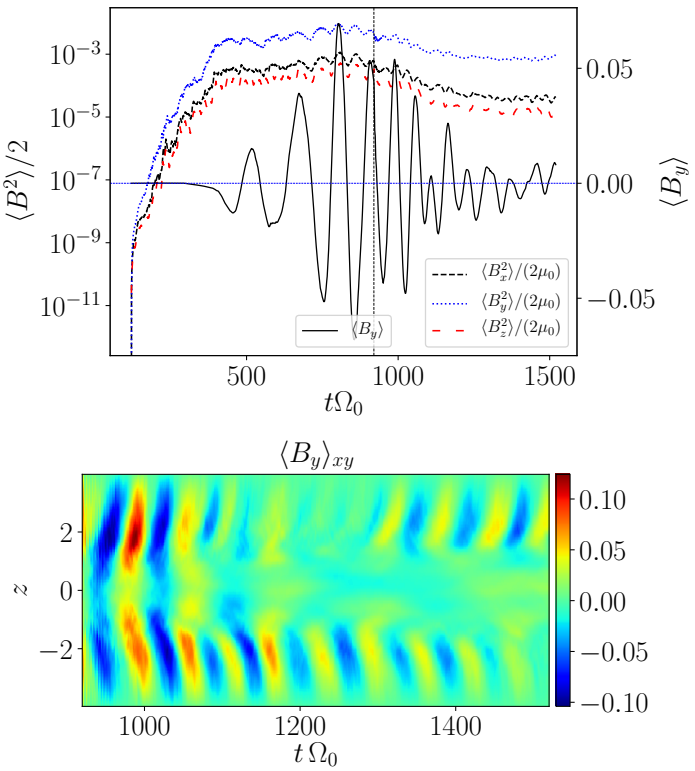

Fig. 9. Time evolution for a selection of volume-averaged quantities, related to the magnetic field, and the evolution of the vertical magnetic field structure, for simulation sg-mhd-G001. *First image*: volume-averaged magnetic energy densities separated into components $\langle B_i^2\rangle/2$ (left abscissa) and volume-averaged toroidal field $\langle B_y\rangle$ (right abscissa). *Second image*: horizontally averaged toroidal field component $\langle B_y\rangle_{xy}$ as a function of (z, t).

constant is rescaled by a factor of 100 ($G = 1 \rightarrow G = 0.01$). That simulation is run until $t\Omega_0 = 1520$ and is referred to as sg-mhd-G001. Time evolutions of the $\langle B_y\rangle$-field component and the magnetic energy densities are shown in the first image of Fig. 9. The vertical dashed line marks the time point of rescaling, $t\Omega_0 = 920$. The energy densities are mapped to the left abscissa, with curves for $\langle B_x^2\rangle/2$ (black, dashed), $\langle B_y^2\rangle/2$ (blue, dotted), and $\langle B_z^2\rangle/2$ (red, dash-dotted). The $\langle B_y\rangle$-component is mapped to the right abscissa as the black solid curve. Shown in the second image of Fig. 9 is the toroidal field component, averaged horizontally $\langle B_y\rangle_{xy}$ and as function of (z, t), whereby t starts at $920\Omega_0^{-1}$.

Some observations can immediately be made. The volume-averaged magnetic energy densities decrease significantly. Comparing the time intervals ($500 \leq t\Omega_0 \leq 920$) and ($1200 \leq t\Omega_0 \leq 1520$), one finds that $\langle\langle B_x^2/2\rangle\rangle_t$ decreases by 92%, $\langle\langle B_y^2/2\rangle\rangle_t$ by 84%, and $\langle\langle B_z^2/2\rangle\rangle_t$ by 93%. The oscillations in the volume-averaged $\langle B_y\rangle$ component also have significantly lower amplitudes and appear to be less regular without self-gravity. The oscillation frequency stays roughly equal. The butterfly diagram remains, although the mid-plane activity is significantly reduced (see the second image of Fig. 9).

As the magnetic field energy drops by roughly an order of magnitude, one concludes that the GI dynamo dominates in generating the magnetic field. One also concludes that the influence of GI is especially pronounced near the mid-plane, which is expected, as self-gravity has the most influence there. This also agrees with the last image in Fig. 6 (sg-mhd-1), indicating that Lorentz-forces can exceed self-gravity forces, especially for higher altitudes. The potential of GI to act as a dynamo is also consistent with the findings in Riols & Latter (2018a, 2019). The image that emerges is that MRI is operating on the field generated by the GI-dynamo, thereby leading to nonlinear saturation in the butterfly pattern. It is noted that the lack of coherence in the oscillations in the top image of Fig. 9 probably originates from a decoupling of the regions above and below the mid-plane, with the latter two regions in turn oscillating slightly out of phase. This then causes the volume-averaged values to oscillate more irregularly. The less regular oscillations are also present in the smaller box MRI simulations of Sect. 4.1.

Finally, the fact that one obtains a turbulent state for $1200 \leq t\Omega_0 \leq 1520$ is further proof that in the original simulations one does have both GI and MRI. The stresses found in the new turbulent state are $\alpha_\mathrm{m} = 0.0024$ and $\alpha_\mathrm{r} = 0.00058$, yielding a ratio of $\alpha_\mathrm{m}/\alpha_\mathrm{r} \approx 4.1$, which, as expected, agrees with the typical value for MRI.

9. Dynamo properties

Decomposing the velocity ($\boldsymbol{v} = (3\Omega_0/2)x\mathbf{e}_y + \delta\boldsymbol{v}$) into background shear and perturbation $\delta\boldsymbol{v}$, one can analytically show that the induction equation (Eq. (2d)) is of the following form:

$$\partial_t \mathbf{B} = \frac{3\Omega_0}{2} x\,\partial_y \mathbf{B} - qB_x\mathbf{e}_y + \nabla\times\boldsymbol{\mathcal{E}}, \tag{24}$$

with electromotive force $\boldsymbol{\mathcal{E}} = \delta\boldsymbol{v}\times\mathbf{B}$ (see also Vishniac & Brandenburg 1997; Guan & Gammie 2011; Simon et al. 2011). A horizontal average is applied, yielding for the x and y components, respectively (see also Riols & Latter 2019),

$$\partial_t\langle B_x\rangle_{xy} = -\partial_z\langle\mathcal{E}_y\rangle_{xy}, \tag{25}$$

$$\partial_t\langle B_y\rangle_{xy} = -\frac{3\Omega_0}{2}\langle B_x\rangle_{xy} + \partial_z\langle\mathcal{E}_x\rangle_{xy}. \tag{26}$$

It is then assumed that the connection between turbulent electromotive force and averaged field is of the form $\mathcal{E}_i = \hat{\alpha}_{ij}\langle B_j\rangle_{xy}$, with coefficients $\hat{\alpha}_{ij}$ and $i, j \in \{x, y\}$. The z derivatives in the induction equation are estimated to be of the order of $\partial_z \sim 1/H$. Substitution into Eqs. (25)-(26) and averaging over z yields (see also Guan & Gammie 2011)

$$\partial_t\langle B_x\rangle = \frac{\alpha_{xx}}{H}\langle B_x\rangle + \frac{\alpha_{xy}}{H}\langle B_y\rangle, \tag{27a}$$

$$\partial_t\langle B_y\rangle = \left(-\frac{3\Omega_0}{2} + \frac{\alpha_{yx}}{H}\right)\langle B_x\rangle + \frac{\alpha_{yy}}{H}\langle B_y\rangle. \tag{27b}$$

It is noted that in the two equations above, the more convenient coefficients $\alpha_{xx} = -\hat{\alpha}_{yx}$, $\alpha_{xy} = -\hat{\alpha}_{yy}$, $\alpha_{yx} = \hat{\alpha}_{xx}$, and $\alpha_{yy} = \hat{\alpha}_{xy}$ are defined and are also used throughout the paper.

Depending on the exact choice of the α_{ij}, oscillations in $\langle B_{x,y}\rangle$ will occur. As Eqs. (27a)–(27b) are linear in the field components, one can analytically solve the model with an ansatz of the form $\langle B_j\rangle = A_j\exp(s\,t)$, whereby the both s and the A_j are complex numbers. Elementary analytical calculations then yield

$$s_{1,2} = \frac{Tr}{2} \pm \sqrt{\left(\frac{Tr}{2}\right)^2 - D}, \tag{28a}$$

$$Tr = \alpha_{xx} + \alpha_{yy}, \tag{28b}$$

$$D = \alpha_{xx}\,\alpha_{yy} - \alpha_{xy}\,(\alpha_{yx} - 1.5\Omega_0). \tag{28c}$$

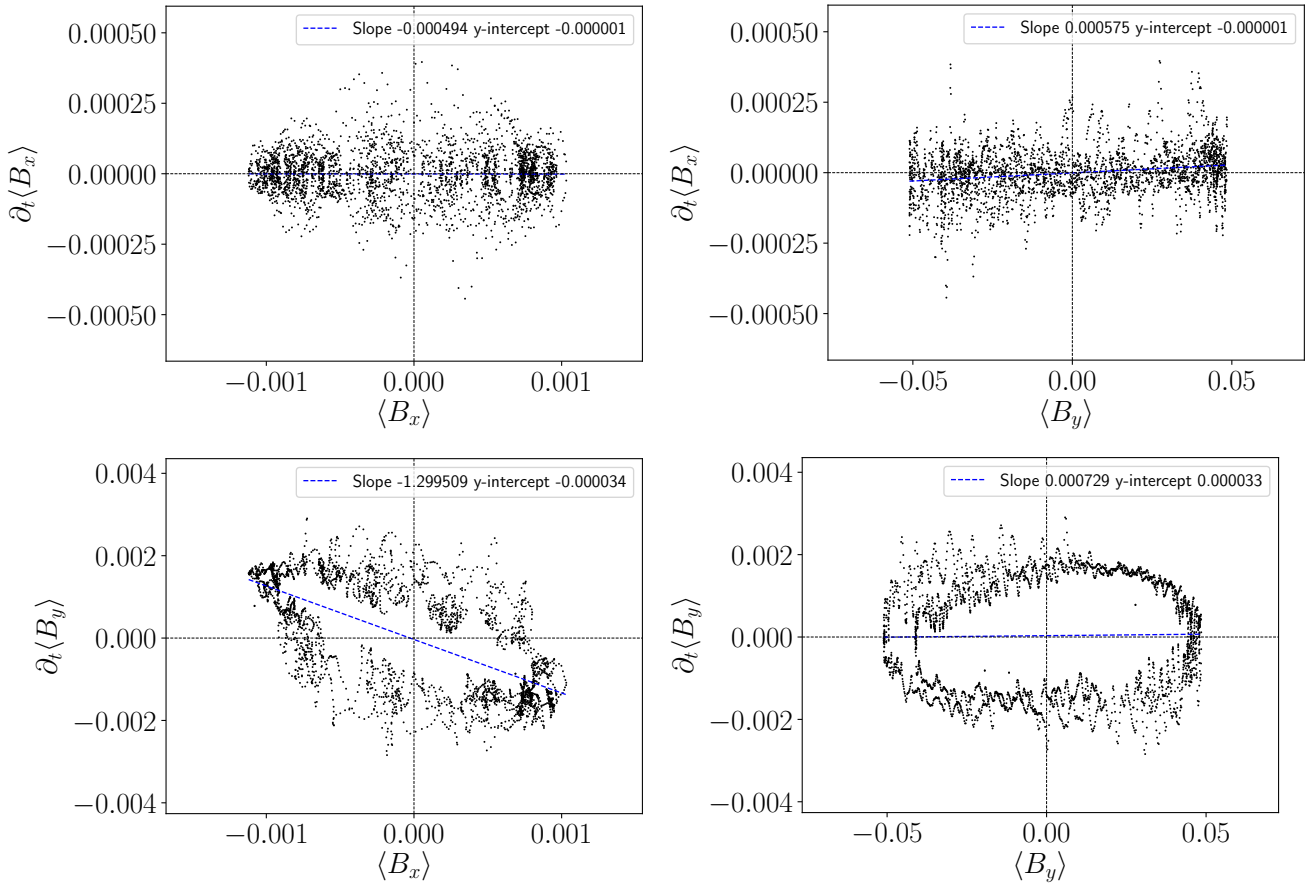

Fig. 10. Time derivatives of the volume-averaged magnetic field components $\partial_t\langle B_i\rangle$ as functions of the field components themselves $\langle B_j\rangle$. Each dot corresponds to a given time point in the interval ($700 \leq t\Omega_0 \leq 1000$) of sg-mhd-2, separated by $\delta t = 0.1\Omega_0^{-1}$. The partial time derivatives are explicitly calculated from the corresponding time series.

Table 6. α_{ij} factors according to Eqs. (27a)–(27b), determined for sg-mhd-2 over the time interval ($700 \leq t\Omega_0 \leq 1000$).

α_{xx}	α_{xy}	α_{yx}	α_{yy}
−0.000494	0.000575	0.200491	0.000729

Notes. The values are obtained from the slopes in Fig. 10.

The second term on the right hand side of Eq. (28a) is important for oscillations. For $(Tr/2)^2 - D < 0$, the solutions oscillate with a frequency of $\omega = \sqrt{D - (Tr/2)^2}$. In the simpler case of vanishing diagonal elements, α_{xx}, α_{yy}, the condition for oscillation reduces to $\alpha_{xy}\,(\alpha_{yx} - 1.5\Omega_0) < 0$. In case oscillations are present, the growth or decay of the latter is set by whether $Tr/2$ is positive or negative.

All simulations carried out in this study show field oscillations in the form of butterfly diagrams. In the early phases of sg-mhd-1 ($t\Omega_0 < 400$), sign reversals of both $\langle B_x\rangle$ and $\langle B_y\rangle$ occasionally occur. This is in contrast to Riols & Latter (2018a), in which irregularly occurring field reversals were found (more akin to the initial phase of sg-mhd-1), and also to Riols & Latter (2019), with field reversals being absent completely.

To test how the simulations relate to the simple dynamo-model of Eqs. (27a)–(27b), correlations between the time derivatives $\partial_t\langle B_i\rangle$ and the components themselves $\langle B_j\rangle$ were studied. This is visualised in the scatter plots of Fig. 10, with $\partial_t\langle B_i\rangle$ mapped to the y-axis and $\langle B_j\rangle$ mapped to the x-axis. Two subsequent time points in the scatter plots are separated by $\delta t = 0.1\Omega_0^{-1}$, and the time derivatives are explicitly calculated from that. The set of all dots corresponds to the time interval ($700 \leq t\Omega_0 \leq 1000$) of sg-mhd-2. Shown in the legends are the slopes and y incidents, which were determined via linear regression. The appearance of ellipsoidal shapes in some plots is an indication that non-zero diagonal elements α_{xx} and α_{yy} also contribute. As $H = 1$ in code units, the slopes can be identified with the coefficients α_{ij} (see Eqs. (27a)–(27b)). The resulting coefficients are summarised in Table 6.

A peculiarity arises for the coefficient α_{yx}, as determining the latter also requires subtracting the shear ($-1.5\Omega_0$), that is, $\alpha_{yx} = \text{slope} + 1.5$. Directly reading off the slope from the bottom left image of Fig. 10, one finds the slope ≈ -1.3. From this, one concludes that the effect of shearing (often called the Ω effect) is the dominant source for $\langle B_y\rangle$ production.

The α_{yx} can be calculated more directly by evaluating the term $\langle\partial_z\langle\mathcal{E}_x\rangle_{xy}\rangle_z$ in Eq. (26) as function of $\langle B_x\rangle$, thereby avoiding to calculate the time derivative. Generating a similar scatter-plot with this term instead, yields $\alpha_{yx} \approx 0.197$. That is in very good agreement with the value derived by explicitly calculating the time derivative $\partial_t\langle B_y\rangle$, providing a direct check.

The analytical dynamo model in Eqs. (28a)–(28c) is then applied to the values in Table 6, yielding

$$s = 0.000118 \pm i \cdot 0.0273. \tag{29}$$

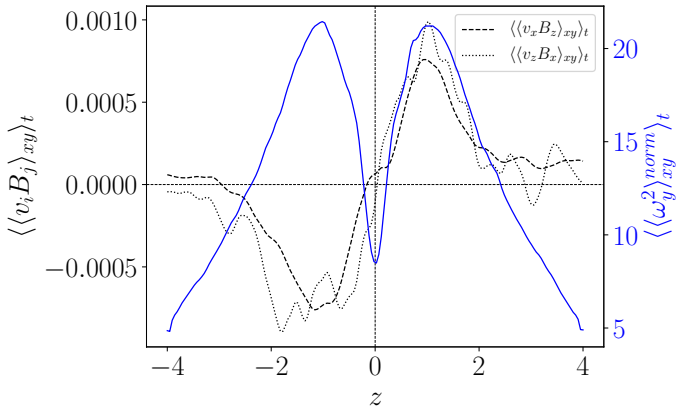

Fig. 11. Vertical profiles for a selection of quantities (averaged over (x, y), and over time). Left (vertical) axis: Vertical, turbulent shearing ($\langle v_x B_z\rangle_{xy}$, black dashed line), and vertical compression ($\langle v_z B_x\rangle_{xy}$, black dotted line) as a function of z. Right (vertical) axis: Toroidal enstrophy normalised by the mean-squared velocity perturbations ($\langle\omega_y^2\rangle_{xy}^{\mathrm{norm}} = \langle\omega_y^2\rangle_{xy}/\langle\delta v^2\rangle_{xy}$, blue solid line) as a function of z.

This implies that oscillations should be present in agreement with the observed butterfly diagram. From $\omega = 2\pi/T$, one finds a time period $T \approx 230\Omega_0^{-1}$. The actual time evolution of $\langle B_y\rangle$, evaluated for sg-mhd-2, is shown via the red solid curve in Fig. 5. The dominant frequency obtained by calculating the Fourier series for the interval $(700 \leq t\Omega_0 \leq 1000)$ yields a period of $T_{\mathrm{sim}} \approx 150\Omega_0^{-1}$. Hence, the measured period is of the same order of magnitude as the period predicted by the model, though they are not exactly equal. The predicted growth rate $(Tr/2)$ is found to be two orders of magnitude lower than the frequency part, which is considered an indication that the simulation is in a quasi-steady state, as amplitude growth stagnates. Doing the same analysis for $(400 \leq t\Omega_0 \leq 700)$, one finds $s \approx 0.0022 \pm i \cdot 0.031$. The frequency is roughly equal in both intervals, though the growth rate is one order of magnitude larger in the earlier time interval. This is expected, as the amplitude growth can clearly be observed for $(400 \leq t\Omega_0 \leq 700)$ (see Fig. 5).

Riols & Latter (2019) proposed a possible mechanism for the GI-dynamo, which involves horizontal rolls (see Riols & Latter 2018b) above and below the density waves in the mid-plane. These rolls are indeed observed in the simulations presented in this paper (see Fig. 3). Also seen in Fig. 3 is that neighbouring rolls often rotate with opposite orientation. Furthermore, as the rolls are connected to density waves, the rolls are often not exactly parallel to the y-axis. Thus, a magnetic field with only a B_y component can be bent by neighbouring rolls to locally produce a B_x component (see the mechanism proposed in Riols & Latter 2019).

As the horizontal rolls appear slightly above and below the mid-plane (see Fig. 3), they tend to separate the upper atmosphere regions from the mid-plane. In order to demonstrate this, the horizontally averaged enstrophy $\langle\omega_y^2\rangle_{xy}^{\mathrm{norm}} = \langle\omega_y^2\rangle_{xy}/\langle\delta\boldsymbol{v}^2\rangle_{xy}$ is calculated, whereby only the y vorticity $\omega_y = \partial_z v_x - \partial_x v_z$ is considered. The enstrophy value is normalised by the mean-squared velocity perturbation $\langle\delta\boldsymbol{v}^2\rangle_{xy}$ in order to isolate changes in the vortical structure from changes in the magnitude of the velocity. The vertical profile, $\langle\langle\omega_y^2\rangle_{xy}^{\mathrm{norm}}\rangle_t$, obtained by averaging over the time interval $(700 \leq t\Omega_0 \leq 1000)$, is depicted in Fig. 11, right abscissa. It is noted that the time average is obtained by evaluating $\langle\omega_y^2\rangle_{xy}^{\mathrm{norm}}$ for ten equidistant time points in the considered interval. As can be seen from Fig. 11, the enstrophy has pronounced maxima at $|z| \approx 1H$, separating the inner regions from regions in the upper atmosphere. Shown in black (left y-axis) are the two contributions to the electromotive force ($\mathcal{E}_y = v_z B_x - v_x B_z$), $\langle\langle v_x B_y\rangle_{xy}\rangle_t$ (dashed) and $\langle\langle v_z B_x\rangle_{xy}\rangle_t$ (dotted). The horizontally averaged magnetic field components periodically change sign, and so do the terms $\langle v_i B_j\rangle_{xy}$. For that reason, the $\langle v_i B_j\rangle_{xy}$ are multiplied with the sign of the volume-averaged field component $\langle B_x\rangle$ at that particular time point. An average over the time interval $(700 \leq t\Omega_0 \leq 1000)$ with ten equidistant time points then yields the black curves in Fig. 11. It can be seen that both $\langle\langle v_x B_z\rangle_{xy}\rangle_t$ and $\langle\langle v_z B_x\rangle_{xy}\rangle_t$ change behaviour at $|z| \approx 1H$, and on average $\partial_z(v_x B_z)$ and $\partial_z(v_z B_x)$ change sign at $|z| \approx 1H$. This is a strong hint that the rolls indeed play an important role in the dynamo mechanism (Riols & Latter 2019).

Table 7. α_{ij} coefficients for simulation sg-mhg-2 $(700 \leq t\Omega_0 \leq 1000)$ and averaged over different altitudes.

Interval	α_{xx}	α_{xy}	$\alpha_{yx} - 1.5$	α_{yy}
I_1	−0.000474	0.001980	−1.286571	0.000223
I_2	0.008092	0.000238	−0.458632	0.002606

Notes. The intervals covered by the vertical average are I_1: $|z| < 1H$ and I_2: $|z| > 1H$.

This is further addressed in Table 7, which shows the α_{ij} one obtains if the field components are not averaged over the entire box height, but only over given height intervals. Two intervals are chosen, separating the mid-plane region $|z| < 1H$ (interval I_1) and the region above the mid-plane $|z| > 1H$ (interval I_2). This also coincides with the regions below and above the rolls, respectively. The values are calculated by reconstructing the $\partial_t\langle B_i\rangle$ from $\partial_z(\langle\mathcal{E}_j\rangle_{xy})$ and averaging over the corresponding height interval in z. The frequencies can also be calculated for intervals I_1 and I_2, yielding $s_1 = 0.000251 \pm i \cdot 0.0505$ and $s_2 = 0.00535 \pm 0.0101$, respectively. In terms of time periods, that is $T = 2\pi/\omega = 124\Omega_0^{-1}$ for I_1 and $T = 624\Omega_0^{-1}$ for I_2. The mid-plane value is by far the closest to the observed butterfly frequency of $150\Omega_0^{-1}$, indicating that the frequency is predominantly set near the mid-plane.

The values in Table 7 demonstrate that the dynamo properties do change as a function of z. At higher altitudes, the Ω-effect is less dominant over the turbulent contributions compared to the volume near the mid-plane. α_{xy} decreases towards higher altitudes. Though, the diagonal elements both increase significantly from the mid-plane to the higher regions. This is in agreement with the situation depicted in Fig. 11 suggesting that the dynamo changes properties at $|z| \approx 1H$.

The simulations presented here are hence consistent with the dynamo mechanism based on rolls, as proposed in Riols & Latter (2019); yet, we come to the opposite conclusion in terms of oscillations. In Riols & Latter (2019), the average field grows without sign reversals; although, it has to be noted that Riols & Latter (2019) also included a finite resistivity. The ideal runs in Riols & Latter (2018a) also show field reversals, though they are much less regular than the butterfly pattern found here. In our understanding, the model relying on the rolls connected with the density waves naturally predicts field reversals. Consider a purely toroidal magnetic field line with $B_y > 0$. The mechanism in Riols & Latter (2019) then suggests that the field line is lifted upwards between two neighbouring rolls. As the rolls are not perfectly aligned with the y-axis, some parts of the field

line come to rest on the first roll, and other parts on the second roll. As the rolls rotate in opposite directions, the field line is bent between the two rolls, producing a positive B_x component. This is in agreement with the observation that α_{xy} is positive. However, the thus produced $B_x > 0$ is subjected to shear, producing a $\delta B_y < 0$. Hence, the newly produced y field has opposite sign to the original field. That will lead to the originally positive B_y being reduced and eventually crossing $B_y = 0$.

10. Summary

We first investigated the direct interaction of gravitational turbulence with magnetic fields by introducing a magnetic seed field into a gravito-turbulent state (simulation sg-mhd-1, with cooling time $\tau_c\Omega_0 = 10$). Significant amplifications in the magnetic energy density and the volume-averaged fields can be observed in the initial phase, shortly after introducing a magnetic seed field. After $\sim 300\Omega_0^{-1}$, the system changes state and a butterfly diagram develops that also extends towards higher altitudes in the z direction. This is in contrast to earlier studies of Riols & Latter (2018a) finding field reversals to occur much less regularly and magnetic activity to be more localised in the mid-plane region. It is noted that a concentration near the mid-plane is found in simulation sg-mhd-1 as well; though, this only occurs in the aforementioned initial phase after introducing the seed-field.

In accordance with the growing magnetic field strength, a Maxwell contribution α_m to the total stress also emerges. As α_m grows, the gravitational stress α_g is found to decrease, whereas the sum total of all stresses slightly increases. At saturation, α_m is the dominant stress contribution, or at least it is of the same order of magnitude as the remaining stress contributions. The reduction in α_g is found to be consistent with an increase in the saturated Toomre parameter $\langle Q \rangle$. In simulation sg-mhd-1, this can mostly be attributed to a reduction of the total mass in the box volume due to vertical wind activity initiated by the magnetic fields. A second simulation (sg-mhd-2) is restarted from the early turbulent state of sg-mhd-1, whereby the sum total mass is then held constant. Hence, the mass is slightly higher in sg-mhd-2, leading to slightly lower $\langle Q \rangle$ values, and α_g indeed saturates at a slightly higher level in sg-mhd-2 compared to sg-mhd-1. The total stress α is equal in both cases (sg-mhd-1 and 2), consequently, the saturation value α_m is lower in sg-mhd-2 compared to sg-mhd-1. In addition to that, a method of separating possible GI and MRI stress contributions ($\alpha = \alpha(\mathrm{GI}) + \alpha(\mathrm{MRI})$) is suggested, and it is found that $\alpha_m/\alpha_r(\mathrm{MRI}) = 3.85$, 4.09 for sg-mhd-1 and 2, respectively. For the ratio of Maxwell stress to magnetic pressure, one obtains values of $\langle\langle -B_xB_y\rangle/\langle B^2/2\rangle\rangle_t = 0.32$, 0.34 for sg-mhd-1 and 2, respectively.

The influence of irradiation is demonstrated by using two restarts of sg-mhd-1, with irradiation being turned off at the restart point. One restart also changes the cooling time from $\tau_c\Omega_0 = 10$ to $\tau_c\Omega_0 = 20$. Both cases still develop butterfly diagrams, whereby the pattern is more pronounced for $\tau_c\Omega_0 = 20$. For $\tau_c\Omega_0 = 20$ especially, the clearly visible butterfly pattern is different from the findings for SGMRI-20 in Riols & Latter (2018a). The ratio of Maxwell stress to magnetic pressure $\langle\langle -B_xB_y\rangle/\langle B^2/2\rangle\rangle_t$ is found to yield values similar to those obtained with irradiation. The averaged stresses for $\tau_c\Omega_0 = 10$ are closest to the values found in Riols & Latter (2018a) (SGMRI-10), though for $\tau_c\Omega_0 = 20$ significant differences remain. Most notably, the Maxwell contribution to the dimensionless stress α_m is dominant for the cases presented here, whereas in (SGMRI-20) of Riols & Latter (2018a), the gravitational contribution is dominant α_g.

The role of self-gravity is elucidated by reducing the gravitational constant G in Poisson's equation to one hundredth of its original value. With self-gravity being effectively removed, the butterfly diagram remains, and we found $\alpha_m/\alpha_r \approx 4.1$. The oscillation amplitude and the magnetic energy in the box volume are significantly reduced (one order of magnitude) once self-gravity is weakened. Significantly larger field strengths are observed with full self-gravity being enabled, especially near the mid-plane.

Finally, the saturated state is shown to be consistent with an α–Ω dynamo of the from shown, for example, in Gressel (2010), Guan & Gammie (2011), and Simon et al. (2011). The measured dynamo coefficients (α_{xx}, α_{xy}, α_{yx}, α_{yy}) agree with the field oscillations apparent in the butterfly diagrams. The order of magnitude of the expected oscillation period, as derived using the simple α–Ω model, is in agreement with the time period observed in the simulations. Taking the intervals $|z| > 1H$ and $|z| < 1H$ separately, it is found that the dynamo coefficients differ in both intervals. This is backed up by the observation that the toroidal vorticity $\langle\omega_y^2\rangle_{xy}^{\mathrm{norm}}$ takes on a maximum at $|z| \approx 1H$. The vorticity-maximum appears to be connected with rolls aligned with the density waves; the importance of these rolls is also pointed out in Riols & Latter (2018b, 2019).

11. Conclusion

Here, the conclusions that can be drawn from the aforementioned findings are summarised. Essentially, there are two important points; gravitational turbulence provides the means to act as a dynamo, and the saturated state of the GI-dynamo is a coexistence between gravitational turbulence and magneto-rotational turbulence. The first point regarding the GI-dynamo agrees with the findings in Riols & Latter (2018a, 2019), whereas differences arise regarding the coexistence of GI and MRI, which does not seem to be the case for the corresponding simulations in Riols & Latter (2018a) (zero-net-flux, with $\tau_c\Omega_0 \sim 10$–20).

The possibility of a GI-dynamo is most prominently demonstrated in the initial phases, shortly after introducing the magnetic seed field. Significant field amplifications are observed, whereas it is shown that MRI is likely not present as the weak initial field renders it highly unresolved. This is further backed up by the fact that field line bending forces are significantly weaker than self-gravity in the early phases. Hence, the field amplifications can only originate from the kinematic effects of GI turbulence. The GI dynamo is also supported by the significant reduction of magnetic energy once self-gravity is effectively removed. As stated in Sect. 9, vortical motions in the (x, z) plane (rolls) seem to play an important role in the dynamo characteristics, which is in agreement with the findings of Riols & Latter (2018b, 2019). Although, in contrast to Riols & Latter (2019), field oscillations and a butterfly pattern are found that might be linked to the pattern observed in the global simulations of Deng et al. (2020). We thus point out that the roll dynamo must not be in opposition to the field oscillations.

Regarding the second point, there are strong hints that the saturated state is comprised of a coexistence between GI and MRI. One direct hint is the previously mentioned oscillating pattern, which is reminiscent of a butterfly diagram for pure MRI. It is also found that the turbulent stresses ($\alpha_r, \alpha_m, \alpha_g$) in the nonlinear state agree with a superposition of GI and MRI turbulence. More precisely, one can self-consistently decompose the stresses into contributions of GI and MRI. Thereby, the ratios α_m/α_r

and α_g/α_r are assumed to be independent of each other and are only determined by pure MRI and pure GI states, respectively. The presence of MRI is also supported by the ratio of Maxwell stress to magnetic pressure $\langle\langle -B_x B_y\rangle/\langle B^2/2\rangle\rangle_t$, it being in the MRI typical interval of 0.3−0.4. Hence, in contrast to Riols & Latter (2018a), we come to the conclusion that the turbulent state is consistent with GI–MRI coexistence. Though, care must be taken, as one can not simply add the MRI stresses to the GI stresses, as these are evaluated before the magnetic field is introduced. This is due to the fact that the growing magnetic field strength reduces the saturated Toomre parameter $\langle Q\rangle$ and, therefore, also the turbulent stresses associated with GI. Cases without irradiation heating are found to be consistent with GI–MRI coexistence as well, and a butterfly diagram also emerges. Riols & Latter (2018a) did not include irradiation, though, and significant differences remain, especially for $\tau_c\Omega_0 = 20$. At this point, we have no clear explanation for the discrepancies, although one might speculate that they are related to possible wind activity at the vertical boundaries. Future work is to be done to clarify how MRI might cause the GI dynamo to saturate. Moreover, the influence of non-ideal effects and winds is to be elucidated in more detail.

References

Armitage, P. J. 2011, ARA&A, 49
Armitage, P. J., Livio, M., & Pringle, J. E. 2001, MNRAS, 324, 705
Bai, X.-N., & Stone, J. M. 2013, ApJ, 767, 30
Balbus, S. A., & Hawley, J. F. 1991, ApJ, 376, 214
Balbus, S. A., & Hawley, J. F. 1998, Rev. Mod. Phys., 70, 1
Binney, J., & Tremaine, S. 1987, Galactic Dynamics (Princeton, NJ: Princeton University Press), 747
Blackman, E., Penna, R., & Varnière, P. 2008, New Astron., 13, 244
Blaes, O. M., & Balbus, S. A. 1994, ApJ, 421, 163
Bodo, G., Cattaneo, F., Mignone, A., & Rossi, P. 2014, ApJ, 787, L13
Boley, A. C., Mejía, A. C., Durisen, R. H., et al. 2006, ApJ, 651, 517
Booth, R. A., & Clarke, C. J. 2019, MNRAS, 483, 3718
Brandenburg, A., & Donner, K. J. 1997, MNRAS, 288, L29
Brandenburg, A., Nordlund, A., Stein, R. F., & Torkelsson, U. 1995, ApJ, 446, 741
Colella, P. 1990, J. Comput. Phys., 87, 171
Colella, P., & Woodward, P. R. 1984, J. Comput. Phys., 54, 174
Cossins, P., Lodato, G., & Clarke, C. J. 2009, MNRAS, 393, 1157
Courant, R., Friedrichs, K., & Lewy, H. 1928, Math. Ann., 100, 32
Davis, S. W., Stone, J. M., & Pessah, M. E. 2010, ApJ, 713, 52
Deng, H., Mayer, L., & Latter, H. 2020, ApJ, 891, 154
Fromang, S. 2005, A&A, 441, 1
Fromang, S., Balbus, S. A., Terquem, C., & De Villiers, J.-P. 2004, ApJ, 616, 364
Fromang, S., Latter, H., Lesur, G., & Ogilvie, G. I. 2013, A&A, 552, A71
Gammie, C. F. 2001, ApJ, 553, 174
Goodman, J. 2003, MNRAS, 339, 937
Gressel, O. 2010, MNRAS, 405, 41
Guan, X., & Gammie, C. F. 2011, ApJ, 728, 130
Hawley, J. F., & Balbus, S. A. 1992, ApJ, 400, 595
Hawley, J. F., Gammie, C. F., & Balbus, S. A. 1995, ApJ, 440, 742
Hawley, J. F., Guan, X., & Krolik, J. H. 2011, ApJ, 738, 84
Hirose, S., & Shi, J.-M. 2019, MNRAS, 485, 266
Jackson, J. D. 2014, Klassische Elektrodynamik (de Gruyter)
Käpylä, P. J., & Korpi, M. J. 2011, MNRAS, 413, 901
Koyama, H., & Ostriker, E. C. 2009, ApJ, 693, 1316
Kratter, K., & Lodato, G. 2016, ARA&A, 54, 271
Lesur, G., & Ogilvie, G. 2008, A&A, 488, 451
Lin, C. C., & Shu, F. H. 1964, ApJ, 140, 646
Lin, M.-K., & Kratter, K. M. 2016, ApJ, 824, 91
Lodato, G., & Rice, W. 2004, MNRAS, 351, 630
Löhnert, L., Krätschmer, S., & Peeters, A. 2020, A&A, 640, A53
Lynden-Bell, D. 1969, Nature, 223, 690
Lynden-Bell, D., & Kalnajs, A. J. 1972, MNRAS, 157, 1
Lynden-Bell, D., & Pringle, J. E. 1974, MNRAS, 168, 603
Martin, R. G., & Lubow, S. H. 2011, ApJ, 740, L6
Martin, R. G., Lubow, S. H., Livio, M., & Pringle, J. 2012, MNRAS, 423, 2718
Masset, F. 2000, A&AS, 141, 165
Menou, K., & Quataert, E. 2001, ApJ, 552, 204
Miller, K. A., & Stone, J. M. 2000, ApJ, 534, 398
Moffatt, H. K. 1978, Field Generation in Electrically Conducting Fluids (Cambridge: Cambridge University Press)
Noble, S. C., Krolik, J. H., & Hawley, J. F. 2010, ApJ, 711, 959
Oishi, J. S., & Low, M.-M. M. 2011, ApJ, 740, 18
Paardekooper, S.-J. 2012, MNRAS, 421, 3286
Rice, W., Armitage, P., Bate, M., & Bonnell, I. 2003, MNRAS, 339, 1025
Rice, W. K. M., Armitage, P. J., Mamatsashvili, G. R., Lodato, G., & Clarke, C. J. 2011, MNRAS, 418, 1356
Riols, A., & Latter, H. 2018a, MNRAS, 474, 2212
Riols, A., & Latter, H. 2018b, MNRAS, 476, 5115
Riols, A., & Latter, H. 2019, MNRAS, 482, 3989
Riols, A., Latter, H., & Paardekooper, S.-J. 2017, MNRAS, 471, 317
Roe, P. 1981, J. Comput. Phys., 43, 357
Rüdiger, G., & Pipin, V. 2000, A&A, 362, 756
Sanders, R., Morano, E., & Druguet, M.-C. 1998, J. Comput. Phys., 145, 511
Sano, T., Ichiro Inutsuka, S., Turner, N. J., & Stone, J. M. 2004, ApJ, 605, 321
Shakura, N. I., & Sunyaev, R. A. 1973, A&A, 24, 337
Shi, J. M., & Chiang, E. 2014, ApJ, 789, 34
Shi, J., Krolik, J. H., & Hirose, S. 2009, ApJ, 708, 1716
Simon, J. B., Hawley, J. F., & Beckwith, K. 2011, ApJ, 730, 94
Stamatellos, D., & Whitworth, A. P. 2008, A&A, 480, 879
Stone, J. M., & Gardiner, T. A. 2010, ApJS, 189, 142
Stone, J. M., Hawley, J. F., Gammie, C. F., & Balbus, S. A. 1996, ApJ, 463, 656
Stone, J. M., Gardiner, T. A., Teuben, P., Hawley, J. F., & Simon, J. B. 2008, ApJS, 178, 137
Suzuki, T. K., & Inutsuka, S.-I. 2009, ApJ, 691, L49
Toomre, A. 1964, ApJ, 139, 1217
Vishniac, E. T., & Brandenburg, A. 1997, ApJ, 475, 263
Young, M. D., & Clarke, C. J. 2015, MNRAS, 451, 3987
Zhu, Z., Hartmann, L., & Gammie, C. 2010, ApJ, 713, 1143
Ziegler, U., & Rüdiger, G. 2000, A&A, 356, 1141
Ziegler, U., & Rüdiger, G. 2001, A&A, 378, 668

Appendix A: Notes on the Poisson solver

Here, the implementation of the Poisson solver described in Sect. 3.4 is outlined in more detail. The method closely follows that suggested in Koyama & Ostriker (2009). In the following, $(x_{n_1}, y_{n_2}, z_{n_3})$ with $n_1, n_2, n_3 \in \mathbb{N}$ refers to a position in the real space grid, and $(\mathbf{k}_{mn} = (2\pi m/L_x, 2\pi n/L_y))$ with $m, n \in \mathbb{N}$ refers to a point in the two-dimensional Fourier grid. Wave numbers with $m, n > N_{x,y}/2$ are interpreted as negative wave numbers $(m - N_x, n - N_y)$. The absolute value of the wave-vector is k_{mn} (see also Eq. 12). Green's function (Eq. 14) is here abbreviated as $G_{mn}(z_{n_3} - z_j) = G(k_{mn}, z_{n_3} - z_j)$. The expression for the potential (Eq. 15) then reads

$$\Phi(x_{n_1}, y_{n_2}, z_{n_3}) = \frac{\delta z}{N_x N_y} \sum_{m=0}^{N_x-1} \sum_{n=0}^{N_y-1} \sum_{j=0}^{N_z-1} \ldots \tag{A.1}$$
$$\ldots \exp\left(2\pi i \left[\frac{n_1 m}{N_x} + \frac{n_2 n}{N_y}\right]\right) \rho_{mn}(z_j)\, G_{mn}(z_{n_3} - z_j),$$

whereby $\delta z = L_z/N_z$ is the vertical discretisation length and

$$\rho_{mn} = \sum_{n_1=0}^{N_x-1} \sum_{n_2=0}^{N_y-1} \rho(x_{n_1}, y_{n_2}, z_{n_3}) \exp\left(-2\pi i \left[\frac{n_1 m}{N_x} + \frac{n_2 n}{N_y}\right]\right) \tag{A.2}$$

is the two-dimensional Fourier transform of the mass density. It is also noted that the mass density is assumed to vanish outside the vertical boundaries. Then, $G_{mn}(z_{n_3} - z_j)$ is expanded as a Fourier series, whereby $z_{n_3} - z_j \in [-L_z, L_z]$ (see also Koyama & Ostriker 2009)

$$G_{mn}(z_{n_3} - z_j) = \frac{1}{2N_z} \sum_{l=0}^{2N_z-1} \exp\left(2\pi i \frac{(n_3 - j)l}{2N_z}\right) G_{mnl} \tag{A.3}$$
$$G_{mnl} = \sum_{q=-N_z}^{N_z-1} \exp\left(-2\pi i \frac{ql}{2N_z}\right) G_{mn}(q).$$

Substituting $G_{mn}(z_{n_3} - z_j)$ from Eq. 14 and evaluating the sum yields

$$G_{mnl} = 4\pi G \begin{cases} \frac{1 - e^{i\pi l} e^{-k_{mn} L_z}}{2k_{mn}} \frac{\sinh(k_{mn}\delta z)}{\cos(\frac{\pi l}{N_z}) - \cosh(k_{mn}\delta z)} & \text{for } k_{mn} \neq 0 \\ \frac{\delta z}{2} \frac{1 + e^{i\pi l}}{\cos(k_{mn}\delta z) - 1} & \text{for } k_{mn} = 0 \end{cases}. \tag{A.4}$$

It is noted that this expression for G_{mnl} is slightly different from that given in Koyama & Ostriker (2009). Though, by expanding the hyperbolic functions and the cosine function for small $k_{mn}\delta z$ and $l\pi/N_z$, respectively, one recovers the result given in Koyama & Ostriker (2009).

Then, substituting the expression obtained in Eq. A.4 into Eq. A.1 yields

$$\Phi(x_{n_1}, y_{n_2}, z_{n_3}) = \frac{\delta z}{N_x N_y (2N_z)} \sum_{m=0}^{N_x-1} \sum_{n=0}^{N_y-1} \sum_{j=0}^{N_z-1} \sum_{l=0}^{2N_z-1} T, \tag{A.5}$$
$$T = G_{mnl}\, \rho_{mn}(z_j) \exp\left(2\pi i \left[\frac{n_1 m}{N_x} + \frac{n_2 n}{N_y} + \frac{(n_3 - j)l}{2N_z}\right]\right).$$

The j summation arises from the convolution and the l summation arises from the substitution of G_{mnl}. The j summation over $\rho_{mn}(z_j) \cdot \exp(-2\pi\, i\, jl/(2N_z))$ can then be carried out. The summation result is abbreviated by ρ^{corr}_{mnl}. The expression for the potential then becomes

$$\Phi(x_{n_1}, y_{n_2}, z_{n_3}) = \frac{\delta z}{N_x N_y (2N_z)} \sum_{m=0}^{N_x-1} \sum_{n=0}^{N_y-1} \sum_{l=0}^{2N_z-1} G_{mnl}\, \rho^{corr}_{mnl} \tag{A.6}$$
$$\exp\left(2\pi i \left[\frac{n_1 m}{N_x} + \frac{n_2 n}{N_y} + \frac{n_3 l}{2N_z}\right]\right),$$

which represents a three-dimensional, inverse Fourier transform of size $(N_x \times N_y \times (2N_z))$. The inverse FFT yields $2N_z$ values in the z direction, but the index n_3 is only defined for N_z values. Hence, the potential is extracted by keeping the first N_z indices of the inverse FFT array.

Analytically evaluating the j-summation in $\rho^{corr}_{mnl,}$ one can show that ρ^{corr}_{mnl} can be calculated using two forward-Fourier transforms of size $N_x \times N_y \times N_z$:

$$\rho^{corr}_{mnl} = \begin{cases} \mathcal{FT}_3\left(\rho(x_{n_1}, y_{n_2}, z_{n_3})\right)(m, n, q) & \text{for } l \text{ even} \\ \mathcal{FT}_3\left(\rho(x_{n_1}, y_{n_2}, z_{n_3}) \exp\left(-i\pi \frac{n_3}{N_z}\right)\right)(m, n, q) & \text{for } l \text{ odd}, \end{cases} \tag{A.7}$$

whereby the Fourier coordinate q relates to l as $l = 2q$ for even l and $l = 2q + 1$ for odd l. It is noted that ρ^{corr}_{mnl} may also be defined differently by calculating two-dimensional FFTs for each z_j instead of two three-dimensional FFTs. To use the latter method, G_{mnl} also needs to be modified (see e.g., Koyama & Ostriker 2009). We used three-dimensional FFTs as outlined above, and it is pointed out that our method may deviate from that used in Koyama & Ostriker (2009) at that point.

Appendix B: GI benchmark

As noted in Sect. 4.2, the simulations listed in Table 2 are restarted from an initial simulation that has been brought into the nonlinear state. The initial simulation (initGI18) is started with adiabatic index $\gamma = 1.8$, cooling-time $\tau_c\Omega_0 = 10$, and initial Toomre-parameter $Q_0(t = 0) = 0.6 = \langle Q \rangle$. A CFL number of 0.06 is used. The choice $\gamma = 1.8$ is only applied to initGI18 and has turned out to be necessary, as the linear-nonlinear transition is rather disruptive and directly choosing $\gamma = 1.64$ has always lead to a clumping state. Occasionally, the simulation can also halt at the transition point. Choosing a time step that is too large (CFL > 0.06) turns out to also produce clumping states after entering the nonlinear phase. The linear-nonlinear transition occurs roughly $40\Omega_0^{-1}$ after the start of the simulation. After a total of $80\Omega_0^{-1}$, initGI18 is restarted with $\gamma = 1.64$ (GI072) and run for $160\Omega_0^{-1}$. Simulations GI058, GI087, and GI095 are restarted from GI072 at $t\Omega_0 = 120$ ($40\Omega_0^{-1}$ after initial restart from initGI18) by rescaling the density on every grid point with a fixed factor to yield different box masses ($\Rightarrow$ different Q_0). However, the exact value of Q_0 may later depend on time due to losses over the vertical boundaries.

Appendix C: Parallel computation

For all simulations shown, the computation has been parallelised over the x and y directions. The Poisson solver implemented here does not allow for parallelisation in the z direction. All calculations were run on the high-performance computing cluster at the University of Bayreuth (centre for scientific computing at the University of Bayreuth [2]). The computation nodes used each

[2] see also https://www.bzhpc.uni-bayreuth.de/de/keylab/index.html

have 20 physical processors. Hence, the chosen number of processors is ideally divisible by 20. For the MRI simulations, ten processors are used in the x direction and 20 processors are used in the y direction, yielding $10 \times 20 = 200$ in total. For the pure GI as well as the sg-mhd simulations, $20 \times 20 = 400$ processors were chosen. Hence, the number of grid points used for the GI simulations is $N_{x,y} = 440$, which is not a power of 2 (as would be convenient for a Fourier solver), but is divisible by 20. The latter has also turned out to be a reasonable compromise between computational effort and resolution.

Appendix D: Note about the comparison with Riols & Latter (2018a)

The values of Riols & Latter (2018a), used for the comparison in Sect. 7, Table 5, are briefly outlined here. All values used are taken from Table 1 in Riols & Latter (2018a). There, Reynolds, gravitational, and Maxwell stresses are $H_{xy} = 0.0034\,(0.0064)$, $G_{xy} = 0.007\,(0.010)$, and $M_{xy} = 0.0017\,(0.0071)$, respectively; whereby the values without brackets are for SGMRI-20 and the values in brackets are for SGMRI-10. Thermal and magnetic energy densities are $E_{th} = 0.362\,(0.363)$ and $E_{mag} = 0.0061\,(0.021)$. The dimensionless stresses in Table 5 are then obtained by multiplying the above stresses with $2/(3\gamma(\gamma-1)E_{th})$, for example, $\alpha_{\rm r} = 2H_{xy}/(3\gamma(\gamma-1)E_{th})$, with $\gamma = 5/3$. The ratio of Maxwell stress to magnetic pressure is $r_{\rm sp} = M_{xy}/E_{mag}$.

Chapter 9

The Persistence of Magneto-Rotational Turbulence in Gravitationally-Turbulent Accretion Disks

L. Löhnert, and A. G. Peeters

This chapter has been published in the journal Astronomy & Astrophysics:

▷ Löhnert, L. & Peeters, A. G., 2023, Astronomy & Astrophysics, 677, A173
URL: https://doi.org/10.1051/0004-6361/202244608 (as of 14.10.2023)

A&A 677, A173 (2023)
https://doi.org/10.1051/0004-6361/202244608

Astronomy & Astrophysics

The persistence of magneto-rotational turbulence in gravitationally turbulent accretion disks

L. Löhnert and A. G. Peeters

Physics Department of Bayreuth, Universitätsstraße 30, Bayreuth, Germany
e-mail: lucas.loehnert@uni-bayreuth.de

Received 27 July 2022 / Accepted 24 July 2023

ABSTRACT

Aims. Our main goal is to probe the persistence of turbulence originating from the magneto-rotational instability (MRI) in gravito-turbulent disks. This state is referred to here as GI-MRI coexistence, with GI standing for gravitational instability. We test the influence of GI strength, controlled by the cooling law, and the impact of Ohmic resistivity.
Methods. Our starting point was three-dimensional, ideal, magnetohydrodynamic (MHD) simulations of gravitational turbulence in the local shearing-box approximation using the code Athena. We introduced a zero-net-flux magnetic seed field in a GI-turbulent state and investigated the nonlinear evolution. The GI strength was varied by modifying the cooling parameters. We tested the cooling times $\tau_c\Omega_0 = 10$, $\tau_c\Omega_0 = 20$, and $\tau_c\Omega_0 = 10$, with additional background heating. For some resistive cases, ideal-MHD simulations, which had already developed GI-MRI coexistence, were restarted with a finite Ohmic resistivity enabled at the moment of restart.
Results. It appears that there are two possible saturated dynamo states in the ideal-MHD regime: a state of GI-MRI coexistence (for low GI activity) and a strong-GI dynamo. The cases with lower GI activity eventually develop a clearly visible butterfly pattern. For the case with the highest GI activity ($\tau_c\Omega_0 = 10$, no heating), a clearly visible butterfly pattern is absent, though more chaotic field reversals are observed above (and below) the mid-plane. We were also able to reproduce the results of previous simulations. With Ohmic resistivity, the simulation outcome can be substantially different. There exists a critical magnetic Reynolds number, $\langle \mathrm{Rm} \rangle \sim 500$, below which the ideal-MHD outcome is replaced by a new dynamo state. For larger Reynolds numbers, one recovers turbulent states that are more reminiscent of the ideal-MHD states, and especially the strong-GI case. This new state leads to oscillations, which are caused by a significant heat production due to the resistive dissipation of magnetic energy. The additional heat periodically quenches GI, and the quenching events correspond to maxima of the Toomre value, Q.

Key words. accretion, accretion disks – magnetic fields – instabilities – turbulence – dynamo

1. Introduction

In accretion disks, instabilities are an important ingredient as they allow turbulence to emerge, which in turn leads to an effective viscosity that largely exceeds the molecular viscosity. The turbulent viscosity allows angular momentum to be transported outwards (Lynden-Bell 1969; Shakura & Sunyaev 1973; Balbus & Hawley 1998) and thereby allows the process of accretion to occur in the first place. Additionally, certain types of turbulence may also amplify existing magnetic fields by providing a dynamo mechanism (Brandenburg et al. 1995; Brandenburg & Donner 1997; Balbus & Hawley 1998; Rüdiger & Pipin 2000; Ziegler & Rüdiger 2000; Lesur & Ogilvie 2008; Gressel 2010; Salvesen et al. 2016).

Well-known examples of instabilities that sustain turbulence are the gravitational instability (GI; see e.g. Toomre 1964; Lin & Shu 1964; Gammie 2001; Kratter & Lodato 2016) and the magneto-rotational instability (MRI; Balbus & Hawley 1991, 1998; Hawley et al. 1995; Brandenburg et al. 1995). Many numerical studies have been dedicated to both GI (Gammie 2001; Lodato & Rice 2004; Cossins et al. 2009; Rice et al. 2011, 2003; Paardekooper 2012; Young & Clarke 2015; Boley et al. 2006; Shi & Chiang 2014; Riols et al. 2017; Riols & Latter 2018b; Booth & Clarke 2019; Hirose & Shi 2019; Zier & Springel 2023) and MRI (Hawley et al. 1995; Brandenburg et al. 1995; Stone et al. 1996; Suzuki & Inutsuka 2009; Guan & Gammie 2011; Shi et al. 2009; Simon et al. 2011; Käpylä & Korpi 2011; Bai & Stone 2013; Fromang et al. 2013; Coleman et al. 2017). This also includes interactions of the two instabilities. Interactions can occur indirectly via limit cycles, whereby different accretion rates associated with GI and MRI can lead to outbursts of accretion (see e.g. Armitage et al. 2001; Zhu et al. 2009, 2010; Martin & Lubow 2011; Martin et al. 2012). Whether MRI and GI directly coexist is less clear. Some local simulations seem to suggest that MRI is absent (see e.g. Riols & Latter 2018a, 2019), though there are global and local simulations that are consistent with GI-MRI coexistence (Fromang et al. 2004; Fromang 2005; Löhnert & Peeters 2022). It is generally found that GI can lead to dynamo activity (Riols & Latter 2018a, 2019; Riols et al. 2021; Deng et al. 2020; Löhnert & Peeters 2022; Béthune & Latter 2022). The interaction of the two instabilities may be important for disk systems that are both heavy enough to be gravitationally unstable,

$$Q = \frac{c_s \Omega_0}{\pi G \Sigma} < Q_c, \tag{1}$$

with $Q_c \gtrsim 1$, and sufficiently ionised to trigger MRI, such as certain regions of active galactic nuclei (see e.g. Menou & Quataert 2001; Goodman 2003). It is noted that linear, axisymmetric GI occurs for $Q < 1$, though non-axisymmetric modes, or systems with additional cooling (heating) physics, can also become unstable for $Q \gtrsim 1$ (see e.g. Kratter & Lodato 2016; Lin & Kratter 2016). Riols & Latter (2019) studied the effect of Ohmic resistivity on the GI dynamo in more detail and conclude that the dynamo operates for a wide range of magnetic

Reynolds numbers, Rm. The dynamo strength, indicated by the growth rate, is found to vary with the exact value of Rm. Magneto-rotational instability is assumed to be absent there. A similar behaviour was found for ambipolar diffusion by Riols et al. (2021) .

In Löhnert & Peeters (2022), we reported that the ideal magnetohydrodynamic (MHD) case leads to a state that is consistent with GI-MRI coexistence. Some of the results shown in Löhnert & Peeters (2022) differ from similar, previous simulations (Riols & Latter 2018a, 2019). Hence, one goal of the present study is to identify possible reasons for theses differences and to further test the persistence of GI-MRI coexistence, by varying the GI strength (e.g. measured by α). This is achieved by modifying the cooling time and by including, or turning off, additional heating. Additionally, the influence of Ohmic resistivity on the dynamo state is tested.

We note that the MRI alone can lead to a more varied behaviour in the presence of resistivity (see e.g. Sano et al. 1998; Ziegler & Rüdiger 2001; Sano & Stone 2002; Fromang et al. 2007; Turner et al. 2007; Simon & Hawley 2009; Oishi & Mac Low 2011; Davis et al. 2010; Simon et al. 2011). This ranges from intermittent bursts of turbulent activity (Simon et al. 2011) to complete quenching, for example in dead zones of protoplanetary disks (see e.g. Turner et al. 2007; Armitage 2011). Magnetohydrodynamic simulations of GI with Ohmic resistivity were also investigated in Riols & Latter (2019), and cases with ambipolar diffusion were presented in Riols et al. (2021). The magnetic Reynolds numbers tested in Riols & Latter (2019) were in the range $\mathrm{Rm} \lesssim 500$. The dynamo states observed there differ from the states of GI-MRI coexistence found in Löhnert & Peeters (2022), though Riols & Latter (2019) also point out that the GI dynamo appears to change its state for $\mathrm{Rm} \gtrsim 500$. We suspect that the new dynamo state might correspond to GI-MRI coexistence. Hence, the goal here is to probe this higher-Rm regime.

The structure of the paper is as follows: Sect. 2 provides a summary of the shearing-box model, including the equations of motion, and the additional physics that is used. Important definitions, quantities, and frequently used averages are detailed in Sect. 3. The applied numerical methods and Athena settings are outlined in Sect. 4. In Sect. 5 ideal-MHD simulations, with varying GI strength, are discussed. Two different saturation states of the dynamo are found, and the possibility of MRI presence in the weak-GI cases is elaborated on. The first resistive simulation ($\langle \mathrm{Rm} \rangle \sim 280$) is provided in Sect. 6, and important observations and differences from the ideal cases are highlighted. We find that the newly formed turbulent state (here referred to as 'resistive-GI dynamo') differs significantly from the ideal state of GI-MRI coexistence. We then show in Sect. 7.1 that the resistive-GI dynamo is obtained for $\langle \mathrm{Rm} \rangle \lesssim 500$. Larger Rm values result in dynamo states that share similarities with the ideal-MHD regime, suggesting a state transition at $\langle \mathrm{Rm} \rangle \sim 500$. In Sect. 7.2 we test whether the transition is indeed physical, and not an artefact of unresolved resistivity. Finally, in Sect. 8, we finish with a conclusion.

2. Model equations

The simulations presented here rely on the same model, as outlined in Löhnert & Peeters (2022). The model includes the equations of motion for MHD as well as self-gravity:

$$\partial_t \rho + \nabla \cdot (\rho \boldsymbol{v}) = 0 \tag{2a}$$

$$\partial_t(\rho \boldsymbol{v}) + \nabla \cdot \left(\rho \boldsymbol{v}\boldsymbol{v} - \frac{1}{\mu_0}\boldsymbol{B}\boldsymbol{B} + (P + \frac{\boldsymbol{B}^2}{2\mu_0})\underline{\boldsymbol{I}} + \underline{\boldsymbol{G}} \right) = -2\rho\Omega_0 \boldsymbol{e}_z \times \boldsymbol{v} + 3\rho\Omega_0^2 x\, \boldsymbol{e}_x - \rho\Omega_0^2 z\, \boldsymbol{e}_z \tag{2b}$$

$$\partial_t \boldsymbol{B} - \nabla \times (\boldsymbol{v} \times \boldsymbol{B}) = \frac{\eta}{\mu_0}\nabla^2 \boldsymbol{B} \tag{2c}$$

$$\partial_t E + \nabla \cdot \left(\left[E + P + \frac{\boldsymbol{B}^2}{2\mu_0} \right] \boldsymbol{v} - \boldsymbol{B}(\boldsymbol{B} \cdot \boldsymbol{v}) \right) = -\rho \boldsymbol{v} \cdot \nabla\Phi + 3\Omega_0^2 x\, v_x - \Omega_0^2 z\, v_z + \rho\dot{q} \tag{2d}$$

$$\nabla^2 \Phi = 4\pi G \rho. \tag{2e}$$

From top to bottom, these are the continuity equation, the Euler equation, the induction equation, energy conservation, and the Poisson equation for the gravitational potential. The equations are formulated in the local, shearing-box approximation. Thereby, the fluid is described by a mass density, ρ, a thermal pressure, P, and a velocity, $\boldsymbol{v}$. The corresponding sound speed is defined as $c_\mathrm{s} = \sqrt{\gamma P/\rho}$, with adiabatic index γ. For all simulations shown here, we used an adiabatic index of $\gamma = 1.64$. We note that this value might not be realistic for all possible situations; weakly ionised states yield values closer to $\gamma \sim 1.4$. The magnetic field vector is denoted by $\boldsymbol{B}$ and is related to the current density, $\boldsymbol{J}$, via Ampere's law:

$$\nabla \times \boldsymbol{B} = \mu_0 \boldsymbol{J}. \tag{3}$$

The induction equation (Eq. (2c)) also contains the Ohmic resistivity η. The sum total of kinetic, thermal, and magnetic energy is given by

$$E = \frac{\rho \boldsymbol{v}^2}{2} + \frac{P}{\gamma - 1} + \frac{\boldsymbol{B}^2}{2\mu_0}. \tag{4}$$

The energy equation also includes an additional source term of the form

$$\rho\dot{q} = -\frac{P}{(\gamma-1)\tau_\mathrm{c}} + \frac{\rho\, c_{\mathrm{s},0}^2}{\gamma(\gamma-1)\tau_\mathrm{c}}. \tag{5}$$

The first term represents cooling, with timescale τ_c, and the second mimics heating (e.g. via irradiation, or embedded stars in active galactic nuclei). Of course, this is a somewhat crude model that does not properly account for radiative transport and can, therefore, be expected to have a limited accuracy for cases that are optically thick. The cooling law corresponds to that used in Gammie (2001), and the additional heating term is equivalent to that used in Rice et al. (2011). In the absence of turbulence, the balance of heating and cooling would lead to a thermal equilibrium with constant temperature ($c_\mathrm{s} = c_{\mathrm{s},0} = \mathrm{const}$) everywhere. Assuming a given surface-mass density Σ, then this also corresponds to a background Toomre parameter $Q_0 = c_{\mathrm{s},0}\Omega_0/(\pi G\Sigma)$.

Self-gravity is modelled by the potential Φ and the corresponding gravitational stress tensor (see e.g. Lynden-Bell & Kalnajs 1972),

$$\underline{\boldsymbol{G}} = \frac{1}{4\pi G}\left(\nabla\Phi\nabla\Phi - \frac{1}{2}(\nabla\Phi \cdot \nabla\Phi)\underline{\boldsymbol{I}} \right). \tag{6}$$

The potential is obtained by solving the Poisson equation (Eq. (2e)) for a given mass density, ρ.

In the local shearing-box approximation, the term $3\rho\Omega_0^2\, x\, \boldsymbol{e}_x$ (in Eq. (2b)) represents the net force, arising from the radial component of the central object's gravity and the centrifugal force. Thereby, Ω_0 is the angular velocity, corresponding to the Kepler

orbit of the co-rotating box centre. Similarly, the vertical contribution from the central object's gravity is given by $-\rho\Omega_0^2 z\,\boldsymbol{e}_z$. As the box is co-rotating with the disk, Coriolis forces $-2\rho\Omega_0\boldsymbol{e}_z\times\boldsymbol{v}$ also arise. Corresponding terms appear in the energy balance equation as well. The net of vertical gravity (stellar and self-gravity) and pressure forces leads to a vertical density stratification. In the absence of turbulence, tidal and Coriolis forces support a shear flow $\boldsymbol{v}_0 = -(3\Omega_0/2)\,x\,\boldsymbol{e}_y$. The latter is the local approximation of the Kepler flow, as seen from the co-moving shearing box.

To obtain reasonable values in simulations, all quantities are made dimensionless (see also Löhnert & Peeters 2022). Thereby, a quantity f is decomposed into a characteristic scale, $f_{\rm ch}$, and a dimensionless part, $\hat{f}$, with $f = \hat{f}\,f_{\rm ch}$. For the characteristic timescale, $t_{\rm ch} = \Omega_0^{-1}$ is chosen; hence, $t = \hat{t}\,\Omega_0^{-1}$. For a typical velocity, the initial sound speed is used, $v_{\rm ch} = c_{\rm s,0}$. In cases with additional heating, $c_{\rm s,0}$ also corresponds to the aforementioned equilibrium between heating and cooling. This suggests a characteristic length, given by the scale height, $l_{\rm ch} = H = c_{\rm s,0}/\Omega_0$. For mass densities, a typical scale $\rho_{\rm ch} = \Omega_0^2/G$ is used. A typical thermal pressure can be obtained from the typical mass density, by using the sound speed, $P_{\rm ch} = c_{\rm s,0}^2\rho_{\rm ch}$. And from the pressure, one obtains a typical magnetic field strength, $B_{\rm ch} = \sqrt{\mu_0 P_{\rm ch}}$ ($\mu_0 = 1$). A characteristic gravitational potential follows from the Poisson equation, $\Phi_{\rm ch} = c_{\rm s,0}^2$. Values in tables and figures are always dimensionless (the hat is then omitted), unless units are explicitly given.

3. Frequently used quantities and averages

Here, some frequently used averages are defined. In general, averages of a quantity f are indicated by angled brackets $\langle f\rangle$. Without further specifications, $\langle f\rangle$ denotes a volume average $(\int_V f\,\mathrm{d}V)/V$. Differing averages are indicated by subscripts; for example, $\langle f\rangle_{xy} = (\int f\,\mathrm{d}x\,\mathrm{d}y)/(L_x\,L_y)$ indicates a surface average over planes of constant z, where L_x and L_y are the horizontal domain sizes. Similarly, time averages are denoted by $\langle f\rangle_{\rm t}$. For example, the expression $\langle\langle f\rangle\rangle_{\rm t}$ implies that $f(\boldsymbol{x},t)$ is first averaged over the volume, at each time point, and afterwards averaged over time.

An important parameter, which quantifies the importance of self-gravity, is the Toomre parameter, $Q = c_{\rm s}\Omega_0/(\pi G\Sigma)$ (see e.g. Toomre 1964; Kratter & Lodato 2016; Gammie 2001). The sound speed, $c_{\rm s}$, as well as the surface mass density, Σ, can in general be used as a function of space and time. However, for the considerations here, Σ was always used as an area-averaged value. Hence, $\Sigma = \langle\int\rho\,\mathrm{d}z\rangle_{xy} = \langle\rho\rangle\,L_z$, with vertical domain size L_z and mass density, averaged over the box volume, $\langle\rho\rangle$. For the sound speed, two different values may be used, the value for the background (heating) equilibrium $c_{\rm s,0}$, or the volume-averaged value $\langle c_{\rm s}\rangle = \sqrt{\gamma\langle P\rangle/\langle\rho\rangle}$. Hence, the Toomre values

$$Q_0 = \frac{c_{\rm s,0}\Omega_0}{\pi G\Sigma}, \quad \langle Q\rangle = \frac{\langle c_{\rm s}\rangle\Omega_0}{\pi G\Sigma} \tag{7}$$

are defined. As $c_{\rm s,0}$ is constant ($c_{\rm s,0} = 1$ in code units), the value of Q_0 only depends on the mass contained in the box volume. If the latter remains constant throughout the simulation, then also Q_0 remains constant. In contrast to that, the value of $\langle Q\rangle$ can vary with time, as the value of $\langle c_{\rm s}\rangle$ depends on the momentary thermal energy, contained in the box volume. A further parameter, important as a measure for turbulent energy production as well as the systems ability to transport angular momentum, is the dimensionless turbulent stress (see e.g. Shakura & Sunyaev 1973; Gammie 2001)

$$\alpha = \frac{2\langle S_{xy}\rangle}{3\gamma\langle P\rangle}, \tag{8}$$

where

$$S_{xy} = \rho v_x\delta v_y - \frac{1}{\mu_0}B_xB_y + \frac{1}{4\pi G}\partial_x\Phi\,\partial_y\Phi, \tag{9}$$

the un-normalised stress. The first term is the Reynolds stress (the δ... indicates deviations from the shear flow: $\delta v_y = v_y + (3\Omega_0/2)x$ and $\delta v_x = v_x$), the second term is the Maxwell stress, and the third term the gravitational stress. The separation into contributions may also be applied to α, yielding $\alpha_{\rm r}$, $\alpha_{\rm m}$, and $\alpha_{\rm g}$, respectively. We note that the factor $2/(3\gamma)$, in Eq. (8), is often used in the context of GI, but this is a matter of definition, and it is often absent in MRI-related contexts. The values of α may be interpreted as a dimensionless measure for the rate of energy input into the system. More precisely, for a Keplerian differential rotation, it represents, up to factors of order unity, the net-input rate of energy per volume, normalised by both the pressure and the local shear rate ($\propto\Omega_0$). Without additional losses (e.g. at the vertical boundaries), this production rate should balance with the net cooling (heating) rate (see Gammie 2001; Rice et al. 2011). Hence, a corresponding, dimensionless cooling (heating) rate is defined:

$$\alpha_{\rm cool} = \frac{4}{9\Omega_0\gamma\langle P\rangle}\left(-\langle\rho\dot{q}\rangle\right) = \frac{4}{9\gamma(\gamma-1)\tau_{\rm c}\Omega_0}\left(1-\frac{c_{\rm s,0}^2\langle\rho\rangle}{\gamma\langle P\rangle}\right). \tag{10}$$

In a steady state, one would thus expect to find $\alpha \sim \alpha_{\rm cool}$ (Gammie 2001; Rice et al. 2011). For easier use in later sections, the volume-averaged energy densities are also defined:

$$E_{\rm kin} = \left\langle\frac{1}{2}\rho\boldsymbol{v}^2\right\rangle, \tag{11a}$$

$$E_{\rm mag} = \left\langle\frac{1}{2\mu_0}\boldsymbol{B}^2\right\rangle \quad \text{and} \tag{11b}$$

$$E_{\rm th} = \langle E\rangle - E_{\rm kin} - E_{\rm mag}, \tag{11c}$$

the kinetic, magnetic, and thermal energy densities, respectively. Here, E is the total energy (see also Eq. (2d)). The volume-averaged pressure is related to that by $\langle P\rangle = (\gamma-1)\,E_{\rm th}$.

An important parameter, quantifying the relative strength of magnetic fields, is the plasma β, the ratio of thermal pressure to magnetic pressure, $\beta = 2\mu_0 P/\boldsymbol{B}^2$. Averages of the plasm -β are here calculated as follows:

$$\langle\beta\rangle = \frac{2\mu_0\langle P\rangle}{\langle\boldsymbol{B}^2\rangle} = \frac{\langle P\rangle}{E_{\rm mag}}. \tag{12}$$

The importance of Ohmic resistivity is indicated by the magnetic Reynolds number. Choosing $c_{\rm s}$ as the typical velocity and H as the typical length scale ($H = c_{\rm s}/\Omega_0$), one finds for the magnetic Reynolds number $\mathrm{Rm} = c_{\rm s}^2/(\eta\Omega_0)$. Similar to the Toomre parameter, one may use either $c_{\rm s,0}$ or $\langle c_{\rm s}\rangle$. Hence, the following definitions are used:

$$\mathrm{Rm} = \frac{c_{\rm s,0}^2}{\eta\Omega_0}, \quad \langle\mathrm{Rm}\rangle = \frac{\langle c_{\rm s}\rangle^2}{\eta\Omega_0}. \tag{13}$$

Finally, the ratio of Maxwell stress to magnetic pressure (energy density) is defined as

$$r_{\rm sp} = \frac{\langle-\frac{1}{\mu_0}B_xB_y\rangle}{E_{\rm mag}} = \frac{\langle-2B_xB_y\rangle}{\langle|\boldsymbol{B}|^2\rangle}. \tag{14}$$

4. Numerical methods

Both the code used and the applied numerical methods are equivalent to those outlined in Löhnert & Peeters (2022). A summary is given below.

4.1. Code

We used the MHD code Athena[1] (see Stone et al. 2008), in which the Roe solver (Roe 1981) is applied and the integration is achieved using the corner transport upwind algorithm with constrained transport (CTU+CT; see Colella 1990; Stone et al. 2008). The integrated equations of motion are given in Eqs. (2a)–(2d) (see also Stone & Gardiner 2010). For the spatial reconstruction, a third order scheme (Colella & Woodward 1984) is used. Additionally enabled is the method FARGO (fast advection in rotating gaseous objects; see Masset 2000; Stone & Gardiner 2010). Thereby, the Kepler shear is separated from the velocity perturbations $\boldsymbol{v} = -(3\Omega_0/2)x\boldsymbol{e}_y + \delta\boldsymbol{v}$. To summarise, one first solves the equations of motion for the perturbation and the result is advected by the amount of shear that occurred during one time step. This helps in reducing the time step, it is then not limited by the Courant-Friedrichs-Lewy (CFL) condition (see e.g. Courant et al. 1928) connected with the shear flow. In order to account for shocks, also H-correction (see Sanders et al. 1998) is included. The Athena problem generator that is used is based off the stratified, shearing-sheet generator related to Hawley & Balbus (1992) and Stone et al. (1996). The Poisson solver we implemented is based on both the existing Athena solver and the method outlined in Koyama & Ostriker (2009) and Shi & Chiang (2014). The goal is to avoid periodic boundary conditions for the potential in the vertical direction, allowing one to find the potential for vertical density stratification with vanishing mass density outside the box domain. For that purpose, one first obtains a Green's function for the vertical direction, by solving for a density $\rho' \propto \delta(z)$. The full potential is then obtained by convolving Green's function with the full mass density in the z direction. The directions x and y are evaluated in Fourier space. The total of the two-dimensional Fourier transform and the convolution in the z direction can be represented as one three-dimensional Fourier transform that is twice as large in the z direction ($2N_z$). We note that the Fourier transform in xy cannot directly be applied, because shearing periodicity is not exactly equal to simple periodicity. For this purpose, Athena provides a re-map function for the mass density. The latter applies a coordinate transformation, such that the transformed density is periodic in x direction. The potential is then calculated for the re-mapped density. After the calculation, the re-mapping is undone for the potential. More details on both the method and implementation of the Poisson solver are given in Löhnert & Peeters (2022). Finally, we note that all simulations, shown here, solve the full set of MHD equations. Pure-GI simulations are obtained, by setting $\boldsymbol{B} = 0$.

4.2. Boundary conditions

Based on the shearing-box model, the boundaries are periodic in the y direction and shearing periodic in the x direction. A comprehensive overview for shearing periodicity can, for example, be found in Hawley et al. (1995), Balbus & Hawley (1998), and Stone & Gardiner (2010). These conditions apply to all quantities, except the y velocity, as the background shear is proportional to x and, therefore, jumps from the positive x boundary to the negative x boundary. In the vertical (z) direction, outflow boundaries are used. The velocity components v_x and v_y are extrapolated constantly into the vertical boundary cells (ghost zones) ($\partial_z v_{x,y} = 0$). For v_z, a case separation is applied. Velocities v_z at the vertical boundary, pointing away from the mid-plane are extrapolated constantly into the ghost zones ($\partial_z v_z = 0$) and velocities pointing towards the mid-plane are set to zero ($v_z = 0$). The mass density ρ is also extrapolated constantly into the ghost zones ($\partial_z \rho = 0$). The pressure is reconstructed from the density by assuming a constant sound speed in the ghost zones. We note that, for density and pressure, a lower limit $\rho_{\min}, P_{\min} = c_{s,0}^2 \rho_{\min}/\gamma$ is applied. The chosen values are of the order $\rho_{\min} \lesssim 10^{-4}$, with the exact values depending on the initial mid-plane density. For the magnetic field, vertical field boundary conditions are used. Hence, the horizontal fields are set to zero in the boundary cells ($B_x = B_y = 0$) and the vertical field is extrapolated constantly ($\partial_z B_z = 0$; see e.g. Brandenburg et al. 1995; Ziegler & Rüdiger 2001; Käpylä & Korpi 2011; Oishi & Mac Low 2011). For the potential due to self-gravity, vacuum boundary conditions are applied. The latter assume a vanishing mass density, and the boundary values of Φ are constructed by explicitly integrating $\nabla^2\Phi = 0$ in the z direction at the vertical boundaries. Finally, we note that the open vertical boundaries allow mass to leave the box volume, and the total contained mass tends to shrink. To prevent this, the mass is replenished to its starting value, when it deviates by more than 1% from the latter. The replenishing is achieved by adding a small density correction $\delta\rho(x, y, z)$. The correction $\delta\rho$ was chosen to be homogeneous in the (x, y) directions and Gaussian in the z direction: $\delta\rho = \triangle M \exp(-0.5(z/h)^2)/(\sqrt{2\pi}hL_xL_y)$, with $h = 0.5$ and $\triangle M$ being the small mass deviation (see also Löhnert & Peeters 2022).

5. The influence of GI strength

Löhnert & Peeters (2022) report on a turbulent state that is consistent with a coexistence between gravitational and magneto-rotational turbulence (see simulations sg-mhd-1 and 2 therein). Initially, a zero-net-flux (ZNF) magnetic field was introduced, and as the magnetic energy increases, the strength of GI declines, indicated by a lower value of the gravitational stress, α_g. The question arises as to how the GI activity is actually reduced. As an example, one can consider GI with the cooling (heating) law, given by Eq. (5). At first, heating is ignored, reducing the cooling law to the simple form $\rho\dot{q} = -E_{\rm th}/\tau_c$. In a stationary state, the turbulent energy input is balanced by cooling and wind losses at the vertical boundaries. This energy balance can be written as follows: $(3\Omega_0/2)\langle S_{xy}^{\rm GI}\rangle = -E_{\rm th}^{\rm GI}/\tau_c + \langle F_W^{\rm GI}\rangle$, where $\langle S_{xy}^{\rm GI}\rangle$ is the averaged turbulent stress (due to GI), and $\langle F_W^{\rm GI}\rangle$ is the averaged wind loss. We note that this form of the energy balance follows by volume-averaging the energy-evolution equation (Eq. (2d)), over the shearing-box domain (see also Gammie 2001; Riols & Latter 2018a). If wind losses are neglected, then this form of the energy balance, together with Eq. (8), immediately leads to the relation $\alpha = 4/(9\gamma(\gamma - 1)\tau_c\Omega_0)$, shown in Gammie (2001). One can then consider a second mechanism, capable of extracting energy from the background (e.g. MRI). The corresponding turbulent stress is referred to here as $S_{xy}^{\rm MRI}$; we note that the mechanism generating the stress does not necessarily have to be MRI. Considering this second process alone, an equivalent energy balance must hold

[1] https://princetonuniversity.github.io/Athena-Cversion/

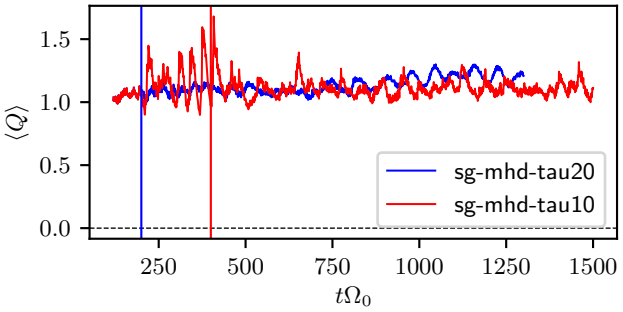

Fig. 1. Volume-averaged Toomre parameter, $\langle Q \rangle$, evaluated for simulations sg-mhd-tau10 (red) and sg-mhd-tau20 (blue). The vertical lines indicate the times at which the seed fields were introduced.

$(3\Omega_0/2)\langle S_{xy}^{\rm MRI}\rangle = -E_{\rm th}^{\rm MRI}/\tau_{\rm c} + \langle F_W^{\rm MRI}\rangle$. In the case of MRI, significant wind losses can occur (see Suzuki & Inutsuka 2009; Bai & Stone 2013; Fromang et al. 2013); in compressible simulations, MRI also gives rise to turbulent heating (see e.g. Brandenburg et al. 1995). This heating is partly balanced by cooling (see e.g. Brandenburg et al. 1995), but the wind losses can also increase due to an increased temperature and, thus, scale height. The important point is that, also here, the energy sink is a combination of cooling and wind losses. One can then consider a case where this second process (e.g. MRI) occurs on top of a GI-turbulent state. For a superposition, one then finds the combined energy balance

$$\frac{3\Omega_0}{2}\left(\langle S_{xy}^{\rm GI}\rangle + \langle S_{xy}^{\rm MRI}\rangle\right) = -\frac{E_{\rm th}^{\rm GI} + E_{\rm th}^{\rm MRI}}{\tau_{\rm c}} + \langle F_W^{\rm GI}\rangle + \langle F_W^{\rm MRI}\rangle. \quad (15)$$

At first glance, this energy balance appears reasonable. The combined energy input, $\propto \langle S_{xy}^{\rm GI}\rangle + \langle S_{xy}^{\rm MRI}\rangle$, is balanced by the net wind losses, $\langle F_W^{\rm GI}\rangle + \langle F_W^{\rm MRI}\rangle$, and the new cooling rate, which is now larger, due to the increased thermal energy level, $E_{\rm th}^{\rm GI} + E_{\rm th}^{\rm MRI}$. However, the last point is at odds with the thermal self regulation of gravito-turbulence. There are limits to the increase in $E_{\rm th}$, as GI saturates such that the Toomre value is roughly critical, $\langle Q \rangle \sim Q_{\rm c}$, with $Q_{\rm c} \gtrsim 1$ (see e.g. Gammie 2001). The latter is best exemplified by the $\langle Q \rangle$ curves, in Fig. 1. Since the mass density is constant, this effectively provides a thermostat, preventing significant increases in the temperature $\langle c_{\rm s}\rangle$ and, thus, $E_{\rm th}$. Small increases in $\langle Q \rangle$ are possible and were also observed in Löhnert & Peeters (2022) and the simulations here. The main point is that an increase in $E_{\rm th}$ alone will not be sufficient to account for the significant Maxwell stresses, which additionally arise in the MHD-saturated regime. Put differently, the GI self regulation prevents a significant increase in the cooling rate, and the latter is roughly constant, $\rho\dot{q} \sim -E_{\rm th}^{\rm GI}/\tau_{\rm c}$, even if additional energy sources emerge. If everything else was kept equal, then the energy balance would no longer be satisfied, and an energy sink of the order $-E_{\rm th}^{\rm MRI}/\tau_{\rm c}$ is missing. Essentially, there are two ways, the system can adjust to this energy imbalance: (1) the wind losses increase, and (2) the energy input is reduced, that is, the stresses do not exactly add. A combination of the two processes may also be possible. Route (1) implies that the interaction of the two mechanisms modifies the wind losses in such a way that the latter increase significantly, beyond the mere addition of both individual wind contributions: $\langle F_W^{\rm GI}\rangle + \langle F_W^{\rm MRI}\rangle + \delta F_W^{\rm inter}$. If only the extra wind, $\delta F_W^{\rm inter}$, were to balance the additional energy input, then Eq. (15) would give rise to the condition $(3\Omega_0/2)\langle S_{xy}^{\rm MRI}\rangle = \langle F_W^{\rm MRI}\rangle + \delta F_W^{\rm inter}$. As discussed below, in Sect. 5.1, the additional Maxwell stress alone ($\alpha_{\rm m}$) is more than twice as large, as the net wind losses ($\alpha - \alpha_{\rm cool}$). Put differently, this implies that $(3\Omega_0/2)\langle S_{xy}^{\rm MRI}\rangle > \langle F_W^{\rm GI}\rangle + \langle F_W^{\rm MRI}\rangle + \delta F_W^{\rm inter}$. Hence, this effect alone cannot account for the imbalance (this does not mean that $\delta F_W^{\rm inter} = 0$). In route (2), the stresses do not exactly add, but are weakened. That is consistent with the severe reduction of GI activity (reduced gravitational stress, $\alpha_{\rm g}$) observed in Löhnert & Peeters (2022) and the simulations discussed below. The increasing, dimensionless Maxwell stress, $\alpha_{\rm m}$, is always accompanied by a decreasing gravitational stress, $\alpha_{\rm g}$. Such reductions in GI activity are not uncommon. It is known that additional heating, for example the second term in the cooling (heating) model, Eq. (5), can cause a reduction of GI strength even for a specific cooling time and a given box mass (see Rice et al. 2011). Thereby, $\alpha_{\rm g}$ may be reduced significantly, but the saturated Toomre parameter, $\langle Q \rangle$, increases only slightly. There is also an intuitive interpretation of this behaviour. The second term, in Eq. (5), leads to an equilibrium at a finite temperature ($c_{\rm s} = c_{\rm s,0}$), even in the absence of turbulence, and for a given total mass, this corresponds to a Toomre value Q_0. One can then ask what will happen, if Q_0 is gradually increased, approaching $Q_{\rm c}$. Taking into account that GI cannot deviate by much from $\langle Q \rangle \sim Q_{\rm c} \gtrsim 1$, then this implies that the GI-strength must decline, as otherwise the background heating would add to the turbulent heating, increasing $\langle Q \rangle$. In Rice et al. (2011), the relation between α and $\tau_{\rm c}$ was therefore extended by incorporating the additional heating (see Eq. (10)). Hence, additional stresses (e.g. due to MRI), may themselves act as a form of background heating, compromising parts of GI. In Löhnert & Peeters (2022), background heating was explicitly included, and two different Q_0 values indeed caused two different stress levels of GI. In Löhnert & Peeters (2022), the values of Q_0 were chosen relatively large ($Q_0 \sim 0.75$–0.86). Hence, one can expect the strength of GI to be weakened significantly, by the cooling model alone, and one might ask how the GI-MHD state saturates for significantly stronger GI (e.g. $Q_0 = 0$, or no heating). In Löhnert & Peeters (2022), this was tested, by turning off the heating term (second term in Eq. (5)) in the cooling law. This was done after the system has already reached a saturated state (likely a form of GI-MRI coexistence), and it was found that this state persists. However, two points of concern arise from this. For one, the pre-existing GI-MRI coexistence may be a bias, and it may not have emerged if the seed field was directly introduced into a GI state without heating. Hence, one goal of the following sections is to further test cases without additional heating. Furthermore, the outcome for a cooling time of $\tau_{\rm c}\Omega_0 = 20$ was significantly different from a similar simulation (SGMRI-20) carried out by Riols & Latter (2018a). Riols & Latter (2018a) also suggested that MRI may be suppressed in the presence of GI. One further goal is thus to resolve this difference (see Sect. 5.2). An overview over the simulations, discussed in the following sections, is provided in Table 1.

5.1. Simulations without background heating

In Löhnert & Peeters (2022), GI simulations with cooling and additional background heating (second term in Eq. (5)) were studied in which a small ZNF-type magnetic seed field was introduced into a fully GI-turbulent state. The runs, shown here, also introduce a initial-ZNF field, into GI turbulence, though now without additional background heating. The two main simulations are sg-mhd-tau20 and sg-mhd-tau10, with cooling times $\tau_{\rm c}\Omega_0 = 20$ and $\tau_{\rm c}\Omega_0 = 10$, respectively. sg-mhd-tau20 was restarted from the pure-GI simulation GI072 of Löhnert & Peeters (2022) at $t\Omega_0 = 120$. Simulation GI072 uses

Table 1. Summary of all ideal-MHD simulations.

	sg-mhd-2	sg-mhd-tau10	sg-mhd-tau20	sg-mhd-tau20-Lz6	MRI-compare
$L_x \times L_y \times L_z$	$20 \times 20 \times 8$ H	$20 \times 20 \times 8$ H	$20 \times 20 \times 8$ H	$20 \times 20 \times 6$ H	$2 \times 4 \times 8$ H
$N_x \times N_y \times N_z$	$440 \times 440 \times 170$	$440 \times 440 \times 170$	$440 \times 440 \times 170$	$500 \times 500 \times 150$	$50 \times 100 \times 200$
CFL	0.06	0.3	0.3	0.3	0.1
γ	1.64	1.64	1.64	1.64	1.64
$\tau_c\Omega_0$	10	10	20	20	–
Q_0 (heating)	0.75	0	0	0	–
$\langle\rho\rangle$	0.0536	0.0556	0.0556	0.0531	0.2408
$\rho_{\min}, P_{\min}$	$10^{-4},\ 6.1 \times 10^{-5}$	$6 \times 10^{-5},\ 3.7 \times 10^{-5}$	$10^{-4},\ 6.1 \times 10^{-5}$	$3.2 \times 10^{-5},\ 2.0 \times 10^{-5}$	$10^{-4},\ 0$
Interval in Ω_0^{-1}	700–1000	1000–1500	800–1300	800–1100	100–1000
$\langle\langle Q\rangle\rangle_t$	1.138	1.113	1.187	1.281	–
$\langle\langle\beta\rangle\rangle_t$	16.43	11.66	12.23	12.42	17.09
$\langle\langle c_s\rangle\rangle_t$	1.525	1.547	1.650	1.276	1.0
$\langle\alpha_r\rangle_t$	0.0074	0.01364	0.0069	0.0070	0.0023
$\langle\alpha_m\rangle_t$	0.0092	0.01357	0.0119	0.0111	0.0088
$\langle\alpha_g\rangle_t$	0.0095	0.0183	0.0067	0.0075	–
$\langle\alpha\rangle_t$	0.0261	0.0455	0.0255	0.0256	0.0112
$\langle\alpha_{cool}\rangle_t$	0.0241	0.0423	0.0212	0.0212	–
$\langle r_{sp}\rangle_t$	0.3426	0.3677	0.3190	0.3206	0.3487

Notes. The first five lines provide general simulation settings (box size, grid points, Courant number, cooling time, and background Toomre parameter). The form of the cooling law is provided in Eq. (5), and in all GI simulations, except sg-mhd-2, the second term in Eq. (5) (heating) was turned off. The pure-MRI simulation, MRI-compare, uses an isothermal equation of state. In cases with heating, the amount of heating is quantified by the background Toomre parameter Q_0 (see the discussion in Sects. 2 and 3). The remaining lines provide a selection of important, volume- and time-averaged, dimensionless quantities. The corresponding time intervals are shown in the fifth line, and the latter are chosen such that they reasonably cover the saturated phases. Hence, the last included time point is also the last time point of the simulation.

the full cooling law given in Eq. (5) with both heating and cooling and with a cooling timescale of $\tau_c\Omega_0 = 10$. The averaged mass density in GI072 is such that the background speed of sound ($c_{s,0} = 1$) is related to a background Toomre parameter of $Q_0 = 0.72$. At the moment sg-mhd-tau20 is restarted from GI072 ($t\Omega_0 = 120$), the heating term (second term in Eq. (5)) was turned off, and the cooling time was set to $\tau_c\Omega_0 = 20$. At first, $\boldsymbol{B} = 0$, in order to achieve a new stationary GI state with the new cooling law. At $t\Omega_0 = 200$, the ZNF magnetic field is then seeded into the GI-turbulent state. Simulation sg-mhd-tau10 was restarted from sg-mhd-tau20 at $t\Omega_0 = 200$, but instead of introducing a seed field, the cooling time was reduced to $\tau_c\Omega_0 = 10$. One might ask why sg-mhd-tau10 was not restarted from GI072 as well. It turns out that removing background heating at $\tau_c\Omega_0 = 10$ can cause numerical instabilities; hence, first removing heating at $t\Omega_0 = 20$ and afterwards reducing the cooling time was the more reliable choice. In sg-mhd-tau10, the pure-GI state was then evolved until $t\Omega_0 = 400$. At that point, the ZNF field was introduced. In both sg-mhd-tau20 and 10, the ZNF-seed field is of the form $\boldsymbol{B}_0 = B_0 \sin(2\pi x/L_x)\hat{\boldsymbol{e}}_z$, with a field amplitude, B_0, chosen such that $\langle\beta\rangle_{xy} = 10^7$, at the mid-plane. More details about the numerical settings of these simulations are provided in Table 1. Additionally, a pure-MRI simulation, in the following referred to as MRI-compare, was set up, in order to provide a comparison. The latter is an isothermal simulation, that is, the equation of state is given by $P = c_{s,i}^2\rho$, where the isothermal sound speed, $c_{s,i}$, was chosen such that $\sqrt{\gamma}c_{s,i} = 1.0$. This choice is deliberate, in order to allow an easier comparison to the GI cases. We note that H-correction was not used here as it is not required and in fact caused numerical difficulties. The seed-field configuration is exactly equal to that of the GI cases, except that $\langle\beta\rangle_{xy} = 100$, at the mid-plane. More details about the simulation parameters are provided in Table 1. Also shown in Table 1 is the ideal-MHD simulation sg-mhd-2, which is discussed in detail in Löhnert & Peeters (2022). The latter uses a cooling time of $\tau_c\Omega_0 = 10$, but also includes background heating, second term of Eq. (5), with $c_{s,0} = 1$, and a corresponding Toomre value of $Q_0 \sim 0.75$.

The time evolutions of the volume-averaged, dimensionless turbulent stresses, for simulations sg-mhd-tau20, sg-mhd-tau10, sg-mhd-2, and MRI-compare, are shown in Fig. 2. The stresses were calculated using Eqs. (8) and (9). We note that the factor γ, in Eq. (9), is also used for the isothermal MRI case, in order to retain comparability. In all GI cases, the vertical solid line marks the time point, at which the ZNF-seed field is introduced.

After the introduction of the seed, the dimensionless Maxwell stress, α_m, grows significantly, yielding values that are larger, or comparable to the remaining stresses. For the case with the longest cooling time (sg-mhd-tau20, $\tau_c\Omega_0 = 20$), α_m grows to become the dominant stress contribution. Contrary to that, the gravitational stress contribution, α_g, decreases in all cases. The smallest changes occur to the dimensionless Reynolds stress, α_r. All GI simulations require a considerable amount of time to saturate, $\gtrsim 200$–$800\,\Omega_0^{-1}$; the $\tau_c\Omega_0 = 10$ case appears to saturate the fastest. Volume- and time-averaged values, for the saturated phases of all runs, are provided in Table 1. One can then compare sg-mhd-tau20 and sg-mhd-2 at their initial phases with no or a vanishing magnetic field. It is apparent from Fig. 2 that the stress levels are comparable, despite sg-mhd-2 having a cooling time of $\tau_c\Omega_0 = 10$ and sg-mhd-tau20 a cooling time of $\tau_c\Omega_0 = 20$. Yet, this demonstrates the point, raised earlier, that additional heating can weaken GI, similar to a longer cooling time. The case with strongest GI is clearly sg-mhd-tau10, with the latter yielding a total stress, α, almost twice as large as the α-values obtained from the remaining simulations. In the dynamo-saturated phases, the Maxwell contributions are of equal magnitude for all GI simulations, $\alpha_m = 0.0119$, 0.0136, and 0.0092 for sg-mhd-tau20, 10, and sg-mhd-2, respectively. These values can be compared

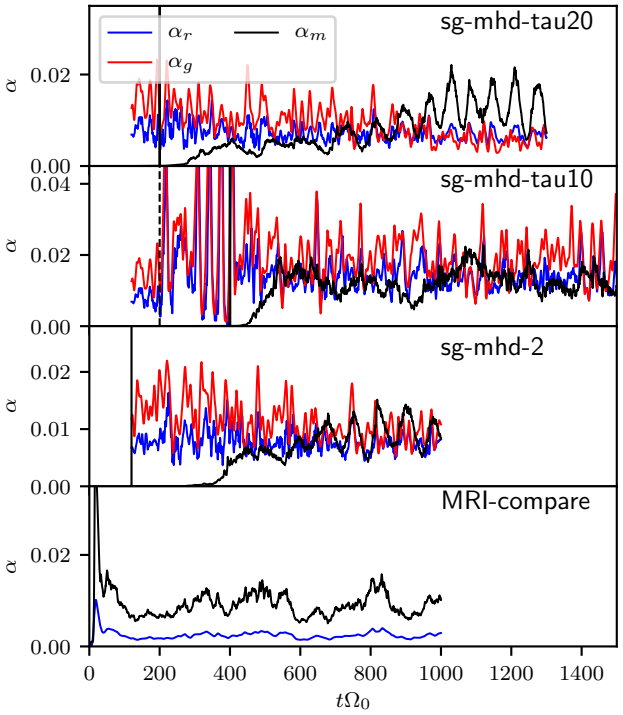

Fig. 2. Dimensionless stresses as a function of time for simulations sg-mhd-tau20 ($\tau_c\Omega_0 = 20$), sg-mhd-tau10 ($\tau_c\Omega_0 = 10$), sg-mhd-2 ($\tau_c\Omega_0 = 10$, $Q_0 \sim 0.75$), and MRI-compare. Shown in blue is the Reynolds contribution, α_r, in red the gravitational contribution, α_g, and in black the Maxwell part, α_m. All stresses were calculated using Eqs. (8) and (9), and the factor $\gamma = 1.64$ was also used for the isothermal MRI, allowing for an easier comparison. The curves for sg-mhd-tau20 and 10 start at $t\Omega_0 = 120$, at which point the simulations were restarted from the pure-GI state of GI072 (see Löhnert & Peeters 2022). Then, the cooling time was set to $\tau_c\Omega_0 = 20$, and background heating was turned off (only cooling). At $t\Omega_0 = 200$, either one of two things happens, depending on the simulation. In sg-mhd-tau20, the ZNF field was introduced directly at $t\Omega_0 = 200$, highlighted by the solid vertical line. In sg-mhd-tau10, the pure-GI phase was prolonged from $t\Omega_0 = 200$ (vertical dashed line) to $t\Omega_0 = 400$ (vertical solid line), but the cooling time was reduced to $\tau_c\Omega_0 = 10$. At $t\Omega_0 = 400$, the ZNF field was introduced. For both sg-mhd-tau20 and 10, the values of α_g and α_r were smoothed by convolving the respective time series with a Gaussian function (standard deviation $\sigma = 3\Omega_0^{-1}$).

to the dimensionless Maxwell stress, observed in the pure-MRI simulation, $\alpha_m = 0.0088$. The GI values are consistently larger than the pure-MRI value; the largest deviation is observed for the strongest-GI case, sg-mhd-tau10. The deviations, relative to the pure-MRI value, are 5%, 35%, and 55%, for sg-mhd-2, sg-mhd-tau20, and sg-mhd-tau10, respectively.

It is also interesting to compare the pure-GI with the dynamo-saturated phases. The comparison is here provided for the simulations sg-mhd-tau10 and sg-mhd-tau20. The time intervals used for the initial and saturated phases as well as a selection of important, time-averaged values are shown in Table 2. The pure-GI phase ($\boldsymbol{B} = 0$) of sg-mhd-tau10 exhibits significant oscillations. Hence, in order to obtain more reliable statistics, the GI-only state was prolonged from $t\Omega_0 = 400$, to 700; the corresponding time evolutions for α and $\langle Q\rangle$ are shown in Appendix A. The time average was then applied to the last $200\Omega_0^{-1}$. One feature becomes immediately clear, the gravitational stress, α_g, decreases significantly (from the GI-only to the dynamo-saturated state). The absolute reduction of α_g is roughly

Table 2. Comparison of the initial and saturated phases for simulations sg-mhd-tau20 and 10.

	sg-mhd-tau20		sg-mhd-tau10	
	I_1	I_2	I_1'	I_2'
α_r	0.0081	0.0069	0.0192	0.0136
α_g	0.0141	0.0067	0.0270	0.0183
α_m	8.5×10^{-5}	0.0119	0	0.0136
α	0.0223	0.0255	0.0462	0.0455
α_{cool}	0.0212	0.0212	0.0423	0.0423
$\langle Q\rangle$	1.0747	1.1870	1.1208	1.1129
α_g/α_m	–	0.56	–	1.35
$\alpha_g(I_2)-\alpha_g(I_1)$	−0.0074		−0.0087	
$\frac{\alpha_g(I_2)-\alpha_g(I_1)}{\alpha_g(I_1)}$	−52%		−32%	

Notes. For sg-mhd-tau20, the initial phase is $I_1 := [160 - 260\Omega_0^{-1}]$, and the saturated phase is $I_2 := [800 - 1300\Omega_0^{-1}]$ (see also Fig. 2). For sg-mhd-tau10, the initial interval is $I_1' := [500 - 700\Omega_0^{-1}]$, but evaluated for the prolonged GI-phase (see Appendix A). For the dynamo-saturated phase, the interval $I_2' := [1000 - 1500\Omega_0^{-1}]$ is used.

equal for the two simulations. The total stress, $\alpha = \alpha_r + \alpha_g + \alpha_m$, remains almost constant in comparison. In the dynamo-saturated state, the stress ratio, gravitational-to-Maxwell, α_g/α_m, is ∼0.56, for sg-mhd-tau20 and ∼1.35, for sg-mhd-tau10. Hence, in sg-mhd-tau20 the Maxwell stress dominates, whereas in sg-mhd-tau10 the gravitational stress is dominant. Since α_m is almost equal in the two simulations, this reflects the fact that GI is stronger for $\tau_c\Omega_0 = 10$, as compared to $\tau_c\Omega_0 = 20$. Differences between sg-mhd-tau10 and 20, can also be seen in the time evolution of α_m. In sg-mhd-tau20, at saturation, α_m develops distinct oscillations, whereas sg-mhd-tau10 gives rise to more irregular α_m-fluctuations. One can also compare the evolution of the Toomre values, from the GI-only to the saturated state. The Toomre value of sg-mhd-tau20 slightly increases, by roughly 10%. For sg-mhd-tau10, the saturation value slightly decreases by ∼8%. However, it has turned out that the exact value in the GI-only phase sensitively depends on momentary $\langle Q\rangle$ fluctuations. This can be seen in Fig. A.1, where the spike at the end of the averaging period leads to a significant contribution. If this spike is excluded, then the initial value is slightly smaller than the dynamo-saturated one. Hence, there is some statistical uncertainty in the exact values of $\langle Q\rangle$, for sg-mhd-tau10. A significant change in $\langle Q\rangle$, is not expected in any event, as GI saturates at marginal, gravitational stability, $\langle Q\rangle \sim Q_c$, with $Q_c \gtrsim 1$. We note that this is also the case for all simulations, shown in Tables 1 and 2, and for both GI-only and the saturated phases. The time evolution of $\langle Q\rangle$ is shown in Fig. 1, for sg-mhd-tau10 (red) and sg-mhd-tau20 (blue). The vertical lines highlight the time points, at which the seed fields were introduced.

As discussed at the beginning of Sect. 5, it is this self-regulation to marginal stability, which necessitates a reduction of GI activity, as additional Maxwell stresses emerge. Hence, the reduction of α_g in both simulations is in agreement with the simultaneous increase in α_m. It is always possible that winds contribute to the overall energy balance. Whether winds are of importance can be tested, by comparing the stress values α, to the values $\alpha_{cool} = 4/(9\gamma(\gamma-1)\tau_c\Omega_0)$ (see Eq. (10) and Gammie 2001). If wind losses were absent, a stationary turbulent state would require $\alpha = \alpha_{cool}$. In the saturated phase, $(\alpha - \alpha_{cool})/\alpha \sim 20\%$ for sg-mhd-tau20 and ∼8%, for sg-mhd-tau10 (see Table 2). Yet, the Maxwell contributions are $\alpha_m/\alpha \sim 47\%$

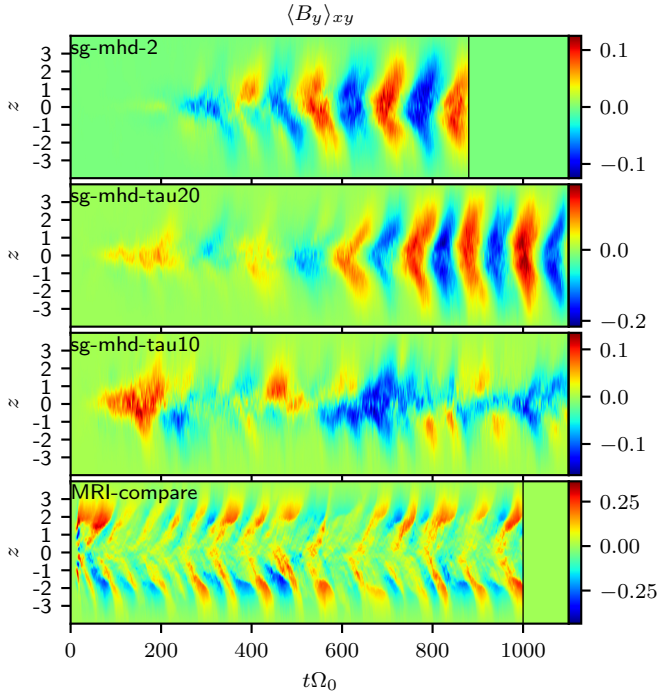

Fig. 3. Horizontally averaged toroidal magnetic field component, $\langle B_y \rangle_{xy}$, as a function height, z, and time, t. The zt diagrams are shown for simulations sg-mhd-2, sg-mhd-tau20, sg-mhd-tau10, and MRI-compare. The time axis is chosen such that $t = 0$ corresponds to the moment of field seeding.

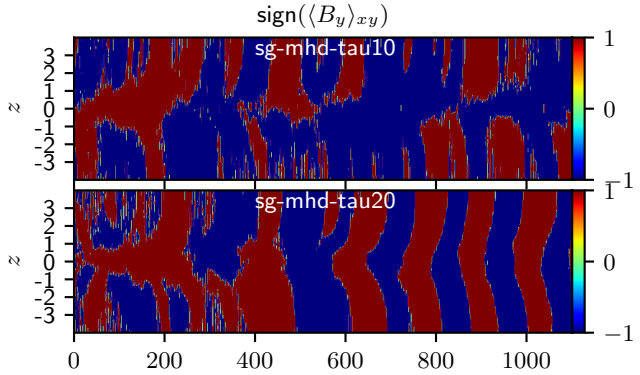

Fig. 4. Sign of the horizontally averaged toroidal magnetic field component. In this case, the "sign" has been intended to be a mathematical function, returning the sign of a value. sign($\langle B_y \rangle_{xy}$), shown for simulations sg-mhd-tau10 and sg-mhd-tau20. The images can be directly compared to the corresponding zt diagrams in Fig. 3.

for sg-mhd-tau20 and ∼30% for sg-mhd-tau10. Hence, the additional energy input, associated with α_m, cannot completely be captured by wind cooling. Put differently, some of the additional energy input, associated with α_m, contributes to heating. Regarding a possible GI-MRI coexistence, no definitive conclusion can be drawn, from α alone. One can say that sg-mhd-2 and sg-mhd-tau20 give rise to a similar, dynamo-saturated state, which is in agreement with the observation that the GI strength is roughly equal in the two cases. For the case with strongest GI activity, sg-mhd-tau10, the saturated state is qualitatively different from those of sg-mhd-tau20 and sg-mhd-2 in some aspects (e.g. more irregular α_m-fluctuations, larger values of α_g/α_m). In Löhnert & Peeters (2022), it was argued that sg-mhd-2 is a state of GI-MRI coexistence. Hence, this suggests that stronger GI cases might lead to a qualitatively different saturation state of the dynamo.

As a further test, one can evaluate the vertical magnetic-field structure. Shown in Fig. 3 are zt diagrams of the horizontally averaged magnetic field component, $\langle B_y \rangle_{xy}$, for simulations sg-mhd-2, sg-mhd-tau20, sg-mhd-tau10, and MRI-compare. The pure-MRI case develops an oscillating butterfly pattern, shortly after initialisation. Simulations sg-mhd-2 (see also Löhnert & Peeters 2022) and sg-mhd-tau20 develop a clearly visible butterfly diagram as well, but it takes several $100\Omega_0^{-1}$ to reach a stationary pattern. We note that the diagrams, seen in sg-mhd-tau20 and sg-mhd-2, differ in some aspects from the pure-MRI butterfly diagram. Most notably, in MRI-compare, the magnetic-field strength peaks at ∼2 H above (below) the mid-plane. In contrast to that, the GI-MHD cases sg-mhd-tau20 and sg-mhd-2 develop significant field strengths, also within $|z| \leq 2$ H. The field pattern for sg-mhd-tau10 is less regular than in the other cases. Near the mid-plane, $\langle B_y \rangle_{xy}$ can retain its polarity for over $\sim 200\Omega_0^{-1}$, whereas, away from the mid-plane, the field changes polarity more frequently. It is also noted that the irregular field reversals are very similar to those seen in the ideal simulation PL-ZNF-ideal, in Riols et al. (2021). A nonlinear cooling model was used in the latter simulation, and the exact cooling time might depend on temperature fluctuations. However, the effective timescale, $\tau_{\rm eff}$, evaluated for PL-ZNF-ideal in Riols et al. (2021) is also close to 10. Hence, for $\langle B_y \rangle_{xy}(z, t)$, qualitative differences arise between the weaker GI cases (sg-mhd-2 and sg-mhd-tau20) and sg-mhd-tau10. The former lead to a butterfly diagram with clearly visibly field reversals that bears similarities with the pure-MRI butterfly diagram. For the case with highest GI activity, sg-mhd-tau10, a clearly visible butterfly diagram is absent, and more irregular field variations are observed. This, in combination with the more irregular α_m variations, suggests that sg-mhd-tau20 and 10 lead to two different saturated dynamo states: a weak-GI dynamo, which shares some characteristics with the pure-MRI dynamo and a strong-GI dynamo, which is qualitatively different, and where MRI may be absent.

One can directly check for sign reversals of $\langle B_y \rangle_{xy}$, in the zt diagrams of both sg-mhd-tau20 and 10. This is demonstrated in Fig. 4, depicting sign$\left(\langle B_y \rangle_{xy}\right)$, for sg-mhd-tau10 (first image) and sg-mhd-tau20 (second image). The mid-plane, in sg-mhd-tau10, can retain its polarity for extended periods of time, whereas frequent polarity reversals occur at higher altitudes. This state is similar to the intermediate regime, $100 \leq t\Omega_0 \leq 500$, of sg-mhd-tau20. Differences arise at $\sim 600\Omega_0^{-1}$, after field seeding, at which point the high-altitude oscillations form a coherent phase relation with the mid-plane field, in sg-mhd-tau20, magnetising the entire vertical extent of the disk. A similar phase locking does not occur in sg-mhd-tau10.

Magneto-rotational instability is possibly absent, in sg-mhd-tau10, though, for now, this cannot definitively be decided. We note that more irregular field reversals have been observed in stratified, zero-net-vertical-flux MRI simulations (see e.g. Hirose et al. 2014; Coleman et al. 2017). There, vertical mixing, due to convection, prevents coherent sign reversals. It is not unreasonable that a similar, vertical mixing can be initiated by GI (see the horizontal rolls, above (below) density waves, in Riols & Latter 2018b). This may be related to the rather long time period ($\sim 800\Omega_0^{-1}$), required to reach coherent $\langle B_y \rangle_{xy}$ oscillations, in sg-mhd-tau20, though the exact reasons for this are not entirely clear. To be sure, we checked whether accumulating,

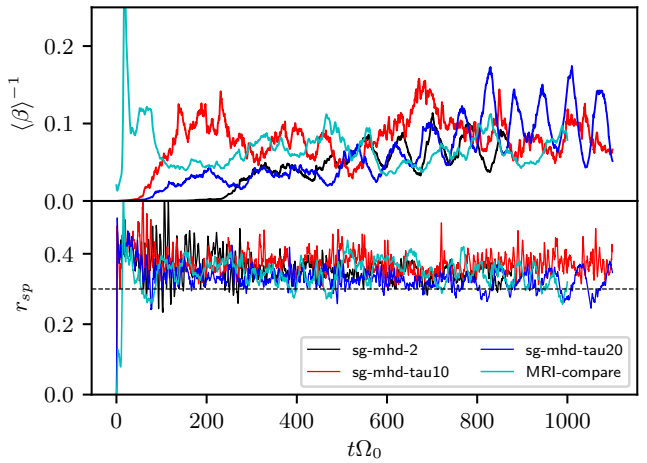

Fig. 5. Inverse volume-averaged plasma β, $\langle\beta\rangle^{-1} = \langle|\boldsymbol{B}|^2\rangle/(2\mu_0\langle P\rangle)$, and the ratio of Maxwell stress to magnetic pressure, $r_{\rm sp} = \langle -2B_xB_y\rangle/(|\boldsymbol{B}|^2)$, as a function of time. The depicted simulations are sg-mhd-tau10 (red), sg-mhd-tau20 (blue), sg-mhd-2 (black), and MRI-compare (cyan). In all cases, the time $t = 0$ corresponds to the moment of field seeding.

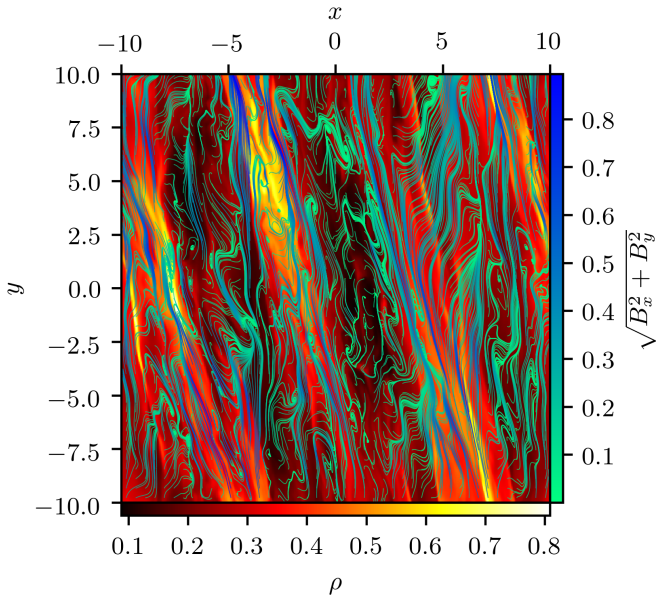

Fig. 6. Mid-plane mass density, $\rho(x, y, z = 0)$, for simulation sg-mhd-tau20 evaluated at $t\Omega_0 = 1200$. The mass density is superimposed with magnetic field lines traced in the (x, y) plane with only the B_x and B_y components used for the tracing.

numerical errors have violated the ZNF condition, $\langle B_z\rangle_{xy} = 0$, over time (see e.g. Silvers 2008), effectively leading to a net-flux case. However, it appears that this is not the case, and $\langle B_z\rangle_{xy}$ values are at most of the order of 10^{-9}, or, in terms of a plasm β, $\langle\beta_z\rangle_{xy} = 2\mu_0\langle P\rangle_{xy}/\langle B_z\rangle^2_{xy} = 10^{14}$.

Also evaluated are the volume-averaged plasma β, $\langle\beta\rangle = 2\mu_0 P/|\boldsymbol{B}|^2$, and the ratio of Maxwell stress to magnetic pressure, $r_{\rm sp} = \langle -2B_xB_y\rangle/|\boldsymbol{B}|^2$, for simulations sg-mhd-2, sg-mhd-tau20, 10, and MRI-compare. This is shown in Fig. 5, where $\langle\beta\rangle^{-1}$ is depicted in the first image and $r_{\rm sp}$ in the second image. The time axes are chosen such that $t = 0$ corresponds to the moment when the seed field is introduced. The plasma β saturates at values $\langle\beta\rangle \gtrsim 10$ (see also Table 1), and this is true for both the pure-MRI case and the GI simulations. All cases settle into a state with $r_{\rm sp} \gtrsim 0.3$, and the saturation values are also robust in the sense that the fluctuations, with respect to the absolute values, are small in comparison. The value range $0.3 \lesssim r_{\rm sp} \lesssim 0.4$ is shown to be typical for MRI, in a variety of studies (see e.g. Hawley et al. 1995, 2011; Blackman et al. 2008; Simon et al. 2011; Salvesen et al. 2016). Shortly after field seeding (for the first 100 to $200\Omega_0^{-1}$), the magnetic field strength is too low for MRI to be fully resolved (see also Löhnert & Peeters 2022), and only a pure-GI dynamo operates. The $r_{\rm sp}$ values, evaluated in that period, are only slightly larger ($r_{\rm sp} \gtrsim 0.4$). Hence, this indicates that the initial, pure-GI dynamo also saturates at a roughly similar magnetic stress-to-pressure ratio. It is interesting that all simulations, including the MRI case, saturate at roughly the same $\langle\beta\rangle$ and $r_{\rm sp}$ level, despite sg-mhd-tau20 and sg-mhd-tau10 leading to a qualitatively different dynamo appearance.

Finally, a visual representation of the saturated, turbulent state is provided in Fig. 6, for sg-mhd-tau20. Shown is the mid-plane mass density $\rho(x, y)$, superimposed with magnetic field lines, traced in the (x, y) plane (only B_x and B_y are used for the tracing). The image was generated at $t\Omega_0 = 1200$. One observes a significant alignment of the field lines with GI-related density waves. A similar behaviour was also observed in Riols & Latter (2018a, 2019).

5.2. Comparison to previous simulations

Löhnert & Peeters (2022) report differences to the previous comparable simulations provided in Riols & Latter (2018a), especially the $\tau_c\Omega_0 = 20$ case, SGMRI-20, therein. The goal of this section is to single out the reason for the observed differences. In Löhnert & Peeters (2022), we argued that effects due to winds, crossing the vertical box boundaries, might have an influence on the simulation outcome. The corresponding simulation in Riols & Latter (2018a), SGMRI-20, uses a slightly smaller, vertical box size of 6 H, compared to our standard 8 H. We note that, due to the uncertainty of the exact value of c_s in a turbulent state, an exact one-to-one comparison of box-sizes may be misleading. Hence, we provide a new simulation, sg-mhd-tau20-Lz6, with settings equal to run SGMRI-20 from Riols & Latter (2018a). Simulation sg-mhd-tau20-Lz6 is also listed in Table 1. All horizontal box dimensions are similar to the previous simulations, but the vertical box size is chosen to be $L_z = 6$ H, and the number of grid points is slightly increased to 500 per 20 H. This should provide a setup that is almost identical to SGMRI-20. Simulation sg-mhd-tau20-Lz6 is a completely new simulation and has not been restarted from any previous simulation. The simulation starts with a density and pressure distribution that is homogeneous in the horizontal directions (i.e. homogeneous across xy planes). In the vertical direction, a density and pressure stratification is established such that $c_s = 1$ for all z. For the stratification equilibrium the contribution of self-gravity was included (see also the method in Löhnert & Peeters 2022). This initial state is perturbed by small, random deviations in both density and pressure (the deviation amplitude is 1% of the background value). The equilibrium is chosen such that $\langle Q\rangle = c_s\Omega_0/(\pi G\langle\rho\rangle L_z) = 1.0$, at the start of the simulation. The simulation does not include background heating (no second term in Eq. (5)). Hence, cooling quickly causes the Toomre parameter, $\langle Q\rangle$, to drop below one. One then immediately observes the growth of GI; after $\sim 40\Omega_0^{-1}$, the linear axisymmetric GI modes break up into non-axisymmetric turbulence. After $\sim 130\Omega_0^{-1}$, almost axisymmetric modes occur again, but they are less pronounced and quickly break up into GI turbulence again. The system then evolves into a stationary, turbulent state. The turbulent state is prolonged until $t\Omega_0 = 200$, where

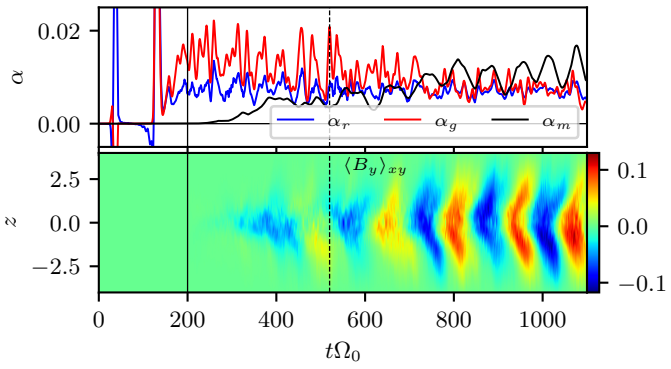

Fig. 7. Time evolution for a selection of quantities evaluated for sg-mhd-tau20-Lz6. First image: Dimensionless stresses as a function of time. Shown in blue is the Reynolds contribution, α_r, in red the gravitational contribution, α_g, and in black the Maxwell part, α_m. All stresses were calculated, using Eqs. (8) and (9). The values of α_r, and α_g were smoothed using a Gaussian function (see also Fig. 2). Second image: Horizontally averaged magnetic field component, $\langle B_y \rangle_{xy}$, as a function of height, z, and time, t. At $t\Omega_0 = 200$ (vertical solid line), the magnetic seed field is introduced. The vertical dashed line corresponds to $320\Omega_0^{-1}$ after field seeding.

the ZNF magnetic field is seeded into the GI-turbulent state. The time evolution of the turbulent stresses is shown in the first image of Fig. 7. The two GI-break-up events at 40 and $130\Omega_0^{-1}$ can be seen as the two spikes in the initial (GI) phase of the simulation. The seeding of the ZNF field is marked as the vertical dashed line ($t\Omega_0 = 200$). After seeding of the field, the behaviour of the stresses is very similar to that seen in sg-mhd-tau20. As α_m increases significantly, the gravitational part α_g drops, and α_m eventually becomes the dominant contribution. And a butterfly diagram, equal to that of sg-mhd-tau20, also develops here, shown in the second image of Fig. 7.

The reason for the differences is the amount of time required to reach a saturated state. In Riols & Latter (2018a), the stresses where evaluated for the first $320\Omega_0^{-1}$, after the magnetic seed field was introduced. We, therefore, followed the same procedure and took a time average of the dimensionless turbulent stresses over the first $320\Omega_0^{-1}$ after seeding of the field. This is done for sg-mhd-tau20-Lz6 and the previously discussed simulation, sg-mhd-tau20. The resulting stress values are provided in Table 3. We note that the stress values for SGMRI-20, obtained from Riols & Latter (2018a), have been multiplied by a factor $2/(3\gamma)$, in order to be consistent with the definition in Eq. (8). As one can see, the values are almost equal for all three simulations. Moreover, the zt diagram (second image of Fig. 7) for the first $320\Omega_0^{-1}$ is very similar to that shown in Riols & Latter (2018a). One can therefore conclude that this is the reason why differences were observed in Löhnert & Peeters (2022). It is also noted that the zt diagram of the $\tau_c\Omega_0 = 10$ simulation, SGMRI-10, shown in Riols & Latter (2018a), is qualitatively close to the more irregular field reversals seen in sg-mhd-tau-10 here. Hence, sg-mhd-tau10 is also compared to SGMRI-10 in the fourth and fifth rows of Table 3. One finds comparable values for the two simulations. Here, however, the average was taken over the saturated phase of sg-mhd-tau10. This is also reasonable as SGMRI-10 was restarted from SGMRI-20 and not completely run anew, indicating that it is perhaps closer to a saturated state. It appears that, at least for lower cooling times (weaker GI), one has to run simulations of the GI dynamo sufficiently long, in order to obtain the dynamo-transition to a defined butterfly diagram. We note that this is not an obvious point. The typical timescales for

Table 3. Dimensionless stress comparison.

	$\langle \alpha_r \rangle_t$	$\langle \alpha_g \rangle_t$	$\langle \alpha_m \rangle_t$	$\langle \alpha \rangle_t$
sg-mhd-tau20-Lz6	0.0074	0.0130	0.0028	0.0232
sg-mhd-tau20	0.0077	0.0119	0.0027	0.0223
SGMRI-20	0.0056	0.012	0.0028	0.02
sg-mhd-tau10	0.0136	0.0183	0.0136	0.0455
SGMRI-10	0.011	0.017	0.012	0.04

Notes. Shown in the first three lines are the volume- and time-averaged dimensionless stresses for simulations sg-mhd-tau20, sg-mhd-tau20-Lz6, and SGMRI-20 of Riols & Latter (2018a). In all cases, the time interval spans $320\Omega_0^{-1}$, after the field is seeded. The same is shown in the fourth and fifth lines, though now for sg-mhd-tau10 and SGMRI-10 of Riols & Latter (2018a). The values for sg-mhd-tau10 were here averaged over the saturated phase, $1000 < t\Omega_0 < 1500$.

GI are of the order of the cooling time, here $\sim 10\Omega_0^{-1}$. Hence, it is surprising that the GI-MRI combined state requires $\sim 600\Omega_0^{-1}$ to reach saturation. It is currently not clear why that is the case, and it is certainly an interesting question for upcoming research. However, as speculated in the previous section, this may be related to the time, required for the butterfly diagram to lock to the mid-plane field.

5.3. Field generation

One can show that, in the local shearing box, the induction equation for the horizontally averaged fields ($\langle B_x \rangle_{xy}$, and $\langle B_y \rangle_{xy}$) takes the following form (see e.g. Riols & Latter 2018a; Löhnert & Peeters 2022):

$$\partial_t \langle B_x \rangle_{xy} = -\partial_z \langle \mathcal{E}_y \rangle_{xy} \tag{16}$$

$$\partial_t \langle B_y \rangle_{xy} = \partial_z \langle \mathcal{E}_x \rangle_{xy} - \frac{3\Omega_0}{2} \langle B_x \rangle_{xy}, \tag{17}$$

where $\mathcal{E} = \delta \boldsymbol{v} \times \boldsymbol{B}$, is the electromotive force (EMF). This definition of $\mathcal{E}$ does not distinguish between the averaged and the fluctuating field, whereas $\delta \boldsymbol{v}$ represents only the deviations from the shear flow. In the following, the vertical profiles of the field components and the EMFs are compared for simulations sg-mhd-tau20, 10, and MRI-compare. As one can see from the butterfly diagrams in Fig. 3, the horizontally averaged field components can change sign rather frequently. A direct time average leads to a cancellation, which is not desired. This can be circumvented by choosing a sign convention, before the time average is applied. If $\langle f \rangle_{xy}$ is a horizontally averaged dummy variable, depending on t and z, then the time-average is carried out as follows:

$$\langle \langle f \rangle_{xy} \rangle_t^{\pm} := \left\langle \langle f \rangle_{xy} \operatorname{sign}\left(\langle B_y \rangle_{xy} \right) \right\rangle_t. \tag{18}$$

This method certainly has caveats, since $\langle \langle B_y \rangle_{xy} \rangle_t^{\pm}$ must necessarily be positive for all z. The signs of $\langle \langle B_x \rangle_{xy} \rangle_t^{\pm}$, $\langle \langle \mathcal{E}_x \rangle_{xy} \rangle_t^{\pm}$, and $\langle \langle \mathcal{E}_y \rangle_{xy} \rangle_t^{\pm}$ are always relative to B_y. However, one has to choose a height-dependent sign convention, as otherwise certain contributions would be lost. For example, in the zt diagram of sg-mhd-tau10, one can see that oscillations with a higher frequency occur for larger z values, but only a few field reversals are observed near the mid-plane. Choosing a fix sign for every time point would cancel out some contributions. However, applying the same averaging technique, $\langle \langle f \rangle_{xy} \rangle_t^{\pm}$, to all simulations still allows for a comparison of those simulations. The technique is first applied to simulation sg-mhd-tau20, and the resulting profiles are shown in Fig. 8. From top to bottom,

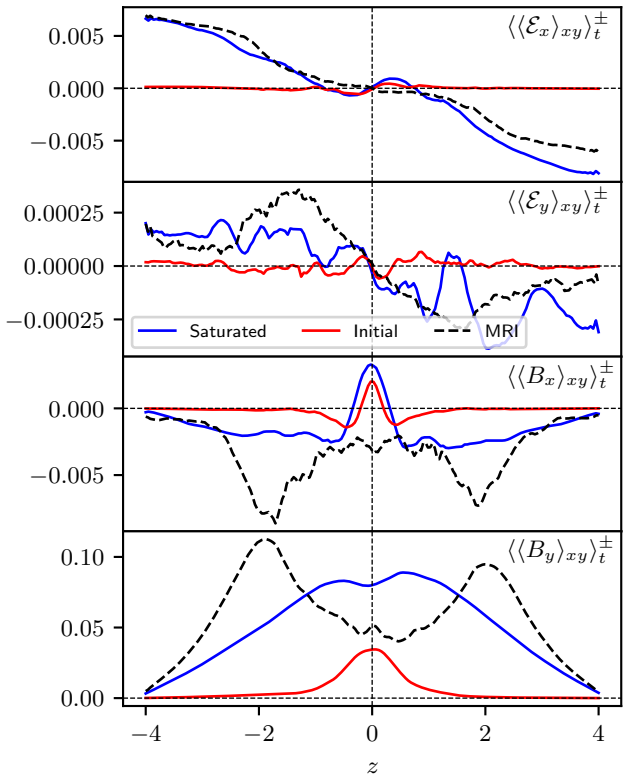

Fig. 8. Horizontally averaged field components and EMFs as a function of z. Solid curves correspond to sg-mhd-tau20, and dashed curves correspond to MRI-compare. The first two images depict $\mathcal{E}_x$, and $\mathcal{E}_y$, respectively. Images three and four show the magnetic field components B_x and B_y, respectively. The red curves were averaged over the $200{-}400\Omega_0^{-1}$ interval of sg-mhd-tau20, and the blue profiles over the $800{-}1300\Omega_0^{-1}$ interval. The time samples were evaluated every $2\Omega_0^{-1}$. The dashed curves correspond to MRI-compare and were averaged over the $100{-}1000\Omega_0^{-1}$ interval, with time samples every $1\Omega_0^{-1}$. All components change signs, and some even oscillate over time. Hence, a special time-averaging technique, $\langle f\rangle_{\rm t}^{\pm}$, was applied to all shown profiles, $f(z)$. Thereby, each quantity is multiplied by the momentary sign of $\langle B_y\rangle_{xy}(z,t)$ before the time average is applied.

the images show $\langle\langle\mathcal{E}_x\rangle_{xy}\rangle_{\rm t}^{\pm}$, $\langle\langle\mathcal{E}_y\rangle_{xy}\rangle_{\rm t}^{\pm}$, $\langle\langle B_x\rangle_{xy}\rangle_{\rm t}^{\pm}$, and $\langle\langle B_y\rangle_{xy}\rangle_{\rm t}^{\pm}$, respectively. The red line is a time average over the initial, weak-field phase ($200 \leq t\Omega_0 \leq 400$), and the blue line is an average over the saturated phase ($800 \leq t\Omega_0 \leq 1300$); the seed field is introduced at $200\Omega_0^{-1}$. For comparison, the same method is applied to the pure-MRI simulation, MRI-compare, and the resulting profiles are shown as the black, dashed curves. For MRI-compare, the time-average is over the $100 \leq t\Omega_0 \leq 1000$ interval.

Considering the field components first, two features become immediately apparent, both components are mirror-symmetric with respect to $z = 0$, and in the initial phase the two field components are more localised near the mid-plane than in the saturated phase. In the initial phase, the toroidal component, B_y, is a decreasing function with $|z|$. In the saturated phase, B_y develops a dip at the mid-plane, which is not present in the initial profile. The radial component, B_x, changes sign, close to the mid-plane ($|z| < 1\,\mathrm{H}$), in the initial phase, which is also the case in the saturated phase. The two field components have in common that, in the saturated phase, significant field contributions arise at higher elevations, $|z| > 1\,\mathrm{H}$. The MRI does also lead to field contributions at higher altitudes, though there are qualitative differences to the saturated state of sg-mhd-tau20. Most notably, in MRI-compare, both field components have a distinct peak at $|z| \sim 2$, which is not the case for the sg-mhd-tau20 profiles, showing a more monotonous z dependence. Regarding the EMFs, the latter are, as expected, anti-symmetric with respect to the mid-plane. At saturation, a significant $\mathcal{E}_x$ contribution arises for higher altitudes. And one can see that, for $|z| \gtrsim 1\,\mathrm{H}$, $\mathcal{E}_x$ is in agreement with the pure-MRI case. However, at the mid-plane, $|z| \lesssim 1\,\mathrm{H}$, $\mathcal{E}_x$ is almost equivalent to the initial case. We note that $\partial_z\langle\mathcal{E}_x\rangle_{xy}$ corresponds to the rate of change, of $\langle B_y\rangle_{xy}$. Hence, from the image, one can tell that the vertical derivative must change sign, from higher altitudes to the mid-plane region. This is in agreement with the dip (at the mid-plane), observed for B_y. However, we note that, due to the averaging technique, an exact sign comparison of the EMFs and fields may be misleading. For $\mathcal{E}_y$, a similar behaviour is observed. The initial phase only develops contributions near the mid-plane. In the saturated phase, the observed $\mathcal{E}_y$ profile approaches that seen in the pure-MRI case, though superimposed with significant noise. Taken together, one can conclude that the saturated phase, of sg-mhd-tau20, is not inconsistent with a coexistence between GI and MRI. This is best represented by the $\mathcal{E}_x$ component, which definitively shows characteristics of the initial (GI) phase near the mid-plane and characteristics of the pure-MRI case for higher altitudes. The field components in the saturated phase of sg-mhd-tau20 lack the field-strength peaks seen for the pure-MRI case, though. Yet, one can still observe that the saturated state of sg-mhd-tau20 gives rise to additional field contributions, at higher altitudes, which are less pronounced in the initial phase.

The same method is then applied to the strong-GI case, sg-mhd-tau10. Fig. 9 shows both the initial weak-field phase, $200\Omega_0^{-1}$ after field seeding (red), and the saturated phase, $1000 \leq t\Omega_0 \leq 1500$ (blue). There are similarities to the sg-mhd-tau20 case, though there are also significant differences. Considering the field components first, one can see that the initial profiles are qualitatively similar to those seen in sg-mhd-tau20. The field profiles at saturation are much closer to the initial profile, than is the case in the weaker-GI simulation, sg-mhd-tau20. One can still see that saturation gives rise to additional field contributions, at $|z| \sim 1{-}2$, though they are less pronounced and certainly far from the field-strength peaks observed in the pure-MRI case. For the EMFs, one finds that, near the mid-plane, the $\mathcal{E}_x$ profile almost does not change, from the initial to saturated phase. For higher $|z|$, saturation gives rise to larger $\mathcal{E}_x$ values, though they do not reach the pure-MRI level. The toroidal component ($\mathcal{E}_y$) is different from the pure-MRI case and significantly dominated by noise.

Hence, the EMF analysis also suggests that there are two, qualitatively different ideal-MHD dynamo states: a (1) weak-GI state that is consistent with additional MRI contributions (GI-MRI coexistence) and (2) a strong-GI dynamo with significant mid-plane contributions and possibly no MRI. In the strong-GI case, the initial, weak-field phase is also similar to the dynamo-saturated state.

5.4. Exchange between magnetic and kinetic energy

In the local shearing box approximation, the magnetic energy balance can be written as follows (see also Brandenburg et al. 1995):

$$\partial_{\rm t}E_{\rm mag} = \frac{3\Omega_0}{2}\left\langle -\frac{1}{\mu_0}B_xB_y\right\rangle + \langle(\boldsymbol{v}\times\boldsymbol{B})\cdot\boldsymbol{J}\rangle + F_z - \langle\eta|\boldsymbol{J}|^2\rangle. \quad (19)$$

The term $\partial_{\rm t}E_{\rm mag}$, on the left hand side, represents the net rate of change, of the volume-averaged magnetic energy density.

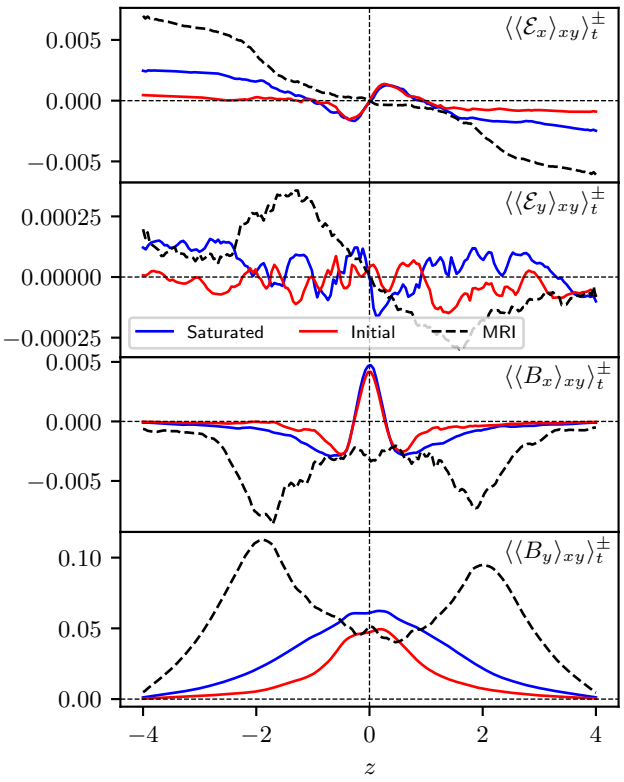

Fig. 9. Horizontally averaged field components and EMFs as a function of z, equivalent to Fig. 8 except now evaluated for simulation sg-mhd-tau10. Red curves are averages over the $400{-}600\Omega_0^{-1}$ interval, and the blue profiles are averages over the $1000{-}1500\Omega_0^{-1}$ interval. The dashed black curves correspond to MRI-compare ($100{-}1000\Omega_0^{-1}$). For the time average, $\langle f\rangle_t^{\pm}$ is used (see Fig. 8 or the main text for more details).

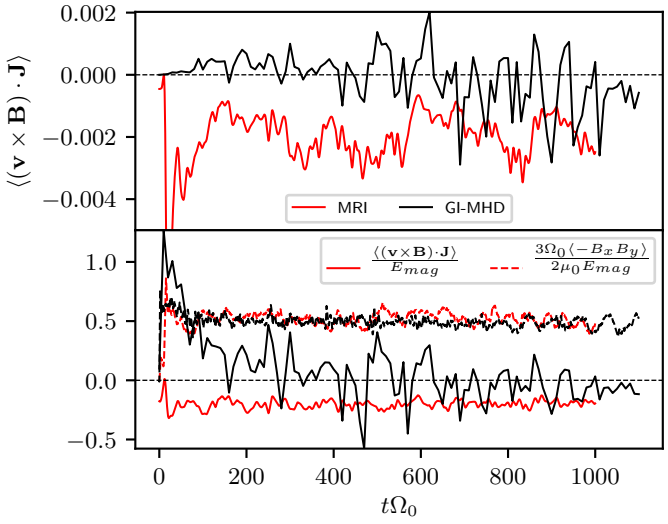

Fig. 10. Magnetic energy fluxes as a function of time evaluated for both sg-mhd-tau20 (black curves) and MRI-compare (red curves). Shown in the first image is the conversion rate from magnetic to kinetic energy, $\langle(\boldsymbol{v}\times\boldsymbol{B})\cdot\boldsymbol{J}\rangle$. This rate was calculated using the central differences from the full three-dimensional output data every $10\Omega_0^{-1}$. Shown in the second image are the terms $\langle(\boldsymbol{v}\times\boldsymbol{B})\cdot\boldsymbol{J}\rangle$ (solid curves) and $(3\Omega_0/2)\langle -B_xB_y/\mu_0\rangle$ (dashed curves), normalised by the momentary magnetic energy density, $E_{\rm mag}$.

The terms on the right hand side represent the causes for that change. The first term, $(3\Omega_0/2)\langle -B_xB_y/\mu_0\rangle$, is written as a volume average, though it really originates from a boundary integral, that is, from the divergence of the Poynting flux. Hence, this term represents the rate, at which energy enters (leaves) the box through the horizontal boundaries. This is similar to the kinetic energy balance, which has a contribution $(3\Omega_0/2)\langle\rho v_x\delta v_y\rangle$. In the global picture, this corresponds to the energy, locally released by the accretion process. The second term, $\langle(\boldsymbol{v}\times\boldsymbol{B})\cdot\boldsymbol{J}\rangle$, is the volume-averaged exchange rate, between the magnetic and kinetic energy budgets. We note that $\boldsymbol{v}$ is the actual velocity, containing both the shear flow and all perturbations. The third term, F_z, accounts for all losses of magnetic energy, over the vertical boundaries. The last term measures the rate at which magnetic energy is lost, due to resistive dissipation. The analytical form of $\langle\eta|\boldsymbol{J}|^2\rangle$ represents Ohmic dissipation, though even in ideal-MHD cases, dissipation can still occur at the grid scale, and, in conservative codes, this energy enters the thermal budget implicitly. We then analysed the terms $\langle(\boldsymbol{v}\times\boldsymbol{B})\cdot\boldsymbol{J}\rangle$ and $(3\Omega_0/2)\langle -B_xB_y/\mu_0\rangle$ for MRI-compare and sg-mhd-tau20 as a function of time. The result is shown in Fig. 10.

Shown in the first image are the volume-averaged kinetic-magnetic exchange rates, $\langle(\boldsymbol{v}\times\boldsymbol{B})\cdot\boldsymbol{J}\rangle$. A special feature of MRI is that the latter yields values smaller zero. This has already been observed in early simulations of MRI (see Brandenburg et al. 1995). At first, this may seem counter-intuitive as one would expect a dynamo to turn kinetic energy into magnetic energy, and not vice versa. For the cases here, this is not a contradiction, and the energy input is actually related to $(3\Omega_0/2)\langle -B_xB_y/\mu_0\rangle$ (see below). First, one can analyse the same exchange rate for sg-mhd-tau20, shown as the solid black line in the first image. During the initial phase, the exchange rate appears to be positive, on average. However, at later times, starting at $t\Omega_0 \sim 750$, the exchange rate turns negative, similar to the pure-MRI case. This raises the questions as to where the magnetic energy is coming from in the first place and how the negative exchange rate should be interpreted since GI seems to provide a dynamo. Here, the dominant input of magnetic energy originates from the contribution of the Maxwell stress, $3\Omega_0\langle -B_xB_y\rangle/(2\mu_0)$. To put this into perspective, both $3\Omega_0\langle -B_xB_y\rangle/(2\mu_0)$ and $\langle(\boldsymbol{v}\times\boldsymbol{B})\cdot\boldsymbol{J}\rangle$ are shown in the second image. All values were normalised by the momentary value of $E_{\rm mag}$, as this allows a direct comparison of the initial and saturated phases. We note that, normalised by $E_{\rm mag}$, the stress contribution is essentially $(3\Omega_0/2)\,r_{\rm sp}$. Hence, this demonstrates explicitly that $r_{\rm sp}$ yields exactly equal values in the GI-MHD state and in the MRI state. It becomes clear that, in the saturated phase of sg-mhd-tau20 and in the pure-MRI case, the term $3\Omega_0\langle -B_xB_y\rangle/(2\mu_0)$ represents the dominant energy input. Hence, the energy input actually originates from the stresses. However, during the initial phase of sg-mhd-tau20, one finds $\langle(\boldsymbol{v}\times\boldsymbol{B})\cdot\boldsymbol{J}\rangle > 0$, which is in agreement with the proposed GI dynamo. After $\sim 250\Omega_0^{-1}$, the values $\langle(\boldsymbol{v}\times\boldsymbol{B})\cdot\boldsymbol{J}\rangle$ gradually approach zero, on average. This is not entirely unexpected, as the GI dynamo must eventually saturate. However, the question remains as to why this exchange rate eventually turns negative, after $t\Omega_0 \sim 750$. In the case of MRI, this may be understood as a consequence of the instability mechanism itself. In the ideal-MHD limit, the presence of a sub-thermal magnetic field is sufficient to induce MRI (see e.g. Balbus & Hawley 1998). Without that field, no instability occurs. In the context of a dynamo, MRI is special, as Lorentz forces are important from the very start. Put differently, MRI must not only sustain its own field, it must also sustain its own turbulence via Lorentz forces (see Balbus & Hawley 1998). Hence, it is not unreasonable to find

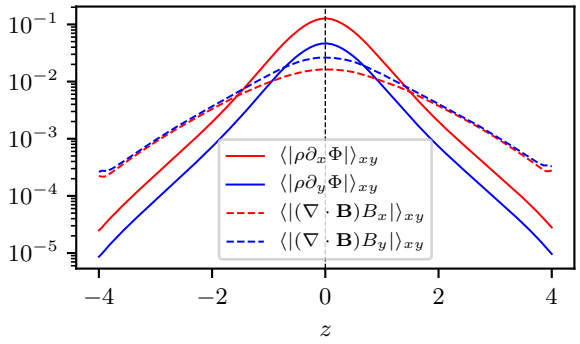

Fig. 11. Absolute values of the field line bending forces, $\langle\langle|(\boldsymbol{B}\cdot\nabla)B_{x,y}|\rangle_{xy}\rangle_t$ (solid curves), and the self-gravity forces, $\langle\langle|\rho\partial_{x,y}\Phi|\rangle_{xy}\rangle_t$ (dashed curves), in directions x (red) and y (blue), evaluated for simulation sg-mhd-tau20. The time average is over the interval $800 \leq t\Omega_0 \leq 1300$. The force densities were calculated using finite differences from the full three-dimensional output data of Athena every $10\Omega_0^{-1}$. We note that $\mu_0 = 1$ in code units.

$\langle(\boldsymbol{v}\times\boldsymbol{B})\cdot\boldsymbol{J}\rangle < 0$, as, in the case of MRI, Lorentz forces are the primary cause why fluid elements move in the first place. This suggests that some type of mechanism capable of generating kinetic energy from magnetic energy must also be present in sg-mhd-tau20. Magneto-rotational instability would provide such a mechanism, and this falls in line with the butterfly diagram, as well as the vertical EMF profiles.

5.5. Interpretation and summary

Considering all previous simulations, one can conclude that there appear to be two different dynamo states, associated with GI, in an ideal-MHD regime. A weak-GI case, which shares similarities with the MRI dynamo and a strong, possibly pure, GI state. All regimes have in common that the gravitational stress contribution, α_g, decreases significantly, as the Maxwell stress, α_m, increases. Simulation sg-mhd-tau20 offers a good reference point for a closer inspection. In sg-mhd-tau20, α_g decreases by more than a factor of two, from the GI-only phase ($160-260\Omega_0^{-1}$), to the dynamo-saturated phase ($800-1300\Omega_0^{-1}$) (see also Table 2). GI-only here means that $\boldsymbol{B} = 0$ or at least negligible (the seed field is introduced at $t\Omega_0 = 200$). The volume-averaged Toomre parameter, $\langle Q\rangle$, increases slightly, by ∼10%. In sg-mhd-tau20, the total mass and the cooling time are held constant and no additional heating (second term in Eq. (5)) is used. Hence, one can ask how GI activity is actually reduced. Clearly, some back-reaction, via Lorentz forces, must occur. For example, one might take into account the stabilising effect of magnetic pressure forces. Considering the magnetic pressure in the definition of the Toomre parameter (see e.g. the approach in Riols & Latter 2019), one finds $Q_{\rm eff} \sim Q\sqrt{1+1/\langle\beta\rangle}$, which, for $\langle\beta\rangle = 12$ (see Table 1), yields an increase of $\sqrt{1+1/\langle\beta\rangle} - 1 \sim 4\%$. The increase by thermal means alone, is already at ∼10%, and hence, if pressure forces are responsible for the GI reduction, then thermal pressure forces are the dominant contribution. A back-reaction can also occur via field-line bending forces $\propto(\boldsymbol{B}\cdot\nabla)\boldsymbol{B}$.

The xy components, of these bending forces, are compared to the xy components of the self-gravity forces, for sg-mhd-tau20, in Fig. 11, where the absolute values of the force densities were averaged horizontally and over time ($800-1300\,\Omega_0^{-1}$). At the mid-plane, self-gravity forces in the x direction are stronger by a factor of ∼7.8, and in the y direction by a factor of ∼1.8. Hence, the radial motions should be largely unaffected. One could argue that motions in the y direction are affected, by field-line bending forces. However, one has to keep in mind that GI saturation is induced by thermal self regulation. Heat, generated by GI itself, brings the system to the instability threshold $\langle Q\rangle \sim Q_c$. If a non-thermal force, such as field-line bending, was to contribute to GI saturation, then GI does not saturate by thermal means alone. In fact, as GI is weakened, producing less heat, one would actually expect a lower $\langle Q\rangle$ value. The question thus remains as to how GI activity is reduced. In light of the previous findings, we suggest that the mechanism of GI weakening is related to a coexistence with MRI, at least in sg-mhd-tau20. How this can be achieved is discussed at the beginning of Sect. 5. The mechanism of MRI leads to an additional energy input. The latter cannot completely be captured by wind losses, and some parts must contribute to heating. However, in the presence of GI, the thermal energy level cannot rise indefinitely, as GI-turbulent states self-regulate to marginal stability, $\langle Q\rangle \sim Q_c$, with $Q_c \gtrsim 1$ (see e.g. Gammie 2001). Significantly larger $\langle Q\rangle$ values result in a GI-stable configuration. Hence, the additional energy production rate, due to MRI, enforces a reduced energy production rate, due to GI, in order to sustain $\langle Q\rangle \sim Q_c$. This is not to say that $\langle Q\rangle$ cannot increase, it only means that $\langle Q\rangle$ cannot increase by much (e.g. 10% for sg-mhd-tau20). Moreover, from Fig. 11, one can deduce that field line bending forces dominate over self-gravity forces, above $|z| \sim 2\,H$. This is also where the highest field strengths were observed, in the pure-MRI case. The mechanism of MRI is indeed based on the bending of field lines and, in combination with differential rotation, is capable of drawing free energy from the background flow. Put differently, it is not so much a direct back-reaction of Lorentz-forces that causes a reduction of GI activity, but rather the fact that a positive correlation $\langle -B_xB_y\rangle$ is established. The latter leads to a net input of magnetic energy, which, at least in parts, must contribute to heating. This, in combination with the $\langle Q\rangle \sim Q_c$ requirement, necessitates a reduction of GI activity (see also Sect. 5).

We note that each diagnostic, on its own, cannot definitively proof the presence of MRI, in the dynamo-saturated state. However, one has to consider the net of all diagnostics, and the latter suggest a form of GI-MRI coexistence, in the weak-GI case, sg-mhd-tau20. And the presence of MRI can explain the observed reduction of GI activity. We note that the exact mechanisms leading to saturation in the strong-GI simulation, sg-mhd-tau10, are less clear, and MRI is possibly absent. However, also in sg-mhd-tau10, an additional α_m contribution arises, and the energy balance has to account for that, MRI or not. Finally, one also has to distinguish between a turbulence and a dynamo mechanism. Magneto-rotational instability alone has to sustain both, as the turbulence mechanism requires a field to operate on. One might even speculate whether GI is beneficial for MRI, as GI can sustain a background field for the MRI to operate on. But we acknowledge that the definitive mechanism for how the ideal GI dynamo saturates is still elusive.

6. Including resistivity, a new nonlinear state

As discussed in the previous sections, additional, turbulent energy production (e.g. due to MRI) can cause GI to weaken, given that the cooling physics does not change. Thereby, the excess-energy input can effectively act as an additional heating source. The additional heat may arise from the dissipation of kinetic energy (e.g. generated by MRI), or by dissipation of magnetic energy at the grid scale, which is implicitly turned into thermal energy via energy conservation. Considering the last point,

Table 4. Scan over different values of η.

Shared-parameters	L_x, L_y, L_z 20, 20, 8 H	N_x, N_y, N_z 440, 440, 170	$\tau_c\Omega_0$ 10	γ 1.64	Q_0 0.75	$\langle\rho\rangle$ 0.0536	ρ_{min} 10^{-4}	P_{min} 6.1×10^{-5}	CFL 0.3	
Specific values	$t_{start} - t_{end}$, in Ω_0^{-1}	η	$\langle\langle Rm\rangle\rangle_t$	$\langle\langle c_s\rangle\rangle_t$	$\langle\langle Q\rangle\rangle_t$	$\langle\langle\beta\rangle\rangle_t$	$\langle\alpha_r\rangle_t$	$\langle\alpha_m\rangle_t$	$\langle\alpha_g\rangle_t$	$\langle r_{sp}\rangle_t$
sg-eta01	1300 – 2400	0.01	~282	1.677	1.252	4.256	0.0090	0.0195	0.0053	0.1725
sg-eta005	1000 – 1600	0.005	~477	1.543	1.152	16.49	0.0079	0.0089	0.0093	0.2372
sg-eta0033	1000 – 1600	0.0033	~675	1.492	1.111	30.96	0.0077	0.0044	0.0115	0.2758
sg-eta0025	1000 – 1600	0.0025	~907	1.506	1.124	26.90	0.0078	0.0049	0.0116	0.2883
sg-eta002	1000 – 1600	0.002	~1129	1.502	1.121	25.63	0.0076	0.0056	0.0109	0.2940
sg-eta00167	1000 – 1600	0.00167	~1346	1.499	1.118	28.32	0.0076	0.0048	0.0114	0.3003
sg-eta0006	1000 – 1400	0.0006	~4032	1.553	1.160	14.00	0.0077	0.0115	0.0086	0.3077

Notes. General settings that are constant with time, and shared by all simulations, are provided in the upper table block. A selection of time-averaged quantities is provided in the lower table block, with the corresponding time intervals ($t_{start} - t_{end}$).

it is worth to introduce explicit Ohmic dissipation, in order to test the influence of magnetic heating on GI, by resolving the magnetic dissipation at small scales. The first resistive simulation presented here is sg-eta01. The latter is restarted from the ideal-MHD simulation sg-mhd-2, at $t\Omega_0 = 1000$, but with a finite resistivity value, being introduced at the moment of restart. Simulation sg-mhd-2 is discussed in Sect. 5.1 and in more detail in Löhnert & Peeters (2022). As can be seen in Fig. 3, sg-mhd-2 develops a clearly visible butterfly diagram. The value of Ohmic resistivity, in sg-eta01, is $\eta = 0.01$. Using the background value of the sound speed, $c_{s,0} = 1.0$, then this corresponds to a magnetic Reynolds number of Rm = 100 (see Eq. (13)). However, using the volume- and time-averaged sound speed, $\langle\langle c_s\rangle\rangle_t$, one finds a larger value of $\langle\langle Rm\rangle\rangle_t \sim 281$. A detailed list of the simulation parameters to sg-eta01 is provided in the first line of Table 4. The total mass content in the box volume is held constant via the replenishing method, detailed in Sect. 4.1. As sg-eta01 was restarted from sg-mhd-2, it also includes background heating (second term in Eq. (5)). Without turbulence, the balance of heating and cooling would cause a state with a constant normalised sound speed of $c_{s,0} = 1$, which corresponds to a Toomre parameter of $Q_0 \sim 0.75$, given the constant box mass. In the following, we show that this value of resistivity leads to a new turbulent state that differs from the ideal-MHD states shown so far, particularly the GI-MRI coexistence states. Hence, a new saturation mechanism is established, which, considering the uncertain case sg-mhd-tau10, possibly provides a third dynamo state.

6.1. Observed time evolution

Shown in the first image of Fig. 12 is the time evolution of the dimensionless turbulent stresses α_r (Reynolds), α_m (Maxwell), and α_g (gravitational). The time before $t\Omega_0 = 1000$ corresponds to simulation sg-mhd-2 (see Sect. 5.1 and Löhnert & Peeters 2022), and the time afterwards is sg-eta01, with resistivity being enabled at the transition. The values of both α_g and α_r were smoothed, by convolving the respective time series with a Gaussian function with standard deviation $\sigma = 3\Omega_0^{-1}$. Directly after enabling resistivity, the Maxwell stress α_m drops significantly, whereas the gravitational and Reynolds stresses remain mostly unchanged. However, α_m immediately enters a growth phase, growing even larger than the initial, non-resistive value at $t\Omega_0 \sim 1200$. At that point, the gravitational stress α_g is dropping significantly. Eventually, α_m and α_g reach a maximum and a minimum, respectively. The gravitational stress then recovers to the previous value. At $t\Omega_0 = 1500$ the stresses are similar to the state at $t\Omega_0 = 1200$ and the process repeats. Hence, the system settles into a new nonlinear state, with effective oscillations occurring in both α_g and α_m. During the oscillations, it is apparent that the Reynolds stress remains relatively constant, with only small spikes occurring during maxima in α_g.

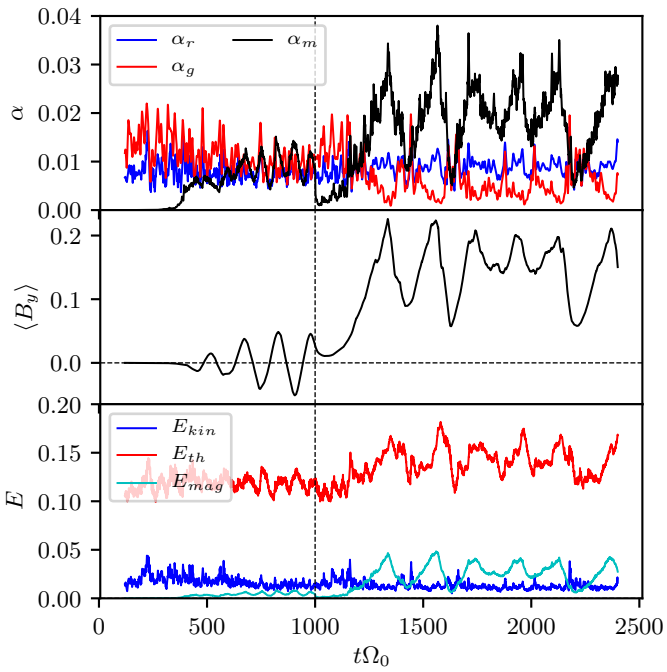

Fig. 12. Time evolutions for a selection of volume-averaged quantities evaluated for sg-eta01. First image: Turbulent stresses α_r (Reynolds), α_m (Maxwell), and α_g (gravitational) as a function of time. The values for both α_g and α_r were smoothed by convolving the respective time series with a Gaussian function and with a standard deviation of $\sigma = 3\Omega_0^{-1}$. Second image: Volume-averaged toroidal magnetic field component, $\langle B_y\rangle$. Third image: Volume-averaged energy densities E_{kin} (blue), E_{th} (red), and E_{mag} (cyan). In all images, the vertical dashed line marks the time point when resistivity is enabled.

The second image in Fig. 12 depicts the volume-averaged toroidal magnetic field component $\langle B_y\rangle$ as a function of time. For $t\Omega_0 < 1000$ (ideal-MHD phase, sg-mhd-2), one can clearly observe the field oscillations indicating the butterfly diagram, detailed in Löhnert & Peeters (2022). After resistivity is enabled at $1000\Omega_0^{-1}$, the oscillation is disrupted, and for $t\Omega_0 \gtrsim 1300$ a new oscillating state develops, but with the oscillations now centred around a finite, positive $\langle B_y\rangle$. It is also easily seen that the averaged field strength is significantly larger in the newly developed nonlinear state. In Löhnert & Peeters (2022), we remarked that the periodically occurring field reversals are a distinguish-

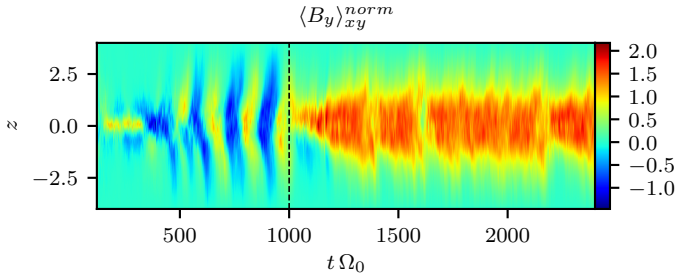

Fig. 13. Vertical profile of the normalised, horizontally averaged magnetic field component, $\langle B_y \rangle_{xy}^{\rm norm} = \langle B_y \rangle_{xy} / \sqrt{\langle B_y^2 \rangle}$, evaluated for sg-eta01. The vertical dashed line marks the time point ($t\Omega_0 = 1000$) when resistivity is added.

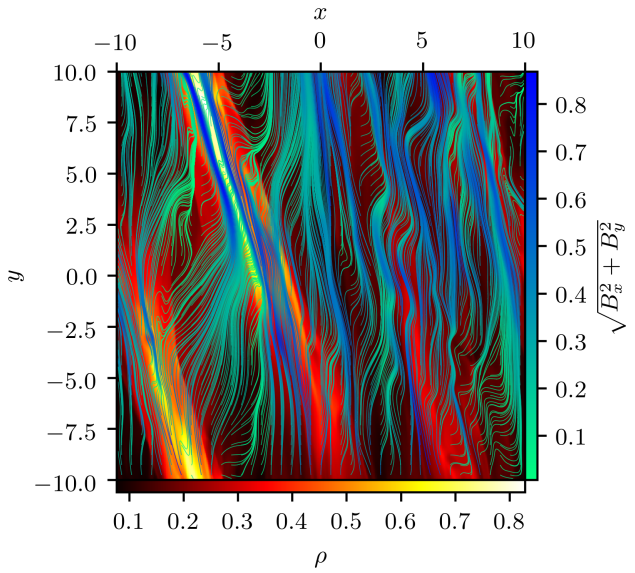

Fig. 14. Mass density at $z = 0$ and $t\Omega_0 = 2000$ for simulation sg-eta01. The image is overlayed with magnetic field lines traced in the (x, y) plane and only using the field components (B_x, B_y).

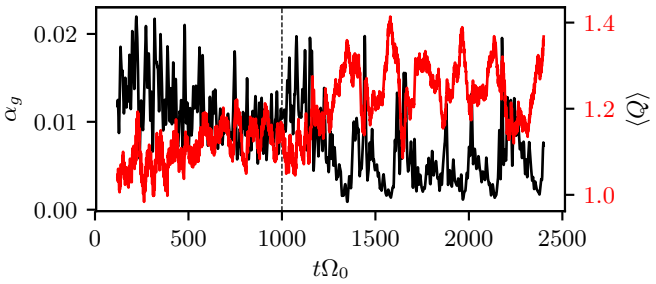

Fig. 15. Time evolution of the volume-averaged Toomre parameter, $\langle Q \rangle$ (red curve), and the dimensionless gravitational stress, α_g (black curve), evaluated for sg-eta01. The vertical dashed line at $t\Omega_0 = 1000$ marks the time point at which resistivity is introduced. The α_g values were smoothed using a Gaussian function with standard deviation $\sigma = 3\Omega_0^{-1}$.

ing feature from the findings in Riols & Latter (2018a), where field oscillations occur less regularly. In the resistive cases in Riols & Latter (2019), field reversals are even absent completely. Hence, these findings might be more reminiscent of the case sg-eta01 studied here. The oscillatory behaviour can also be observed in the volume-averaged energy densities (see the third image of Fig. 12). At each time point, the energy densities are obtained using Eqs. (11a)–(11c). At $t\Omega_0 \sim 1200$, the magnetic energy density is equal in magnitude to the kinetic energy density and is continuing to grow. Similar to $\alpha_{\rm m}$, also $E_{\rm mag}$ eventually reaches a maximum value and oscillates from then on. The oscillations are also observed for the thermal energy density $E_{\rm th}$. The kinetic energy density $E_{\rm kin}$ remains almost constant from $1200\Omega_0^{-1}$ onwards, with only short fluctuations occurring. The latter fluctuations (short spikes in $E_{\rm kin}$) seem to solely appear during minima in the magnetic energy $E_{\rm mag}$.

Shown in Fig. 13 is a (z, t) diagram of the horizontally averaged, toroidal magnetic field component, normalised by the root-mean-squared (rms) value, $\langle B_y \rangle_{xy}^{\rm norm} = \langle B_y \rangle_{xy} / \sqrt{\langle B_y^2 \rangle}$. Most notably, the butterfly pattern, occurring during the ideal phase, is disrupted, after resistivity is enabled. A field modulation still occurs (see also the second image of Fig. 12), but the clearly visible field reversals are absent. Finally, in Fig. 14, the mid-plane mass density, evaluated at $t\Omega_0 = 2000$, is superimposed with magnetic field lines, traced in the (x, y) plane. Similar to Fig. 6, the field lines are mostly aligned with the GI density waves, but, in contrast to the ideal-MHD cases, the field lines develop fewer small-scale structures. In Fig. 6, one can see that, especially in the regions between density waves, the field lines change direction rather frequently. This is not the case in Fig. 14, and the field lines bridge the gap between density waves more straightly.

Considering the previous findings, it becomes clear that the new nonlinear state, after enabling resistivity, is qualitatively different from the ideal-MHD state. The aim of the following section is to elucidate the physical mechanisms of this new, nonlinear state.

6.2. Saturation mechanism

It is clear from the first image of Fig. 12 that oscillation maxima in the Maxwell stress, $\alpha_{\rm m}$, correspond to minima in the gravitational stress, $\alpha_{\rm g}$, and vice versa. During minima, the gravitational stress is reduced to almost zero. As can be seen in Fig. 15, the oscillations also occur for the volume-averaged Toomre parameter (red curve), and maxima of $\langle Q \rangle$ correspond to minima in $\alpha_{\rm g}$.

These oscillations, in the Toomre values $\langle Q \rangle$, are close to those observed in the resistive simulations of Riols & Latter (2019) and the ambipolar diffusion simulations in Riols et al. (2021). There, it is suggested that changes in both the magnetic and the thermal pressure might cause changes in Q. The magnetic pressure increases as the GI dynamo generates magnetic energy, and the thermal energy increases due to resistive dissipation of magnetic energy. The increased Toomre parameter is then related to a weaker GI, corresponding to lower $\alpha_{\rm g}$ values. One usually expects the stress α to be determined by the cooling time alone (see Gammie 2001). However, as pointed out earlier, additional heating can also reduce the strength of GI, even for a given cooling time (see e.g. Rice et al. 2011). This may lead to a slightly larger Toomre value, $\langle Q \rangle$, though this increase is usually small, as a GI-turbulent state saturates at marginal stability $\langle Q \rangle \sim Q_{\rm c}$, with $Q_{\rm c} \gtrsim 1$. Significantly larger values indicate stability against GI and are not compatible with a GI-turbulent state. As can be seen in Fig. 15, the increase in $\langle Q \rangle$ is rather significant, up to values of $\langle Q \rangle \sim 1.4$. An those maxima correspond to drops in $\alpha_{\rm g}$, to almost zero. As the mass density is held constant, one can infer that some form of heating arises that is significant enough to render the system almost gravitationally stable.

The question then arises as to how the excess thermal energy, which increases the Toomre parameter, is produced. Here, ther-

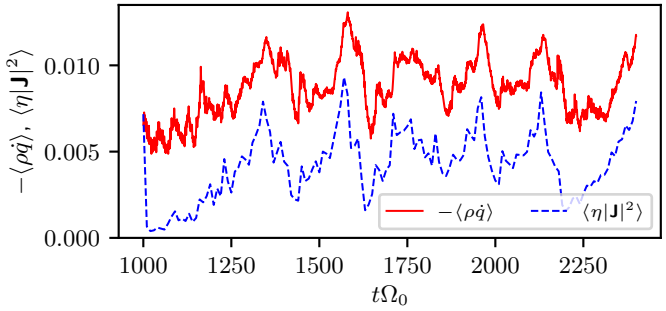

Fig. 16. Negative cooling (heating) rate ($-\rho\dot{q}$, solid red curve) and the resistive dissipation rate ($\langle\eta|\boldsymbol{J}|^2\rangle$, dashed blue curve) evaluated for sg-eta01 as a function of time. Resistivity was enabled at $t\Omega_0 = 1000$. The values of $\langle\eta|\boldsymbol{J}|^2\rangle$ were calculated from the full three-dimensional output data using central differences for derivatives every $10\Omega_0^{-1}$.

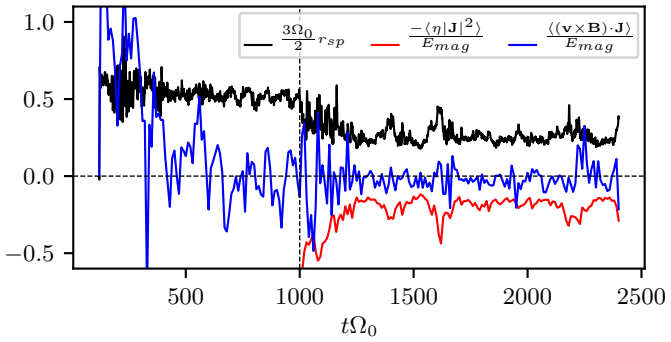

Fig. 17. Contributions to the magnetic energy balance evaluated for sg-eta01 as a function of time. All values are normalised by the momentary magnetic energy density, $E_{\rm mag}$. Shown in blue is the volume-averaged rate at which magnetic energy is converted to kinetic energy, $\langle\boldsymbol{v}\times\boldsymbol{B}\cdot\boldsymbol{J}\rangle$. The values were calculated from the full three-dimensional output data using central differences every $10\Omega_0^{-1}$. The contribution arising from the Maxwell stress is shown as the black curve. Shown in red is the volumetric Ohmic dissipation rate, $\langle-\eta|\boldsymbol{J}|^2\rangle$, also evaluated every $10\Omega_0^{-1}$ (see also Fig. 16). The time before $t\Omega_0 = 1000$ corresponds to the ideal simulation, sg-mhd-2 (see also Löhnert & Peeters 2022). The resistive phase of sg-eta01 starts at $t\Omega_0 = 1000$.

mal energy can change due to radiative cooling (heating), conversion of kinetic energy via compression (expansion), conversion of magnetic energy due to Ohmic resistivity, and fluxes across the vertical boundaries. From the first image in Fig. 12, one can immediately conclude that the thermal energy density $E_{\rm th}$ is correlated with the oscillations in the magnetic energy density $E_{\rm mag}$, whereas the kinetic contribution remains almost unchanged. This suggests that the resistive dissipation of magnetic energy is causing the oscillations in the thermal energy density and subsequently the oscillations in $\langle Q\rangle$. To test this, one can analyse the energy balance in the resistive state, in more detail. For this, the volume-averaged, resistive dissipation rate, $\langle\eta|\boldsymbol{J}|^2\rangle$, is calculated explicitly, as a function of time. One would then expect to find oscillations in $\langle\eta|\boldsymbol{J}|^2\rangle$ as well. This is indeed the case, as can be seen in Fig. 16, which shows the net cooling rate, according to Eq. (5), with $c_{\rm s,0} = 1$. The latter depends directly on $E_{\rm th}$ and, therefore, also develops oscillations. One notices that the oscillations of the resistive dissipation rate, $\langle\eta|\boldsymbol{J}|^2\rangle$, and the oscillations of the cooling (heating) rate are of the same order of magnitude, which indicates that resistive dissipation is indeed responsible for the periodically occurring heating events. The curves do not fit exactly though, and the cooling (heating) rate $|\rho\dot{q}|$ is always larger than $\langle\eta|\boldsymbol{J}|^2\rangle$. The difference originates from the remaining thermal energy production via dissipation of turbulent kinetic energy. However, the oscillations occurring in both $\langle\eta|\boldsymbol{J}|^2\rangle$ and $|\rho\dot{q}|$ are in good agreement. Observing Fig. 16 closely, one also notices that $\langle\eta|\boldsymbol{J}|^2\rangle$ and $|\rho\dot{q}|$ are slightly out of phase, with $\langle\eta|\boldsymbol{J}|^2\rangle$ slightly leading. That is reasonable since $\langle\eta|\boldsymbol{J}|^2\rangle$ really needs to increase first, before the thermal energy, and with it the cooling rate can rise.

Additionally, one can analyse the magnetic energy balance, according to Eq. (19), for sg-eta01. Shown in Fig. 17 is the time evolution of the terms $(3\Omega_0/2)\langle-B_xB_y/\mu_0\rangle$, $\langle\boldsymbol{v}\times\boldsymbol{B}\cdot\boldsymbol{J}\rangle$, and $\langle-\eta|\boldsymbol{J}|^2\rangle$. All values were normalised by the momentary values of $E_{\rm mag}$, that is, all rates are in units of Ω_0. The time before $t\Omega_0$ (vertical, dashed line), corresponds to the ideal case sg-mhd-2, and the resistive phase of sg-eta01 starts immediately after that time. The Ohmic dissipation, $\langle-\eta|\boldsymbol{J}|^2\rangle$, is only shown for the resistive phase. We note that, in Code units ($\Omega_0 = 1$), the Maxwell-stress contribution is essentially given by $1.5\,r_{\rm sp}$. In the ideal phase of sg-mhd-2, the time evolution of $\langle\boldsymbol{v}\times\boldsymbol{B}\cdot\boldsymbol{J}\rangle$ (blue curve) is similar to that of sg-mhd-tau20, detailed in Sect. 5.4. Directly after field seeding, the values are positive, and kinetic energy is converted into magnetic energy. In the saturated, ideal phase (GI-MRI coexistence $\sim$700−1000Ω_0^{-1}), the values are, on average, negative (see also the discussion in Sect. 5.4). During the ideal phase, most of the energy input arises from the stress contribution, $1.5\,r_{\rm sp}$. Time-averaged over the 700 − 1000Ω_0^{-1} interval, one finds $r_{\rm sp} = 0.34$ (see Table 1). As resistivity is enabled, the values of $r_{\rm sp}$ drop significantly, leaving the MRI-typical range $r_{\rm sp} \gtrsim 0.3$. Time-averaged over the 1300−2400Ω_0^{-1} interval, one finds $r_{\rm sp} = 0.17$ (see Table 4). It is again noted that all values, shown in Fig. 10 are normalised by $E_{\rm mag}$. The absolute values of $E_{\rm mag}$ and $\alpha_{\rm m}$ increase as resistivity is enabled (see Fig. 12). However, the ratio $r_{\rm sp} = \langle-B_xB_y/\mu_0\rangle/E_{\rm mag}$ decreases. From dimensional grounds one can say that $\langle-B_xB_y/\mu_0\rangle$ scales with the magnetic energy. Hence, whatever generates the additional magnetic energy, in the resistive phase, is related to a comparatively smaller Maxwell stress, as compared to the ideal phase. Similarly, the relative importance of $\langle\boldsymbol{v}\times\boldsymbol{B}\cdot\boldsymbol{J}\rangle$ drops. This is consistent with the suppression of MRI, once resistivity is enabled. Moreover, one can see that most of the energy input, arising from $1.5\,r_{\rm sp}$, is thermalised by Ohmic dissipation, $\langle-\eta|\boldsymbol{J}|^2\rangle$ (red curve). This demonstrates that most of the magnetic energy production is passed through to thermal energy, which is in agreement with the significant heating.

The previous findings point to a possible process for nonlinear saturation. The causal steps leading to one oscillation are reminiscent of those proposed in Riols & Latter (2019) and are outlined in more detail below. As resistivity is enabled, the previous saturation mechanism (possibly MRI) fails and the GI dynamo continues to produce net-magnetic flux, $\langle B_{x,y}\rangle$, as well as magnetic energy, $E_{\rm mag}$. As the magnetic energy density increases, the resistive dissipation rate also increases. The latter leads to heat production $\langle\eta|\boldsymbol{J}|^2\rangle$ and, consequently, an increasing thermal energy density, $E_{\rm th}$. The excess thermal energy, in turn, causes an increase in the saturated Toomre parameter $\langle Q\rangle$, which corresponds to a significantly reduced GI activity. The reduced (almost vanished) GI means that the dynamo is also weakened and the magnetic energy increase stagnates, reaching a maximum. In consequence, resistivity leads to the decay of remaining, excess magnetic energy. With the decreasing magnetic energy, the resistive heat production is also decreasing. Eventually, the system cools to its original state, yielding a minimum in both the thermal energy level and the magnetic energy

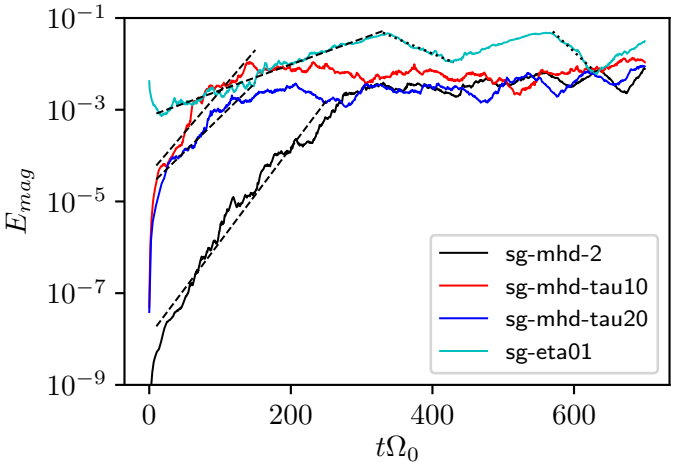

Fig. 18. Volume-averaged magnetic energy density, $E_{\rm mag}$, for the ideal-MHD simulations sg-mhd-2 (black), sg-mhd-tau10 (red), and sg-mhd-tau20 (blue) and the resistive simulation sg-eta01 (cyan). The time axis starts at $t = 0$ for all simulations. For the ideal-MHD runs, this corresponds to the moment of field seeding and for the resistive run, ($t = 0$) corresponds to the moment when resistivity was introduced. The dashed black lines correspond to linear fits, according to the values in Table 5.

level. At that point, GI can reignite turbulence. One might speculate that this reignition causes the short spikes in the kinetic energy, $E_{\rm kin}$, occurring during minima of $E_{\rm mag}$ (see the third image of Fig. 12). The revived GI also reignites the dynamo and the magnetic energy starts to increase again, starting a new cycle. Due to the nature of this cycle, we refer to this new nonlinear state in the following as 'resistive-GI dynamo'. We note that Riols et al. (2021) found similar results for MHD simulations of GI with ambipolar diffusion instead of Ohmic resistivity. There, oscillations in $\langle Q \rangle$ were also observed. Furthermore, Riols et al. (2021) also tested a nonlinear cooling law, of the form $E_{\rm th}\tau_0^{-1}(T/T_0)^3$ (τ_0 =const.), and claim that this does not lead to oscillations. Finally, the magnetic Reynolds number Rm = 100 lies in the range of values, studied in Riols & Latter (2019). Hence, one might speculate that, for GI-MRI coexistence, the Rm values need to be significantly larger than 100.

6.3. Timescales

The previous discussion suggests that one might distinguish between three different dynamo regimes: two ideal-MHD states (GI-MRI coexistence, with weak GI and a strong-GI dynamo) and the resistive-GI dynamo. The goal of this section is to obtain estimates for the dynamo growth rates. We distinguish between the ideal-MHD growth rates and the resistive growth rates. The ideal-MHD simulations, for which the field growth was evaluated, are sg-mhd-tau10, sg-mhd-tau20, and sg-mhd-2. The evaluation was also applied to simulation sg-eta01, though here, the growth rate was measured for the interval after resistivity was enabled ($1000 \lesssim t\Omega_0 \lesssim 1300$). The growth rates were calculated, by evaluating the time evolution of the volume-averaged magnetic energy density, $E_{\rm mag}$. This is shown in Fig. 18, where the ideal simulations sg-mhd-2, sg-mhd-tau10, and 20 are shown along with the resistive case, sg-eta01. The time axis starts at zero for all simulations. For the ideal cases, $t = 0$ corresponds to the seeding of the field, whereas for sg-eta01, it corresponds to the introduction of Ohmic resistivity. The plot for $E_{\rm mag}$ is logarithmic, and growth phases can be identified as phases with almost linear increase in $\log(E_{\rm mag})$. These are shown for each simulation as the dashed black lines. The corresponding time intervals are provided in Table 5. To avoid artefacts of the initial state, all intervals start $10\Omega_0^{-1}$ after seeding, or introduction of resistivity. Assuming the magnetic energy grows exponentially ($E_{\rm mag} \propto \exp(g\,t)$), the growth rates g can be determined from the linear slopes m, in Fig. 18, via $g = m/\log_{10}e$. The resulting values are provided in Table 5. In addition to the growth rates, the resistive damping rates were also evaluated for two decay phases of sg-eta01, shown in the last two rows. The corresponding linear trends are depicted as the dotted lines in Fig. 18. We note that the growth rates were determined here with respect to the magnetic energy density. Since the latter scales quadratically with the magnetic field strength, the growth rates, evaluated for the actual field strength, can be lower by a factor of two.

Table 5. Growth and damping rates for each simulation.

	Interval	Growth (damping) rate
sg-mhd-2 (ideal)	$10 - 250\,\Omega_0^{-1}$	$0.0472\,\Omega_0$
sg-mhd-tau10 (ideal)	$10 - 150\,\Omega_0^{-1}$	$0.0415\,\Omega_0$
sg-mhd-tau20 (ideal)	$10 - 150\,\Omega_0^{-1}$	$0.0346\,\Omega_0$
sg-eta01 ($\eta = 0.01$)	$10 - 350\,\Omega_0^{-1}$	$0.0130\,\Omega_0$
sg-eta01 ($\eta = 0.01$)	$330 - 430\,\Omega_0^{-1}$	$-0.0150\,\Omega_0$
sg-eta01 ($\eta = 0.01$)	$570 - 630\,\Omega_0^{-1}$	$-0.0338\,\Omega_0$

Notes. The rates, g, were calculated by applying a linear fit for the provided time intervals and reading the slopes ($g = m/\log_{10}e$, with slope m). The growth phases are depicted as the dashed lines in Fig. 18, and the decay phases (last two rows) are shown as the dotted lines.

For the ideal-MHD cases, the lowest growth rate ($g = 0.0346$) was determined for sg-mhd-tau20, which corresponds to the largest cooling time of $\tau_c\Omega_0 = 20$. However, the value for the $\tau_c\Omega_0 = 10$ case ($g \sim 0.0415$) is only slightly different, despite using a twice shorter cooling time. The largest growth rate was determined for the heated case, sg-mhd-2 (see also Löhnert & Peeters 2022). We point out, though, that the selection of time intervals used to calculate the growth rates is a matter of choice and that, especially for sg-mhd-tau10 and 20, there is some ambiguity. Also, the ideal growth rates do not deviate by much and are all roughly consistent with $g_i \sim 0.04$. Hence, whether definitive trends can be derived from this is questionable. However, one can clearly see that the ideal growth rates are larger (by roughly a factor of three to four) than the resistive growth rate ($g_{\rm r} \sim 0.013$), obtained for sg-eta01, in the initial growth phase after the introduction of resistivity. Additionally, the damping rates were calculated, by evaluating the negative slopes (see the dotted lines in Fig. 18). The corresponding values are provided in the last two lines of Table 5. The two decay phases lead to two differing values, $g_d = 0.014$ and 0.0338, with a mean value of $g_d = 0.0244$. We note that this value is roughly equal to the difference between the ideal and the resistive growth rate, $g_i - g_{\rm r} \sim 0.027$.

However, the original two damping rates deviate rather substantially, and this may well be a coincidence. However, one important feature of the resistive state is that the magnetic energy increases in the first place as resistivity is enabled. This may point to a slow dynamo process whereby resistivity is actually beneficial for the GI dynamo (see also Riols & Latter 2019).

Finally, one can also compare the growth rate obtained for the resistive state with the growth rates found in the resistive simulations of Riols & Latter (2019). The latter find, for a case with $\tau_c\Omega_0 = 20$ and Rm = 200, a growth rate of $g \sim 0.028\Omega_0$.

This can best be compared to our simulation sg-eta01, as the latter yields a volume-averaged magnetic Reynolds number of $\langle\langle \mathrm{Rm}\rangle\rangle_\mathrm{t} \sim 280$. For the latter, the obtained growth rate is ~0.013 (see Table 5). Hence, the values clearly have the same order of magnitude, though they are not equal. However, we note that there is some ambiguity, regarding the exact values of Rm, as the latter can strongly depend on the exact choice of the sound speed c_s (mid-plane, volume-averaged, initialisation value, etc.). Also, the cooling time used in sg-eta01 is only half as long ($\tau_\mathrm{c}\Omega_0 = 10$). Comparing, instead, the growth rate for the ideal run sg-mhd-tau20 ($g \sim 0.0346$), one recovers a slightly larger value, than that seen in Riols & Latter (2019). Taking into account the ambiguity arising from the calculation of g and the limited overlap of our parameter space with that used in Riols & Latter (2019), one can argue that the order of magnitude is well reproduced.

7. GI-MRI coexistence in resistive states

It is shown in Sect. 6 that resistivity can lead to a gravito-turbulent state that is qualitatively different from ideal-MHD states, and it seems that MRI is absent. This raises the question of whether GI-MRI coexistence (comparable to sg-mhd-2 and sg-mhd-tau20) can also be maintained when explicit resistivity is enabled. Early simulations suggested that the saturation level of MRI may depend on non-ideal effects, such as Ohmic resistivity (η) and viscosity (ν; see e.g. Sano et al. 1998; Ziegler & Rüdiger 2001; Sano & Stone 2002; Fromang et al. 2007; Simon & Hawley 2009; Oishi & Mac Low 2011; Simon et al. 2011). Fromang et al. (2007) found that no turbulence is sustained for magnetic Prandtl numbers, $\mathrm{Pm} = \nu/\eta$, below a critical value, $\mathrm{Pm}_\mathrm{c} \sim 1$. However, this may not be the case in vertically stratified systems (see e.g. Davis et al. 2010; Oishi & Mac Low 2011; Simon et al. 2011). A detailed discussion is beyond the scope of this work though. However, large enough resistivity (low enough Rm) can generally cause MRI to decay (see e.g. Sano & Stone 2002; Ziegler & Rüdiger 2001; Simon & Hawley 2009; Simon et al. 2011); the critical Rm values in these cases can vary from several hundred to 10^4, depending on the exact system parameters (e.g. stratification, field strength, or viscosity). Hence, this certainly raises the question of whether the proposed GI-MRI coexistence can be sustained with explicit resistivity as well. Simon et al. (2011) showed that, whether MRI can be sustained or not, can also depend on the momentary magnetic field strength. Hence, it is not unreasonable to speculate that GI may actually help MRI, as the GI dynamo can provide a background field for the MRI to operate on. In Sect. 7.1, a scan over different resistivity values, η, is provided, testing whether a transition between the resistive-GI dynamo state (see Sect. 6) and one of the ideal-MHD states (e.g. GI-MRI coexistence) occurs, for accessible values of resistivity. Such a transition can indeed be found. That this is not an artefact of insufficient resolution is then checked in Sect. 7.2, by providing a simulation with twice the original resolution.

7.1. Critical value of Rm (η)

As a starting point, one can estimate the effective resistivity caused by the grid in the ideal-MHD simulations, shown in Table 1. Effective means that the diffusivity does not follow from an explicit diffusion scheme, but simply from the finite spatial resolution. Hence, the associated magnetic diffusion cannot be expected to be of the form $\eta\nabla^2\boldsymbol{B}$ ($\mu_0 = 1$ is assumed); however, for an order of magnitude estimate, it is treated as if it were the case. In Fourier space, the diffusive operator then reads $-\eta k^2$ and is thus most dominant for small structures (i.e. large wave numbers k). Grid dissipation is assumed to be important for spatial scales $2\delta_x = 2L_x/N_x$, where the factor two is used, because the smallest possible wavelength requires at least two discretisation intervals, to be resolved. Hence, one finds $k = \pi/\delta_x = \pi N_x/L_x$. Using the aforementioned wave number, one can assign a value η_eff to the effective grid resistivity, by demanding, $\eta_\mathrm{eff}k^2 \sim 1$. Put differently, this means that one has to choose η_eff such that the dimensionless term is of the order of one at the grid scale (represented by k). Hence,

$$\eta_\mathrm{eff} = \frac{1}{k^2} = \frac{1}{\pi^2}\left(\frac{L_x}{N_x}\right)^2 \sim 2\times10^{-4} \tag{20}$$

for grid dimensions $L = 20.0$ and $N = 440$ (see Table 1). This corresponds to an effective magnetic Reynolds number of $\mathrm{Rm}_\mathrm{eff} \sim 5000$, assuming $c_\mathrm{s} \sim 1$, in code units. However, care must be taken at this point, as the accuracy of such estimates is always uncertain. For example, using $k = N_x/L_x$, instead of $k = \pi N_x/L_x$, it is obtained that $\eta_\mathrm{eff} \sim 2\times10^{-3}$, or $\mathrm{Rm}_\mathrm{eff} \sim 500$. Due to the length scale being squared, a factor of π can cause roughly an additional order of magnitude. For Rm, also the sound speed might have an influence, as in all simulations, shown here, one finds $1 \lesssim \langle c_\mathrm{s}\rangle \lesssim 2$.

Choosing η to be roughly the grid value, η_eff, one would expect to recover the ideal-MHD result. However, due to the aforementioned uncertainty in the exact grid resistivity, we provide a scan over seven different η values, in order to (roughly) locate the transition, where GI-MRI coexistence turns into the resistive-GI dynamo of Sect. 6. The corresponding simulations are listed in Table 4. One data point for $\eta = 0.01$ is already provided, by simulation sg-eta01. Similar to sg-eta01, all other simulations, listed in Table 4, were restarted from sg-mhd-2 (Löhnert & Peeters 2022) at $t\Omega_0 = 1000$ and with exactly equal parameters, except for different values of η. The η values are chosen such that, assuming $c_\mathrm{s} = 1$, the corresponding magnetic Reynolds numbers are $\mathrm{Rm} \in \{100, 200, 300, 400, 500, 600, 1667\}$. As noted previously, the sound speed usually self adjusts to $\langle c_\mathrm{s}\rangle \gtrsim 1$; hence, one really has to use the volume-averaged values $\langle\langle \mathrm{Rm}\rangle\rangle_\mathrm{t}$, provided in Table 4; the values were obtained using Eq. (13). The lowest value, $\eta = 6\times10^{-4}$, corresponds to three-times the value of the lowest estimate for grid resistivity, $\eta_\mathrm{eff} = 2\times10^{-4}$.

Shown in the first image of Fig. 19 is the time evolution of the volume-averaged, toroidal magnetic field component $\langle B_y\rangle$. The time before $1000\Omega_0^{-1}$ corresponds to the ideal-MHD simulation sg-mhd-2, similar to in Sect. 6. One can clearly see the field oscillations with periodic polarity reversals. These reversals are connected to the butterfly pattern shown in the first image of Fig. 3. At $1000\Omega_0^{-1}$, resistivity, with the values provided in Table 4, is introduced into the GI-MRI coexistence state of sg-mhd-2. As one can tell immediately, the case with the lowest resistivity value, sg-eta0006, leads to prolonged field oscillations, similar to the ideal-MHD phase. One can also see that the runs sg-eta01 and sg-eat005 lead to qualitatively different field evolutions. More precisely, they do not lead to field reversals, at least not in the time span covered by the simulations. For sg-eat01, this is also discussed in Sect. 6, where it is argued that a new nonlinear state, the resistive-GI dynamo, is established. From the first image of Fig. 19 one might guess that sg-eta005 also settles into this new state. Except for the sign, the evolution of $\langle B_y\rangle$ is very similar in sg-eta01 and sg-eta005. However, the situation is less clear for the remaining, intermediate cases. They

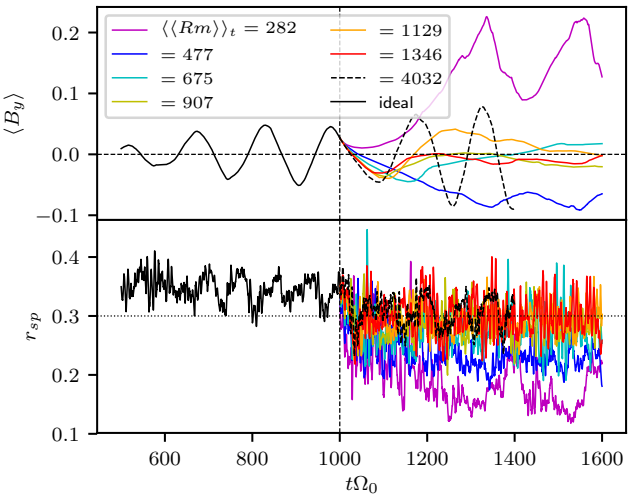

Fig. 19. Time evolution of the volume-averaged magnetic field component ($\langle B_y\rangle$; first image) and the magnetic stress to pressure ratio ($r_{sp} = \langle -2B_xB_y\rangle/\langle|\boldsymbol{B}|^2\rangle$, second image). The time axis starts at $t\Omega_0 = 600$ and extends towards $t\Omega_0 = 1600$. Simulation sg-eta01 was run until $2400\Omega_0^{-1}$, but for comparison it is only plotted for $t\Omega_0 \leq 1600$. The case sg-eta0006 was only run to $1400\Omega_0^{-1}$. The $t\Omega_0 \leq 1000$ interval corresponds to the ideal-MHD case sg-mhd-2 (see Löhnert & Peeters 2022, or Table 1). All resistive simulations were restarted from sg-mhd-2 at $1000\Omega_0^{-1}$. The horizontal dashed line in the second image indicates $r_{sp} = 0.3$.

tend to yield polarity reversals of $\langle B_y\rangle$, though they lack the clear periodicity of the ideal-MHD state, or sg-eta0006. Additionally, the averaged magnetic fields are also weaker in those cases.

In Sect. 6.2 it is demonstrated that the magnetic stress to pressure ratio, $r_{sp} = \langle -2B_xB_y\rangle/\langle|\boldsymbol{B}|^2\rangle$, significantly decreases in the new, resistive state. Hence, r_{sp} is chosen as a second indicator for resistive runs, shown in the second image of Fig. 19. For comparison, MRI-typical values are in the range 0.3–0.4. The line $r_{sp} = 0.3$ is highlighted in Fig. 19, as the horizontal, dashed line. Clearly, the ideal-MHD case yields MRI-typical values, as discussed previously. And almost all resistive simulations are also consistent with $r_{sp} \sim 0.3$, except the cases sg-eta01 and sg-eta005. This can also be seen from the time-averaged values $\langle r_{sp}\rangle_t$, provided in the last column of Table 4. This is consistent with the previously discussed time evolution of $\langle B_y\rangle$. From this, one might conclude that the qualitative transition, from the ideal-MHD regime to the resistive-GI dynamo, occurs for $\langle\langle \mathrm{Rm}\rangle\rangle_t \lesssim 500$, or $\eta \gtrsim 0.005$ in code units.

7.2. Testing whether resistive GI-MRI coexistence is resolved

As can be seen from the first image of Fig. 19, only the lowest resistivity simulation (sg-eta0006) and the two simulations with the largest resistivity values (sg-eta01 and sg-eta005) yield clearly interpretable states. Simulation sg-eta0006 clearly shows a prolongation of the periodic field reversals, whereas sg-eta01 and sg-eta005 evolve into the new resistive-GI dynamo state. All simulations in between, are not easily interpretable. For the latter, one can see field reversals, or at least the tendency towards field reversals, but they occur in a significantly less periodic pattern. One possible explanation is that the intermediate simulations tend towards GI-MRI coexistence, but their proximity to the transition from GI-MRI coexistence to the resistive-GI dynamo, may cause the more irregular field reversals. This is supported by the magnetic stress to pressure ratio, r_{sp}. Alternatively, these states may be comparable to the ideal-MHD, strong-GI case, sg-mhd-tau10, where field-reversals are also more irregular and where MRI may be absent. However, it is also possible that resistivity in sg-eta-0006 is not properly resolved and one essentially recovers the ideal-MHD case. One possible way to resolve the uncertainty is to simulate a state with one of the lower resistivity values and with higher resolution. One should then be able to discern possible differences. For that reason, two additional simulations with the second lowest resistivity value, $\eta = 0.00167$, are presented. The latter are in the following referred to as gi-mri-res-1 and gi-mri-res-2. The difference between the two simulations is that gi-mri-res-2 uses roughly twice the resolution of gi-mri-res-1; the resolution of gi-mri-res-1 is equal to that used in sg-eta00167. Important parameters for the two simulations are provided in Table 6. In contrast to sg-eta00167, gi-mri-res-1 was not restarted from the GI-MRI coexistence in sg-mhd-2 but instead from the pure-GI simulation GI072 (see Löhnert & Peeters 2022), at $t\Omega_0 = 120$. A magnetic seed field of ZNF type was introduced such that one obtains $\langle\beta\rangle_{xy} = 10^7$ at the mid-plane, and the resistivity of $\eta = 0.00167$ was enabled at that moment. We note that this is equivalent to the ideal-MHD simulation sg-mhd-2 (also restarted from GI072; see Löhnert & Peeters 2022), except that now resistivity was enabled directly at field seeding. This is meant to avoid possible biases from the fact that GI-MRI coexistence was already present in sg-mhd-2, when resistivity was introduced. The second simulation addresses the possibility of unresolved resistivity. Assuming that the effective grid resistivity is in the range $\eta_{\mathrm{eff}} = 2\times10^{-4}$–$2\times10^{-3}$, for the lower resolution of 440 points per 20 H, than the chosen resistivity is at best an order of magnitude above the grid value, or in the worst case roughly equal to the grid value. Using the same estimate for the higher resolution of 800 points per 20 H, one obtains $\eta_{\mathrm{eff}} = 6\times10^{-5}$–$2\times10^{-4}$, which is significantly smaller than $\eta = 0.00167$, in any case. By comparing gi-mri-res-1 and 2, one should be able to locate differences originating from insufficient resolution. We note that gi-mri-res-2 required significantly more computational resources, than the other simulations presented here. For that reason, we chose the vertical box size of 7 H, instead of the usual 8 H. But, as shown in Sect. 5.2, changing the vertical box size to 6 H did not change the simulation outcome of sg-mhd-tau20, and the latter yields essentially equal stress levels to sg-mhd-2. Additionally, it was possible to run the simulation with a slightly larger Courant number, of CFL = 0.5, without causing numerical instabilities. The field initialisation in gi-mri-res-2 is equal to that in gi-mri-res-1. We first set up a simulation with only GI and the same physical parameters ($\tau_c\Omega_0$, Q_0, γ, and η), as those, used in gi-mri-res-1, except with higher resolution. The simulation was initialised in a homogeneous, stratified state (stratification includes self-gravity), and small (1% of the background value) random perturbations in density and pressure were added. At first, the growth of axisymmetric GI modes is observed, which break up into turbulence after $\sim 40\Omega_0^{-1}$. The pure-GI state is then prolonged until $t\Omega_0 = 100$. At that moment, similar to gi-mri-res-1, a ZNF field with $\langle\beta\rangle_{xy} = 10^7$ was introduced, and resistivity with $\eta = 0.00167$ was enabled.

Similar to the first image of Fig. 19, one can analyse the time evolution of the volume-averaged, toroidal magnetic field component, $\langle B_y\rangle$, for both simulations gi-mri-res-1 and 2. This is shown in the first image of Fig. 20. Both simulations display field reversals, although the reversals seen in gi-mri-res-2 appear to be slightly less periodic than those in gi-mri-res-1. But it is possible that the latter is merely a statistical coincidence. The oscillation amplitudes (for $\langle B_y\rangle$) observed for the

Table 6. Important parameters and quantities for the resistive simulations gi-mri-res-1 and 2.

	gi-mri-res-1	gi-mri-res-2
$L_x \times L_y \times L_z$	$20 \times 20 \times 8$ H	$20 \times 20 \times 7$ H
$N_x \times N_y \times N_z$	$440 \times 440 \times 170$	$800 \times 800 \times 280$
CFL	0.3	0.5
$\tau_c \Omega_0$	10	10
Q_0	~0.72	~0.72
η	0.00167	0.00167
γ	1.64	1.64
$\langle\rho\rangle$	0.0554	0.0635
$\rho_{\min}$	6×10^{-5}	6×10^{-5}
Time interval	$500-1400\,\Omega_0^{-1}$	$500-1200\,\Omega_0^{-1}$
$\langle\langle \mathrm{Rm} \rangle\rangle_t$	~1405	~1374
$\langle\langle c_s \rangle\rangle_t$	1.531	1.514
$\langle\langle Q \rangle\rangle_t$	1.105	1.090
$\langle\langle \beta \rangle\rangle_t$	23.67	21.71
$\langle \alpha_r \rangle_t$	0.0081	0.0082
$\langle \alpha_m \rangle_t$	0.0058	0.0064
$\langle \alpha_g \rangle_t$	0.0117	0.0113
$\langle \alpha \rangle_t$	0.0256	0.0258
$\langle \alpha_{cool} \rangle_t$	0.0238	0.0239
$\langle r_{sp} \rangle_t$	0.3045	0.3187

Notes. Values in the upper block are independent of time. The remaining lines provide quantities, time-averaged over the shown time interval.

two simulations are in good agreement. We note that the field reversals seen in Fig. 20 are more pronounced than those in Fig. 19, despite sg-eta00167 having equal parameters. This may be indicative that the simulations, shown in Fig. 19 may indeed require more time to obtain a new, saturated state. Moreover, the mean time period for one field reversal is longer, compared to the ideal-MHD cases (see also the discussion about the butterfly diagram below). We also evaluated the magnetic stress-to-pressure ratio, $r_{sp} = \langle -2B_xB_y \rangle / \langle |\boldsymbol{B}|^2 \rangle$, for simulations gi-mri-res-1 and 2. The corresponding time evolution of r_{sp} is shown in the second image of Fig. 20. One first notices that the time evolutions for gi-mri-res-1 and 2 are in good agreement. Secondly, the values are in the range $r_{sp} \gtrsim 0.3$, in agreement with the ideal-MHD cases and the pure-MRI simulation. Shown in Fig. 21, are zt diagrams of the horizontally averaged, toroidal magnetic field component, $\langle B_y \rangle_{xy}$. These diagrams can be compared to the ideal cases, shown in Fig. 3. One notices that the field reversals of gi-mri-res-1 and 2 are not as coherent as those seen in sg-mhd-2 and sg-mhd-tau20. Interestingly, the seed fields in both gi-mri-res-1 and sg-mhd-2 were introduced into the same GI-turbulent state, yet the butterfly pattern, in the resistive case, is less pronounced than that in the ideal case. More precisely, the zt diagrams of gi-mri-res-1 and 2 are more reminiscent to the ideal case sg-mhd-tau10. And also here, one can see the tendency to field oscillations with a shorter time period, above and below the mid-plane. This es especially pronounced in the zt diagram of gi-mri-res-2. Hence, this resistive dynamo state has similarities with the strong-GI dynamo state, observed in the ideal-MHD regime. Interestingly, the GI activity in gi-mri-res-1 and 2 is equal to that of the weak-GI cases in the ideal regime. Thus, resistivity clearly has an influence.

The dimensionless, turbulent stresses are compared in Fig. 22, where the Reynolds, gravitational, and Maxwell contributions are shown from top to bottom. For gi-mri-res-2, the pure-

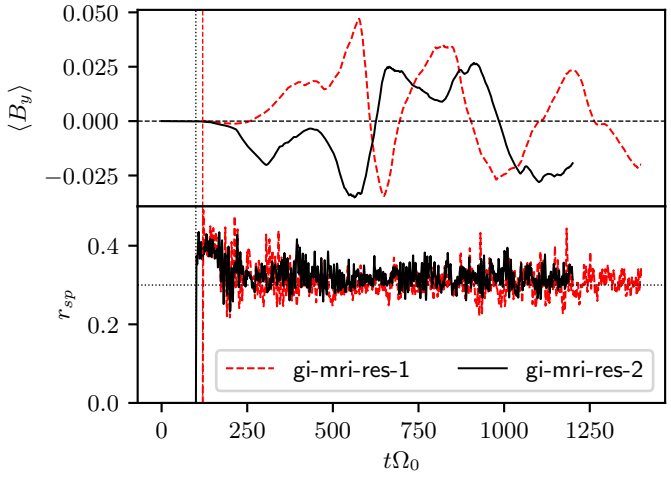

Fig. 20. Time evolution for both the volume-averaged magnetic field component, $\langle B_y \rangle$ (first image) and the magnetic stress-to-pressure ratio, $r_{sp} = \langle -2B_xB_y \rangle / \langle |\boldsymbol{B}|^2 \rangle$ (second image). Simulation gi-mri-res-1 is depicted as the dashed red curve, and gi-mri-res-2 is shown as the black curve. For reference, the value $r_{sp} = 0.3$ is shown as the horizontal dashed line in the second image. The vertical, dashed, and dotted lines mark the time points when the seed fields are introduced.

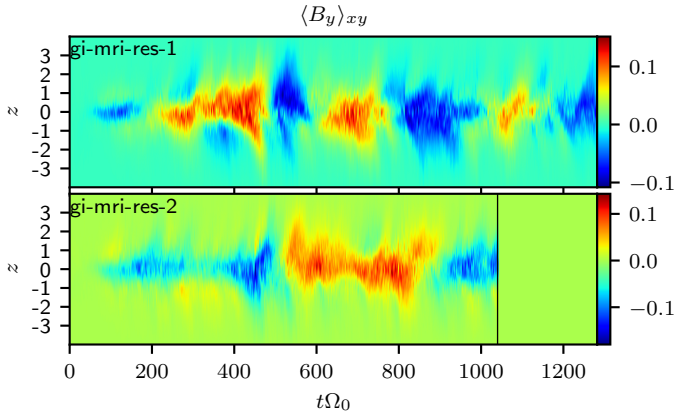

Fig. 21. zt diagrams of the horizontally averaged, toroidal magnetic field component, $\langle B_y \rangle_{xy}$, for simulations gi-mri-res-1 and 2.

GI phase ($t\Omega_0 < 100$) is depicted as well, and one can see a sharp spike (the spike was cut at the upper plot boundary), corresponding to the transition from the linear state to the nonlinear regime. Generally, the two simulations coincide well, which can also be read off from the time-averaged stresses, shown in Table 6. The absolute values of α_m observed for gi-mri-res-1 and 2 are of the order of $\alpha_m \sim 0.006$. This is slightly smaller than the pure MRI value ($\alpha_m \sim 0.0088$) and smaller than the ideal-MHD runs with GI. Hence, it appears that Ohmic resistivity causes a reduction of α_m. This is consistent with the observation that saturation of gi-mri-res-1 and 2 is similar to the strong-GI, ideal-MHD case, sg-mhd-tau10. Instead of GI being stronger, α_m is here lower. Whether gi-mri-res-1 and 2 are states of GI-MRI coexistence is, similar to sg-mhd-tau10, not certain. A lower α_m value, in the presence of resistivity, is at least not inconsistent with MRI. But the largest α_m value, observed in this study, occurs for the most resistive simulation, sg-eta01 ($\alpha_m \sim 0.019$; see Table 4). This implies that α_m cannot decrease indefinitely, as η increases, and eventually some type of phase transition must occur. Taking into account the findings for the ideal-MHD cases, then this suggests

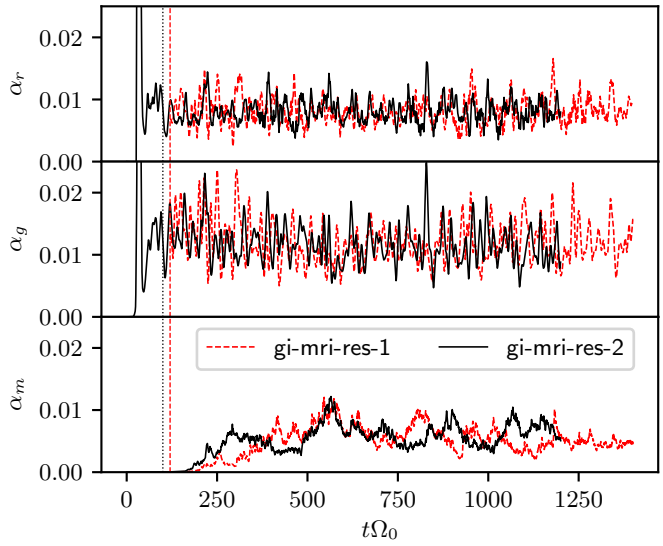

Fig. 22. Dimensionless turbulent stresses (Reynolds, gravitational, and Maxwell contributions, from top to bottom) as a function of time. The stresses for simulation gi-mri-res-1 are shown in dashed red, and the corresponding stresses for gi-mri-res-2 are shown as solid black curves. The vertical dashed and dotted lines correspond to the moments of field seeding for gi-mri-res-1 and 2, respectively.

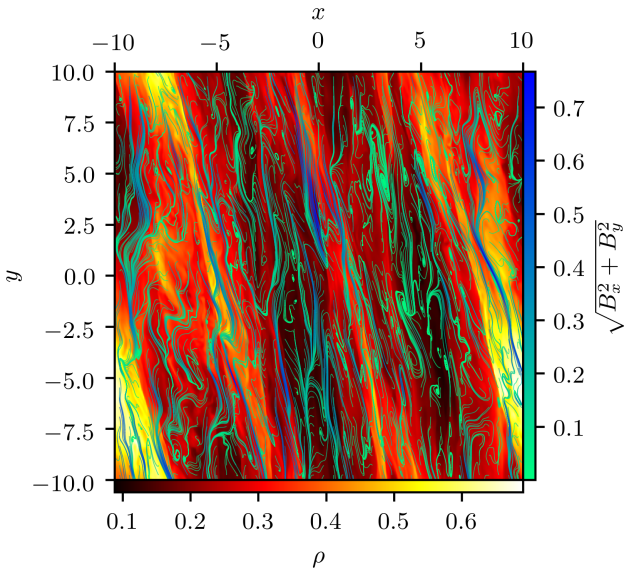

Fig. 23. Mid-plane mass density ($z = 0$) evaluated for gi-mri-res-2 at $t\Omega_0 = 580$. Superimposed are magnetic field lines traced in the (x, y) plane (only (B_x, B_y) were used for the tracing).

that MRI fails at this point. But at the very least, some type of transition occurs. We note that this is consistent with the findings of Riols & Latter (2019), who also pointed out the possibility of a dynamo-state transition at Rm~500 – 600.

For reference, the mid-plane mass density, evaluated for gi-mri-res-2, at $t\Omega_0 = 580$, is shown in Fig. 23. The density plot is overlayed with a series of magnetic field lines, traced in the (x, y) plane, by only considering the field components (B_x, B_y). Similar to the previous cases, one observes a clearly visible alignment of the field lines with the density waves, related to GI. But similar to the ideal-MHD case, the field lines frequently change direction, in the regions between the density waves. Hence, small-scale structures are definitively present.

One can conclude that doubling the resolution did not cause significant changes in the simulation outcome. And one can also see that a state with field reversals, and which has resemblance with the ideal-MHD states, can also be obtained from scratch, that is, without introducing resistivity into an already dynamo-saturated state. Hence, we conclude that the state, observed in Sect. 6, is indeed a new (third) dynamo state, and the observed transition, as Rm decreases, is indeed a physical effect originating from a significant heat production due to Ohmic resistivity.

8. Conclusion

Löhnert & Peeters (2022) report on the observation that the combined effects of self-gravity and magnetic fields can lead to a turbulent state that is consistent with a coexistence between GI and MRI. Here, this was further tested by varying the strength of GI, where strength refers to the pure-GI stress level (α, α_g). The strength was controlled by varying the cooling law. Cases with $\tau_c\Omega_0 = 10$ and additional heating were tested in Löhnert & Peeters (2022). Hence, additional simulations with cooling times $\tau_c\Omega_0 = 10$ (strong-GI case) and 20 (weak-GI case) are provided here, and no additional heating was used. The strong-GI case ($\tau_c\Omega_0 = 10$) leads to GI-only stresses that are larger by roughly a factor of two compared to the other simulations. At dynamo saturation, the weak-GI simulation leads to a clearly visible butterfly pattern, with sign reversals of $\langle B_y \rangle_{xy}$, that is equivalent to those seen in Löhnert & Peeters (2022). That is different from the strong-GI case ($\tau_c\Omega_0 = 10$). Clearly visible polarity reversals of $\langle B_y \rangle_{xy}$ are absent at the mid-plane, but one can see the tendency towards sign reversals above and below the mid-plane. The vertical EMF profiles, obtained for the weak-GI case ($\tau_c\Omega_0 = 20$), are largely consistent with the EMFs derived from a pure-MRI reference simulation, though differences can be seen in the vertical field-strength distribution. For the strong-GI case ($\tau_c\Omega_0 = 10$), differences to the pure-MRI simulation also arise in the vertical EMF profile. Hence, it appears that the weak-GI case ($\tau_c\Omega_0 = 20$) and the strong-GI case ($\tau_c\Omega_0 = 10$) lead to qualitatively different dynamo states. The $\tau_c\Omega_0 = 20$ case has similarities to the pure-MRI simulation and is possibly a state of GI-MRI coexistence. The strong-GI case cannot be categorised exactly and is possibly a pure-GI dynamo. However, we note that the two states also share some similarities: the Maxwell stress, α_m, is roughly equal in both the weak- and strong-GI cases, and the absolute reduction in the gravitational stress, α_g (measured from the GI-only to the MHD-saturated state), is also equal. Hence, the absence (or presence) of MRI in the strong-GI case cannot definitively be settled in this context, though it appears that there are two different ideal-MHD dynamo states.

Löhnert & Peeters (2022) also report on differences to the simulations in Riols & Latter (2018a, 2019), especially the $\tau_c\Omega_0 = 20$ case SGMRI-20 therein. They proposed that vertical outflows might be a possible source for discrepancies. For this purpose, an additional simulation with no heating, $\tau_c\Omega_0 = 20$, and all remaining parameters equal to those in Riols & Latter (2018a) is presented here. This includes a slightly smaller box size, 6 H instead of our standard 8 H. The resulting turbulent state is equal to that of our standard runs, both qualitatively and quantitatively. We find that the discrepancies with Riols & Latter (2018a) arise from the difference in the duration (e.g. in units of Ω_0^{-1}) of the simulations, not the box size. For the first $320\Omega_0^{-1}$, after field seeding (duration of SGMRI-20) we find agreement. However, we find that, for the $\tau_c\Omega_0 = 20$ case, saturation occurs $\sim 600\Omega_0^{-1}$ after field seeding. At that point, a butterfly diagram that spans the entire vertical domain emerges. It is currently not

clear why such a long saturation time is observed. One might speculate that it is related to vertical mixing due to GI. This may, at first, prevent field reversals near the mid-plane, though eventually the field strength can phase-lock the mid-plane field, inducing field reversals over the entire vertical domain. As a further test, we compared the $\tau_c\Omega_0 = 10$ simulation to SGMRI-10 from Riols & Latter (2018a). The observed stresses for this cooling time are in agreement as well, though here we used the saturated phase for the average. We note that SGMRI-10 from Riols & Latter (2018a) was restarted from SGMRI-20, indicating that this case was closer to saturation.

We then tested how Ohmic resistivity influences GI-MRI coexistence. For that purpose, ideal-MHD simulations with fully developed turbulence and saturated dynamo were restarted with a finite value of Ohmic resistivity, η. The initial, ideal-MHD state can be characterised as a state of coexistence between gravitational turbulence and magneto-rotational turbulence, outlined in more detail in Löhnert & Peeters (2022). When the restart is undertaken with a resistivity, η, such that the magnetic Reynolds number is $\langle \mathrm{Rm} \rangle \sim 280$ ($\eta = 0.01$ in code units), the system is at first disrupted but settles into a new nonlinear state after $\sim 300\Omega_0^{-1}$. The new turbulent state is qualitatively different from the original state in the ideal-MHD regime. Most notably, the saturation level of the magnetic field strength doubles, reducing the plasma β by roughly a factor of four. The vertical geometry of the magnetic field also changes: the butterfly diagram, which is clearly visible in the ideal-MHD regime, is no longer visible with the introduction of resistivity. Additionally, the ratio of Maxwell stress to magnetic pressure in the resistive state is $r_{\mathrm{sp}} \sim 0.17$, which is half the expected value for MRI ($0.3 - 0.4$). This shows that the newly developed state is qualitatively different from the ideal-MHD states and that MRI is effectively suppressed. The turbulent state develops oscillatory behaviour in time, but the origin of the oscillations is not an MRI-related butterfly diagram. Rather, it is the heat production due to Ohmic resistivity. As the GI dynamo builds up further magnetic energy, the Ohmic dissipation also increases, giving rise to enhanced heat production. The additional heat weakens the GI, which corresponds to a larger Toomre parameter value. This reduces dynamo activity, and the magnetic energy decays. Eventually, cooling reduces the thermal-energy level enough to reignite GI, and a new cycle begins. We refer to the new state as resistive-GI dynamo.

We then demonstrated that states consistent with the ideal-MHD regime can also occur when explicit resistivity is enabled. This was achieved in two steps. First, we derived an estimate for the effective grid resistivity, which we then used as a reference when scanning different resistivity values. The scan contains resistivity values in the range $6 \times 10^{-4} \leq \eta \leq 0.01$, which corresponds to magnetic Reynolds numbers of $280 \lesssim \langle\langle \mathrm{Rm} \rangle\rangle_t \lesssim 4000$. The transition appears to occur in the range $\mathrm{Rm} \sim 470{-}680$, although the value may be higher because the newly formed turbulent states could not easily be attributed to either GI-MRI coexistence or the resistive-GI dynamo. We argue that the best qualifier for this type of turbulence is the magnetic stress-to-pressure ratio, $r_{\mathrm{sp}} = \langle -2B_xB_y \rangle / \langle |\boldsymbol{B}|^2 \rangle$, which shows a clear transition in the range $\eta \sim 0.033{-}0.005$ ($\langle\langle \mathrm{Rm} \rangle\rangle_t \sim 470{-}680$). In a second step, we tested whether this transition is the artefact of an unresolved resistive dissipation scale or if it is due to the fact that the resistive simulations were restarted from an ideal-MHD state with GI-MRI coexistence. For this purpose, two additional simulations were provided; both simulations start with GI-only turbulence, and a small ZNF-type magnetic seed field was introduced. Both simulations used the same value of resistivity, $\eta = 0.00167$, or $\langle\langle \mathrm{Rm} \rangle\rangle_t \sim 1400$, which correspond to the second lowest value of the previous scan, but the second simulation used roughly twice the resolution of the first simulation. A turbulent state, consistent with the ideal-MHD regime, was obtained in both cases. This is implied by the magnetic stress-to-pressure ratio $r_{\mathrm{sp}} \gtrsim 0.3$ and the field reversals seen in the volume-averaged magnetic field component, $\langle B_y \rangle$. Furthermore, all quantitative measures that were tested are almost equal for the two simulations. Hence, we conclude that resolution does not change the simulation outcome and that states consistent with the ideal-MHD regime can also be found with explicit Ohmic resistivity. Whether MRI is present in these resistive cases is not entirely clear, as the saturated states are, in some aspects, akin to the ideal-MHD strong-GI case sg-mhd-tau10. The simulation outcomes do clearly suggest that some form of state transition must occur for Rm ~500.

References

Armitage, P. J. 2011, ARA&A, 49, 409
Armitage, P. J., Livio, M., & Pringle, J. E. 2001, MNRAS, 324, 705
Bai, X.-N., & Stone, J. M. 2013, ApJ, 767, 30
Balbus, S. A., & Hawley, J. F. 1991, ApJ, 376, 214
Balbus, S. A., & Hawley, J. F. 1998, Rev. Mod. Phys., 70, 1
Béthune, W., & Latter, H. 2022, A&A, 663, A138
Blackman, E. G., Penna, R. F., & Varnière, P. 2008, New Astron., 13, 244
Boley, A. C., Mejía, A. C., Durisen, R. H., et al. 2006, ApJ, 651, 517
Booth, R. A., & Clarke, C. J. 2019, MNRAS, 483, 3718
Brandenburg, A., & Donner, K. J. 1997, MNRAS, 288, L29
Brandenburg, A., Nordlund, A., Stein, R. F., & Torkelsson, U. 1995, ApJ, 446, 741
Colella, P. 1990, J. Comput. Phys., 87, 171
Colella, P., & Woodward, P. R. 1984, J. comput. Phys., 54, 174
Coleman, M. S. B., Yerger, E., Blaes, O., Salvesen, G., & Hirose, S. 2017, MNRAS, 467, 2625
Cossins, P., Lodato, G., & Clarke, C. J. 2009, MNRAS, 393, 1157
Courant, R., Friedrichs, K., & Lewy, H. 1928, Math. Ann., 100, 32
Davis, S. W., Stone, J. M., & Pessah, M. E. 2010, ApJ, 713, 52
Deng, H., Mayer, L., & Latter, H. 2020, ApJ, 891, 154
Fromang, S. 2005, A&A, 441, 1
Fromang, S., Balbus, S. A., Terquem, C., & De Villiers, J.-P. 2004, ApJ, 616, 364
Fromang, S., Papaloizou, J., Lesur, G., & Heinemann, T. 2007, A&A, 476, 1123
Fromang, S., Latter, H., Lesur, G., & Ogilvie, G. I. 2013, A&A, 552, A71
Gammie, C. F. 2001, ApJ, 553, 174
Goodman, J. 2003, MNRAS, 339, 937
Gressel, O. 2010, MNRAS, 405, 41
Guan, X., & Gammie, C. F. 2011, ApJ, 728, 130
Hawley, J. F., & Balbus, S. A. 1992, ApJ, 400, 595
Hawley, J. F., Gammie, C. F., & Balbus, S. A. 1995, ApJ, 440, 742
Hawley, J. F., Guan, X., & Krolik, J. H. 2011, ApJ, 738, 84
Hirose, S., & Shi, J.-M. 2019, MNRAS, 485, 266
Hirose, S., Blaes, O., Krolik, J. H., Coleman, M. S. B., & Sano, T. 2014, ApJ, 787, 1
Käpylä, P. J., & Korpi, M. J. 2011, MNRAS, 413, 901
Koyama, H., & Ostriker, E. C. 2009, ApJ, 693, 1316
Kratter, K., & Lodato, G. 2016, ARA&A, 54, 271
Lesur, G., & Ogilvie, G. I. 2008, A&A, 488, 451
Lin, C. C., & Shu, F. H. 1964, ApJ, 140, 646
Lin, M.-K., & Kratter, K. M. 2016, ApJ, 824, 91
Lodato, G., & Rice, W. K. M. 2004, MNRAS, 351, 630
Löhnert, L., & Peeters, A. G. 2022, A&A, 663, A176
Lynden-Bell, D. 1969, Nature, 223, 690
Lynden-Bell, D., & Kalnajs, A. J. 1972, MNRAS, 157, 1
Martin, R. G., & Lubow, S. H. 2011, ApJ, 740, L6
Martin, R. G., Lubow, S. H., Livio, M., & Pringle, J. E. 2012, MNRAS, 423, 2718
Masset, F. 2000, A&AS, 141, 165
Menou, K., & Quataert, E. 2001, ApJ, 552, 204
Oishi, J. S., & Mac Low, M.-M. 2011, ApJ, 740, 18
Paardekooper, S.-J. 2012, MNRAS, 421, 3286
Rice, W. K. M., Armitage, P. J., Bate, M. R., & Bonnell, I. A. 2003, MNRAS, 339, 1025
Rice, W. K. M., Armitage, P. J., Mamatsashvili, G. R., Lodato, G., & Clarke, C. J. 2011, MNRAS, 418, 1356

Riols, A., & Latter, H. 2018a, MNRAS, 474, 2212
Riols, A., & Latter, H. 2018b, MNRAS, 476, 5115
Riols, A., & Latter, H. 2019, MNRAS, 482, 3989
Riols, A., Latter, H., & Paardekooper, S.-J. 2017, MNRAS, 471, 317
Riols, A., Xu, W., Lesur, G., Kunz, M. W., & Latter, H. 2021, MNRAS, 506, 1407
Roe, P. L. 1981, J. Comput. Phys., 43, 357
Rüdiger, G., & Pipin, V. V. 2000, A&A, 362, 756
Salvesen, G., Simon, J. B., Armitage, P. J., & Begelman, M. C. 2016, MNRAS, 457, 857
Sanders, R., Morano, E., & Druguet, M.-C. 1998, J. Comput. Phys., 145, 511
Sano, T., & Stone, J. M. 2002, ApJ, 577, 534
Sano, T., Inutsuka, S.-I., & Miyama, S. M. 1998, ApJ, 506, L57
Shakura, N. I., & Sunyaev, R. A. 1973, A&A, 24, 337
Shi, J.-M., & Chiang, E. 2014, ApJ, 789, 34
Shi, J., Krolik, J. H., & Hirose, S. 2009, ApJ, 708, 1716
Silvers, L. J. 2008, MNRAS, 385, 1036
Simon, J. B., & Hawley, J. F. 2009, ApJ, 707, 833
Simon, J. B., Hawley, J. F., & Beckwith, K. 2011, ApJ, 730, 94
Stone, J. M., & Gardiner, T. A. 2010, ApJS, 189, 142
Stone, J. M., Hawley, J. F., Gammie, C. F., & Balbus, S. A. 1996, ApJ, 463, 656
Stone, J. M., Gardiner, T. A., Teuben, P., Hawley, J. F., & Simon, J. B. 2008, ApJS, 178, 137
Suzuki, T. K., & Inutsuka, S.-I. 2009, ApJ, 691, L49
Toomre, A. 1964, ApJ, 139, 1217
Turner, N. J., Sano, T., & Dziourkevitch, N. 2007, ApJ, 659, 729
Young, M. D., & Clarke, C. J. 2015, MNRAS, 451, 3987
Zhu, Z., Hartmann, L., & Gammie, C. 2009, ApJ, 694, 1045
Zhu, Z., Hartmann, L., & Gammie, C. 2010, ApJ, 713, 1143
Ziegler, U., & Rüdiger, G. 2000, A&A, 356, 1141
Ziegler, U., & Rüdiger, G. 2001, A&A, 378, 668
Zier, O., & Springel, V. 2023, MNRAS, 520, 3097

Appendix A: Prolongation of sg-mhd-tau10

In Sect. 5.1, a direct comparison between the pure-GI phase and the dynamo-saturated phase of simulation sg-mhd-tau10 is provided. The pure-GI phase ($\boldsymbol{B} = 0$), of simulation sg-mhd-tau10, exhibits significant oscillations in α_{r} and α_{g}. This is not the case in the dynamo-saturated phase. Hence, in order to obtain more reliable statistics, the pure-GI phase, of sg-mhd-tau10, was prolonged, from $t\Omega_0 = 400$ to 700. The corresponding stresses and the Toomre parameter are shown in Fig. A.1. At $t\Omega_0 = 200$ (vertical, dashed line), sg-mhd-tau10 was restarted from sg-mhd-tau20, but with a lower cooling time of $\tau_c\Omega_0 = 10$. In the original simulation, the ZNF-seed field is introduced at $t\Omega_0 = 400$. Here, the pure-GI phase ($\boldsymbol{B} = 0$) is prolonged, instead. The average is then taken over the $500 - 700\Omega_0^{-1}$ interval, highlighted by the black, vertical lines. The resulting, time-averaged values are shown in Table 2.

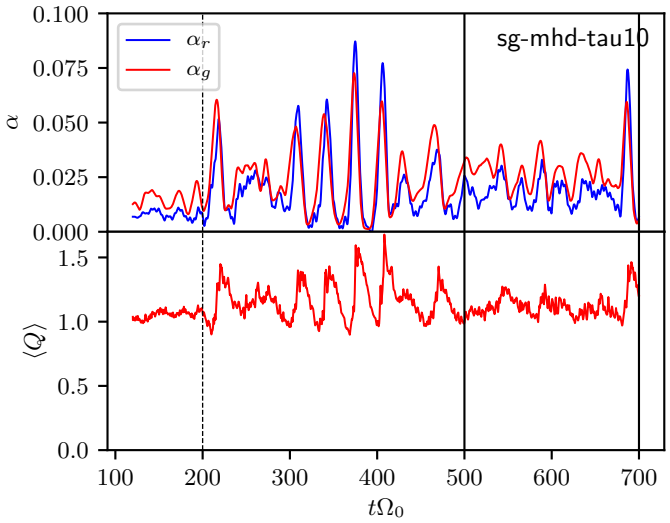

Fig. A.1. Prolonged, pure-GI phase of simulation sg-mhd-tau10. At $t\Omega_0 = 200$ (vertical dashed line), sg-mhd-tau10 was restarted from the pure-GI phase of sg-mhd-tau20. The boundaries of the interval used for the time average are depicted as the vertical black lines.

Chapter 10

Notes, and Additional Results

Shown here is research, related, or additional to the works Löhnert, Krätschmer, & Peeters (2020), Löhnert & Peeters (2022), and Löhnert & Peeters (2023). This includes, for example, more detailed analytical derivations, or additional diagnostics, that have not been published.

Sect. 10.1, provides an analytical derivation of the linear stability criterion, for the gravitational instability (GI). The derivation is for the local, razor-thin shearing-box, and the effects of cooling, and additional heating (see Sect. 4.5.3) are included. The so-obtained growth rates are of importance for the work Löhnert, Krätschmer, & Peeters (2020). Another diagnostic, shown in Löhnert, Krätschmer, & Peeters (2020), compares the Fourier-power spectrum of turbulent velocity fluctuations, to the spectrum of a typical shock geometry. For the shock, a generic analytical function is used, and the Fourier transform is calculated analytically, which is shown here, in Sect. 10.2. For the GI-MHD simulations with Athena, a special Poisson solver (see Sect. 4.6.4) was implemented. Sect. 10.3 estimates the Poisson-solver accuracy, by utilising simulation results of Löhnert & Peeters (2022), and Löhnert & Peeters (2023). Sect. 10.4 provides an analytical derivation for the dynamo oscillation frequency, $s_{1/2} = \mathrm{Tr}/2 \pm \sqrt{(\mathrm{Tr}/2)^2 - \mathrm{D}}$, used in Löhnert & Peeters (2022). Finally, Sect. 10.5 provides a more detailed analysis of the electromotive forces (EMFs), that were also discussed in Löhnert & Peeters (2023).

10.1 Gravitational stability of the razor-thin shearing sheet, with cooling, and additional heating

In Löhnert, Krätschmer, & Peeters (2020), see also Sect. 7, a dispersion relation for the growthrate of GI, g, as a function of Q_0, and k, was provided. This section aims to provide a more detailed, analytical derivation of both the dispersion relation and the resulting stability criteria for GI, with the cooling (heating) model, detailed in Sect. 4.5.3.

GI occurs as a consequence of the disk-materials interaction with itself, via self-gravity. The gravitational potential, associated with self-gravity, is referred to as Φ. Starting point are the two-dimensional equations of motion in the local shearing-box approximation, see Eqs. 4.41 - 4.43. The equations are linearised with respect to small deviations from the background equilibrium. The background equilibrium is given by a shear flow, with velocity $\mathbf{v}_0 = -(3\Omega_0/2)\, x\, \mathbf{e}_y$, a constant surface density, Σ_0, and a constant surface pressure, P_0. The two-dimensional, thermal-energy density follows from $P_0 = (\gamma - 1)U_0$. Similarly, the corresponding, two-dimensional sound speed of

the background is $c_{s,0} = \sqrt{\gamma(\gamma-1)U_0/\Sigma_0}$. The equilibrium is then perturbed,

$$\begin{aligned} \Sigma &= \Sigma_0 + \delta\Sigma \\ U &= U_0 + \delta U \\ \mathbf{v} &= \mathbf{v}_0 + \delta\mathbf{v}, \end{aligned} \tag{10.1}$$

whereby the deviations are indicated by a δ. In Cartesian components, the velocity deviation reads $\delta\mathbf{v} := (v_x, \delta v_y)$, and in the radial velocity component ($v_x = \delta v_x$), the δ is omitted, because all radial velocity components are, per definition, deviations from the background shear flow. For the potential of self-gravity, Φ, a similar argument holds, and the δ is omitted. That is, because constant gravitational potential does not contribute a gravitational acceleration $\mathbf{g} = -\nabla\Phi$.

What remains to be discussed is the treatment of the cooling law. As motivated in Sect. 4.5.3, two different cooling laws are considered, both related to that outlined in Rice et al. (2011). One of the cooling laws assumes a constant background temperature, $c_{s,0} = \text{const.}$, and the other assumes a constant background thermal energy density, $U_0 = \text{const}$. In order to prevent a case separation, the parameter $\xi \in [0,1]$ is introduced, such that the cooling law reads:

$$\begin{aligned} \Sigma\dot{q} &= -\frac{1}{\tau_c}\left(U - U_0 - \xi\frac{(\Sigma-\Sigma_0)c_{s0}^2}{\gamma(\gamma-1)}\right) \\ &= -\frac{1}{\tau_c}\left(U - U_0 + \xi U_0 - \xi\Sigma\frac{U_0}{\Sigma_0}\right). \end{aligned} \tag{10.2}$$

Hence, for $\xi = 0$, the cooling law tends to regulate the system towards a constant thermal energy density, U_0 (see also Eq. 4.45), and for $\xi = 1$, the cooling law tends to achieve a constant temperature $c_{s,0} = \text{const.}$ (see also Eq. 4.46). This construction, using ξ, allows one to analyse both cooling cases, simultaneously. The cooling law still needs to be linearised, with respect to the deviations. This is achieved most easily by considering the first line of Eq. 10.2, as the deviations from the background can directly be read off

$$\begin{aligned} \Sigma\dot{q} &= -\frac{1}{\tau_c}\left(\delta U - \xi\frac{c_{s0}^2}{\gamma(\gamma-1)}\delta\Sigma\right) \\ &= -\frac{1}{\tau_c}\left(\delta U - \xi\frac{U_0}{\Sigma_0}\delta\Sigma\right). \end{aligned} \tag{10.3}$$

This analytical form of the linearised cooling law is equivalent to that described in Lin & Kratter (2016). The factor $\Theta = T_{\text{irr}}/T_{\text{eq}}$, in Lin & Kratter (2016), corresponds to the factor ξ here. It is noted though, that the cooling model is applied in a different context, in Lin & Kratter (2016). The latter use the cooling law to mimic two separate effects, simultaneously: A constant background heating, and, in addition to that, irradiation heating. This leads to a new background temperature $T_{\text{eq}} \neq T_{\text{irr}}$. Their goal is not to evaluate the stability of the shear flow, but rather the stability of the GI-turbulent state itself. Thereby, Kratter & Lodato (2016) model the turbulent heating of GI via the constant heating in the cooling model.

For the stability analysis here, only the most unstable, axisymmetric modes, are considered. That is, the deviations δf have no y dependence. With these preparing steps, one can now derive the linearised equations of motion, from Eqs. 4.41 - 4.43, yielding (see also Löhnert, Krätschmer, &

Peeters 2020):

$$\begin{aligned}
\partial_t \delta\Sigma + \Sigma_0 \partial_x v_x &= 0 \\
\partial_t v_x + \frac{\gamma-1}{\Sigma_0}\partial_x \delta U - 2\Omega_0 \delta v_y + \partial_x \Phi(x,y,0) &= 0 \\
\partial_t \delta v_y - \frac{3\Omega_0}{2} v_x + 2\Omega_0 v_x &= 0 \\
\partial_t \delta U + \gamma U_0 \partial_x v_x + \frac{\delta U}{\tau_c} - \xi \frac{U_0}{\Sigma_0}\frac{\delta\Sigma}{\tau_c} &= 0.
\end{aligned} \tag{10.4}$$

One then separates the perturbations, δf, into Fourier modes with wave vector $\mathbf{k}$, and frequency ω. Due to the translational symmetry in y direction, one finds $k_y = 0$, or, $\delta f = \delta\hat{f}(k_x)\,\exp\left(-i\omega t + ik_x x\right) + c.c.$. The complex conjugate ($c.c.$) can be omitted here, as all terms are linear in the perturbations. For the gravitational potential, the razor-thin result of Sect. 4.5.5, Eq. 4.50, can be used, and for one single Fourier mode, one thus obtains

$$\begin{aligned}
\Phi(x,y,0) &= -\frac{2\pi G}{k}\delta\hat{\Sigma}(k_x)\exp\left(-i\omega t + ik_x x\right), \quad k := |k_x| \\
\Rightarrow \partial_x \Phi(x,y,0) &= -ik_x \frac{2\pi G}{k}\delta\hat{\Sigma}(k_x)\exp\left(-i\omega t + ik_x x\right) \\
&= -i\,2\pi G\,\mathrm{sign}(k_x)\,\delta\hat{\Sigma}(k_x)\exp\left(-i\omega t + ik_x x\right) \\
&= -A\,\delta\hat{\Sigma}(k_x)\exp\left(-i\omega t + ik_x x\right).
\end{aligned} \tag{10.5}$$

In the last line, the abbreviation $A = i\,2\pi G\,\mathrm{sign}(k_x)$ was introduced. The Fourier mode is then substituted into Eqs. 10.4, yielding

$$\begin{aligned}
-i\omega\delta\hat{\Sigma} + ik_x\Sigma_0\hat{v}_x &= 0 \\
-i\omega\hat{v}_x + \frac{\gamma-1}{\Sigma_0}ik_x\delta\hat{U} - 2\Omega_0\delta\hat{v}_y - A\,\delta\hat{\Sigma} &= 0 \\
-i\omega\delta\hat{v}_y - \frac{3\Omega_0}{2}\hat{v}_x + 2\Omega_0\hat{v}_x &= 0 \\
-i\omega\delta\hat{U} + i\gamma U_0 k_x\hat{v}_x + \frac{1}{\tau_c}\delta\hat{U} - \frac{\xi}{\tau_c}\frac{U_0}{\Sigma_0}\delta\hat{\Sigma} &= 0,
\end{aligned} \tag{10.6}$$

whereby the exponent, $\exp\left(-i\omega t + ik_x x\right)$, cancels in all equations. What is left are algebraic equations for the perturbation amplitudes, $\delta\hat{f}$. This set of equations can be expressed in the more convenient matrix-times-vector form

$$\underbrace{\begin{pmatrix}
\Sigma_0 k_x & 0 & -\omega & 0 \\
-i\omega & -2\Omega_0 & -A & \frac{\gamma-1}{\Sigma_0}ik_x \\
\frac{\Omega_0}{2} & -i\omega & 0 & 0 \\
i\gamma U_0 k_x & 0 & -\frac{\xi U_0}{\Sigma_0\tau_c} & \frac{1}{\tau_c} - i\omega
\end{pmatrix}}_{\underline{\underline{\mathbf{M}}}} \cdot \begin{pmatrix} \hat{v}_x \\ \delta\hat{v}_y \\ \delta\hat{\Sigma} \\ \delta\hat{U} \end{pmatrix} = \begin{pmatrix} 0 \\ 0 \\ 0 \\ 0 \end{pmatrix}. \tag{10.7}$$

In order to find the non-trivial solutions for this system, $\det(\underline{\underline{\mathbf{M}}}) = 0$ is demanded (see, e.g.,

Bronstein et al. 2012). Hence, one first needs to calculate the determinant:

$$\begin{aligned}
\det(\underline{\underline{\mathbf{M}}}) &= \Sigma_0 k_x \begin{vmatrix} -2\Omega_0 & -A & \frac{\gamma-1}{\Sigma_0} ik_x \\ -i\omega & 0 & 0 \\ 0 & -\xi \frac{U_0}{\Sigma_0 \tau_c} & \frac{1}{\tau_c} - i\omega \end{vmatrix} - \omega \begin{vmatrix} -i\omega & -2\Omega_0 & \frac{\gamma-1}{\Sigma_0} ik_x \\ \Omega_0/2 & -i\omega & 0 \\ i\gamma U_0 k & 0 & \frac{1}{\tau_c} - i\omega \end{vmatrix} \\
&= \Sigma_0 k_x \left(i\omega \frac{\gamma-1}{\Sigma_0} ik_x \frac{\xi U_0}{\Sigma_0 \tau_c} - iA\omega (\frac{1}{\tau_c} - i\omega) \right) \\
&\quad -\omega \left(-\omega^2 (\frac{1}{\tau_c} - i\omega) - \frac{\gamma-1}{\Sigma_0} ik_x \omega \gamma U_0 k_x + \Omega_0^2 (\frac{1}{\tau_c} - i\omega) \right) \\
&= -\frac{\xi(\gamma-1)\omega U_0}{\Sigma_0 \tau_c} k_x^2 - iA\Sigma_0 \omega (\frac{1}{\tau_c} - i\omega) k + \omega^3 (\frac{1}{\tau_c} - i\omega) + i\frac{\gamma(\gamma-1)\omega^2 U_0}{\Sigma_0} k_x^2 \\
&\quad -\omega \Omega_0^2 (\frac{1}{\tau_c} - i\omega) \\
&= -i\omega^4 + \frac{1}{\tau_c}\omega^3 + \left(-A\Sigma_0 k_x + \frac{i\gamma(\gamma-1)U_0 k_x^2}{\Sigma_0} + i\Omega_0^2 \right) \omega^2 \\
&\quad + \left(-\frac{\xi(\gamma-1)U_0}{\Sigma_0 \tau_c} k_x^2 - \frac{iA\Sigma_0}{\tau_c} k_x - \frac{\Omega_0^2}{\tau_c} \right) \omega \\
&= -i\omega^4 + \frac{1}{\tau_c}\omega^3 + \left(-i2\pi G\Sigma_0 \mathrm{sign}(k_x) k_x + i\gamma(\gamma-1)\frac{U_0}{\Sigma_0} k_x^2 + i\Omega_0^2 \right) \omega^2 \\
&\quad + \left(-\frac{\xi(\gamma-1)U_0}{\Sigma_0 \tau_c} k_x^2 + \frac{2\pi G\Sigma_0}{\tau_c} \mathrm{sign}(k_x) k_x - \frac{\Omega_0^2}{\tau_c} \right) \omega. \qquad (10.8)
\end{aligned}$$

As can be seen in the last line, the wave vector occurs as either k_x^2 or $\mathrm{sign}(k_x)k_x$, and, hence, the system is invariant under sign reversal of k_x. Therefore, $k_x > 0$ is assumed, without loss of generality. And one may further use the background speed of sound $c_{s0}^2 = \gamma(\gamma-1)U_0/\Sigma_0$, to simplify the expression,

$$\begin{aligned}
\det(\underline{\underline{\mathbf{M}}}) &= -i\omega^4 + \frac{1}{\tau_c}\omega^3 + \left(-i2\pi G\Sigma_0 k_x + ic_{s0}^2 k_x^2 + i\Omega_0^2 \right) \omega^2 \\
&\quad + \left(-\frac{\xi c_{s0}^2}{\gamma \tau_c} k_x^2 + \frac{2\pi G\Sigma_0}{\tau_c} k_x - \frac{\Omega_0^2}{\tau_c} \right) \omega. \qquad (10.9)
\end{aligned}$$

One then sets $\det(\underline{\underline{\mathbf{M}}}) = 0$, and the resulting equation is divided by ω, thereby excluding the trivial solution $\omega = 0$, yielding

$$\begin{aligned}
i\omega^3 \tau_c - \omega^2 &= \left(-i2\pi G\Sigma_0 k_x + ic_{s0}^2 k_x^2 + i\Omega_0^2 \right) \tau_c \omega \\
&\quad - \frac{\xi c_{s0}^2}{\gamma} k_x^2 + 2\pi G\Sigma_0 k_x - \Omega_0^2. \qquad (10.10)
\end{aligned}$$

One can then introduce the Toomre parameter (see, e.g., Toomre 1964; Kratter & Lodato 2016), $Q := c_{s0}\Omega_0/(\pi G\Sigma_0)$, and, where possible, factor out $(i\tau_c\omega - 1)$, in order to obtain

$$\begin{aligned}
\omega^2 (i\tau_c\omega - 1) &= \Omega_0^2 (i\tau_c\omega - 1) - \frac{2c_{s0}\Omega_0}{Q} k_x (i\tau_c\omega - 1) \\
&\quad + i\tau_c \omega c_{s0}^2 k_x^2 - \frac{\xi c_{s0}^2}{\gamma} k_x^2 \\
\Rightarrow \quad \omega^2 &= \Omega_0^2 - \frac{2c_{s0}\Omega_0}{Q} k_x + \frac{\left(i\tau_c\omega - \frac{\xi}{\gamma} \right) c_{s0}^2}{i\tau_c\omega - 1} k_x^2. \qquad (10.11)
\end{aligned}$$

For convenience, the frequency ω is replaced by a growthrate, via $\omega = ig$ (see also Löhnert, Krätschmer, & Peeters 2020):

$$g^2 = -\Omega_0^2 + \frac{2c_{s0}\Omega_0}{Q}k_x - \frac{\left(\tau_c g + \frac{\xi}{\gamma}\right)c_{s0}^2}{\tau_c g + 1}k_x^2. \tag{10.12}$$

This result is equivalent to the inviscid case in Lin & Kratter (2016), whereby ξ corresponds to Θ, in their setup.

The Toomre criterion for instability, as it is usually formulated ($Q < 1$, see, e.g., Toomre 1964; Binney & Tremaine 2008; Kratter & Lodato 2016), is obtained, by considering the case of very inefficient cooling, that is, $\tau_c \to \infty$. Eq. 10.12, then becomes:

$$g^2 = -\Omega_0^2 + \frac{2c_{s0}\Omega_0}{Q}k_x - c_{s,0}^2 k_x^2. \tag{10.13}$$

This form of the dispersion relation is convenient, because the left hand side only contains the squared growthrate g^2. Hence, one obtains growing modes only for a positive right hand side. Otherwise, the growthrate is either zero, or imaginary (oscillations). The right hand side is a downward-opened parabola in k_x. Hence, if the parabola has no real roots ($g^2 = 0$), one will always find $g^2 < 0$, and the system is stable. As it turns out, the parabola has no real roots for $Q > 1$, and thus, instability can only occur for $Q < 1$, which corresponds to the aforementioned Toomre criterion, for gravitational instability (see, e.g., Toomre 1964; Binney & Tremaine 2008; Kratter & Lodato 2016).

Stability criteria can also be obtained for a finite cooling time, τ_c. Complications arise, because the right hand side contains g, then. But also for the full form of Eq. 10.12, the left hand side is g^2, and an instability will only occur if the right hand side is positive. And roots, of the right hand side, can immediately be obtained by setting $g = 0$, in Eq. 10.12. The result is a polynomial, quadratic in k_x, which has the solutions

$$k_x H_0 = \frac{\gamma}{\xi Q} \mp \sqrt{\left(\frac{\gamma}{\xi Q}\right)^2 - \frac{\gamma}{\xi}}, \tag{10.14}$$

with a constant scale height $H_0 = c_{s,0}/\Omega_0$. For $Q > \sqrt{\gamma/\xi}$, the wave vector, k_x, becomes a complex number, implying that $g = 0$ is not possible, for real-valued k_x. Put differently, the solution, $g(k_x)$, of Eq. 10.12, does not cross zero for $Q > \sqrt{\gamma/\xi}$. Hence, we now know the critical value, $Q_c = \sqrt{\gamma/\xi}$, for marginal stability. Whether $Q > \sqrt{\gamma/\xi}$ corresponds to stability, or instability, is not yet determined. For this, one can evaluate Eq. 10.12, at $k_x = 0$, yielding $g^2 = -\Omega_0^2 < 0$. Note that this does not depend on the choice of Q, and, hence, is also valid for $Q > \sqrt{\gamma/\xi}$. In the latter case, $g(k_x)$ does not cross zero, and $g^2(0) < 0$ then requires that $g^2(k_x) < 0$, for all k_x. Hence, one concludes

$$\begin{aligned} Q &< \sqrt{\gamma/\xi} \quad \Rightarrow \quad \text{unstable} \\ Q &> \sqrt{\gamma/\xi} \quad \Rightarrow \quad \text{stable} \end{aligned} \tag{10.15}$$

Since $\gamma = c_P/c_V > 1$ (c_P, and c_V are the specific heats, see, e.g., Regev, Umurhan, & Yecko 2016), and $\xi \in [0, 1]$, one always finds $\sqrt{\gamma/\xi} > 1$. Hence, the cooling models, applied here, destabilise the system against self-gravity. The criterion for instability can be written in the form $Q < Q_c$, whereby $Q_c \geq 1$. Hence, states that will be linearly stable without cooling, can be unstable with cooling. For the special case of $\zeta = 1$ (constant target temperature, $c_{s,0}$, see also Eq. 4.45), this yields $Q < \sqrt{\gamma}$ as a criterion for instability. Assuming the case $\zeta = 0$ (constant, target thermal

energy density, U_0, see also Eq. 4.46), the system is unstable for all values of Q, as $\sqrt{\gamma/\xi} \to \infty$. However, in the latter case, the growthrates for $Q \gg 1$ can be very low (see also the discussion below).

Now assume that the small perturbations, δf, are a mixture of different Fourier modes. As the above instability is linear, all unstable modes can start to grow exponentially, with their respective growthrate $g(k_x)$. This implies that the fastest growing mode will eventually dominate. Hence, one would wish to determine the fastest growing mode, analytically. In order to achieve this, one can use the special form of Eq. 10.12,

$$g^2 = f(k_x, g(k_x)), \tag{10.16}$$

whereby the right-hand side is interpreted as a function of both k_x, and g, with $g(k_x)$ being a function of k_x itself. The objective is then to find the maximum of $g(k_x)$. Hence, we demand

$$\frac{dg}{dk_x} = 0. \tag{10.17}$$

One can then take the total derivative of Eq. 10.16, towards k_x, yielding

$$\begin{aligned} 2g\frac{dg}{dk_x} &= \frac{\partial f}{\partial k_x} + \frac{dg}{dk_x}\frac{\partial f}{\partial g} \\ \Rightarrow \left(2g - \frac{\partial f}{\partial g}\right)\frac{dg}{dk_x} &= \frac{\partial f}{\partial k_x}. \end{aligned} \tag{10.18}$$

It is then assumed that $(2g - \partial_g f) \neq 0$, up to a zero set of k_x values. That leads to the equivalence

$$\frac{dg}{dk_x} = 0 \Leftrightarrow \frac{\partial f}{\partial k_x} = 0. \tag{10.19}$$

Lin & Kratter (2016) use a similar technique to obtain their fastest growing modes. Reading of $f(k_x, g)$ form Eq. 10.12, it is found that

$$\frac{\partial f}{\partial k_x} = \frac{2c_{\mathrm{s},0}\Omega_0}{Q_0} - \frac{2c_{\mathrm{s},0}^2(g\tau_c + \frac{\xi}{\gamma})}{1 + g\tau_c}k_x. \tag{10.20}$$

Hence, one obtains

$$\frac{\partial f}{\partial k_x} = 0 \quad \Rightarrow \quad \hat{k}_x = \frac{\Omega_0}{c_{\mathrm{s},0}}\frac{\tau_c g + 1}{\left(\tau_c g + \frac{\xi}{\gamma}\right)Q}. \tag{10.21}$$

The value $\hat{k}_x$ corresponds to the Fourier mode where $g(\hat{k}_x)$ is extremal, here, the fastest growing mode. The growthrate $g(\hat{k}_x)$ is obtained by substituting the expression for $\hat{k}_x$ back into Eq. 10.12, which gives (see also Löhnert, Krätschmer, & Peeters (2020))

$$\frac{g^3}{\Omega_0^3} = \left(\frac{1}{Q^2} - 1\right)\frac{g}{\Omega_0} - \frac{\xi}{\gamma(\tau_c\Omega_0)}\frac{g^2}{\Omega_0^2} + \frac{1}{(\tau_c\Omega_0)}\left(\frac{1}{Q^2} - \frac{\xi}{\gamma}\right). \tag{10.22}$$

The latter is a cubic polynomial in g, which may be solved numerically, or by applying further simplifying assumptions. The simplest case is that of very inefficient cooling, that is, $\tau_c\Omega_0 \to \infty$. The second, and the third term, on the right-hand side, then vanish, yielding

$$\frac{g}{\Omega_0} = \sqrt{\frac{1}{Q^2} - 1}. \tag{10.23}$$

From that one can also read off the criterion for instability, $Q < 1$, as there exist no real-valued g, for $Q > 1$. Put differently, the maximum growthrate corresponds to the vertex of the downward-opened parabola, given in Eq. 10.13. For $Q > 1$, the parabola has no real roots.

Another special case is obtained for the cooling law $\xi = 0$ (target thermal energy density). In Eq. 10.22, all terms proportional to ξ drop out, simplifying the equation considerably. As mentioned previously, the system is then unstable for all values of Q, but for larger values of Q, the growthrate can become very low. This is most easily seen by assuming $g/\Omega_0 \ll 1$ from the start, and neglecting all terms higher than linear in g/Ω_0, in Eq. 10.22. This directly leads to

$$\frac{g}{\Omega_0} = \frac{1}{\tau_c \Omega_0} \frac{1}{Q^2 - 1}, \tag{10.24}$$

whereby the latter expression is also used in Löhnert, Krätschmer, & Peeters (2020). As this assumes small values of g/Ω_0, this also implies that the values for Q must be much larger than one.

10.2 Fourier transform of a shock

In Löhnert, Krätschmer, & Peeters (2020) (see Sect. 7), the Fourier-power spectrum for a typical, hydrodynamical shock geometry is analysed. The goal here is to provide a detailed, analytical derivation, for the Fourier series of a typical shock profile. A shock usually manifests as a discontinuity in, for example, the velocity (see, e.g., Regev, Umurhan, & Yecko 2016). More precisely, in Löhnert, Krätschmer, & Peeters (2020), especially the radial velocity component, v_x, is considered. It is found, in Löhnert, Krätschmer, & Peeters (2020), that the velocity profiles, $v_x(x)$, often exhibit patters that may best be described by an antisymmetric velocity jump. The typical geometry of such a velocity jump is here described by the generic function $\Psi^\mu_\lambda(x)$, with width λ, and height μ:

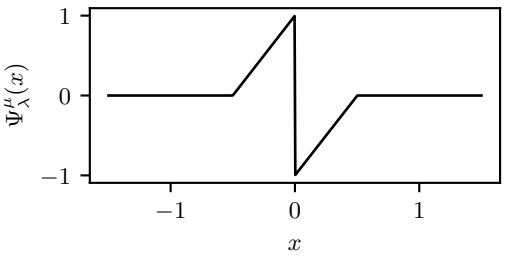

Figure 10.1: Demonstration of a typical shock geometry. Shown is a shock $\Psi^\mu_\lambda(x)$, according to Eq. 10.25, with $\mu = \lambda = 1$.

$$\Psi^\mu_\lambda(x) = \begin{cases} \frac{2\mu}{\lambda}(x + \frac{\lambda}{2}) & -\lambda/2 \leq x \leq 0 \\ \frac{2\mu}{\lambda}(x - \frac{\lambda}{2}) & 0 < x \leq \lambda/2 \\ 0 & \text{else} \end{cases} . \tag{10.25}$$

Note that the total shock height, from bottom to top, is 2μ. An example profile is shown in Fig. 10.1, for $\lambda = \mu = 1$. Lets then assume that the shock is placed in a one dimensional periodic

box, of size L. One can then calculate the Fourier series of $\Psi^\mu_\lambda(x)$, yielding

$$\begin{aligned}
\Psi^\mu_\lambda(k) &:= \frac{1}{L}\int_{-L/2}^{L/2}\Psi^\mu_\lambda(x)\,e^{-ik\,x} \\
&= \frac{1}{L}\left(\int_{-\lambda/2}^{0}\frac{2\mu}{\lambda}(x+\frac{\lambda}{2})e^{-ik\,x}\,dx+\int_{0}^{\lambda/2}\frac{2\mu}{\lambda}(x-\frac{\lambda}{2})e^{-ik\,x}\,dx\right) \\
&= \frac{1}{L}\left[-\frac{2\mu}{ik\lambda}(x+\frac{\lambda}{2})\,e^{-ik\,x}\right]_{-\lambda/2}^{0}+\frac{1}{L}\int_{-\lambda/2}^{0}\frac{2\mu}{ik\lambda}\,e^{-ik\,x}\,dx \\
&\quad +\frac{1}{L}\left[-\frac{2\mu}{ik\lambda}(x-\frac{\lambda}{2})\,e^{-ik\,x}\right]_{0}^{\lambda/2}+\frac{1}{L}\int_{0}^{\lambda/2}\frac{2\mu}{ik\lambda}\,e^{-ik\,x}\,dx \\
&= \frac{i}{L}\frac{\mu}{k}+\frac{2\mu}{\lambda k^2 L}(1-e^{ik\lambda/2})+\frac{i}{L}\frac{\mu}{k}+\frac{2\mu}{\lambda k^2 L}(e^{-ik\lambda/2}-1) \\
&= \frac{2i\mu}{Lk}+\frac{2\mu}{\lambda k^2 L}(e^{-ik\lambda/2}-e^{ik\lambda/2})=\frac{2i\mu}{Lk}-\frac{4i\mu}{\lambda k^2 L}\,\sin\left(\frac{k\lambda}{2}\right) \\
&= i\frac{4\mu}{\lambda L}\frac{1}{k}\left(\frac{\lambda}{2}-\frac{\sin(k\lambda/2)}{k}\right).
\end{aligned} \tag{10.26}$$

As expected, the Fourier coefficients are purely imaginary, as the original function $\Psi^\mu_\lambda(x)$ is real-valued, and antisymmetric with respect to $x=0$. If the shock were placed at an arbitrary position x_0 (then, $\Psi^\mu_\lambda(x-x_0)$), within the box, one would find an additional phase factor $e^{-ik\,x_0}$:

$$\Psi^\mu_\lambda(k)=i\frac{4\mu}{\lambda L}e^{-ik\,x_0}\frac{1}{k}\left(\frac{\lambda}{2}-\frac{\sin(k\lambda/2)}{k}\right). \tag{10.27}$$

The discussion in Löhnert, Krätschmer, & Peeters (2020) is mostly concerned with the power spectrum, that is, the absolute value of the Fourier coefficients, squared. Hence, additional phase factors are of no concern, and one obtains:

$$\mathcal{E}_k^{shock} = |\Psi^\mu_\lambda(k)|^2=\frac{16\mu^2}{\lambda^2 L^2}\left(\frac{\sin^2(k\lambda/2)}{k^2}+\frac{\lambda^2}{4}-\frac{\lambda\,\sin(k\lambda/2)}{k}\right)k^{-2}. \tag{10.28}$$

Especially important is the k^{-2}-scaling. This power spectrum is depicted in Fig. 10.2, for the original shock profile ($\mu=\lambda=1$, $L=3$), in Fig. 10.1. For reference, a k^{-2}-scaling law is shown, as the red-dashed line.

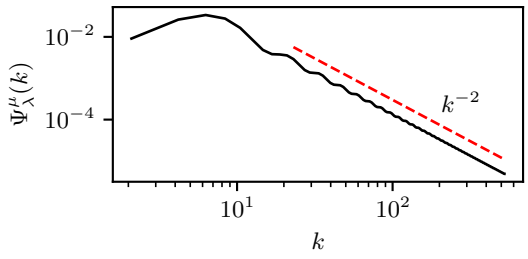

Figure 10.2: Fourier transform $\Psi^\mu_\lambda(k)=\mathcal{FT}\left(\Psi^\mu_\lambda(x)\right)$, shown for $\mu=\lambda=1$, and $L=3$. Shown as the red-solid line, is the k^{-2} scaling.

10.3 Testing the Poisson solver

The goal of this section is to provide tests of the Athena-Poisson solver, detailed in Sect. 4.6.4, by providing estimates for the solver accuracy. This is demonstrated for three different simulations, taken from Löhnert & Peeters (2022), and Sect. 9 (LP23). The Poisson solver determines a Potential, Φ, such that the Poisson equation, $\nabla^2\Phi = 4\pi G\rho$, is satisfied, for a given mass density, ρ. Hence, one way of testing the solver is to calculate $\nabla^2\Phi/(4\pi G)$, for a given time point, and to compare the result to the actual mass density, ρ, at that time point. Athena provides a fully three-dimensional data output, for a user-selected sampling rate, containing all relevant fluid variables. This three-dimensional data set can be used to calculate $\nabla^2\Phi/(4\pi G)$, explicitly, using second-order, central differences. Say $\Phi_{k,j,i}$ is the potential, at the grid location (x_k, x_j, x_i), then the Laplace operator is evaluated as follows

$$\begin{aligned}\left[\nabla^2\Phi\right]_{k,j,i} &= \frac{\Phi_{k,j,i+1} - 2\Phi_{k,j,i} + \Phi_{k,j,i-1}}{\delta x^2} + \frac{\Phi_{k,j+1,i} - 2\Phi_{k,j,i} + \Phi_{k,j-1,i}}{\delta y^2} \\ &\quad + \frac{\Phi_{k+1,j,i} - 2\Phi_{k,j,i} + \Phi_{k-1,j,i}}{\delta z^2}. \end{aligned} \tag{10.29}$$

For a simulation domain, $L_x \times L_y \times L_z$, with $N_x \times N_y \times N_z$ grid points, the discretisation lengths are defined as $\delta_x = L_x/N_x$, $\delta_y = L_y/N_y$, and $\delta_z = L_z/N_z$, respectively. With this procedure, one obtains two, three-dimensional arrays (for ρ, and $\nabla^2\Phi/(4\pi G)$), with values for each grid location. The latter can then be compared to estimate the accuracy of the Poisson solver.

Table 10.1: Simulation settings, and parameters, for sg-mhd-2 (Löhnert & Peeters 2022), sg-mhd-tau20-Lz6 (LP23, see Sect. 9), and gi-mri-res-2 (LP23). The physical box sizes are given by (L_x, L_y, L_z), in scale heights, whereby $c_s = 1$ is used for the scale height. The domain is discretised by $N_x \times N_y \times N_z$ grid points. CFL is the Courant-Friedrichs-Lewy number (see, e.g., Toro 2009). The value γ is the adiabatic index. The cooling time (see also Sect. 4.6.3), is given in the dimensionless form $\tau_c\Omega_0$. Whether additional, background heating, second term in Eq. 4.54, is used, is marked in the "heating"-row. For completeness, the volume-averaged mass density, $\langle\rho\rangle$, is also provided. In sg-mhd-2, mass was allowed to leave the box, hence, the mass density can change over time (see also Löhnert & Peeters 2022; Löhnert & Peeters 2023). For reasons of numerical stability, minima in both density and pressure were applied, and the corresponding values are given by $\rho_{\min}$, and $P_{\min}$, respectively.

	sg-mhd-2	sg-mhd-tau20-Lz6	gi-mri-res-2
L_x, L_y, L_z, in H	20, 20, 8	20, 20, 8	20, 20, 7
N_x, N_y, N_z	440, 440, 170	500, 500, 150	800, 800, 280
CFL	0.06	0.3	0.5
γ	1.64	1.64	1.64
$\tau_c\Omega_0$	10	20	10
heating	yes ($c_{s,0} = 1$)	no	yes ($c_{s,0} = 1$)
$\langle\rho\rangle$	0.053 - 0.0717	0.053	0.0635
$\rho_{\min}$, $P_{\min}$	10^{-4}, $6.1 \cdot 10^{-5}$	$3.2 \cdot 10^{-5}$, $2 \cdot 10^{-5}$	$6 \cdot 10^{-5}$, $3.7 \cdot 10^{-5}$

sg-mhd-2:

The first simulation, that this method is applied to, is sg-mhd-2, of Löhnert & Peeters (2022). Important simulation settings are also provided in Table 10.1. It is convenient to briefly summarise the simulation setup of sg-mhd-2. The initial state is in vertical, hydrostatic equilibrium, see the discussion of stratification in Sect. 4.6.2, and both density and pressure are horizontally homogeneous. Added are small, random density perturbations, with an amplitude of 1% of the background density. Initially, the adiabatic index is set to $\gamma = 1.8$. That is required, because the transition from the

linear-growth phase, to the nonlinar state can be rather violent, leading to numerical instabilities, or clumping. It was found that a larger adiabatic index can help to avoid this. At $t\Omega_0 = 80$, the transition has occurred, and the adiabatic index is set to the more realistic value of $\gamma = 1.64$. This state is then prolonged until $t\Omega_0 = 120$, at which point a magnetic-seed field, of zero-net-flux type is introduced, $\mathbf{B}_0 = B_0 \sin(2\pi x/L_x)\,\hat{\mathbf{e}}_y$ (see also Löhnert & Peeters 2022). The field strength is chosen such that $B_0 = 10^{-5}$, which corresponds to a plasma-β of $\beta_0 = \sqrt{2\mu_0 P(z=0)/B_0} \sim 10^{-10}$, at the mid plane ($\mu_0 = 1$ in code units). Shown in the first image of Fig. 10.3 are the volume-averaged energy densities, $E_{\rm kin} = \langle \rho \mathbf{v}^2/2 \rangle$, $E_{\rm th}$, $E_{\rm mag} = \langle \mathbf{B}^2/(2\mu_0) \rangle$, and $E_{\rm grav} = \langle \rho\Phi \rangle$. The volume-average, of a quantity f, is defined as follows:

$$\langle f \rangle = \frac{1}{L_x L_y L_z} \int f \,\mathrm{d}x\mathrm{d}y\mathrm{d}z = \frac{1}{N_x N_y N_z} \sum_{k,j,i=0}^{N_z,N_y,N_z} f_{k,j,i}. \tag{10.30}$$

It is noted that the thermal energy density briefly turns negative, during the linear-nonlinear transition. It is currently not clear why this happened, but a pressure floor, $P_{\rm min} < 10^{-4}$ was introduced as a response. All subsequent simulations did not develop such an artefact. Shown in the second image, are the dimensionless, turbulent stresses (see also Eq. 3.34),

$$\alpha_r = \frac{2\langle \rho v_x \delta v_y \rangle}{3\gamma \langle P \rangle}, \quad \alpha_g = \frac{2\langle G_{xy} \rangle}{3\gamma \langle P \rangle}, \quad \text{and} \quad \alpha_m = \frac{2\langle -B_x B_y/\mu_0 \rangle}{3\gamma \langle P \rangle}, \tag{10.31}$$

as a function of time. The xy component of the gravitational-stress tensor, $G_{xy} = \partial_x\Phi\partial_y\Phi/(4\pi G)$, is calculated from the potential, using central differences, during the simulation runtime. The main goal is to test the Poisson solver. Hence, the fully three-dimensional output data, here sampled every $10\Omega_0^{-1}$, is used to calculate the following, relative deviation:

$$\delta_{\rm rel} = \frac{\langle |\frac{\nabla^2\Phi}{4\pi G} - \rho| \rangle}{\langle \rho \rangle}. \tag{10.32}$$

Thereby, the Laplace operator is evaluated, using Eq. 10.29. The mass density, ρ, can directly be read off from the fully three-dimensional output data. The time evolution of $\delta_{\rm rel}$ is shown, in percent, in the third image of Fig. 10.3. The relative error saturates at $\delta_{\rm rel} \sim 0.4\%$. It is pointed out that $\nabla^2\Phi$ was retroactively calculated, using second-order central differences, see Eq. 10.29. Hence, this differencing technique may also contribute to the observed error. In summary, this demonstrates that the Poisson equation is solved, with acceptable accuracy. This is also demonstrated visually, in Fig. 10.4, depicting xy ($z = 0$), xz ($y = 0$), and yz ($x = 0$) slices. The images on the left show the actual mass density, ρ, and the images on the right depict $\nabla^2\Phi/(4\pi G)$, calculated via Eq. 10.29. Fig. 10.4 provides a qualitative demonstration that the Poisson equation is adequately satisfied.

sg-mhd-tau20-Lz6:

The same diagnostic is also evaluated for simulation sg-mhd-tau20-Lz6, of Löhnert & Peeters (2023). Important simulation parameters are listed in Table 10.1. In contrast to sg-mhd-2, sg-mhd-tau20-Lz6 does not include additional heating (no second term in Eq. 4.6.3), and the cooling time has doubled, from $\tau_c\Omega_0 = 10$, to $\tau_c\Omega_0 = 20$. Similar to sg-mhd-2, the simulation starts with a vertical density, and pressure stratification, homogeneous in directions x, and y. Small, random density perturbations, (1% of the background value) are added, as a seed for GI. It has turned out that, for $\tau_c\Omega_0 = 20$, the adiabatic index can be set to $\gamma = 1.64$, from the start, as the linear-nonlinear transition is less disruptive (see also Löhnert & Peeters 2022). The volume-averaged energy densities, dimensionless turbulent stresses, and the relative deviation, $\delta_{\rm rel}$, are shown in Fig. 10.5. In sg-mhd-tau20-Lz6, the magnetic-seed field ($\beta_0 = 10^7$) was introduced at $t\Omega_0 = 200$, highlighted by the vertical-dashed line (see also Löhnert & Peeters 2022). From the last image, one can read off that $\delta_{\rm rel} \sim 0.4\%$. Hence, the Poisson equation is satisfied, within an acceptable error range. This error range is also identical

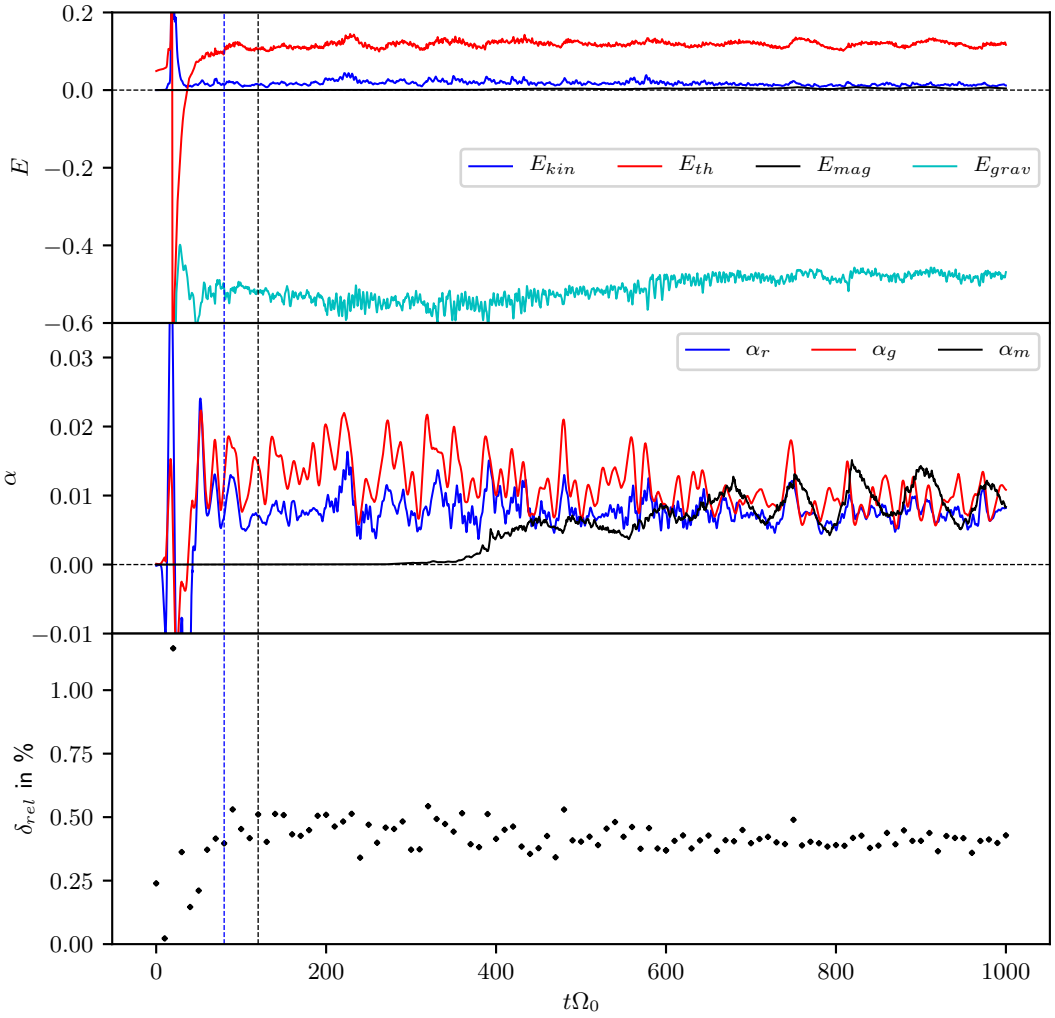

Figure 10.3: Shown are the time evolutions, for a selection of quantities, evaluated for simulation sg-mhd-2, (see Löhnert & Peeters 2022). **First image:** Volume-averaged energy densities, E_{kin}, E_{th}, E_{mag}, and E_{grav}. **Second image:** Dimensionless, turbulent stress contributions, α_r (blue), α_g (red), and α_m (black). **Third image:** Relative density error, δ_{rel} (see Eq. 10.32), in percent. The blue, vertical-dashed line ($t\Omega_0 = 80$) represents the time point at which the adiabatic index is switched from $\gamma = 1.8$ to $\gamma = 1.64$. At $t\Omega_0 = 120$ (black, vertical-dashed line) the magnetic-seed field is introduced.

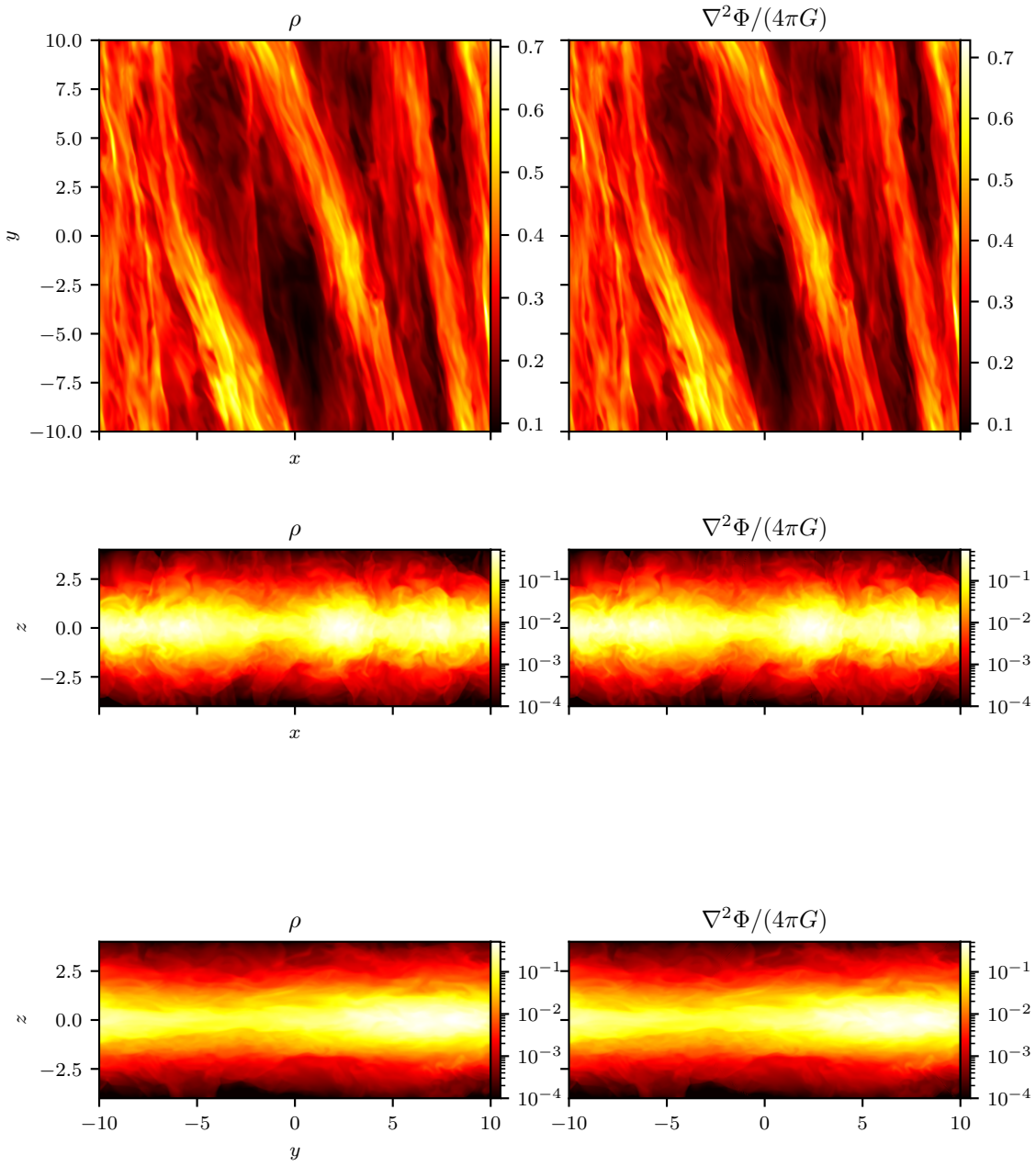

Figure 10.4: Mass density, evaluated for simulation sg-mhd-2, of Löhnert & Peeters (2022), at $t\Omega_0 = 650$. Images on the left-hand side depict the actual mass density, ρ, whereas the images on the right-hand side were determined indirectly, via $\nabla^2\Phi/(4\pi G)$, using Eq. 10.29. From top to bottom, the images depict xy ($z = 0$), xz ($y = 0$), and yz ($x = 0$) slices. For the xz, and yz images, the base-ten logarithm is shown, for reasons of visibility.

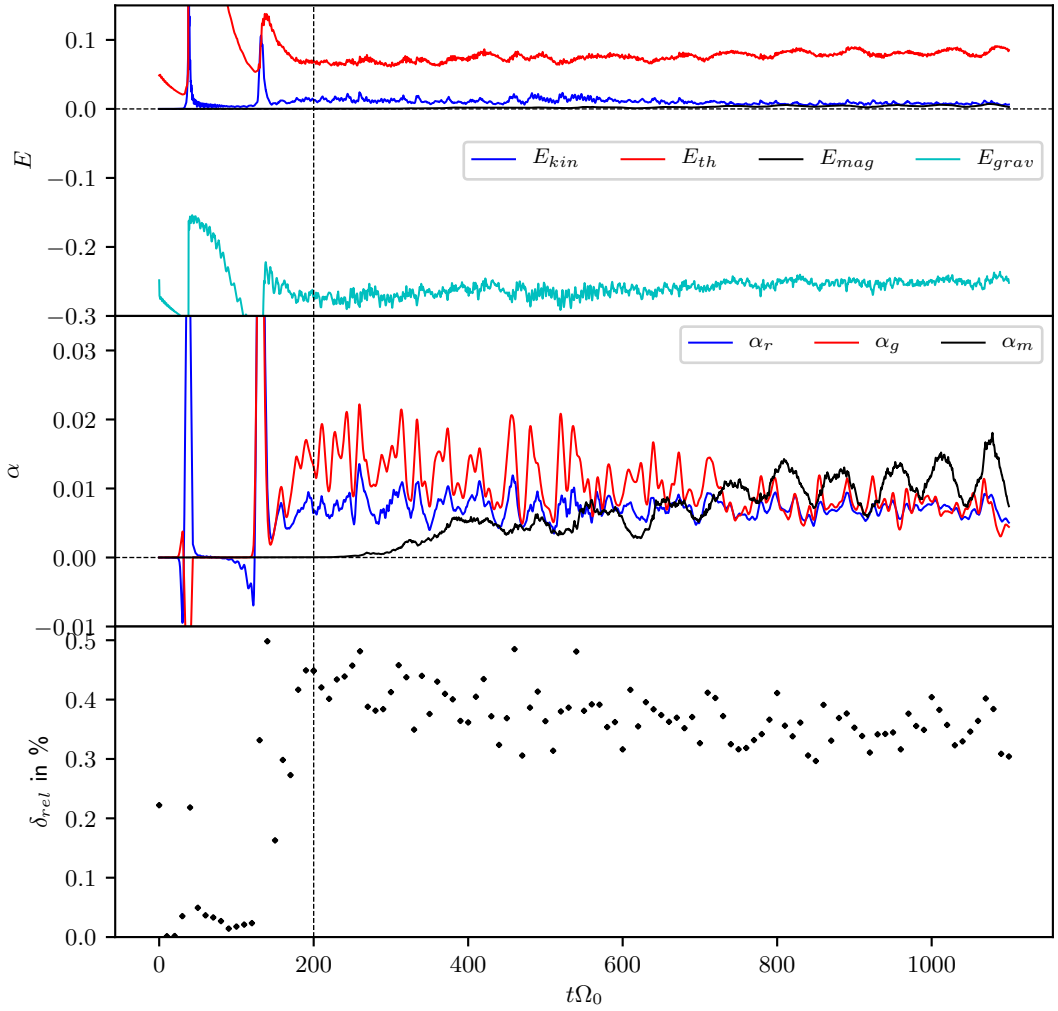

Figure 10.5: Shown are the time evolutions, for a selection of quantities, evaluated for simulation sg-mhd-tau20-Lz6 (see Löhnert & Peeters 2023). **First image:** Volume-averaged energy densities, E_{kin}, E_{th}, E_{mag}, and E_{grav}. **Second image:** Dimensionless, turbulent stress contributions, α_r (blue), α_g (red), and α_m (black). **Third image:** Relative density error, δ_{rel} (see Eq. 10.32), in percent. The magnetic-seed field is introduced at $t\Omega_0 = 200$ (vertical-dashed line).

to that, obtained for sg-mhd-2.

gi-mri-res-2:
Finally, the accuracy is also evaluated for simulation gi-mri-res-2, of Löhnert & Peeters (2023). This simulation uses twice the resolution of the previous two simulations, see also Table 10.1. The setup of gi-mri-res-1 is equivalent to that of sg-mhd-2, including the additional background heating (see also Löhnert & Peeters 2023). The magnetic-seed field is introduced at $t\Omega_0 = 100$, with $\beta_0 = 10^7$. Also here, the energy densities, and the turbulent stresses, are shown in the first and second images, of Fig. 10.6, respectively. The estimated, relative error of the Poisson solver is shown in the third image. As one can see, the error saturates at $\delta_{\rm rel} \sim 0.2\%$, for gi-mri-res-2. This is twice lower than for the previous two cases, sg-mhd-2, and sg-mhd-tau20-Lz6, which is not unexpected, since the resolution is also twice larger in this case. Shown in Fig. 10.7 are density slices, which are compared to slices, determined via $\nabla^2\Phi/(4\pi G)$.

One can conclude that the Poisson solver operates within an acceptable error range. It is noted that $\delta_{\rm rel}$ is only used as an estimate for the accuracy. The calculation, using central differences, introduces an error as well, and $\delta_{\rm rel}$ may only be considered as an upper limit.

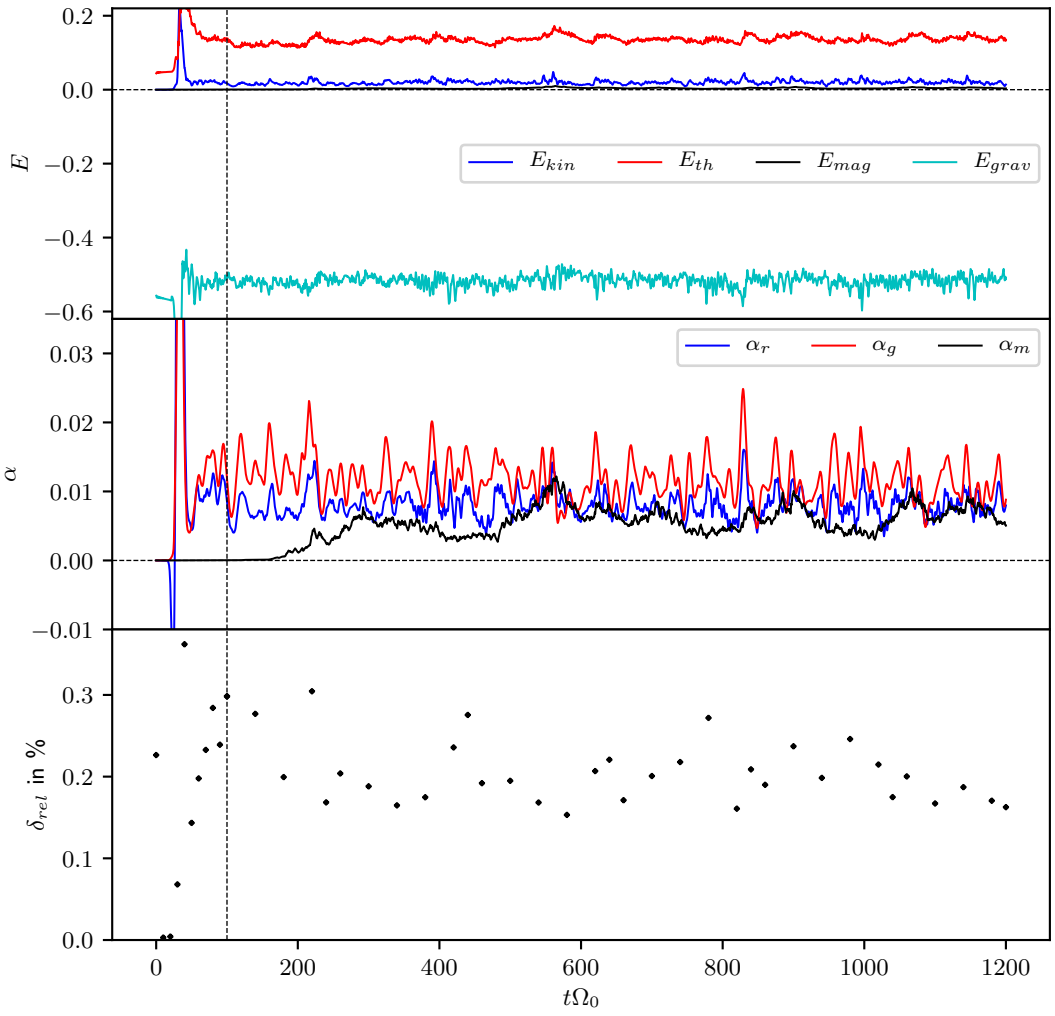

Figure 10.6: Shown are the time evolutions, for a selection of quantities, evaluated for simulation gi-mri-res-2 (see Löhnert & Peeters 2023). **First image:** Volume-averaged energy densities, E_{kin}, E_{th}, E_{mag}, and E_{grav}. **Second image:** Dimensionless, turbulent stress contributions, α_r (blue), α_g (red), and α_m (black). **Third image:** Relative density error, δ_{rel} (see Eq. 10.32), in percent. At $t\Omega_0 = 100$ (vertical-dashed line), the magnetic-seed field is introduced.

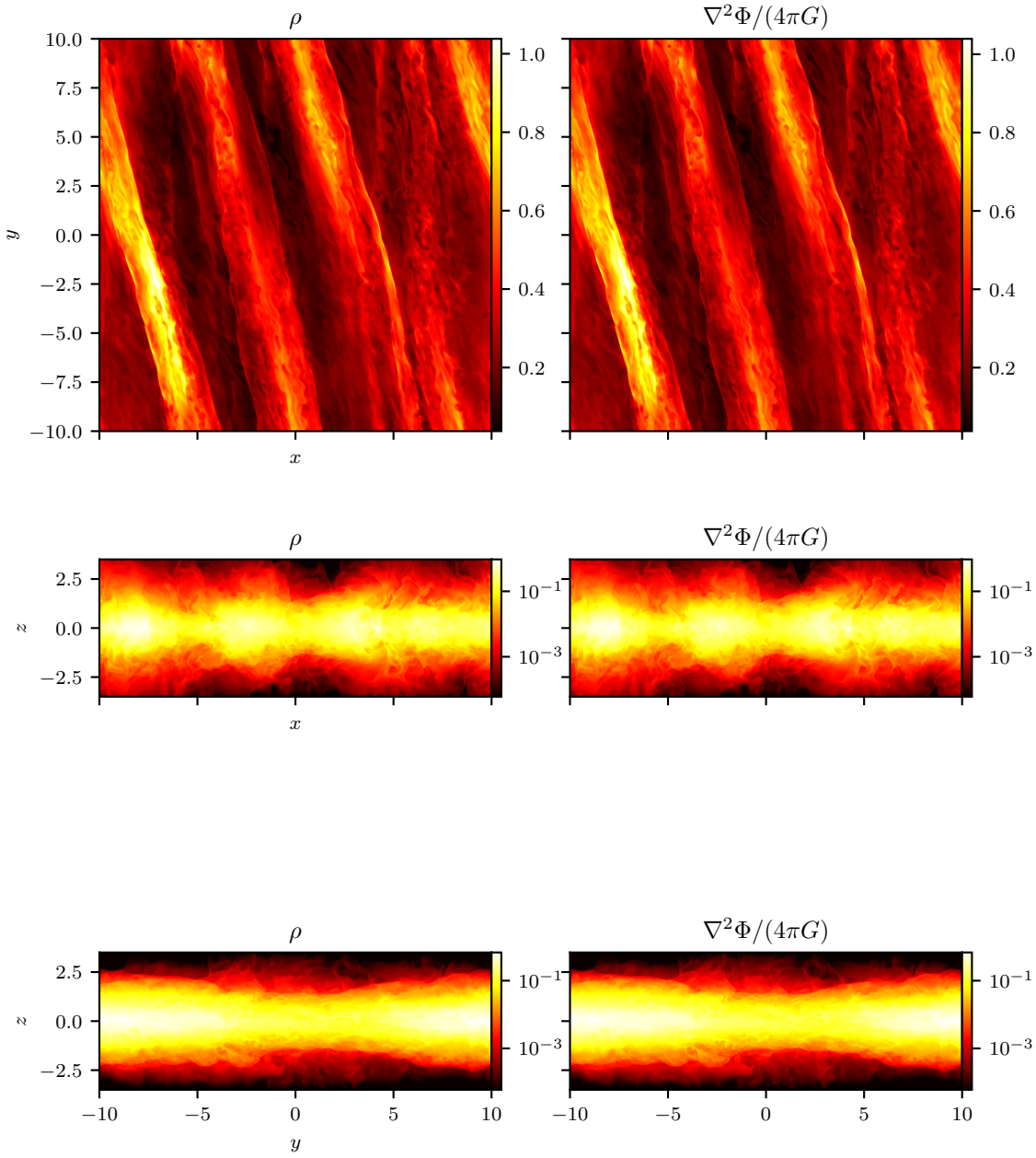

Figure 10.7: Mass density, evaluated for simulation gi-mri-res-2, of Löhnert & Peeters (2023) (see Sect. 9), at $t\Omega_0 = 100$. Images on the left-hand side depict the actual mass density, ρ, whereas the images on the right-hand side were determined indirectly, via $\nabla^2\Phi/(4\pi G)$, using Eq. 10.29. From top to bottom, the images depict xy ($z = 0$), xz ($y = 0$), and yz ($x = 0$) slices. For the xz, and yz images, the base-ten logarithm is shown, for reasons of visibility.

10.4 Dynamo-oscillation frequency: A simple analytical model

In Löhnert & Peeters (2022), see Sect. 8, the dynamo properties of the ideal-MHD, GI-MRI-coexistence state are discussed. Thereby, a simple analytical model for the field oscillations is applied, and the oscillation frequency is calculated. The goal of this section is to provide a more detailed analytical derivation of this frequency.

It is convenient to first recall the induction equation, in the local shearing-box. The general induction equation, in the ideal-MHD limit is

$$\partial_t \mathbf{B} = \nabla \times (\mathbf{v} \times \mathbf{B}) \,. \tag{10.33}$$

One can then separate the background-shear flow from the turbulent fluctuations, $\mathbf{v} = -(3\Omega_0/2)\hat{\mathbf{e}}_y + \delta\mathbf{v}$, yielding (see, e.g., Löhnert & Peeters 2022, or Appendix G), for a detailed derivation)

$$\begin{aligned} \partial_t \mathbf{B} &= \frac{3\Omega_0}{2} x \partial_y \mathbf{B} - \frac{3\Omega_0}{2} B_x \hat{\mathbf{e}}_y + \nabla \times \mathcal{E} \\ \text{with} \quad & \mathcal{E} = \delta\mathbf{v} \times \mathbf{B}. \end{aligned} \tag{10.34}$$

It is noted that, in the above-defined EMF, $\mathcal{E}$, one does not discriminate between the mean (or averaged) and fluctuating fields. The first term, on the right hand side, $(3\Omega_0/2)x\partial_y\mathbf{B}$, simply represents the change of $\mathbf{B}$, due to a fixed field distribution, passing by with the shear velocity. The second term is also related to the shear (see, e.g., Vishniac & Brandenburg 1997; Brandenburg & Subramanian 2005; Kulsrud 2005; Chiuderi & Velli 2015), and represents the shearing of a radial field, B_x, into a toroidal field, B_y. The latter effect is depicted in Fig. 10.8. Finally, the third term, on the right hand side, represents the field production rate, due to the electromotive force, $\mathcal{E}$. The latter is related to the turbulent velocity fluctuations, $\delta\mathbf{v}$, that is, the deviations from the shear flow. As in Löhnert & Peeters (2022), one can then apply a horizontal average (over xy planes) to this form of the induction equation. Thereby, one takes into account the boundary conditions in the local shearing-box approximation. That is, the boundaries are periodic in the y direction, and shearing-periodic in the x direction. This immediately implies that the term $(3\Omega_0/2)x\partial_y\mathbf{B}$ drops out[1]. The remaining terms can also be simplified significantly, and one finds, for the x, and y components of the induction equation (see also Löhnert & Peeters 2022, LP23, and Appendix G),

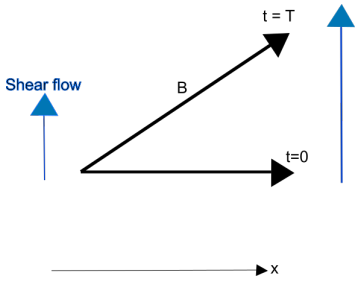

Figure 10.8: Depiction of the shear effect. An initially, purely-radial field, B_x (at $t = 0$), is sheared into a field, with both radial, and toroidal components, at a later time point ($t = T$).

$$\begin{aligned} \partial_t \langle B_x \rangle_{xy} &= -\partial_z \langle \mathcal{E}_y \rangle_{xy} \\ \partial_t \langle B_y \rangle_{xy} &= \partial_z \langle \mathcal{E}_x \rangle_{xy} - \frac{3\Omega_0}{2} \langle B_x \rangle_{xy}. \end{aligned} \tag{10.35}$$

A similar form of the induction equation was also used in Guan & Gammie (2011), Simon, Hawley, & Beckwith (2011), and Riols & Latter (2019). It is noted that $\partial_t \langle B_z \rangle_{xy} = 0$, and due to the initial, ZNF field, one finds $\langle B_z \rangle_{xy} = 0$, for all t. In the theory of mean-field electrodynamics, the averaged EMF is often expanded as follows: $\langle \mathcal{E}_j \rangle = \alpha_{jl} \langle B_l \rangle + \eta_{jkl} \partial_k \langle B_l \rangle$, whereby $\mathcal{E} = \delta\mathbf{v} \times \delta\mathbf{B}$, only considers velocity, and field perturbations (see, e.g., Biskamp 2003; Brandenburg & Subramanian 2005). The first term represents the direct feedback from the mean field, which can then lead to field growth, whereas the second term acts as a form of turbulent diffusivity. It is noted that the definition of $\mathcal{E}$, used here (see Eq. 10.35), deviates from the strict definition in mean-field electrodynamics, since

[1] $\int_{-L_x/2}^{L_x/2} dx \int_{-L_y/2}^{L_y/2} dy \, (x\partial_y \mathbf{B}) = \int_{-L_x/2}^{L_x/2} dx \, [x\mathbf{B}]_{-L_y/2}^{L_y/2} = \int_{-L_x/2}^{L_x/2} 0 \, dx = 0.$

it includes both the background field and the perturbation. Taking the average should cancel all mean-field contributions, unless there is a finite mean velocity, besides the shear flow, $\langle \delta \mathbf{v} \rangle_{xy} \neq 0$. For the simulations, shown in Löhnert & Peeters (2022), and Sect. 9 (LP23), the height-resolved mean velocity was not enabled as a diagnostic, and a more detailed test can thus not be provided. Hence, in the following discussion, the above definition $\mathcal{E} = \delta \mathbf{v} \times \mathbf{B}$ is used. In Löhnert & Peeters (2022), a simplified dynamo model is motivated, based on Eqs. 10.35. Thereby, a decomposition $\langle \mathcal{E}_j \rangle_{xy} = \alpha_{jl} \langle B_l \rangle_{xy}$ is assumed, whereby the η_{jkl} are discarded. In Löhnert & Peeters (2022), the vertical derivatives, of the EMFs, are estimated to be inversely proportional to the vertical disk-scale height, H (see also Guan & Gammie 2011). Hence, this suggests a simple model of the following form (see Löhnert & Peeters 2022):

$$\partial_t \langle B_x \rangle = \frac{\hat{\alpha}_{xx}}{H} \langle B_x \rangle + \frac{\hat{\alpha}_{xy}}{H} \langle B_y \rangle \tag{10.36}$$

$$\partial_t \langle B_y \rangle = \left(-\frac{3\Omega_0}{2} + \frac{\hat{\alpha}_{yx}}{H} \langle B_x \rangle \right) + \frac{\hat{\alpha}_{yy}}{H} \langle B_y \rangle. \tag{10.37}$$

A similar model has previously been used by Guan & Gammie (2011), and Simon, Hawley, & Beckwith (2011), in the pure-MRI context. The $\hat{\alpha}_{ji}$ should not be confused with the dimensionless, turbulent stress. They are also different from the usual dynamo-α_{ji}, as they refer to the vertical EMF derivatives, and not the EMFs themselves. It is noted that $H = 1$, in code units (see Löhnert & Peeters 2022), or least $H \sim 1$, if the turbulent fluctuations of the sound speed are considered. Hence, with $\langle \mathbf{B}_{(2)} \rangle = (\langle B_x \rangle, \langle B_y \rangle)$, the previous two equations can be represented as follows:

$$\partial_t \langle \mathbf{B}_{(2)} \rangle = \underline{\hat{\alpha}} \cdot \mathbf{B}_{(2)}, \qquad \text{with} \qquad \underline{\hat{\alpha}} = \begin{pmatrix} \hat{\alpha}_{xx} & \hat{\alpha}_{xy} \\ \hat{\alpha}_{yx} - \frac{3\Omega_0}{2} & \hat{\alpha}_{yy}. \end{pmatrix}. \tag{10.38}$$

One can then use the ansatz $\langle \mathbf{B}_{(2)} \rangle = \mathbf{A} e^{st}$, with complex exponent, $s \in \mathbb{C}$, and constant amplitude $\mathbf{A} = (A_x, A_y)$. The above differential equation then reduces to an algebraic equation,

$$s \langle \mathbf{A} \rangle = \underline{\hat{\alpha}} \cdot \mathbf{A} \qquad \Rightarrow \qquad (\underline{\hat{\alpha}} - s \underline{\mathbf{I}}) \cdot \mathbf{A} = 0, \tag{10.39}$$

with the unity matrix, $\underline{\mathbf{I}}$. Non-trivial solutions are only obtained for a vanishing determinant, $\det(\underline{\hat{\alpha}} - s\underline{\mathbf{I}}) = 0$. One can rewrite this condition as follows:

$$\begin{aligned} 0 &= \det(\underline{\hat{\alpha}} - s\underline{\mathbf{I}}) = (\hat{\alpha}_{xx} - s)(\hat{\alpha}_{yy} - s) - \hat{\alpha}_{xy} \left(\hat{\alpha}_{yx} - \frac{3\Omega_0}{2} \right) \\ &= s^2 - \underbrace{(\hat{\alpha}_{xx} + \hat{\alpha}_{yy})}_{=\mathrm{Tr}} s + \underbrace{\left(\hat{\alpha}_{xx}\hat{\alpha}_{yy} - \hat{\alpha}_{xy} \left(\hat{\alpha}_{yx} - \frac{3\Omega_0}{2} \right) \right)}_{=\mathrm{D}} \\ &= s^2 - \mathrm{Tr} s + \mathrm{D}. \end{aligned} \tag{10.40}$$

This is a quadratic equation in s, with the solutions

$$s_{1/2} = \frac{\mathrm{Tr}}{2} \pm \sqrt{\left(\frac{\mathrm{Tr}}{2} \right)^2 - \mathrm{D}}. \tag{10.41}$$

This corresponds to the result, used in Löhnert & Peeters (2022).

10.5 Electro-motive forces, additional analysis

In Sect. 9 (LP23), the electro-motive forces (EMFs) were discussed for three different simulations. The goal here is to provide further details about the EMFs, and an additional analysis. Starting

point is, as in the previous Sect. 10.4, the induction equation, in the horizontally-averaged form,

$$\begin{aligned} \partial_t \langle B_x \rangle_{xy} &= -\partial_z \langle \mathcal{E}_y \rangle_{xy} \\ \partial_t \langle B_y \rangle_{xy} &= \partial_z \langle \mathcal{E}_x \rangle_{xy} - \frac{3\Omega_0}{2} \langle B_x \rangle_{xy}, \end{aligned} \tag{10.42}$$

with $\mathcal{E} = \delta\mathbf{v} \times \mathbf{B}$. In Löhnert & Peeters (2023), the EMFs were evaluated for the shearing-box simulations sg-mhd-tau20, sg-mhd-tau10, and MRI-compare. Simulations sg-mhd-tau20, and 10 are MHD simulations of gravito-turbulence (GI). The difference between both simulations is their respective cooling-time value (see also Sect. 4.6.3). For sg-mhd-tau20, $\tau_c\Omega_0 = 20$, and for sg-mhd-tau10, $\tau_c\Omega_0 = 10$. Due to the different cooling times, the GI is roughly twice stronger in sg-mhd-tau10, compared to sg-mhd-tau20. After a stationary, GI-turbulent state has developed, a magnetic-seed field was introduced into the GI state. The seed field is of the form $\mathbf{B}_0 = B_0 \sin(2\pi x/L_x)\hat{\mathbf{e}}_z$, with L_x being the box size in the x direction (see also Löhnert & Peeters 2023). In both sg-mhd-tau20, and 10, the constant, initial field strength, B_0, is chosen such that $\langle \beta \rangle_{xy}(z = 0) = 2\mu_0 \langle P \rangle_{xy}(z = 0)/B_0^2 = 10^{-7}$. Thereby, $\langle f \rangle_{xy}$ is an average over slices of constant altitude, z. The field is of zero-net-flux (ZNF) type, that is, $\langle \mathbf{B} \rangle_{xy} = 0$, initially. MRI-compare is a simulation without self-gravity, and only MRI develops. The initial field geometry is equal to that of sg-mhd-tau20, or 10, except that here, $\langle \beta \rangle_{xy}(z = 0) = 100$ is set at the simulation start. For more simulation details, see Löhnert & Peeters (2023). The goal of this section is to provide further results, about both the magnetic field components, and especially the EMFs, that have not been published.

Shown in Figs. 10.9 - 10.11 are the quantities, $\langle B_x \rangle_{xy}$, $\langle B_y \rangle_{xy}$, $\langle \mathcal{E}_x \rangle_{xy}$, and $\langle \mathcal{E}_y \rangle_{xy}$, as a function of time and height, z, for simulations sg-mhd-tau20, sg-mhd-tau10, and MRI-compare (see Löhnert & Peeters 2023). The time axes all start at the moment of field seeding. One notices that, for the GI case, sg-mhd-tau20, and the pure-MRI case, MRI-compare, periodic field reversals emerge. Oscillations of this type are a characterising feature of MRI-induced turbulence (at least in the zero-net-flux case), often in combination with a outward vertical advection of magnetic field patterns, so-called butterfly diagrams (see, e.g., Brandenburg et al. 1995; Stone et al. 1996; Miller & Stone 2000; Shi, Krolik, & Hirose 2010; Simon, Beckwith, & Armitage 2012; Salvesen et al. 2016). Hence, it is argued, in Löhnert & Peeters (2023), that sg-mhd-tau20 is a state of GI-MRI coexistence. In sg-mhd-tau10, fluctuations also occur, but the latter are less regular, an more localised to the regions above, and below the mid plane (see Löhnert & Peeters 2023). To some extent this may be expected, as sg-mhd-tau10 is the case with the strongest GI activity, but the exact reasons for the more irregular pattern are not yet clear (see also Löhnert & Peeters 2023).

One can now use the horizontally-averaged variables to directly test Eq. 10.42. This is demonstrated in Fig. 10.12. Shown are the volume-averaged values, $\langle B_x \rangle$, $\langle B_y \rangle$, $\langle \partial_z \mathcal{E}_x \rangle$, and $\langle \partial_z \mathcal{E}_y \rangle$, for simulation sg-mhd-tau20. The volume averages were determined by starting with the horizontal averages, and subsequently averaging the latter over z, for example, $\langle \partial_z \mathcal{E}_x \rangle = \langle \partial_z \langle \mathcal{E}_x \rangle_{xy} \rangle_z$. The vertical derivative was calculated using central differences. The image demonstrates that the observed fields, and EMFs, are consistent with Eq. 10.42. That is, the net-field production rates, $-\langle \partial_z \mathcal{E}_y \rangle$ (first image), and $\langle \partial_z \mathcal{E}_x \rangle - (3\Omega_0/2)\langle B_x \rangle$ (third image, black curve), are out-of-phase, with respect to the field components (second image), by 90°. Hence, the fields grow the fastest during maxima of the field-production rates. Interestingly, from the third image, of Fig. 10.12, one can also see that the Ω-effect, $-(3\Omega_0/2)\langle B_x \rangle$ (red curve), and $\langle \partial_z \mathcal{E}_x \rangle$ (blue curve), are roughly of equal magnitude, but are phase-shifted by approximately 180°.

Then, a decomposition of the form $\langle \mathcal{E}_j \rangle = \alpha_{jl} \langle B_l \rangle$ (see, e.g., Biskamp 2003; Brandenburg & Subramanian 2005, and Sect. 10.4) is assumed. The goal is to find values for α_{ji}, such that $\hat{\mathcal{E}}_j$,

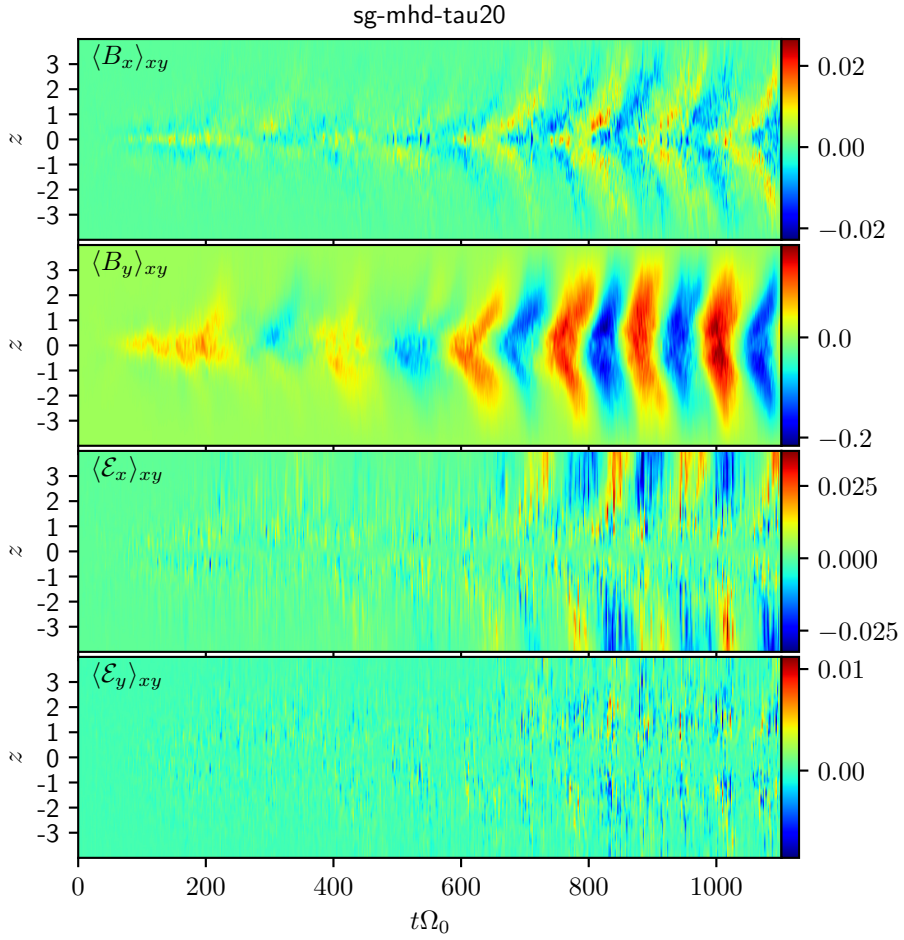

Figure 10.9: Depicted is a selection of horizontally-averaged quantities, as a function of height, z, and dimensionless time, $t\Omega_0$, for simulation sg-mhd-tau20 (see Löhnert & Peeters 2023). **First image:** Horizontally-averaged, radial field component, $\langle B_x \rangle_{xy}$. **Second image:** Horizontally-averaged, toroidal field component, $\langle B_y \rangle_{xy}$. **Third image:** Horizontally-averaged, radial EMF, $\langle \mathcal{E}_x \rangle_{xy}$. **Fourth image:** Horizontally-averaged, toroidal EMF, $\langle \mathcal{E}_y \rangle_{xy}$. In each plot, the time axis starts at the moment of field seeding.

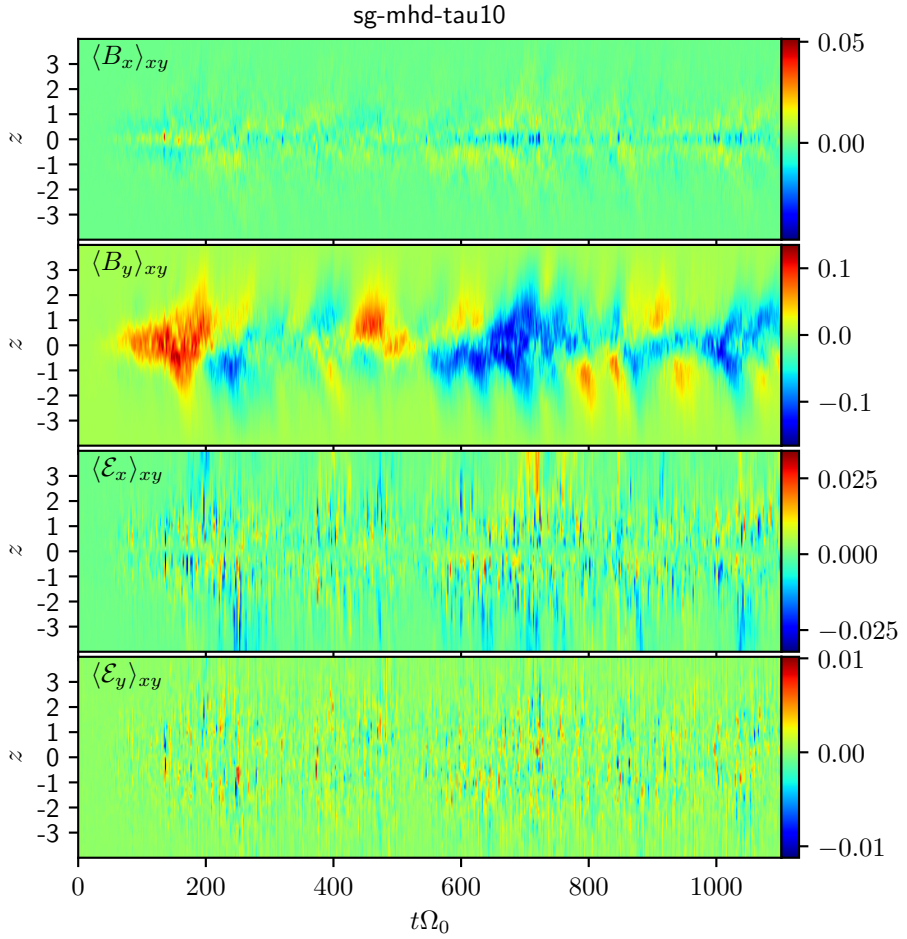

Figure 10.10: Similar to Fig. 10.9, but evaluated for simulation sg-mhd-tau10 (see Löhnert & Peeters 2023). **First image:** Horizontally-averaged, radial field component, $\langle B_x \rangle_{xy}$. **Second image:** Horizontally-averaged, toroidal field component, $\langle B_y \rangle_{xy}$. **Third image:** Horizontally-averaged, radial EMF, $\langle \mathcal{E}_x \rangle_{xy}$. **Fourth image:** Horizontally-averaged, toroidal EMF, $\langle \mathcal{E}_y \rangle_{xy}$.

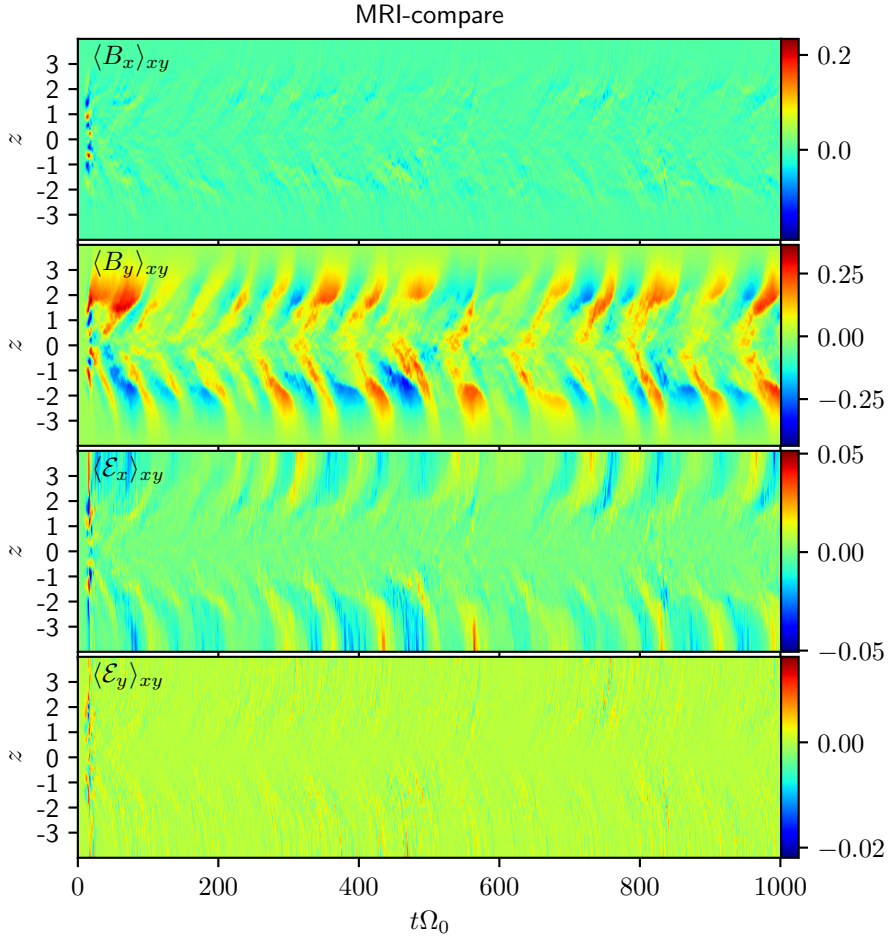

Figure 10.11: Similar to Fig. 10.9, but evaluated for simulation MRI-compare (see Löhnert & Peeters 2023). **First image:** Horizontally-averaged, radial field component, $\langle B_x \rangle_{xy}$. **Second image:** Horizontally-averaged, toroidal field component, $\langle B_y \rangle_{xy}$. **Third image:** Horizontally-averaged, radial EMF, $\langle \mathcal{E}_x \rangle_{xy}$. **Fourth image:** Horizontally-averaged, toroidal EMF, $\langle \mathcal{E}_y \rangle_{xy}$.

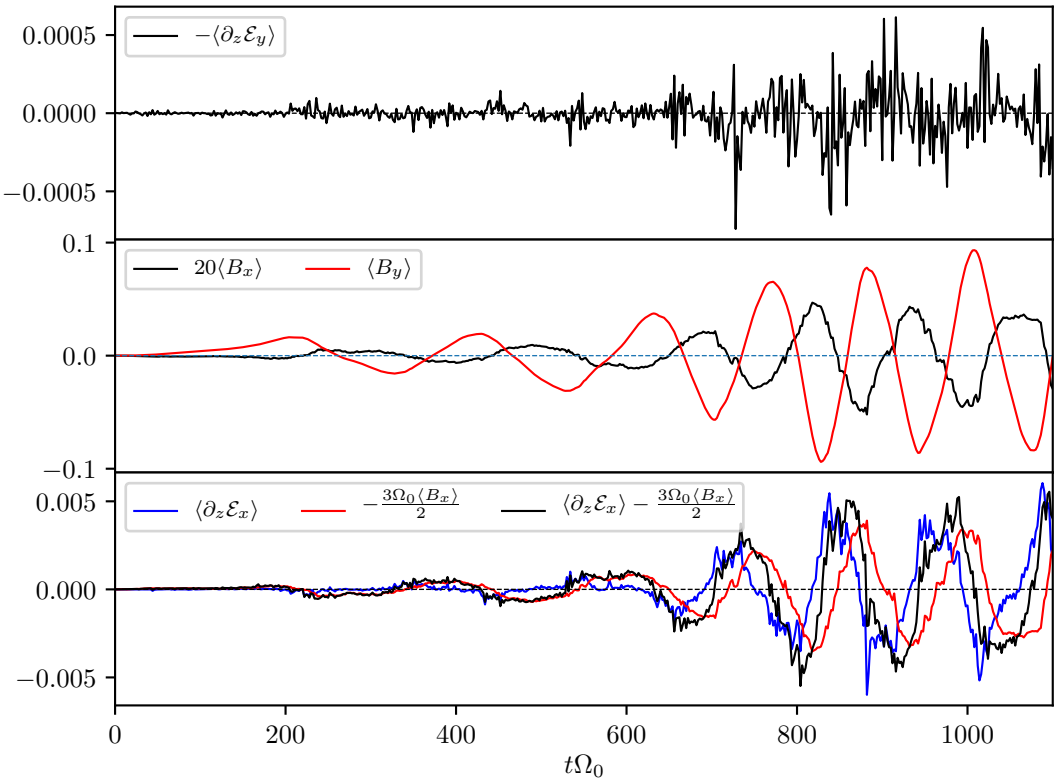

Figure 10.12: Show are the volume-averaged field components, and field-production rates, according to Eqs. 10.42, as a function of time. In all images, the time axis starts at the moment of field seeding. **First image:** Shown is the production rate of the radial magnetic field component, that is, $-\langle\partial_z\mathcal{E}_y\rangle$. **Second image:** Magnetic field components, $\langle B_x\rangle$, and $\langle B_y\rangle$, shown in black, and red, respectively. Note that the radial field component, $\langle B_x\rangle$, was multiplied by a factor of 20, for reasons of readability. **Third image:** Depicted are the individual contributions to the net production rate of $\langle B_y\rangle$. The blue curve corresponds to the EMF contribution, $\langle\partial_z\mathcal{E}_x\rangle$, and the red curve represents the shear effect, $-3\Omega_0\langle B_x\rangle/2$. Shown in black is the net of both contributions, $\langle\partial_z\mathcal{E}_x\rangle - 3\Omega_0\langle B_x\rangle/2$.

defined by

$$\langle\hat{\mathcal{E}}_x\rangle_{xy} = \alpha_{xx}\langle B_x\rangle_{xy} + \alpha_{xy}\langle B_y\rangle_{xy} \tag{10.43}$$

$$\langle\hat{\mathcal{E}}_x\rangle_{xy} = \alpha_{yx}\langle B_x\rangle_{xy} + \alpha_{yy}\langle B_y\rangle_{xy}, \tag{10.44}$$

is closest to the actually observed $\langle\mathcal{E}_j\rangle_{xy}$ values. The hat indicates that this is only a model for $\mathcal{E}$, and not the EMF itself. Horizontally-averaged quantities are generally a function of height and time, $\langle f\rangle_{xy}(t,z)$. Hence, one also has to decide what variables the α_{ji} should be allowed to depend on. If one were to allow dependencies on both space and time, $\alpha_{ji}(t,z)$, then Eqs. 10.43, and 10.44 could be fulfilled exactly. However, as a consequence, this model lacks predictive power. On the other hand, the simulation results, in Löhnert & Peeters (2023), suggest that the dynamo properties do depend on the distance from the mid plane, $|z|$. More precisely, GI-related dynamo properties are more prevalent near the mid plane, and MRI-related attributes dominate at higher altitudes. Hence, a reasonable approach is to allow a z dependence, $\alpha_{ji}(z)$. Optimal values for α_{ji} are then obtained via the method of least-squares (see, e.g., Bronstein et al. 2012). In the following, it is assumed that the EMFs, and fields, are available on vertical grid locations, z_k ($k \in \{0,1,...,N_z-1\}$), and at time points t_l ($l \in \{0,1,...,N_t-1\}$). Hence, for each z_k, the α_{ji} values have to be optimised over all t_l simultaneously. For that purpose, the N_t-dimensional, squared Euclidean distance, between the model ($\hat{\mathcal{E}}_j(t_l,z_k)$), and the data points ($\mathcal{E}_j(t_l,z_k)$), is defined as follows:

$$\begin{aligned} f_j(\alpha_{jx},\alpha_{jy},z_k) &= \sum_{l=0}^{N_t-1}\left[\langle\mathcal{E}_j\rangle_{xy}(t_l,z_k) - \langle\hat{\mathcal{E}}_j\rangle_{xy}(t_l,z_k)\right]^2 \\ &= \sum_{l=0}^{N_t-1}\left[\langle\mathcal{E}_j\rangle_{xy}(t_l,z_k) - \alpha_{jx}(z_k)\langle B_x\rangle_{xy}(t_l,z_k) - \alpha_{jy}(z_k)\langle B_y\rangle_{xy}(t_l,z_k)\right]^2, \end{aligned} \tag{10.45}$$

with $j \in \{x,y\}$. In this case, the optimal coefficients, α_{ji}, can explicitly be calculated. One first notices that, at the optimum, the gradient of f_j, with respect to the α_{ji}, vanishes:

$$\begin{aligned} 0 &= \frac{\partial f_j(\alpha_{jx},\alpha_{jy},z_k)}{\partial\alpha_{jx}} \\ &= \sum_{l=0}^{N_t-1} -2\left(\langle\mathcal{E}_j\rangle_{xy}(t_l,z_k) - \langle\hat{\mathcal{E}}_j\rangle_{xy}(t_l,z_k)\right)\langle B_x\rangle_{xy}(t_l,z_k) \end{aligned} \tag{10.46}$$

$$\begin{aligned} 0 &= \frac{\partial f_j(\alpha_{jx},\alpha_{jy},z_k)}{\partial\alpha_{jy}} \\ &= \sum_{l=0}^{N_t-1} -2\left(\langle\mathcal{E}_j\rangle_{xy}(t_l,z_k) - \langle\hat{\mathcal{E}}_j\rangle_{xy}(t_l,z_k)\right)\langle B_y\rangle_{xy}(t_l,z_k). \end{aligned} \tag{10.47}$$

The latter are two equations, for the two coefficients α_{jx} and α_{jy}. This system of equations may also be written as

$$\begin{aligned} A\,\alpha_{jx} + B\,\alpha_{jy} &= E \\ C\,\alpha_{jx} + D\,\alpha_{jy} &= F, \end{aligned} \tag{10.48}$$

whereby the upper-case factors are given by

$$A = \sum_{l=0}^{N_t-1} 2\left(\langle B_x\rangle_{xy}(t_l,z_k)\right)^2 \tag{10.49}$$

$$B = \sum_{l=0}^{N_t-1} 2\langle B_x\rangle_{xy}(t_l,z_k)\langle B_y\rangle_{xy}(t_l,z_k) \tag{10.50}$$

$$C = B \tag{10.51}$$

$$D = \sum_{l=0}^{N_t-1} 2\left(\langle B_y\rangle_{xy}(t_l,z_k)\right)^2 \tag{10.52}$$

$$E = \sum_{l=0}^{N_t-1} 2\langle \mathcal{E}_j\rangle_{xy}(t_l,z_k)\langle B_x\rangle_{xy}(t_l,z_k) \tag{10.53}$$

$$F = \sum_{l=0}^{N_t-1} 2\langle \mathcal{E}_j\rangle_{xy}(t_l,z_k)\langle B_y\rangle_{xy}(t_l,z_k). \tag{10.54}$$

Since Eq. 10.48 is a linear system of equations, the solution can explicitly be evaluated, yielding

$$\alpha_{jx}(z_k) = \frac{DE-BF}{DA-BC} \qquad \alpha_{jy}(z_k) = \frac{F}{D} - \frac{C(DE-BF)}{D(DA-BC)}. \tag{10.55}$$

Using this procedure, the α_{ji} values are calculated for the simulations sg-mhd-tau20, sg-mhd-tau10, and MRI-compare. This is shown, in Figs. 10.13, 10.14, and 10.15, respectively. Shown in the first image, of each figure, is the model prediction, $\langle\hat{\mathcal{E}}_x\rangle_{xy} = \alpha_{xx}\langle B_x\rangle_{xy} + \alpha_{xy}\langle B_y\rangle_{xy}$. The actually observed EMF, $\langle\mathcal{E}_x\rangle_{xy}$, is shown in the second image. Similarly, $\langle\hat{\mathcal{E}}_y\rangle_{xy} = \alpha_{yx}\langle B_x\rangle_{xy} + \alpha_{yy}\langle B_y\rangle_{xy}$, and $\langle\mathcal{E}_y\rangle_{xy}$, are shown in the third and fourth images, respectively. Thereby, it is again noted that the α_{ji} only depend on z.
The actual $\langle\mathcal{E}_j\rangle_{xy}$ values tend to yield a rather high noise level. This is not the case for the field components, $\langle B_j\rangle_{xy}$. Hence, the EMFs, predicted by the linear model, tend to have a reduced noise level. For reference, Fig. 10.16 depicts a comparison of $\langle\mathcal{E}_j\rangle_{xy}$ (red), and $\langle\hat{\mathcal{E}}_j\rangle_{xy}$ (blue), for two different heights, $z_k = 3.1$, and $z_k = 0.26$, as a function of time. The latter image is generated for the simulation sg-mhd-tau20. As can be seen in Figs. 10.13 - 10.16, the main EMF features, can be captured reasonably well by the model, especially for the radial component, $\langle\mathcal{E}_x\rangle_{xy}$. Finally, shown in Fig. 10.17 are the actual dynamo coefficients, α_{ji}, as a function of z. For sg-mhd-tau20, and sg-mhd-tau10, all α_{ji} profiles are qualitatively equal. For higher altitudes, the profiles are also consistent with the pure-MRI case. Near the mid plane, the α_{ji} profiles, for MRI-compare, are different from the GI profiles. More precisely, the antisymmetry, with respect to $z = 0$, can be reversed near the mid plane, see, for example, $\alpha_{yx}(z)$. This can possibly be explained by the strong GI activity near the mid plane (see also Löhnert & Peeters 2023). For $\alpha_{yy}(z)$, the profiles for the pure-MRI simulation, and both GI runs, are qualitatively similar. The α_{yy} component has been evaluated in a variety of MRI-related studies (see, e.g., Brandenburg et al. 1995; Brandenburg & Donner 1997; Ziegler & Rüdiger 2000), with the observation that $\alpha_{yy} < 0$, for $z > 0$, and $\alpha_{yy} > 0$, for $z < 0$. That is consistent with the α_{yy} values obtained here, at lest for the region $|z|< 3$. As one approaches the vertical boundaries, α_{yy} changes sign, and yields significantly larger values. However, by comparing the zt diagrams for $\mathcal{E}_y$, and $\hat{\mathcal{E}}_y$, in Figs. 10.13, and 10.14, one can see that the latter two deviate at the vertical boundaries, whereby the linear model yields values that are too large. That is possibly an artefact from the definition $\mathcal{E} = \delta\mathbf{v}\times\mathbf{B}$, used here, as the latter does not distinguish between the mean field, and the perturbed field. Technically, the average should remove additional mean-field contributions, but the velocity perturbation, $\delta\mathbf{v}$, is relative to the shear flow, and there might still be net vertical motions, $\langle\delta v_z\rangle_{xy} \neq 0$, leading to a contribution

$\langle \delta v_z \rangle_{xy} \langle B_x \rangle_{xy}$. This may be interesting to pursue in more detail, in future projects.

Since the EMFs, generated via the linear model, lack the rather high noise level, it can be interesting to compare $\langle \hat{\mathcal{E}}_x \rangle_{xy}$ for both sg-mhd-tau20 and sg-mhd-tau10. The comparison is shown in Fig. 10.18. The $\mathcal{E}_x$ component is chosen, since, as pointed out earlier, the linear model $\langle \hat{\mathcal{E}}_y \rangle_{xy}$ deviates from the actual values, $\langle \mathcal{E}_y \rangle_{xy}$, at the vertical boundaries. The first image is evaluated for sg-mhd-tau20, and the second image for sg-mhd-tau10. It is noted that the EMF values were normalised with the momentary, volume-averaged magnetic energy density, $E_{\mathrm{mag}} = \langle |\mathbf{B}|^2/(2\mu_0) \rangle$, as this allows an easier comparison of the initial, and saturated phases. One first notices that, in both simulations, the region close to the mid-plane is significantly different from higher-altitude regions (as also observed in Löhnert & Peeters 2023). For $|z| > 1$, one can see that oscillations (or at least pulsations), of the EMF, occur rather early on (see also Löhnert & Peeters 2023). In sg-mhd-tau20, the mid-plane EMF remains, at first ($t\Omega_0 < 300$), relatively constant. However, at $t\Omega_0 \sim 300$, oscillations start to appear, which gradually develop a coherent phase relation, to the field oscillations at higher altitudes. This is qualitatively different in sg-mhd-tau10. There, the oscillations at larger $|z|$, remain mostly decoupled from the mid-plane EMF. In Löhnert & Peeters (2023), it was found that both simulations differ, in the sense that GI is twice stronger in sg-mhd-tau10, compared to sg-mhd-tau20. Hence, it is not unreasonable that the qualitative appearance of the zt diagrams is different. It is possible that sg-mhd-tau10 is a qualitatively different dynamo state, possibly a pure-GI dynamo. But it is also possible that the GI-MRI coexistence, in sg-mhd-tau10, does not lead to mid-plane oscillations, because the significant GI activity, near the mid plane, is preventing that (see Löhnert & Peeters 2023). Coleman et al. (2017) demonstrated that MRI, in combination with convection, can lead to a similar behaviour. It is reasonable to assume that GI can also provide vertical mixing (see, e.g., the horizontall rolls in Riols & Latter 2018). The exact reason for the differences is not yet clear, and this may be a promising route for future investigations. It is again pointed out that, in Fig. 10.18, the model EMF, $\langle \hat{\mathcal{E}}_x \rangle_{xy}$, is shown, and not directly the EMF. But, as can be seen from Figs. 10.13, and 10.14, the model reasonably captures the time evolution of the radial EMF, and it yields a lower noise level, allowing for an easier comparison.

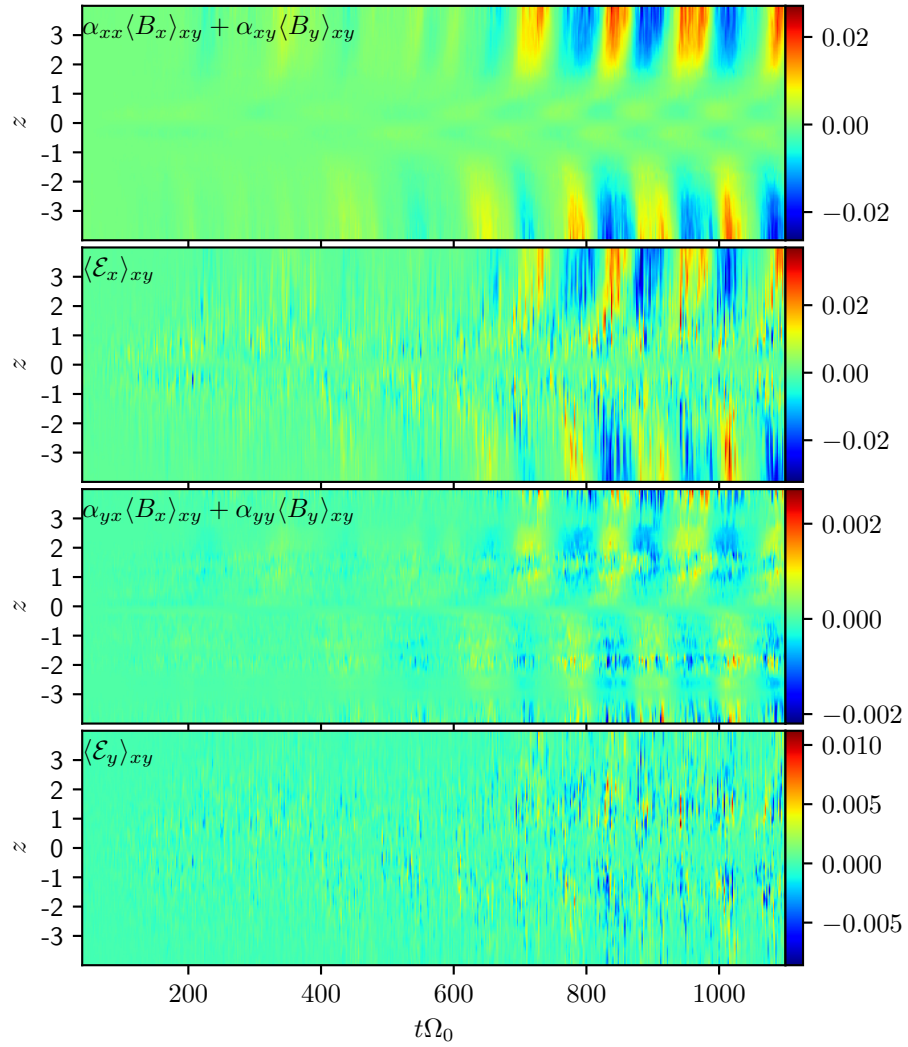

Figure 10.13: EMF values, evaluated for simulation sg-mhd-tau20 (see also Löhnert & Peeters 2023). **First image:** EMF, according to the linear model, $\langle \hat{\mathcal{E}}_x\rangle_{xy} = \alpha_{xx}\langle B_x\rangle_{xy} + \alpha_{xy}\langle B_y\rangle_{xy}$. **Second image:** $\langle \mathcal{E}_x\rangle_{xy}$ values, directly obtained from the simulation output. **Third image:** EMF, according to the linear model, $\langle \hat{\mathcal{E}}_y\rangle_{xy} = \alpha_{yx}\langle B_x\rangle_{xy} + \alpha_{yy}\langle B_y\rangle_{xy}$. **Fourth image:** $\langle \mathcal{E}_y\rangle_{xy}$ values, directly obtained from the simulation output. In all diagrams, the time axis starts at that moment when the magnetic seed field is introduced.

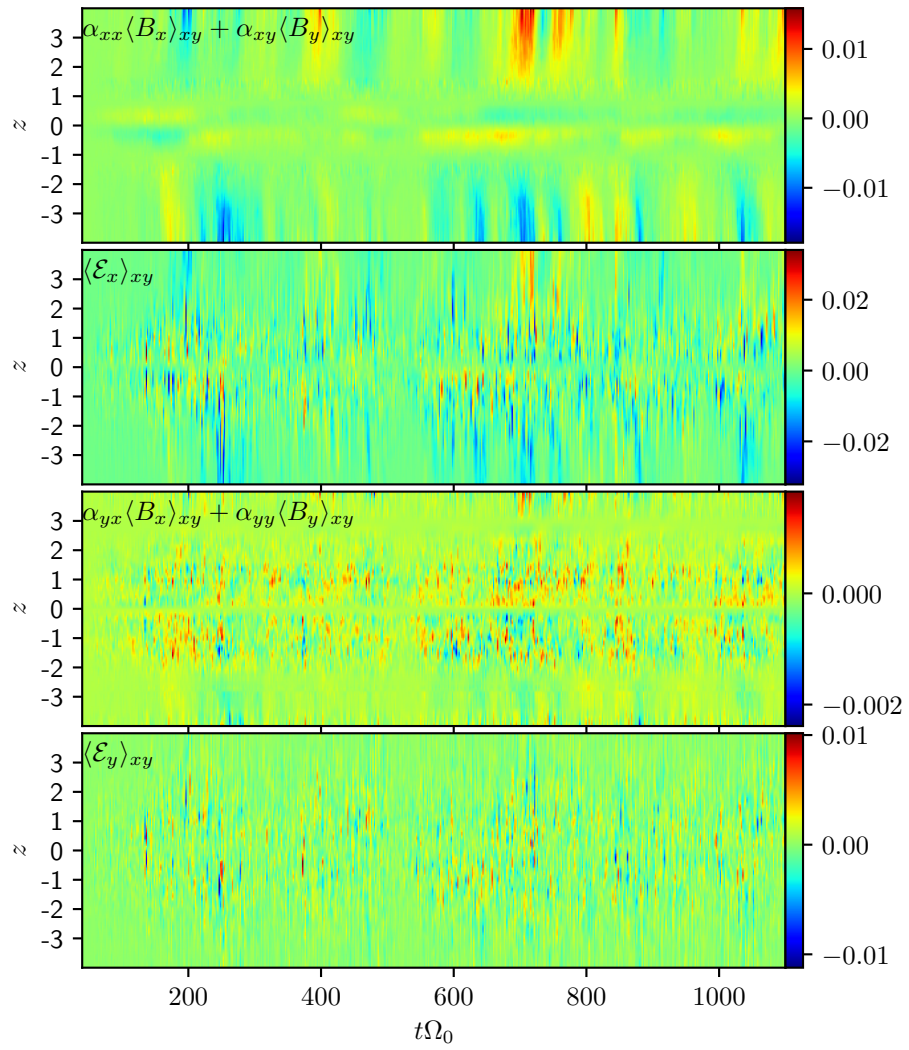

Figure 10.14: Similar to Fig. 10.13, but evaluated for simulation sg-mhd-tau10 (see also Löhnert & Peeters 2023).

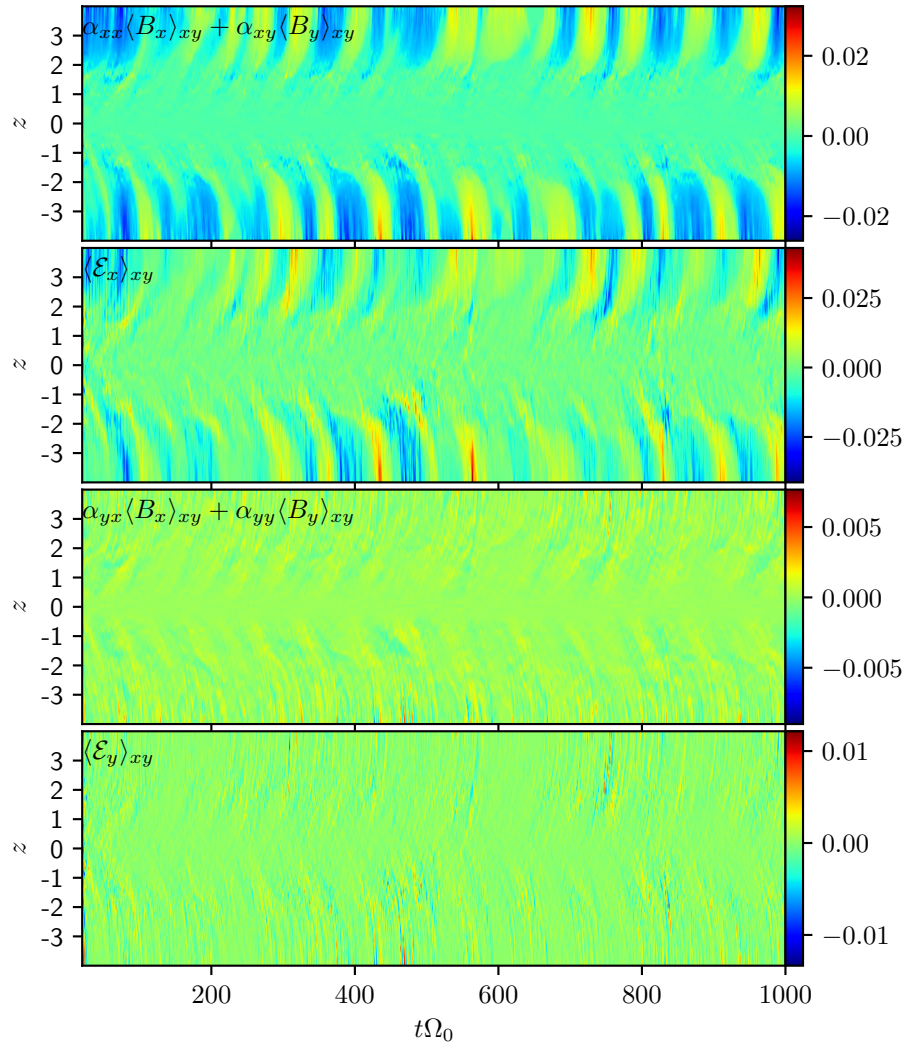

Figure 10.15: Similar to Fig. 10.13, but evaluated for the pure-MRI simulation, MRI-compare (see also Löhnert & Peeters 2023).

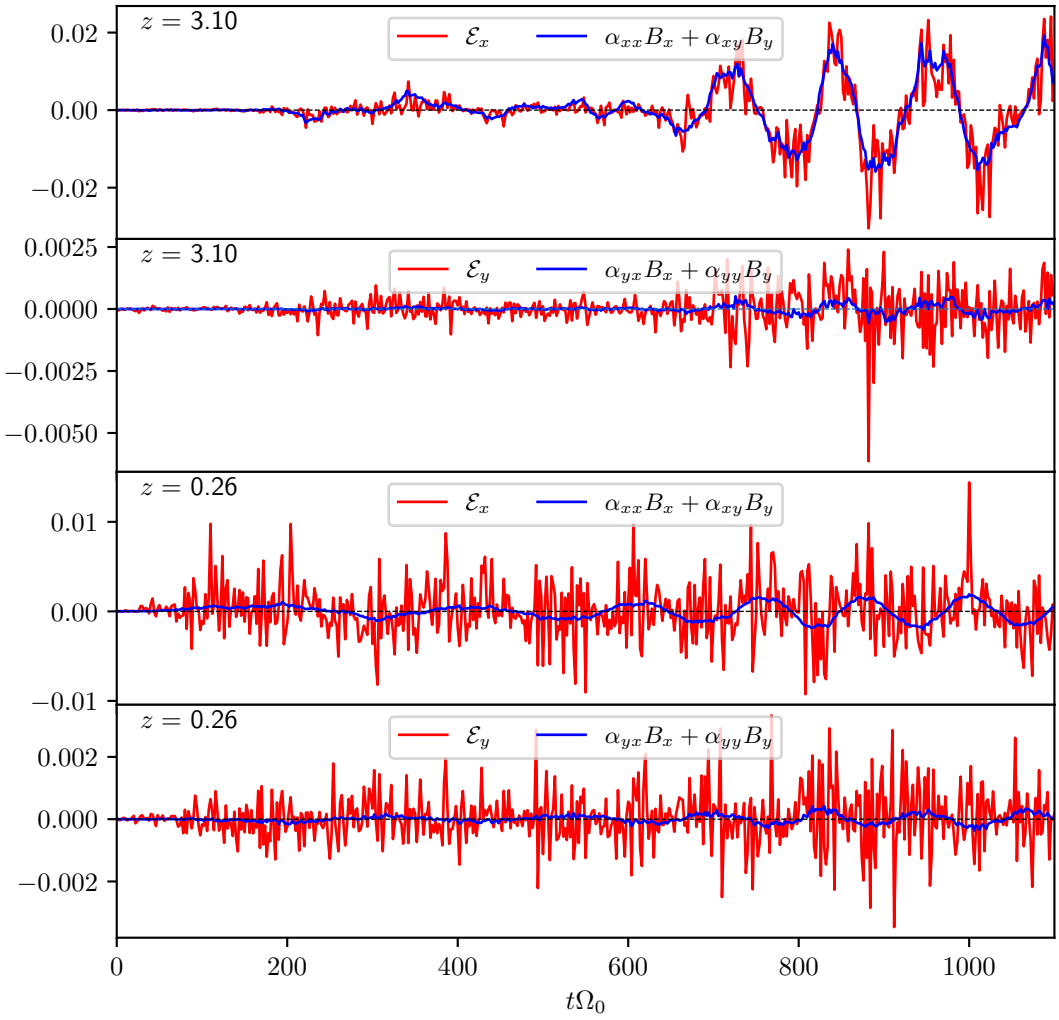

Figure 10.16: Shown is the model, $\langle\hat{\mathcal{E}}_x\rangle_{xy} = \alpha_{xx}\langle B_x\rangle_{xy} + \alpha_{xy}\langle B_y\rangle_{xy}$, evaluated for two different z values ($z = 3.10$, first two images, and $z = 0.26$, last two images), and simulation sg-mhd-tau20. $t = 0$ corresponds to the moment when the magnetic seed field is introduced. The EMFs themselves have a rather high noise level, and the linear model is comparable to a smoothening. That is, because the field components, $\langle B_x\rangle_{xy}$, and $\langle B_y\rangle_{xy}$, have a lower noise level, see, for example, Figs. 10.9 - 10.11.

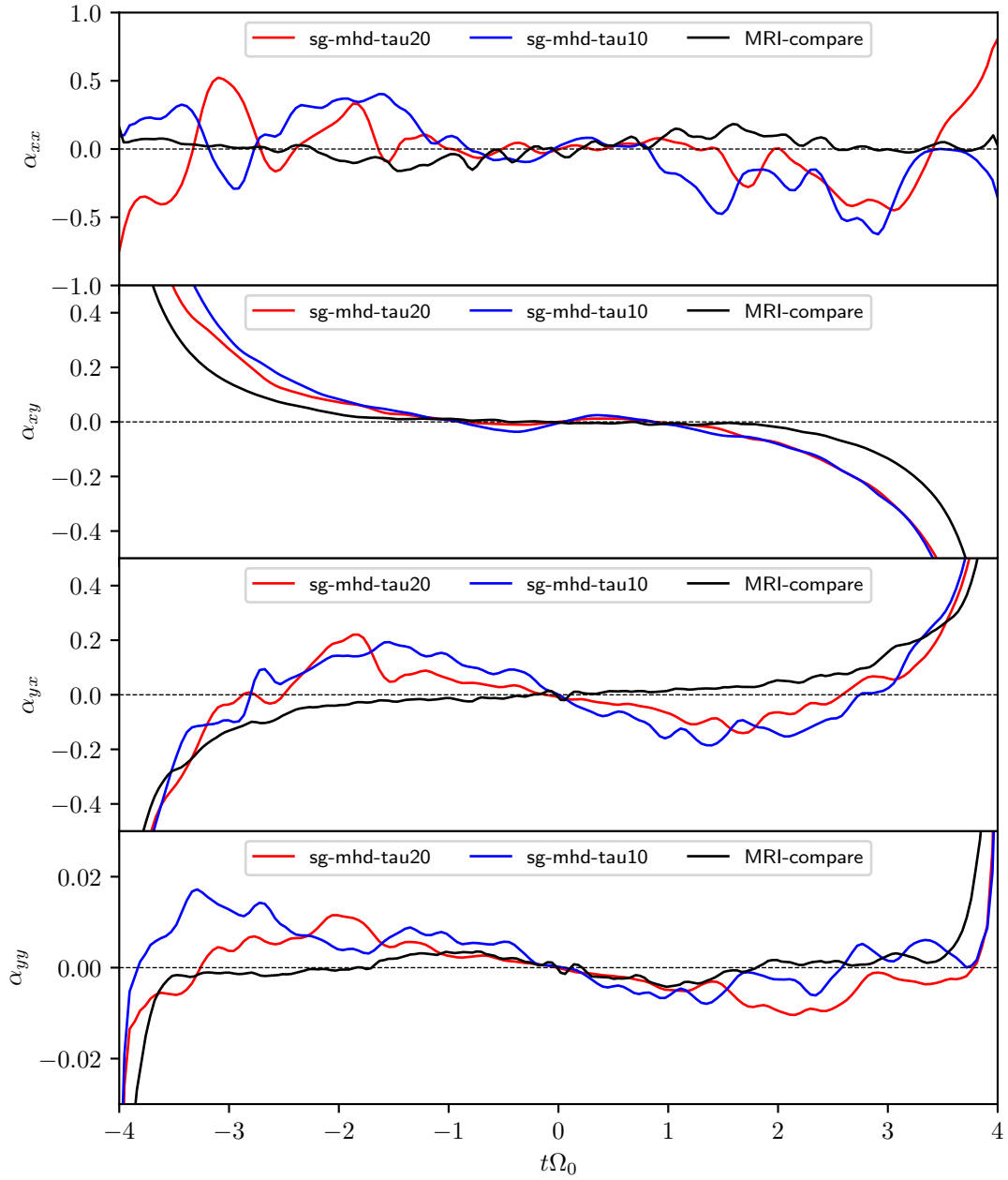

Figure 10.17: Dynamo coefficients, α_{ji}, derived via the linear model, as a function of z. The values were evaluated for simulations sg-mhd-tau20, sg-mhd-tau10, and MRI-compare, shown in red, blue, and black, respectively. The value range, along the vertical axis, has been limited, as otherwise, one would not be able to identify mid-plane features.

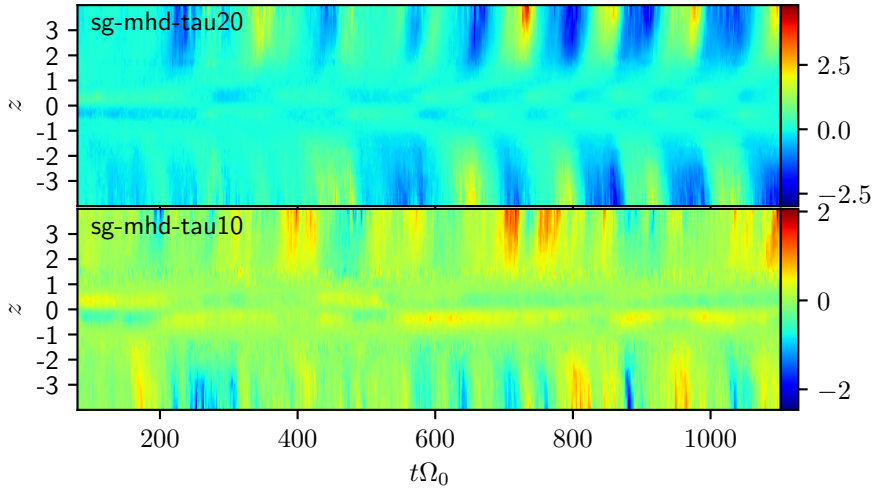

Figure 10.18: Comparison of the models, $\langle\hat{\mathcal{E}}_x\rangle_{xy} = \alpha_{xx}\langle B_x\rangle_{xy} + \alpha_{xy}\langle B_y\rangle_{xy}$, for simulations sg-mhd-tau20 (first image), and sg-mhd-tau10 (second image). The superscript 'norm' indicates that the values $\langle\hat{\mathcal{E}}_x\rangle_{xy}$ were normalised with the momentary, volume-averaged magnetic energy density, $E_{\rm mag} = \langle|\mathbf{B}|^2\rangle/(2\mu_0)$. Hence, shown are values for $\langle\hat{\mathcal{E}}_x\rangle_{xy}(t,z)/E_{\rm mag}(t)$. It is noted that $\mu_0 = 1$, in code units (see Löhnert & Peeters 2023). Both time axes start at the moment of field seeding, except that the first $80\Omega_0^{-1}$ were discarded, as otherwise, the initially low magnetic energy would have led to a misleading color map.

References

Binney, James and Scott Tremaine (2008). *Galactic dynamics*. 2nd ed. Princeton University Press.

Biskamp, Dieter (2003). *Magnetohydrodynamic turbulence*. Cambridge University Press.

Brandenburg, Axel and Karl Johan Donner (1997). "The dependence of the dynamo alpha on vorticity". In: *Monthly Notices of the Royal Astronomical Society* 288.2, pp. L29–L33.

Brandenburg, Axel and Kandaswamy Subramanian (2005). "Astrophysical magnetic fields and nonlinear dynamo theory". In: *Physics Reports* 417.1-4, pp. 1–209.

Brandenburg, Axel et al. (1995). "Dynamo-generated turbulence and large-scale magnetic fields in a Keplerian shear flow". In: *The Astrophysical Journal* 446, p. 741.

Bronstein, Ilja N. et al. (2012). *Taschenbuch der Mathematik*. 8th ed. Harri Deutsch.

Chiuderi, Claudio and Marco Velli (2015). *Basics of Plasma Astrophysics*. Springer.

Coleman, Matthew S. B. et al. (2017). "Convective quenching of field reversals in accretion disc dynamos". In: *Monthly Notices of the Royal Astronomical Society* 467.3, pp. 2625–2635.

Guan, Xiaoyue and Charles F. Gammie (2011). "Radially extended, stratified, local models of isothermal disks". In: *The Astrophysical Journal* 728.2, p. 130.

Kratter, Kaitlin and Giuseppe Lodato (2016). "Gravitational Instabilities in Circumstellar Disks". In: *Annual review of astronomy and astrophysics* 54.1, pp. 271–311.

Kulsrud, R. M. (2005). *Plasma Physics for Astrophysics*. Princeton University Press.

Lin, Min-Kai and Kaitlin M. Kratter (2016). "On the Gravitational Stability of Gravito-turbulent Accretion Disks". In: *The Astrophysical Journal* 824.2, p. 91.

Löhnert, L., S. Krätschmer, and A. G. Peeters (2020). "Saturation mechanism and generated viscosity in gravito-turbulent accretion disks". In: *Astronomy & Astrophysics* 640, A53.

Löhnert, L. and A. G. Peeters (2022). "Combined dynamo of gravitational and magneto-rotational instability in irradiated accretion discs". In: *Astronomy and Astrophysics* 663, A176.

— (2023). "The persistence of magneto-rotational turbulence in gravitationally turbulent accretion disks". In: *Astronomy and Astrophysics* 677, A173.

Miller, Kristen A. and James M. Stone (2000). "The formation and structure of a strongly magnetized corona above a weakly magnetized accretion disk". In: *The Astrophysical Journal* 534.1, p. 398.

Regev, Oded, Orkan M. Umurhan, and Philip A. Yecko (2016). *Modern fluid dynamics for physics and astrophysics*. Springer.

Rice, W. K. M. et al. (2011). "Stability of self-gravitating discs under irradiation". In: *Monthly Notices of the Royal Astronomical Society* 418.2, pp. 1356–1362.

Riols, A. and H. Latter (2018). "Spiral density waves and vertical circulation in protoplanetary discs". In: *Monthly Notices of the Royal Astronomical Society* 476.4, pp. 5115–5126.

— (2019). "Gravitoturbulent dynamos in astrophysical discs". In: *Monthly Notices of the Royal Astronomical Society* 482.3, pp. 3989–4008.

Salvesen, Greg et al. (2016). "Accretion disc dynamo activity in local simulations spanning weak-to-strong net vertical magnetic flux regimes". In: *Monthly Notices of the Royal Astronomical Society* 457.1, pp. 857–874.

Shi, Jiming, Julian H. Krolik, and Shigenobu Hirose (2010). "What is the numerically converged amplitude of magnetohydrodynamics turbulence in stratified shearing boxes?" In: *The Astrophysical Journal* 708.2, p. 1716.

Simon, Jacob B., Kris Beckwith, and Philip J. Armitage (2012). "Emergent mesoscale phenomena in magnetized accretion disc turbulence". In: *Monthly Notices of the Royal Astronomical Society* 422.3, pp. 2685–2700.

Simon, Jacob B., John F. Hawley, and Kris Beckwith (2011). "Resistivity-driven state changes in vertically stratified accretion disks". In: *The Astrophysical Journal* 730.2, p. 94.

Stone, James M. et al. (1996). "Three-dimensional magnetohydrodynamical simulations of vertically stratified accretion disks". In: *The Astrophysical Journal* 463, p. 656.

Toomre, Alar (1964). "On the Gravitational Stability of A Disk of Stars". In: *The Astrophysical Journal* 139, pp. 1217–1238.

Toro, Eleuterio F. (2009). *Riemann solvers and numerical methods for fluid dynamics: a practical introduction*. 3rd ed. Springer.

Vishniac, Ethan T. and Axel Brandenburg (1997). "An Incoherent α-Ω Dynamo in Accretion Disks". In: *The Astrophysical Journal* 475.1, pp. 263–274.

Ziegler, U. and G. Rüdiger (2000). "Angular momentum transport and dynamo-effect in stratified, weakly magnetic disks". In: *Astronomy & Astrophysics* 356, pp. 1141–1148.

Appendix

Appendix A

Viscous-stress tensor in cylindrical coordinates

In Cartesian coordinates, the viscous-stress tensor has components (see, e.g., Clarke & Carswell 2007)

$$\sigma_{jk} = \eta \left(\frac{\partial u_j}{\partial x_k} + \frac{\partial u_k}{\partial x_j} - \frac{2}{3}\delta_{jk}(\nabla \cdot \mathbf{u}) \right) + \zeta \delta_{jk}(\nabla \cdot \mathbf{u}). \tag{10.56}$$

The coefficient η refers to shear viscosity, which may be understood as the friction, occurring between adjacent fluid slices, due to a velocity shear, and the second parameter, ζ, refers to compressional viscosity, which represents friction between adjacent fluid elements due to compressional motions (see, e.g., Clarke & Carswell 2007). In the astrophysical context, the molecular viscosity is usually very small, and especially the second viscosity, ζ, is often neglected (see, e.g., Clarke & Carswell 2007). In cylindrical coordinates, the components of the viscous stress tensor are given by (see, e.g., Shakura 2018)

$$\sigma_{rr} = 2\eta \frac{\partial u_r}{\partial r} + \left(\zeta - \frac{2}{3}\eta \right) \nabla \cdot \mathbf{u} \tag{10.57}$$

$$\sigma_{\phi\phi} = 2\eta \frac{u_r}{r} + \left(\zeta - \frac{2}{3}\eta \right) \nabla \cdot \mathbf{u} \tag{10.58}$$

$$\sigma_{zz} = 2\eta \frac{\partial u_z}{\partial z} + \left(\zeta - \frac{2}{3}\eta \right) \nabla \cdot \mathbf{u} \tag{10.59}$$

$$\sigma_{r\phi} = \eta \left(r \frac{\partial}{\partial r} \left(\frac{u_\phi}{r} \right) \right) = \sigma_{\phi r} \tag{10.60}$$

$$\sigma_{rz} = \eta \left(\frac{\partial u_z}{\partial r} + \frac{\partial u_r}{\partial z} \right) = \sigma_{zr} \tag{10.61}$$

$$\sigma_{\phi z} = \eta \frac{\partial u_\phi}{\partial z} = \sigma_{z\phi} \tag{10.62}$$

In the context of accretion disks, it is often convenient to use the kinematic viscosity, $\nu = \eta/\rho$, with mass density ρ (see, e.g., Shakura 2018).

Appendix B

Note about the sound speed

The adiabatic sound speed is defined as (see, e.g., Regev, Umurhan, & Yecko 2016)

$$c_s := \sqrt{\left(\frac{\partial P}{\partial \rho} \right)_{S=\text{const.}}}, \tag{10.63}$$

whereby P is the pressure, ρ is the mass density, and S is the entropy of a given fluid element. For an ideal gas, one finds $P/\rho^\gamma = K$ (with constant K), under the constraint of constant entropy. Thereby, γ (adiabatic index), is the ratio of specific heats, $\gamma = c_P/c_V$ (see, e.g., Regev, Umurhan, & Yecko 2016). Hence, at constant pressure, a small temperature change, δT, corresponds to the heat exchange, per mass, of $\delta Q = c_P \delta T$. Similarly, at constant volume, the heat exchange per mass, and a small temperature change, δT, is given by $\delta Q = c_V \delta T$. For an ideal gas, with f degrees of freedom, per particle, one can write $\gamma = 1 + 2/f$ (see, e.g., Regev, Umurhan, & Yecko 2016)[2]. For the adiabatic sound speed one thus obtains.

$$c_s = \sqrt{\left(\frac{\partial P}{\partial \rho}\right)_{S=\text{const.}}} = \sqrt{\frac{\partial}{\partial \rho} K \rho^\gamma} = \gamma K \rho^{\gamma-1} = \sqrt{\gamma \frac{P}{\rho}}. \tag{10.64}$$

Unless stated otherwise, the definition $c_s^2 = \gamma P/\rho$ is used here. In the astrophysical context, one also often uses the isothermal sound speed. The corresponding definition is similar, but instead of constant entropy, the temperature is held constant. Hence, for an ideal gas, one finds

$$c_{s,i} := \sqrt{\left(\frac{\partial P}{\partial \rho}\right)_{T=\text{const.}}} = \sqrt{\left(\frac{\partial (\rho R_s T)}{\partial \rho}\right)_{T=\text{const.}}} = \sqrt{R_s T} = \sqrt{\frac{P}{\rho}}, \tag{10.65}$$

whereby $P = \rho R_s T$ was used. The isothermal, and adiabatic sound speeds deviate by only a factor of $\sqrt{\gamma}$. Hence, for order-of-magnitude comparisons, the latter may be used interchangeably.

Appendix C

Derivation of the Kepler orbital velocity

The gravitational potential of the central object, in cylindrical coordinates, (r, ϕ, z), is given by $\Phi^\star = GM_\star/\sqrt{r^2+z^2}$. For thin disks, the latter can be simplified, by applying a Taylor expansion to first order in z/r, around $z/r = 0$, yielding:

$$\Phi^\star = \frac{GM_\star}{r}\left(1 + \frac{z^2}{r^2}\right)^{-1/2} \sim -\frac{GM_\star}{r} + \frac{1}{2}\frac{GM_\star}{r^3} z^2. \tag{10.66}$$

The corresponding force density follows by applying the gradient

$$-\rho \nabla \Phi_\star \sim -\frac{GM_\star \rho}{r^2}\,\hat{\mathbf{e}}_r - \frac{GM_\star \rho}{r^3}\, z\, \hat{\mathbf{e}}_z. \tag{10.67}$$

Using the $\hat{\mathbf{e}}_r$ component, in the radial force balance (at $z = 0$),

$$u_\phi^2/r = -\partial_r \Phi_\star, \tag{10.68}$$

one obtains the radial angular velocity profile

$$\Omega(r) = \sqrt{\frac{GM_\star}{r^3}}, \tag{10.69}$$

The latter is the Kepler angular velocity, whereby the actual orbital velocity is given by $u_\phi = \Omega\, r$. Using $\Omega(r)$, both the potential and force density, can be rewritten, in the following, shorter form:

$$\Phi_\star = -\Omega^2 r^2 + \frac{1}{2}\Omega^2 z^2 \tag{10.70}$$

$$-\rho \nabla \Phi_\star = -\rho \Omega^2 r\, \hat{\mathbf{e}}_r - \rho \Omega^2 z\, \hat{\mathbf{e}}_z. \tag{10.71}$$

[2] For a mono-atomic gas ($f = 3$), that yields $\gamma = 5/3$

For local shearing-box calculations (see Sect. 4.1), one transforms into a system that co-rotates, at a certain radius, say r_0. The corresponding, Kepler angular velocity is given by $\Omega_0 = \Omega(r_0)$. This is not an inertial frame, and fictitious forces occur, for example, the centrifugal force density, $\rho\Omega_0^2 r\,\hat{\mathbf{e}}_r$. For the radial component, one can combine the gravitational force density of the central object, with the centrifugal force, to obtain the tidal force density:

$$\begin{aligned} -\rho\Omega^2\, r + \rho\Omega_0^2\, r &= \rho(\Omega_0^2 - \Omega^2)r = \rho G M_\star \left(\frac{1}{r_0^3} - \frac{1}{(r_0+x)^3}\right)(r_0+x) \\ &= \rho\frac{GM_\star}{r_0^3}\left(1 - \frac{1}{(1+\frac{x}{r_0})^3}\right)(r_0+x) \sim \rho\frac{GM_\star}{r_0^3}\left(1 - 1 + 3\frac{x}{r_0}\right)(r_0+x) \\ &\sim 3\rho\Omega_0^2 x. \end{aligned} \tag{10.72}$$

Thereby, the deviation from the local co-rotation radius, $x = r - r_0$, was introduced.

Appendix D

Gravitational stress tensor

In a fluid (with mass density ρ) that is subject to self-gravity (with potential Φ), the additional force density $-\rho\nabla\Phi$ has to be added to the Euler equation. This term can alternatively be expressed, in the form of a divergence (Lynden-Bell & Kalnajs 1972),

$$-\rho\nabla\Phi = -\nabla\cdot\underline{\mathbf{G}}. \tag{10.73}$$

To see how this follows, one can start with the observation that

$$\partial_j\left(\partial_j\Phi\,\partial_l\Phi\right) = \left(\partial_j\partial_j\Phi\right)\,\partial_l\Phi + \partial_j\Phi\left(\partial_j\partial_l\Phi\right). \tag{10.74}$$

The Einstein-summation convention is used, that is, indices appearing twice are summed over. One can further rewrite the second term, yielding (see also Lynden-Bell & Kalnajs 1972)

$$\begin{aligned} \partial_j\Phi\,\partial_j\partial_l\Phi &= \partial_l\left(\partial_j\Phi\,\partial_j\Phi\right) - \partial_l\partial_j\Phi\,\partial_j\Phi \\ \Rightarrow \partial_j\Phi\,\partial_j\partial_l\Phi &= \frac{1}{2}\partial_l\left(\partial_j\Phi\,\partial_j\Phi\right) \\ &= \frac{1}{2}\partial_k\left(\delta_{kl}\,\partial_j\Phi\,\partial_j\Phi\right). \end{aligned} \tag{10.75}$$

The δ_{kl} was introduced, in order to achieve a divergence representation. Using the previous two results, and the Poisson equation, $\nabla^2\Phi = 4\pi G\rho$, it follows that

$$\begin{aligned} \left[-\rho\nabla\Phi\right]_l &= -\frac{1}{4\pi G}\left[\left(\nabla^2\Phi\right)\nabla\Phi\right]_l = -\frac{1}{4\pi G}\left(\partial_j\partial_j\Phi\right)\,\partial_l\Phi \\ &= -\frac{1}{4\pi G}\partial_j\left(\partial_j\Phi\,\partial_l\Phi\right) + \frac{1}{8\pi G}\partial_k\left(\delta_{kl}\,\partial_j\Phi\,\partial_j\Phi\right) \\ &= \left[-\frac{1}{4\pi G}\nabla\cdot\left(\nabla\Phi\nabla\Phi - \frac{1}{2}(\nabla\Phi\cdot\nabla\Phi)\mathbf{I}\right)\right]_l. \end{aligned} \tag{10.76}$$

Hence, the components of $\underline{\mathbf{G}}$ are given by

$$G_{jk} = \frac{1}{4\pi G}\left(\partial_j\Phi\,\partial_k\Phi - \frac{1}{2}\delta_{jk}\,\left(\nabla\Phi\cdot\nabla\Phi\right)\right). \tag{10.77}$$

Appendix F

Deriving the magnetic energy balance

The goal of this section is to derive the magnetic-energy balance, for the local shearing-box setup. The resulting energy balance is also used in Sect. 9 (LP23).

Starting point is the induction equation (see also Sect. 3.2.3), including Ohmic resistivity:

$$\partial_t \mathbf{B} = \nabla \times (\mathbf{v} \times \mathbf{B}) + \frac{\eta}{\mu_0} \nabla^2 \mathbf{B}. \tag{10.78}$$

One then multiplies the latter equation by $\mathbf{B}/\mu_0$, yielding

$$\partial_t \left(\frac{1}{2\mu_0} |\mathbf{B}|^2 \right) = \frac{1}{\mu_0} \left[\mathbf{B} \cdot \nabla \times (\mathbf{v} \times \mathbf{B}) + \frac{\eta}{\mu_0} \mathbf{B} \cdot \nabla^2 \mathbf{B} \right] \tag{10.79}$$

The first term, on the right hand side, can be rewritten, using index notation:

$$\begin{aligned}
\mathbf{B} \cdot \nabla \times (\mathbf{v} \times \mathbf{B}) &= B_j \epsilon_{jkl} \partial_k \left(\epsilon_{lnq} v_n B_q \right) \\
&= \partial_k \left[\epsilon_{jkl} \epsilon_{lnq} v_n B_j B_q \right] - \epsilon_{jkl} \epsilon_{lnq} v_n B_q (\partial_k B_j) \\
&= \partial_k \left[\epsilon_{klj} (\epsilon_{lnq} v_n B_q) B_j \right] + \left(\epsilon_{lnq} v_n B_q \right) \left(\epsilon_{lkj} \partial_k B_j \right) \\
&= \nabla \cdot [(\mathbf{v} \times \mathbf{B}) \times \mathbf{B}] + (\mathbf{v} \times \mathbf{B}) \cdot (\nabla \times \mathbf{B}) \\
&= \nabla \cdot [(\mathbf{v} \times \mathbf{B}) \times \mathbf{B}] + \mu_0 \, \mathcal{E} \cdot \mathbf{J} \\
&= \nabla \cdot [-(\mathbf{B} \cdot \mathbf{B}) \mathbf{v} + (\mathbf{B} \cdot \mathbf{v}) \mathbf{B}] + \mu_0 \, \mathcal{E} \cdot \mathbf{J}.
\end{aligned} \tag{10.80}$$

Thereby, the ϵ_{jkl} are the components of the epsilon tensor[3], and $\mathcal{E} = \mathbf{v} \times \mathbf{B}$. In the last step, the identity $(\mathbf{v} \times \mathbf{B}) \times \mathbf{B} = -(\mathbf{B} \cdot \mathbf{B}) \mathbf{v} + (\mathbf{B} \cdot \mathbf{v}) \mathbf{B}$ (see, e.g., Bronstein et al. 2012) was used. Substituted, into the energy balance, one finds

$$\partial_t \left(\frac{1}{2\mu_0} |\mathbf{B}|^2 \right) = \nabla \cdot \left[\frac{1}{\mu_0} (\mathbf{v} \cdot \mathbf{B}) \mathbf{B} - \frac{|\mathbf{B}|^2}{\mu_0} \mathbf{v} \right] + \mathcal{E} \cdot \mathbf{J} + \frac{\eta}{\mu_0^2} \mathbf{B} \cdot \nabla^2 \mathbf{B}. \tag{10.81}$$

The Ohmic-resistivity term can also be rewritten, by using

$$\nabla^2 \mathbf{B} = \nabla \underbrace{(\nabla \cdot \mathbf{B})}_{=0} - \nabla \times (\nabla \times \mathbf{B}) = -\mu_0 \, \nabla \times \mathbf{J}, \tag{10.82}$$

yielding

$$\begin{aligned}
\frac{\eta}{\mu_0^2} \mathbf{B} \cdot \nabla^2 \mathbf{B} &= -\frac{\eta}{\mu_0} \mathbf{B} \cdot \nabla \times \mathbf{J} = -\frac{\eta}{\mu_0} \epsilon_{jkl} B_j \partial_k J_l \\
&= -\frac{\eta}{\mu_0} \partial_k (\epsilon_{jkl} B_j J_l) + \frac{\eta}{\mu_0} \epsilon_{jkl} J_l \partial_k B_j = -\frac{\eta}{\mu_0} \nabla \cdot (\mathbf{J} \times \mathbf{B}) - \frac{\eta}{\mu_0} \epsilon_{lkj} J_l \partial_k B_j \\
&= -\frac{\eta}{\mu_0} \nabla \cdot (\mathbf{J} \times \mathbf{B}) - \frac{\eta}{\mu_0} \mathbf{J} \cdot \nabla \times \mathbf{B} = -\frac{\eta}{\mu_0} \nabla \cdot (\mathbf{J} \times \mathbf{B}) - \eta \, |\mathbf{J}|^2.
\end{aligned} \tag{10.83}$$

In the second line, $\epsilon_{jkl} = \epsilon_{ljk} = -\epsilon_{lkj}$ was used. In summary, one thus obtains the following magnetic energy balance:

$$\partial_t \left(\frac{1}{2\mu_0} |\mathbf{B}|^2 \right) = \nabla \cdot \left[\frac{1}{\mu_0} (\mathbf{v} \cdot \mathbf{B}) \mathbf{B} - \frac{|\mathbf{B}|^2}{\mu_0} \mathbf{v} - \frac{\eta}{\mu_0} \, \mathbf{J} \times \mathbf{B} \right] + \mathcal{E} \cdot \mathbf{J} - \eta \, |\mathbf{J}|^2. \tag{10.84}$$

[3] $\epsilon_{jkl} = 1$, if jkl is an even permutation of 123; $\epsilon_{jkl} = -1$, if jkl is an odd permutation of 123; $\epsilon_{jkl} = 0$, if at least to indices of jkl are equal (see, e.g., Bronstein et al. 2012).

The terms, within the divergence, can be further rewritten, yielding

$$\begin{aligned}\frac{1}{\mu_0}(\mathbf{v}\cdot\mathbf{B})\mathbf{B}-\frac{|\mathbf{B}|^2}{\mu_0}\mathbf{v}-\frac{\eta}{\mu_0}\,\mathbf{J}\times\mathbf{B} &= \frac{1}{\mu_0}(\mathbf{v}\times\mathbf{B})\times\mathbf{B}-\frac{\eta}{\mu_0}\,\mathbf{J}\times\mathbf{B}\\ &= \frac{1}{\mu_0}(\mathbf{v}\times\mathbf{B}-\eta\,\mathbf{J})\times\mathbf{B}\\ &= -\frac{1}{\mu_0}\mathbf{E}\times\mathbf{B}=-\mathbf{S},\end{aligned} \tag{10.85}$$

whereby Ohm's law, $\mathbf{E}+\mathbf{v}\times\mathbf{B}=\eta\,\mathbf{J}$, was used, introducing the electric field, $\mathbf{E}$. Hence, $\mathbf{S}$ can directly be interpreted as the Poynting vector (see, e.g., Jackson 2014), and the energy balance is now given by (see also Brandenburg & Subramanian 2005)

$$\partial_t\left(\frac{1}{2\mu_0}|\mathbf{B}|^2\right)=-\nabla\cdot\mathbf{S}+\mathcal{E}\cdot\mathbf{J}-\eta|\mathbf{J}|^2. \tag{10.86}$$

This equation has the form of a conservation law, with the source terms $\mathcal{E}\cdot\mathbf{J}$, and $-\eta|\mathbf{J}|^2$, representing kinetic-energy exchange, and Ohmic heating, respectively. Using Ohm's law, one could also combine the latter two terms, yielding $-\mathbf{J}\cdot\mathbf{E}$, which represents the net-energy exchange between the fluid and the material (see, e.g., Jackson 2014; Chiuderi & Velli 2015). The latter is a detailed balance for the magnetic energy density, at each location in space. One can also derive a volume-integrated, or volume-averaged magnetic energy density. The volume is here chosen to be the shearing-box domain. Hence, a volume average, $\langle ...\rangle$, is applied to the detailed energy balance, yielding

$$\left\langle\partial_t\left(\frac{\mathbf{B}^2}{2\mu_0}\right)\right\rangle=\langle-\nabla\cdot\mathbf{S}\rangle+\langle\mathcal{E}\cdot\mathbf{J}\rangle-\langle\eta|\mathbf{J}|^2\rangle. \tag{10.87}$$

The volume-averaged flux contribution can be written as a surface-integral

$$\begin{aligned}\langle-\nabla\cdot\mathbf{S}\rangle &= \frac{1}{V}\int_V(-\mathbf{S})\,dV=\frac{1}{V}\oint_{\mathcal{A}}(-\mathbf{S})\cdot\mathbf{n}\,d^2A\\ &= \mathcal{F}_x+\mathcal{F}_y+\mathcal{F}_z,\end{aligned} \tag{10.88}$$

whereby $\mathbf{n}$ is the surface norm. The values $\mathcal{F}_x$, $\mathcal{F}_y$, and $\mathcal{F}_z$ are surface integrals over the boundary surfaces of constant x, y, and z, respectively. More precisely,

$$\mathcal{F}_x = \frac{1}{V}\left(\int_{x=L_x/2}(-S_x)\,dydz-\int_{x=-L_x/2}(-S_x)\,dydz\right) \tag{10.89}$$

$$\mathcal{F}_y = \frac{1}{V}\left(\int_{y=L_y/2}(-S_y)\,dxdz-\int_{y=-L_y/2}(-S_y)\,dxdz\right) \tag{10.90}$$

$$\mathcal{F}_z = \frac{1}{V}\left(\int_{z=L_z/2}(-S_z)\,dxdy-\int_{z=-L_z/2}(-S_z)\,dxdy\right) \tag{10.91}$$

One can simplify the integrals considerably, by realising that the boundary conditions are periodic in the y-direction, and shearing-periodic in the x-direction. This has crucial implications for the values, each of the integrals can have. For example, since all quantities are periodic in y-direction, all derived quantities are periodic as well, including, for example, the Poynting-flux component S_y. Hence, on immediately concludes that $\mathcal{F}_y=0$. A similar argument can be made, using the shearing periodic boundary conditions, in the x-direction. Shearing-periodic boundaries differ from periodic boundaries, whereby values on the inner x-boundary are not mapped to the outer x-boundary, at the same y-value, but appear sheared along the y-axis, instead (see also Sect. 4.3). Though, when

integrals over (y,z) are considered, then the distinction between periodic an shearing-periodic is immaterial. Hence, if all quantities were shearing periodic, then also $\mathcal{F}_x$ would vanish. Though, care must be taken here, as all quantities are shearing periodic, except the toroidal velocity component, v_y. The velocity is of the form $\mathbf{v} = (3\Omega_0/2)\, x\, \mathbf{e}_y + \delta\mathbf{v}$, with the first term representing the background shear flow, and $\delta\mathbf{v}$ the velocity perturbation. The perturbation alone is shearing periodic, though the shear, $(3\Omega_0/2)\, x$, jumps, when mapped from the inner radial boundary ($x = -L_x/2$) to the outer radial boundary ($x = L_x/2$). This is of course due to the explicit dependence on the coordinate x. It is noted that this boost is the numerical source of energy replenishing, which accounts for the release of orbital potential energy in the global picture. Hence, in $\mathcal{F}_x$, all terms vanish, except the contribution containing the term $(\mathbf{v}\cdot\mathbf{B})\mathbf{B}$. That is, because the latter term is the only term where the y-velocity can appear, in an integral over surfaces of constant x. More precisely, one obtains

$$
\begin{aligned}
\mathcal{F}_x &= \frac{1}{V}\left(\int_{x=L_x/2}(-S_x)\,dydz - \int_{x=-L_x/2}(-S_x)\,dydz\right)\\
&= \frac{1}{V\mu_0}\left(\int_{x=L_x/2}((-\frac{3\Omega_0}{2}\,x\mathbf{e}_y)\cdot\mathbf{B})B_x\,dydz - \int_{x=-L_x/2}((-\frac{3\Omega_0}{2}\,x\mathbf{e}_y)\cdot\mathbf{B})B_x\,dydz\right)\\
&= -\frac{3\Omega_0}{2}\frac{1}{V\mu_0}\frac{L_x}{2}\underbrace{\left(\int_{x=L_x/2}B_x\,B_y\,dydz + \int_{x=-L_x/2}B_x\,B_y\,dydz\right)}_{=2\int_{x=L_x/2}B_x\,B_y\,dydz,\quad\text{due to shearing-periodicity}}\\
&= -\frac{3\Omega_0}{2}\frac{1}{V\mu_0}\frac{L_x}{2}\cdot 2\int_{x=L_x/2}B_x\,B_y\,dydz\\
&= \frac{3\Omega_0}{2}\frac{1}{\mu_0}\frac{1}{L_y\,L_z}\int_{x=L_x/2}B_x\,B_y\,dydz\\
&= -\frac{3\Omega_0}{2}\Big\langle -\frac{1}{\mu_0}B_x\,B_y\Big\rangle_{yz,x=L_x/2}\\
&\sim \frac{3\Omega_0}{2}\Big\langle -\frac{1}{\mu_0}B_x\,B_y\Big\rangle. \qquad (10.92)
\end{aligned}
$$

In the last step, the surface average, $\langle f\rangle_{yz}$, was replaced by a volume average, $\langle f\rangle$. Statistically, that is possible, because for all quantities, except the shear velocity itself, the shearing-box is homogeneous. One can, for example, consider the magnetic field components, B_x, at a radial position x. The shear flow has the y velocity $-3\Omega_0 x/2$, at this location. One can now apply a Galilean transformation to a different system, moving with velocity $-3\Omega_0 x/2$, in the y direction. In this system, the shear-flow simply appears to be shifted in the x direction. But the magnetic field, B_x, at location x, did not change. Hence, the fact that the $\langle f\rangle_{yz}$-average is over the outer x boundary is really irrelevant, and, statistically, the average should not depend on x. Consequently, the surface average can directly be replaced by a volume average. The interpretation of this term is that it represents the net flux of magnetic energy, into (or out of) the shearing box. The shearing box is a local model, but in a global model, this term represents the release of orbital potential energy, and is (along with the Reynolds and gravitational stresses) one of the main sources to replenish turbulent energy from the background. Here, the released energy is directly deposited as turbulent magnetic energy.

For the vertical-boundary flux, $\mathcal{F}_z$, one has to take into account all terms, as no symmetry argument

can immediately be applied. Hence, one obtains

$$\begin{aligned}\mathcal{F}_z &= \frac{1}{V}\int_{z=L_z/2}\left(\frac{1}{\mu_0}(\mathbf{v}\cdot\mathbf{B})B_z-\frac{\mathbf{B}^2}{\mu_0}v_z-\frac{\eta}{\mu_0}(\mathbf{J}\times\mathbf{B})\cdot\mathbf{e}_z\right)dxdy\\ &\quad -\frac{1}{V}\int_{z=-L_z/2}\left(\frac{1}{\mu_0}(\mathbf{v}\cdot\mathbf{B})B_z-\frac{\mathbf{B}^2}{\mu_0}v_z-\frac{\eta}{\mu_0}(\mathbf{J}\times\mathbf{B})\cdot\mathbf{e}_z\right)dxdy\\ &\sim \frac{1}{V}\int_{z=L_z/2}\left(\frac{1}{\mu_0}(\mathbf{v}\cdot\mathbf{B})B_z-\frac{\mathbf{B}^2}{\mu_0}v_z\right)dxdy\\ &\quad -\frac{1}{V}\int_{z=-L_z/2}\left(\frac{1}{\mu_0}(\mathbf{v}\cdot\mathbf{B})B_z-\frac{\mathbf{B}^2}{\mu_0}v_z\right)dxdy, \end{aligned} \tag{10.93}$$

whereby in the last step, boundary fluxes, due to Ohmic resistivity, were neglected, which is often a realistic choice (see, e.g., Balbus & Hawley 1998). Hence, the overall magnetic energy balance is now of the form (see also Brandenburg et al. 1995)

$$\left\langle \partial_t\left(\frac{\mathbf{B}^2}{2\mu_0}\right)\right\rangle = \underbrace{\frac{3\Omega_0}{2}\Big\langle -\frac{1}{\mu_0}B_x\,B_y\Big\rangle}_{1}+\underbrace{\langle\mathcal{E}\cdot\mathbf{J}\rangle}_{2}\underbrace{-\langle\eta|\mathbf{J}|^2\rangle}_{3}+\underbrace{\mathcal{F}_z}_{4}. \tag{10.94}$$

Qualitatively, this implies that changes of the magnetic energy (left part of the equation) are due to a combination of four different effects. Those are, from left to right:

1 Input of magnetic energy over the shearing-box boundaries, via magnetic energy fluxes. Corresponds to the energy, released by the accretion process.

2 Exchange rate between magnetic and kinetic energy.

3 Ohmic dissipation of magnetic energy. In the total energy balance, the magnetic-energy losses are converted into thermal energy.

4 Magnetic-energy losses over the vertical boundaries, due to winds.

Appendix G

Induction equation in the local shearing box

The goal of this section is to obtain a form of the induction equation, that is tailored to the shearing-sheet, or shearing-box setup. Starting-point is the general induction equation, in the ideal-MHD limit:

$$\partial_t\mathbf{B}=\nabla\times(\mathbf{v}\times\mathbf{B}). \tag{10.95}$$

A central part of the shearing-box approximation is the separation of the velocity field into a background-shear flow, and a perturbed velocity, $\mathbf{v}=-q\Omega_0 x\,\hat{\mathbf{e}}_y+\delta\mathbf{v}$, with $\delta\mathbf{v}=(v_x,\delta v_y,v_z)$. For a Keplerian disk, $q=3/2$. Substituting this velocity decomposition into the induction equation, one obtains

$$\partial_t\mathbf{B}=-q\Omega_0\nabla\times(x\hat{\mathbf{e}}_y\times\mathbf{B})+\nabla\times(\delta\mathbf{v}\times\mathbf{B}). \tag{10.96}$$

The first term, on the right hand side, can be rewritten[4]

$$\begin{aligned}\nabla\times(x\hat{\mathbf{e}}_y\times\mathbf{B}) &= x\hat{\mathbf{e}}_y\underbrace{(\nabla\cdot\mathbf{B})}_{=0}-\mathbf{B}\underbrace{(\nabla\cdot(x\hat{\mathbf{e}}_y))}_{=0}+(\mathbf{B}\cdot\nabla)(x\hat{\mathbf{e}}_y)-(x\hat{\mathbf{e}}_y\cdot\nabla)\mathbf{B}\\ &= B_x\hat{\mathbf{e}}_y-x\partial_y\mathbf{B}. \end{aligned} \tag{10.97}$$

[4] The identity $\nabla\times(\mathbf{A}\times\mathbf{B})=\mathbf{A}(\nabla\cdot\mathbf{B})-\mathbf{B}(\nabla\cdot\mathbf{A})+(\mathbf{B}\cdot\nabla)\mathbf{A}-(\mathbf{A}\cdot\nabla)\mathbf{B}$ (see, e.g., Bronstein et al. 2012) was used.

Hence, the induction equation then reads

$$\partial_t \mathbf{B} = q\Omega_0 x \partial_y \mathbf{B} - q\Omega_0 B_x \hat{\mathbf{e}}_y + \nabla \times \mathcal{E}, \tag{10.98}$$

whereby the electromotive force (EMF), $\mathcal{E} = \delta\mathbf{v} \times \mathbf{B}$, was introduced. In Löhnert & Peeters (2022) (Sect. 8), and Sect. 9 (LP23), the horizontally-averaged fields, and EMFs, are frequently used. Hence, one can horizontally average the above version of the induction equation, obtaining

$$\partial_t \langle \mathbf{B} \rangle_{xy} = q\Omega_0 \langle x \partial_y \mathbf{B} \rangle_{xy} - q\Omega_0 \langle B_x \rangle_{xy} \hat{\mathbf{e}}_y + \langle \nabla \times \mathcal{E} \rangle_{xy}. \tag{10.99}$$

One can now take advantage of the periodicity, and shearing-periodicity, in the y, and x directions, respectively. Since $\langle f \rangle_{xy}$ is essentially an integral over the xy plane, the first term, on the right hand side, vanishes, due to periodicity in the y direction. In the last term, $\langle \nabla \times \mathcal{E} \rangle_{xy}$, all derivatives towards x, and y, vanish. Hence, in components, one finds:

$$\begin{aligned}
\partial_t \langle B_x \rangle_{xy} &= -\partial_z \langle \mathcal{E}_y \rangle_{xy} && (10.100)\\
\partial_t \langle B_y \rangle_{xy} &= \partial_z \langle \mathcal{E}_x \rangle_{xy} - q\Omega_0 \langle B_x \rangle_{xy} && (10.101)\\
\partial_t \langle B_z \rangle_{xy} &= 0. && (10.102)
\end{aligned}$$

Appendix H

The local shearing-box approximation

Starting point is the Euler equation, Eq. 4.1, which is, at first, assumed to apply to the global disk. For reasons of convenience, Eq. 4.1 is expressed in cylindrical coordinates (r, ϕ, z), whereby the z axis is aligned with the rotation axis of the disk, and the disk mid plane is centred at $z = 0$. Further simplifications can be achieved, by assuming that $H/r \ll 1$, whereby $H \sim c_{s,i}/\Omega$ is the vertical scale height, as introduced in Sect. 3.1.2. Hence, one can assume, $|z|/r \ll 1$ for all regions of interest. This can be used to simplify the gravitational potential of the central object, $\Phi^\star = GM_\star/R$, with $R = \sqrt{r^2 + z^2}$, by applying a Taylor expansion round $z = 0$, yielding (see also Appendix C)

$$\Phi^\star \sim -\Omega^2(r) r^2 + \frac{1}{2}\Omega^2(r) z^2 \quad \Rightarrow \quad -\rho \nabla \Phi_\star \sim -\rho \Omega^2(r) r\, \hat{\mathbf{e}}_r - \rho \Omega^2(r) z\, \hat{\mathbf{e}}_z. \tag{10.103}$$

The components of the Euler equation, in cylindrical coordinates, then read (see, e.g., Clarke & Carswell 2007; Shakura 2018):

$$\begin{aligned}
\partial_t u_r + u_r \partial_r u_r + \frac{u_\phi}{r}\partial_\phi u_r + u_z \partial_z u_r - \frac{u_\phi^2}{r} &= -\frac{1}{\rho}\partial_r P - \Omega^2 r + \frac{1}{\rho} f_{\mathrm{ext},r} && (10.104)\\
\partial_t u_\phi + u_r \partial_r u_\phi + \frac{u_\phi}{r}\partial_\phi u_\phi + u_z \partial_z u_\phi + \frac{u_r u_\phi}{r} &= -\frac{1}{\rho r}\partial_\phi P + \frac{1}{\rho} f_{\mathrm{ext},\phi} && (10.105)\\
\partial_t u_z + u_r \partial_r u_z + \frac{u_\phi}{r}\partial_\phi u_z + u_z \partial_z u_z &= -\frac{1}{\rho}\partial_z P - \Omega^2 z + \frac{1}{\rho} f_{\mathrm{ext},z} && (10.106)
\end{aligned}$$

The velocity components are given by $\mathbf{u} = u_r \hat{\mathbf{e}}_r + u_\phi \hat{\mathbf{e}}_\phi + u_z \hat{\mathbf{e}}_z$, with unit-basis vectors $\hat{\mathbf{e}}_j$, in directions $j \in \{r, \phi, z\}$. One can then construct a co-rotating frame of reference. First, a fiducial radius, r_0, is selected, with a corresponding Kepler orbital frequency $\Omega_0 = \Omega(r_0)$. One then transforms to a cylindrical coordinate system, $(\tilde{r}, \tilde{\phi}, \tilde{z})$, that co-rotates with Ω_0:

$$\tilde{r} = r, \quad \tilde{\phi} = \phi - \Omega_0 t, \quad \tilde{z} = z. \tag{10.107}$$

Clearly, r and z do not change under the transformation, and the tilde is omitted for the latter two, $(r, \tilde{\phi}, z)$. It is pointed out that the attribute co-rotating really only applies to the radial location

$r = r_0$, due to the Keplerian differential rotation. Furthermore, this does not mean that $\mathbf{u} = 0$ at $r = r_0$, because the velocity is of the form $\mathbf{u} = \Omega(r)\, r\, \hat{\mathbf{e}}_\phi + \delta\mathbf{u}$. Therein, $\Omega(r)\, r\, \hat{\mathbf{e}}_\phi$ is the Kepler rotation, and $\delta\mathbf{u}$ is, for example, due to turbulence. Hence, one only removes the Kepler part of the velocity, at $r = r_0$. For Eqs. 10.104 - 10.106, the transformation $\phi \to \tilde{\phi}$ has no consequences, except that the time derivatives have to be modified. In order to see how the time derivative has to be adjusted, one can first evaluate an arbitrary velocity component, say u_j. In order to highlight that u_j is evaluated as a function of $\tilde{\phi}$, an additional tilde is introduced:

$$\tilde{u}_j(t, r, \tilde{\phi}, z) = u_j(t, r, \phi = \tilde{\phi} + \Omega_0\, t, z) \tag{10.108}$$

$$\Rightarrow \quad \frac{\partial \tilde{u}_j(t, r, \tilde{\phi}, z)}{\partial \tilde{\phi}} = \frac{\partial \phi(\tilde{\phi}, t)}{\partial \tilde{\phi}} \frac{\partial u_j(t, r, \phi(\tilde{\phi}, t), z)}{\partial \phi} = \frac{\partial u_j(t, r, \phi, z)}{\partial \phi} \tag{10.109}$$

$$\Rightarrow \quad \frac{\partial \tilde{u}_j(t, r, \tilde{\phi}, z)}{\partial t} = \frac{\partial u_j(t, r, \phi, z)}{\partial t} + \frac{\partial \phi(\tilde{\phi}, t)}{\partial t} \frac{\partial u_j(t, r, \phi(\tilde{\phi}, t), z)}{\partial \phi} = \frac{\partial u_j(t, r, \phi, z)}{\partial t} + \Omega_0 \underbrace{\frac{\partial u_j(t, r, \phi, z)}{\partial \phi}}_{=\partial \tilde{u}_j / \partial \tilde{\phi}}. \tag{10.110}$$

Hence, all ϕ derivatives can directly be replaced by derivatives towards $\tilde{\phi}$. For the partial time derivative, the transformation leads to an additional term, proportional to Ω_0. The transformation $\phi \to \tilde{\phi}$ can thus be applied, to Eqs. 10.104 - 10.106, by replacing ϕ with $\tilde{\phi}$, and by replacing the time derivative as follows:

$$\partial_t u_j = \partial_t \tilde{u}_j - \Omega_0 \partial_{\tilde{\phi}} \tilde{u}_j. \tag{10.111}$$

From now on, only the coordinate system $(r, \tilde{\phi}, z)$ is used, and, hence, the tilde in $\tilde{u}_j$ is omitted. Up to now, the velocity, $\mathbf{u}$, has been treated as a vector field, independent from the coordinate system, it is evaluated from. Hence, the latter coordinate transformation did not change the field $\mathbf{u}$, but only replaced its functional dependencies. One could stop here, but $\mathbf{u}$ is also a velocity, evaluated in the non-rotating rest frame. But each location in the co-rotating frame has itself a velocity, with respect to the rest frame, namely $\mathbf{u}_{\rm co} = \Omega_0\, r\, \hat{\mathbf{e}}_\phi$, whereby it is noted that the constant value Ω_0 is used, and not the profile $\Omega(r)$. Hence, it is convenient to introduce a new velocity $\mathbf{v} := \mathbf{u} - \mathbf{u}_{\rm co}$, as seen from the co-rotating frame. One can then substitute this, and the new time derivative, Eq. 10.111, into Eqs. 10.104 - 10.106, yielding:

$$\partial_t v_r + v_r \partial_r v_r + \frac{v_\phi}{r} \partial_{\tilde{\phi}} v_r + v_z \partial_z v_r - \frac{v_\phi^2}{r} = -\frac{1}{\rho} \partial_r P - \Omega^2 r + \frac{1}{\rho} f_{{\rm ext},r} + 2\Omega_0\, v_\phi + \Omega_0^2\, r \tag{10.112}$$

$$\partial_t v_\phi + v_r \partial_r v_\phi + \frac{v_\phi}{r} \partial_{\tilde{\phi}} v_\phi + v_z \partial_z v_\phi + \frac{v_r v_\phi}{r} = -\frac{1}{\rho r} \partial_{\tilde{\phi}} P + \frac{1}{\rho} f_{{\rm ext},\phi} - 2\Omega_0\, v_r \tag{10.113}$$

$$\partial_t v_z + v_r \partial_r v_z + \frac{v_\phi}{r} \partial_{\tilde{\phi}} v_z + v_z \partial_z v_z = -\frac{1}{\rho} \partial_z P - \Omega^2 z + \frac{1}{\rho} f_{{\rm ext},z}. \tag{10.114}$$

As one can see, the additional contribution in the time derivative, $-\Omega_0 \partial_{\tilde{\phi}}$, arising from the coordinates transformation, is compensated by a contribution $\Omega_0 \partial_{\tilde{\phi}}$, arising from the term $(u_\phi / r) \partial_{\tilde{\phi}}$, by substituting $u_\phi = \Omega_0 r + v_\phi$. One can then construct a local model of the near surroundings of r_0, by first introducing a new coordinate (see, e.g., Goldreich & Lynden-Bell 1965; Toomre 1981; Balbus & Hawley 1998)

$$x := r - r_0. \tag{10.115}$$

The transformation from $(r, \tilde{\phi}, z)$ to $(x, \tilde{\phi}, z)$ has only consequences for those terms that contain parameters, which depend on r explicitly. Some of theses parameters are of the form $1/r = 1/(r_0 + x)$.

As the goal is to construct a local model, one can demand that $|x|/r_0 \ll 1$, and use $1/r \sim 1/r_0$. The only remaining dependencies on r, occurring in the radial equation, are $-\Omega^2(r)\, r$ and $\Omega_0^2(r)\, r$, which can be evaluated together, see Appendix C, yielding the specific tidal force

$$-\Omega^2\, r + \Omega_0^2\, r \sim 3\Omega_0^2 x. \tag{10.116}$$

For the corresponding gravity term in the vertical equation, one obtains $-\Omega^2 z \sim -\Omega_0^2 z$. As a final step, one introduces a new coordinate $y = r_0\phi$, changing the angular derivatives to $\partial_{\tilde{\phi}} = r_0 \partial_y$. Note that the dimension of y is now a length, similar to x. Hence, demanding $|y|/r_0 \ll 1$, the new coordinate system (x, y, z) almost resembles a Cartesian coordinate system, co-rotating at $x = y = 0$. In fact, substituting the previous changes into Eqs. 10.112, one obtains a form of the Euler equation that is reminiscent to that in Cartesian coordinates:

$$\frac{\partial \mathbf{v}}{\partial t} + (\mathbf{v}\cdot\nabla)\,\mathbf{v} = -\frac{1}{\rho}\nabla P + \frac{1}{\rho}\mathbf{f}_{\text{ext}} - 2\boldsymbol{\Omega}_0 \times \mathbf{v} + 3\Omega_0^2 x\hat{\mathbf{e}}_x + \Omega_0^2 z\hat{\mathbf{e}}_z + \frac{v_y^2}{r_0}\hat{\mathbf{e}}_x - \frac{v_x v_y}{r_0}\hat{\mathbf{e}}_x. \tag{10.117}$$

The last two terms, v_y^2/r_0 and $v_x v_y/r_0$, represent effects arising from the curvature of the orbital motion. For thin disks, these may also be neglected. To see this, one first introduces typical scales. The time scale is simply given by the inverse orbital frequency, Ω_0^{-1}. The turbulent velocities are typically of the order of the sound speed, c_s, as much higher velocities would quickly dissipate kinetic energy via shocks (see, e.g., Shakura & Sunyaev 1973). Hence, one finds

$$\frac{v_y^2}{r_0} \sim \frac{c_s^2\Omega_0}{r_0\Omega_0} \sim c_s\Omega_0\frac{H}{r_0}, \tag{10.118}$$

whereby in the last step, the vertical scale height $H = c_s/\Omega_0$ (see Sect. 3.1.2) has been used. This can be compared to the term $|\partial_t \mathbf{v}| \sim c_s\Omega_0$, indicating that v_y^2/r_0 (and similarly $v_x v_y/r_0$) is smaller by a factor of H/r_0. Hence, for thin disks, the curvature terms may be neglected. Equivalently, this can be interpreted such that the fluctuating velocity must be much smaller than the orbital velocity (see, e.g., Balbus & Hawley 1998). With that, one obtains the Euler equation in a local, Cartesian coordinate system (x, y, z), co-rotating at $(r_0, \phi_0 = \Omega_0 t)$:

$$\frac{\partial \mathbf{v}}{\partial t} + (\mathbf{v}\cdot\nabla)\,\mathbf{v} = -\frac{1}{\rho}\nabla P + \frac{1}{\rho}\mathbf{f}_{\text{ext}} - 2\boldsymbol{\Omega}_0 \times \mathbf{v} + 3\Omega_0^2 x\hat{\mathbf{e}}_x + \Omega_0^2 z\hat{\mathbf{e}}_z. \tag{10.119}$$

Appendix I

Thermal energy balance

The total energy, used in Eq. 4.8, contains a kinetic part ($\rho|\mathbf{v}|^2/2$), a magnetic part ($|\mathbf{B}|^2/(2\mu_0)$), and a thermal part (E_{th}). Equations for the kinetic energy, and the magnetic energy, follow by multiplying Eq. 4.6 with $\mathbf{v}$, and Eq. 4.7 with $\mathbf{B}$, respectively. What remains, is an equation for the thermal energy density. The latter follows from the first law of thermodynamics, $dU = T\,dS - P\,dV$, whereby U is the internal energy, and S is the entropy, of a mass M of gas, contained in V (see, e.g., Clarke & Carswell 2007). The mass is assumed to be constant, and one can divide the second law by M, yielding (see, e.g., Regev, Umurhan, & Yecko 2016)

$$d\epsilon = T\,ds + \frac{P}{\rho^2}\,d\rho, \tag{10.120}$$

whereby, the mass-specific quantities $\epsilon = U/M$ (specific energy), $s = S/M$ (specific entropy), and $1/\rho = V/M$ (specific volume) were introduced. The thermal energy density is linked to the specific energy via $E_{th} = \rho\epsilon$, and, therefore,

$$dE_{th} = \epsilon\,d\rho + \rho\,d\epsilon = \left(\epsilon + \frac{P}{\rho}\right)\,d\rho + \rho\,T ds. \tag{10.121}$$

In the fluid prescription, V may be interpreted as a volume that is co-moving with the fluid, guaranteeing that the mass content really is constant. Especially, one could consider an infinitesimally small volume element, δV, such that all quantities are constant in δV. Say the volume element follows a trajectory $\mathbf{x}(t)$, then small variations in the quantity $f(t, \mathbf{x}(t))$ can be expressed via the material derivative $df = (\partial_t f + \mathbf{v} \cdot \nabla f)\, dt$ (see, e.g., Clarke & Carswell 2007; Regev, Umurhan, & Yecko 2016). Substituting this into Eq. 10.121, and using the continuity equation to write $-\rho(\nabla \cdot \mathbf{v}) = \partial_t \rho + \mathbf{v} \cdot \nabla \rho$, one obtains

$$\partial_t E_{th} + \nabla \cdot (E_{th} \mathbf{v}) = -P(\nabla \cdot \mathbf{v}) + \rho \dot{q}, \tag{10.122}$$

whereby the term $\rho T\, (\partial_t s + \mathbf{v} \cdot \nabla s)$ is subsumed into $\rho \dot{q}$ (see, e.g., Clarke & Carswell 2007). Hence, this then provides the evolution equation for the thermal energy density. The first term, on the left hand side, represents the net rate of change of the thermal energy, in a given volume. The remaining terms are the causes for that change. The second term, on the left hand side, accounts for the fluxes of thermal energy over the boundary surface of that volume. The first term, on the right hand side, is the volumetric production and reduction of thermal energy, by compression and expansion of the fluid, respectively. To get an interpretation of the the last term, on can rewrite the latter in the following way:

$$\rho \dot{q} = T(\partial_t(\rho s) + \mathbf{v} \cdot \nabla(\rho s)) - Ts(\partial_t \rho + \mathbf{v} \cdot \nabla \rho) = T\left[\partial_t(\rho s) + \nabla \cdot (\rho s \mathbf{v})\right]. \tag{10.123}$$

The quantity ρs is the entropy density, or entropy per volume. Hence, integrated over a given volume, the term $\partial_t(\rho s) + \nabla \cdot (\rho s \mathbf{v})$ represents the net change of entropy in that volume, minus entropy fluxes across the boundaries of that volume. Put differently, it represents sources and sinks for entropy. In the energy equation, this term accounts for all additional heating (cooling) sources. Hence, the term $\rho \dot{q}$ is here referred to as cooling (heating) term (see also Clarke & Carswell 2007). One additional note about the naming: The lower-case q is meant to represent a given amount of heat per mass. Consequently, $\dot{q}$ is a per-mass heating rate. The volumetric heating rate is then proportional to the mass density, $\rho \dot{q}$.

Appendix J

Derivation of the razor-thin equations

The goal here is to briefly demonstrate how the razor-thin version of the momentum equation, Eq. 4.42, in Sect. 4.5.1, follows from the three-dimensional version, Eq. 4.6, by integrating over all z. Starting point is the fully three-dimensional Euler equation, in the following form

$$\rho \partial_t \mathbf{v} + \rho(\mathbf{v} \cdot \nabla \mathbf{v}) = -\nabla P - \rho \nabla \Phi - 2\rho \mathbf{\Omega}_0 \times \mathbf{v} + 3\rho \Omega_0^2 x \mathbf{e}_x - \rho \Omega_0^2 z \mathbf{e}_z. \tag{10.124}$$

One then substitutes the ansatz,

$$\rho(x, y, z) = \Sigma(x, y)\, \delta(z) \qquad P(x, y, z) = P_{(2)}(x, y)\, \delta(z), \tag{10.125}$$

into the Euler equation, yielding

$$\Sigma\, \delta(z) \partial_t \mathbf{v} + \Sigma\, \delta(z)(\mathbf{v} \cdot \nabla \mathbf{v}) = -\nabla \left(P_{(2)}\, \delta(z)\right) - \Sigma\, \delta(z) \nabla \Phi - 2\Sigma\, \delta(z) \mathbf{\Omega}_0 \times \mathbf{v} + 3\Sigma\, \delta(z) \Omega_0^2 x \mathbf{e}_x - \Sigma\, \delta(z) \Omega_0^2 z \mathbf{e}_z. \tag{10.126}$$

It is noted that the velocity, $\mathbf{v}$, technically has three components, but since the fluid is restricted to the mid plane, only v_x, and v_y are non-zero. One then integrates the former equation over all z ($\int_{-\infty}^{\infty} dz ...$), obtaining

$$\Sigma \partial_t \mathbf{v} + \Sigma(\mathbf{v} \cdot \nabla \mathbf{v}) = -\nabla_{(2)} P_{(2)} - \Sigma \nabla_{(2)} \Phi(x, y, 0) - 2\Sigma \mathbf{\Omega}_0 \times \mathbf{v} + 3\Sigma \Omega_0^2 x \mathbf{e}_x. \tag{10.127}$$

Rewriting into conservative form, one exactly recovers Eq. 4.42, of Sect. 4.5.1. The nabla operators, acting on both $P_{(2)}$ and Φ, reduce to the two-dimensional gradient, $\nabla_{(2)} = (\partial_x, \partial_y)$. For the pressure contribution, that is the case because, due to the vertical integration, $\partial_z \left(P_{(2)}\, \delta(z) \right)$ has to be evaluated at infinity, where $\delta(z)$ is zero. The self-gravity term is different, because $\delta(z)$ appears outside of the gradient. Hence, after the integration, the gradient is merely evaluated at $z = 0$. However, the potential must be symmetric, with respect to $z = 0$, and, hence, one can argue that $\partial_z \Phi = 0$, at the mid plane. Obviously, the term $\propto z$, corresponding to the vertical component of the central objects gravity, vanishes in the razor-thin limit. A similar procedure can be applied to the remaining fluid equation, yielding Eqs. 4.41 - 4.43, of Sect. 4.5.1.

Appendix K

Cooling time scale

Provided here is a more in-depth discussion of the cooling time, τ_c, introduced in Sect. 4.5.3. The motivation follows closely that provided in Rafikov (2005), Rafikov (2009), Kratter, Murray-Clay, & Youdin (2010), and Kratter & Lodato (2016). It is first assumed that radiation is emitted and absorbed at the two disk surfaces. Say that the rate of turbulent energy production (energy released by accretion), per area, is denoted by $\mathcal{H}$, and the flux of energy, associated with external irradiation, is denoted by $\mathcal{H}_{\rm ext}$. Assuming that a disk surface radiates like a black body, then a local, stationary energy balance requires that (see, e.g., Rafikov 2009; Kratter, Murray-Clay, & Youdin 2010; Kratter & Lodato 2016):

$$\sigma T_{\rm sur}^4 = \mathcal{H}_{\rm ext} + \frac{1}{2}\mathcal{H}. \tag{10.128}$$

Therein, $T_{\rm sur}$ is the surface temperature of the disk. The factor of $1/2$ arises, because the energy, released by the turbulence, is assumed to distribute equally to both disk surfaces. Hence, $\sigma T_{\rm sur}^4$ represents the overall loss of energy by radiation, at one disk surface, and per unit surface area. This is balanced by the net heating rate per unit surface area, given by $\mathcal{H}_{\rm ext} + \mathcal{H}/2$. One could also associate the irradiation flux with an effective temperature, by defining $\mathcal{H}_{\rm ext} =: \sigma T_0^4$. The thermal energy density per surface area, $E_{th}^{(z)}$, is mostly dominated by the higher mid plane temperature. Hence, it is convenient to first express $T_{\rm sur}$ in terms of the mid-plane temperature T. This is achieved, by estimating the radiative transport properties in the vertical direction, yielding (see, e.g., Balbus & Hawley 1998; Kratter & Lodato 2016)

$$T^4 = \frac{3}{8} f(\tau) T_{\rm sur}^4, \tag{10.129}$$

whereby the optical depth, $\tau = \int \kappa \rho \, dz$, with the opacity κ, was introduced. The function $f(\tau) = \tau + 1/\tau$ transitions continuously from the optically thin ($\tau \ll 1$), to the optically thick ($\tau \gg 1$) regime (see Rafikov 2005). The integral for the optical depth may be estimated to be $\tau \sim \kappa\Sigma/2$ (see, e.g., Rafikov 2005; Kratter & Lodato 2016). For simplicity, we first neglect external irradiation (or other heating sources), and equate the cooling model in Eq. 4.45, with $2\sigma T_{\rm sur}^4$, whereby the latter factor two arises from the two disk surfaces. This then yields (see, e.g., Kratter, Murray-Clay, & Youdin 2010):

$$\frac{16\, T^4}{3\, f(\tau)} = \frac{E_{th}^{(z)}}{\tau_c} = \frac{\Sigma c_{s,i}^2}{(\gamma - 1)\tau_c} \tag{10.130}$$

$$\Rightarrow \tau_c = \frac{3 f(\tau)}{32(\gamma - 1)} \frac{\Sigma c_{s,i}^2}{T^4}. \tag{10.131}$$

Hence, for given radial profiles of the surface density, Σ, and temperature, T, one can estimate the typical cooling time scale. It is noted that one also has to specify the opacity, $\kappa(T)$, which can also

be a function of the temperature. One often uses a temperature dependence of the form $\kappa = \kappa_0 T^b$, with $0 \leq b \leq 2$ (see, e.g., Rafikov 2009; Kratter, Murray-Clay, & Youdin 2010). And in Kratter, Murray-Clay, & Youdin (2010), this expression for the cooling time was extended to cases with additional heating (e.g., via irradiation), yielding:

$$\tau_c = \frac{3\gamma\Sigma c_{s,i}^2 \tau}{32(\gamma-1)\sigma T^4} \begin{cases} 1/(1-b/4) & \text{for } T \gg T_0, b \neq 4 \\ 1 & \text{for } T \sim T_0. \end{cases} \tag{10.132}$$

Appendix L

Vertical stratification

In three-dimensional, shearing-box simulations, with both vertical gravity and self-gravity, some form of vertical stratification must arise. The following consideration aims to convey how such a stratification equilibrium is established. Magnetic fields are not considered for the initial profile. In general, the background equilibrium consists of horizontally homogeneous (no xy dependence) profiles of both density, $\rho(z)$, and a pressure, $P(z)$. The equilibrium solution for the velocity is the shear flow, $\mathbf{v}_0 = -q\Omega_0 x \mathbf{e}_y$. Substituting these assumptions into the Euler equation (i.e., Eq. 4.6), and taking the vertical component, one finds (see also Shi & Chiang 2014)

$$-\frac{1}{\rho}\partial_z P - \partial_z \Phi - \partial_z \Phi^\star = 0. \tag{10.133}$$

Φ is the gravitational potential due to self-gravity, and $\Phi^\star = (1/2)\Omega_0^2 z^2$ is the vertical contribution from the central object's potential (see also Appendix C). Eq. 10.133 contains both ρ and P, and one would wish to express the pressure in terms of the density. It is always possible to write $P(z) = c_{s,i}^2(z)\,\rho(z)$, although this only replaces the pressure by the isothermal sound speed, $c_{s,i}(z)$, as the new variable. Hence, some assumption is required for $c_{s,i}$. As one is only interested in an initial state, it is simplest to assume a vertically constant sound speed, that is $c_{s,i}(z) = \text{const}$. This corresponds to a vertically isothermal disk (although a more general law, $P = C\,\rho^{\gamma_p}$, with polytropic index γ_p, would also work, see, e.g., Shi & Chiang 2014). Using $c_{s,i} = \text{const.}$, and neglecting self-gravity, Eq. 10.133 can be solved analytically, yielding the Gaussian density (and pressure) profile, given by Eq. 3.4, of Sect. 3.1.2. If self-gravity is taken into account, one will have to use a different approach. As a first step, one can calculate the derivative of Eq. 10.133, towards z, yielding

$$\frac{c_{s,i}^2}{\rho^2}(\partial_z\rho)^2 - \frac{c_{s,i}^2}{\rho}\partial_z^2\rho - \partial_z^2\Phi - \partial_z^2\Phi^\star = 0, \tag{10.134}$$

whereby $c_{s,i} = \text{const.}$ is used. One can then use Poisson's equation, to express the potential of self-gravity in terms of the mass density, $\partial_z^2\Phi = 4\pi G\rho$. This then yields

$$\frac{c_{s,i}^2}{\rho^2}(\partial_z\rho)^2 - \frac{c_{s,i}^2}{\rho}\partial_z^2\rho - 4\pi G\rho - \Omega_0^2 = 0, \tag{10.135}$$

whereby $\Phi^\star = (1/2)\Omega_0^2 z^2$ was substituted. The latter is a second order, nonlinear, differential equation for the mass density $\rho(z)$. By introducing the new variable $\psi := \partial_z\rho$, this second order equation can be expressed as a system of two, first-order differential equations:

$$\begin{aligned} \partial_z\psi &= \frac{1}{\rho}(\partial_z\rho)^2 - \frac{4\pi G}{c_{s,i}^2}\rho^2 - \frac{\Omega_0^2}{c_{s,i}^2}\rho \\ \partial_z\rho &= \psi. \end{aligned} \tag{10.136}$$

The latter set of equations is solved once at the simulation start, using a Runge-Kutta fourth-order (RK4) method. The RK4 routine takes the mid-plane density, $\rho_0 = \rho(z=0)$, and the sound speed,

$c_s = \sqrt{\gamma}\, c_{s,i}$, as input parameters. Starting at the mid plane ($z = 0$), the RK4 routine integrates towards the upper z boundary ($z = L_z/2$), thereby assuming $\psi(z = 0) = 0$, due to mirror-symmetry with respect to the mid-plane. The values for $-L_z/2 \leq z < 0$ are obtained by mirroring the values for $0 < z \leq L_z/2$. In cases with additional background heating, see Eq. 4.54, the initial $c_{s,0}$ is mostly chosen such, that it corresponds to the equilibrium between the heating and cooling term. In most of the simulations, shown in Löhnert & Peeters (2022), and Sect. 9, the units are chosen such that $c_{s,0} = 1$.

Appendix M

On the handling of wave-vectors in Athena

The method of calculating the potential of self-gravity, Φ, relies on the usage of FFTs, see Sect. 4.6.4. The indices of the FFT-output array, say n, in a one-dimensional case, are mapped to wave vectors, according to (see also Eq. 4.59)

$$k_n := \begin{cases} \frac{2\pi n}{L} & \text{for} \quad n \in \{0, ..., \frac{N}{2}\} \\ \frac{2\pi(n-N)}{L} & \text{for} \quad n \in \{\frac{N}{2}+1, ..., N-1\} \end{cases} . \tag{10.137}$$

The physical domain size is given by L, and the corresponding number of grid points is N. For $n \leq N/2$, the wave vector increases with n. However, at $N/2$, the wave vector flips sign, cycling through all negative wave vectors. Hence, the absolute value, $|k_n| = \sqrt{k_n^2}$, has an edge at $n = N/2$, see the black curve in Fig. 10.19. For the actual implementation, this means that a case separation for n has to be applied. However, there is a way to avoid this case separation, by deviating from the exact definition of $|k_n|$, for large n. This is shown by the red curve, in Fig. 10.19. Instead of calculating $|k_n| = \sqrt{k_n^2}$, the red curve assumes the modified absolute value

$$|k_n|_{\text{mod}} = \sqrt{2\frac{\cos\left(\frac{2\pi n}{N}\right) - 1}{dx^2}}, \tag{10.138}$$

with $dx = L/N$. This automatically includes the sign-change of k_n, without the need for a case separation, with respect to n. For small $|k_n|$, one finds $|k_n| \sim |k_n|_{\text{mod}}$, and a deviation only occurs for larger n. To see that, one can evaluate $|k_n|_{\text{mod}}$, for $n/N \ll 1$, yielding

$$\begin{aligned} |k_n|_{\text{mod}} &= \sqrt{2\frac{\cos\left(\frac{2\pi n}{N}\right) - 1}{dx^2}} = \sqrt{\frac{4\sin^2\left(\frac{\pi n}{N}\right)}{dx^2}} = \sqrt{\frac{\left(\frac{2\pi n}{N}\right)^2 + \mathcal{O}\left(\left(\frac{2\pi n}{N}\right)^4\right)}{dx^2}} \\ &\sim \sqrt{\frac{\left(\frac{2\pi n}{N}\right)^2}{\left(\frac{L}{N}\right)^2}} = \frac{2\pi n}{L}. \end{aligned} \tag{10.139}$$

This corresponds to the expected result, for small wave vectors. The above method can also be expanded to more than one dimension. For example, in the two-dimensional case, one defines

$$|k_{mn,\text{mod}}| = |(k_{x,n}, k_{y,n})|_{\text{mod}} = \sqrt{2\frac{\cos\left(\frac{2\pi m}{N_x}\right) - 1}{dx^2} + 2\frac{\cos\left(\frac{2\pi n}{N_y}\right) - 1}{dy^2}}, \tag{10.140}$$

with $dx = L_x/N_x$, $dy = L_y/N_y$. Also here, in the limit $m/N_x, n/N_y \ll 1$, one finds $|k_{mn}|^2_{\text{mod}} = (2\pi m/N_x)^2 + (2\pi n/N_y)^2$, consistent with the two-dimensional, Euclidean distance. For the actual implementation of the Poisson solver, detailed in Sect. 4.6.4, the here-described method of calculating k_{mn} is applied. Thereby, it is noted that this is also the pre-implemented version in Athena, used for the original, periodic solver.

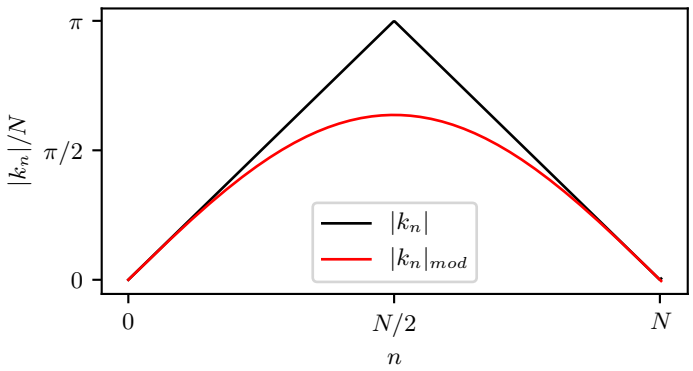

Figure 10.19: Depicted is a visualisation of the method, used to calculate absolute values of wave vectors. The black curve is the actual absolute value. At $n = N/2$, the wave vectors switch to negative values, and the curve for the absolute value has an edge. The red curve is an approximation, continuously switching between the positive, and negative wave-vector regimes.

Appendix N

Alternative derivation of G_{mnl}

Provided here is an alternative derivation for the case $k_{mn} = 0$, in Sect. 4.6.4. One starts by substituting Eq. 4.63 into Eq. 4.65, whereby it is simultaneously assumed that $k_{mn} = 0$:

$$
\begin{aligned}
G_{mnl} &= \frac{4\pi G}{2} \sum_{p=0}^{2N_z-1} \exp\left(-2\pi i \frac{(p-N_z)l}{2N_z}\right) \cdot \left|\frac{(p-N_z)L_z}{N_z}\right| \\
&= \frac{4\pi G}{2} \sum_{p=0}^{N_z-1} e^{i\pi l} \exp\left(-\pi i \frac{pl}{N_z}\right) \frac{(N_z-p)L_z}{N_z} + \frac{4\pi G}{2} \sum_{p=N_z}^{2N_z-1} e^{i\pi l} \exp\left(-\pi i \frac{pl}{N_z}\right) \frac{(p-N_z)L_z}{N_z} \\
&= \frac{4\pi G}{2} \sum_{p=0}^{N_z-1} e^{i\pi l} \exp\left(-\pi i \frac{pl}{N_z}\right) (L_z - p\delta_z) + \frac{4\pi G}{2} \sum_{p=N_z}^{2N_z-1} e^{i\pi l} \exp\left(-\pi i \frac{pl}{N_z}\right) (p\delta_z - L_z) \\
&= \frac{4\pi G}{2} \sum_{p=0}^{N_z-1} e^{i\pi l} \exp\left(-\pi i \frac{pl}{N_z}\right) (L_z - p\delta_z) + \frac{4\pi G}{2} \sum_{p=0}^{N_z-1} \exp\left(-\pi i \frac{pl}{N_z}\right) p\delta_z \\
&= 4\pi G \frac{\delta_z}{2} \left(1 - e^{i\pi l}\right) \sum_{p=0}^{N_z-1} p \cdot \exp\left(-\frac{i\pi l}{N_z} p\right) + 4\pi G \frac{L_z}{2} e^{i\pi l} \sum_{p=0}^{N_z-1} \exp\left(-\frac{i\pi l}{N_z} p\right) \\
&=: 4\pi G \left(\frac{\delta_z}{2}\left(1 - e^{i\pi l}\right) \cdot S_1 + \frac{L_z}{2} e^{i\pi l} \cdot S_2\right). \qquad (10.141)
\end{aligned}
$$

In the last step, the sums S_1 and S_2 were introduced, which can be further simplified, by identifying a geometric series (see, e.g., Bronstein et al. 2012). First, the abbreviation $c_l = \exp\left(-i\pi l/N_z\right)$ is

used, whereby $c_l^{-1} = \exp(i\pi l/N_z) = c_l^\star = c_{-l}$. With that, one finds, for the easier case of S_2,

$$\begin{aligned} S_2 &= \sum_{p=0}^{N_z-1} c_l^p = \frac{1-c_l^{N_z}}{1-c_l} = \frac{1-e^{i\pi l}}{1-c_l} = \\ &\text{(...)} \quad \text{The following manipulations are of use, later} \\ &= \frac{(1-e^{i\pi l})(1-c_l)}{(1-c_l)^2} = \frac{1-c_l-e^{i\pi l}+c_l e^{i\pi l}}{1+2c_l+c_l^2} \\ &= \frac{c_l}{c_l}\cdot\frac{q^{-1}-1-c_l^{-1}e^{i\pi l}+e^{i\pi l}}{c_l^{-1}+c_l+2} = \frac{(e^{i\pi l}-1)(1-c_l^{-1})}{c_l^{-1}+c_l-2}. \end{aligned} \tag{10.142}$$

The remaining sum, S_1, can be evaluated by realizing that it is connected to the derivative of S_2:

$$\begin{aligned} S_1 &= \sum_{p=0}^{N_z-1} p c_l^p = c_l \sum_{p=1}^{N_z-1} p c_l^{p-1} = c_l \frac{d}{dc_l}\left(\sum_{p=1}^{N_z-1} c_l^p\right) = \underbrace{c_l \frac{d}{dc_l}\left(\sum_{p=0}^{N_z-1} c_l^p\right)}_{c_l^p=1 \text{ for } p=1} \\ &= c_l \frac{d}{dc_l}\left(\frac{1-c_l^{N_z}}{1-c_l}\right) = c_l \frac{1-c_l^{N_z}}{(1-c_l)^2} - c_l \frac{N_z c_l^{N_z-1}}{(1-c_l)} = c_l \frac{1-c_l^{N_z}-N_z(c_l^{N_z-1}-c_l^{N_z})}{(1-c_l)^2} \\ &= c_l \frac{1-N_z c_l^{N_z-1}+(N_z-1)c_l^{N_z}}{(1-c_l)^2} = \underbrace{c_l \frac{1-N_z e^{i\pi l}c_l^{-1}+(N_z-1)e^{i\pi l}}{(1-c_l)^2}}_{c_l^{N_z}=e^{i\pi l}} \\ &= \frac{(1-e^{i\pi l})+N_z e^{i\pi l}(1-c_l^{-1})}{c_l^{-1}+c_l-2}. \end{aligned} \tag{10.143}$$

One then substitutes S_1 (Eq. 10.143), and S_2 (Eq. 10.142) into Eq. 10.141. By further utilising that $c_l^{-1} + c_l = 2\cos(i\pi l/N_z)$, one finds

$$\begin{aligned} G_{mnl} &= 4\pi G\left(\frac{\delta_z}{2}(1-e^{i\pi l})\frac{(1-e^{i\pi l})+N_z e^{i\pi l}(1-c_l^{-1})}{c_l^{-1}+c_l-2} + \frac{\delta_z N_z}{2}e^{i\pi l}\frac{(e^{i\pi l}-1)(1-c_l^{-1})}{c_l^{-1}+c_l-2}\right) \\ &= \frac{4\pi G\,\delta_z}{2}\frac{(1-e^{i\pi l})^2+N_z e^{i\pi l}(1-c_l^{-1})(1-e^{i\pi l})+N_z e^{i\pi l}(e^{i\pi l}-1)(1-c_l^{-1})}{2\cos\left(\frac{\pi l}{N_z}\right)-2} \\ &= \frac{4\pi G\,\delta_z}{2}\frac{1-e^{i\pi l}}{\cos\left(\frac{\pi l}{N_z}\right)-1}. \end{aligned} \tag{10.144}$$

Hence, one can also recover Eq. 4.71, by directly evaluating the sum.

References Appendix

Balbus, Steven A. and John F. Hawley (1998). "Instability, turbulence, and enhanced transport in accretion disks". In: *Reviews of modern physics* 70.1, p. 1.

Brandenburg, Axel and Kandaswamy Subramanian (2005). "Astrophysical magnetic fields and nonlinear dynamo theory". In: *Physics Reports* 417.1-4, pp. 1–209.

Brandenburg, Axel et al. (1995). "Dynamo-generated turbulence and large-scale magnetic fields in a Keplerian shear flow". In: *The Astrophysical Journal* 446, p. 741.

Bronstein, Ilja N. et al. (2012). *Taschenbuch der Mathematik*. 8th ed. Harri Deutsch.

Chiuderi, Claudio and Marco Velli (2015). *Basics of Plasma Astrophysics*. Springer.

Clarke, Cathie and Bob Carswell (2007). *Principles of astrophysical fluid dynamics*. Cambridge University Press.

Goldreich, Peter and D. Lynden-Bell (1965). "II. Spiral arms as sheared gravitational instabilities". In: *Monthly Notices of the Royal Astronomical Society* 130.2, pp. 125–158.

Jackson, John David (2014). *Klassische Elektrodynamik*. 3rd ed. de Gruyter.

Kratter, Kaitlin and Giuseppe Lodato (2016). "Gravitational Instabilities in Circumstellar Disks". In: *Annual review of astronomy and astrophysics* 54.1, pp. 271–311.

Kratter, Kaitlin M., Ruth A. Murray-Clay, and Andrew N. Youdin (2010). "The runts of the litter: Why planets formed through gravitational instability can only be failed binary stars". In: *The Astrophysical Journal* 710.2, p. 1375.

Löhnert, L. and A. G. Peeters (2022). "Combined dynamo of gravitational and magneto-rotational instability in irradiated accretion discs". In: *Astronomy and Astrophysics* 663, A176.

Lynden-Bell, D. and A. J. Kalnajs (1972). "On the generating mechanism of spiral structure". In: *Monthly Notices of the Royal Astronomical Society* 157.1, pp. 1–30.

Rafikov, Roman R. (2005). "Can giant planets form by direct gravitational instability?" In: *The Astrophysical Journal* 621.1, p. L69.

— (2009). "Properties of gravitoturbulent accretion disks". In: *The Astrophysical Journal* 704.1, p. 281.

Regev, Oded, Orkan M. Umurhan, and Philip A. Yecko (2016). *Modern fluid dynamics for physics and astrophysics*. Springer.

Shakura, N. (2018). *Accretion flows in astrophysics*. Ed. by N. Shakura. Vol. 454. Springer.

Shakura, N. I. and Rashid Alievich Sunyaev (1973). "Black holes in binary systems. Observational appearance." In: *Astronomy & Astrophysics* 24, pp. 337–355.

Shi, Ji-Ming and Eugene Chiang (2014). "Gravito-turbulent disks in three dimensions: Turbulent velocities versus depth". In: *The Astrophysical Journal* 789.1, p. 34.

Toomre, Alar (1981). "What amplifies the spirals". In: *Structure and evolution of normal Galaxies*. Cambridge University Press, pp. 111–136.

Eidesstattliche Versicherung

Hiermit versichere ich an Eides statt, dass ich die vorliegende Arbeit selbstständig verfasst und keine anderen als die von mir angegebenen Quellen und Hilfsmittel verwendet habe.

Weiterhin erkläre ich, dass ich die Hilfe von gewerblichen Promotionspartnern bzw. -vermittlern oder ähnlichen Dienstleistern weder bisher in Anspruch genommen habe, noch künftig in Anspruch nehmen werde.

Zusätzlich erkläre ich hiermit, dass ich keinerlei frühere Promotionsversuche unternommen habe.

Bayreuth, den

Unterschrift